# The Ultra-Selective Hydrogenation of Furfural on PtCu Supported Bimetallic Nanoparticles and on Pt(111) under Ultra-High Vacuum

being a thesis submitted for the degree of Doctor of Philosophy at

Aston University

Martin J. Taylor
MChem (University of Hull)

Chemical Engineering and Applied Chemistry

&

European Bioenergy Research Institute

June 2017

# Thesis Summary

The selective transformation of furfural, a biomass platform molecule, was studied on Pt based heterogeneous catalysts and model single crystal surfaces. Hydrogenation reactions were carried out at pressures ranging from ultra-high vacuum to 20 bar. Temperature Programmed Desorption data in conjunction with Scanning Tunnelling Microscopy suggest that the decarbonylation of furfural on clean Pt(111) and the hydrogenation of furfural on hydrogen pre-covered Pt(111) is governed by surface crowding, molecular orientation and hydrogen bonding networks of the adsorbed molecules. Liquid phase experimentation on Pt nanoparticles, dispersed on a wide range of oxide supports, show that Pt is a very active hydrogenation catalyst even at very mild temperature and pressure conditions. The reaction was found to be highly dependent on the solvent used, while catalyst support is critical for maintaining thermally stable, monodisperse nanoparticles. The addition of Cu into Pt nanoparticles was investigated in a range of Pt:Cu metal molar ratios varying from pure Pt to pure Cu. This was achieved by using a modified polyol synthesis to generate colloidal nanoparticles, followed by thermal processing. Bimetallic particles synthesized using a sulphur free Cu precursor, were found to be beneficial for the suppression of CO adsorption, normally a poison for this reaction, which is formed from the decarbonylation of furfural. The alloying of these two metals had a profound effect on the overall catalytic activity by providing superior initial rates of reaction and catalytic turnover, as well as achieving high selectivities towards furfuryl alcohol, surpassing the behaviour of pure Pt catalyst across 3 different pressures. Finally, Single Atom Alloys (SAA), formed via the galvanic replacement of dispersed host Cu nanoparticles by Pt was investigated. Pt:Cu nanoparticles with atomic ratios ranging from 1:20 to 0.5:250 were synthesized and tested. After overcoming a brief induction period due to the reduction of surface CuO and possibly the reordering of the surface atoms, SAAs exhibit extremely high rates of hydrogenation, surpassing the catalytic turnover for monometallic and bimetallic catalysts. These cutting edge materials are at the frontier of catalyst research, proving to be ideal materials for the future of green chemistry due to both their activity and economic viability.

# Acknowledgements

To begin with I would like to extend a huge thanks to my supervisor, Dr Georgios Kyriakou. Without his time, effort, style and being an exceptional Surface Scientist, this PhD project would not have been possible. His expert guidance in overcoming the many hurdles I encountered is especially appreciated. My gratitude to the University of Hull, where I began my PhD studies in 2013 before transferring in 2015 to Aston University and continuing in the European Bioenergy Research Institute. I would like to thank Professors Adam F. Lee and Karen Wilson for supplying the means to complete UHV measurements, as well as making it possible for us to relocate to Birmingham.

There are many people I have met along the way and I am sure it would be impossible to name everyone. However, I extend my gratitude to you all! Next, I would like to thank the Surface, Materials and Catalysis group in EBRI for being extremely welcoming and accommodating upon our relocation. Special thanks go to Drs Christopher M. A. Parlett, Mark A. Isaacs and Lee J. Durndell for their expert knowledge and support with TEM and XPS. I would also like to offer my sincere gratitude to collaborators and colleagues who have supported me. Firstly, my thanks go to Dr Simon K. Beaumont (Durham University), whose extensive knowledge has been of great assistance over the past 3 years. Next, a thank you to Dr Anthoula C. Papageorgiou and Professor Johannes V. Barth (Technical University of Munich) for STM measurements. Also, I am grateful to Professor Richard M. Lambert and Dr Juan Pedro Holgado at Cambridge University and the Instituto de Ciencia de Materiales de Sevilla (CSIC) for fruitful discussions and assistance.

Nearer to home, I would like to mention my family. Mam. Dad. Good job for having me! Seriously though, Janice Taylor, Derek Taylor and Kayleigh Taylor, thank you for being supportive over the years. Also, my gratitude goes to Mr Neil Kirman for agreeing to proof read this thesis and correct my often fragmented English and expressive phrasing. Finally, a special heartfelt thank you to Dr Bethany J. Newton, small in stature but large in heart. At the time of writing, you have been with me almost 10 years. College, Undergrad and throughout our PhDs, even during the year apart while I began work in Birmingham. After all this time, I reckon we can say we are still an effective team. I love you x.

# Publications and presentations

I declare that the work presented in this thesis is original, my own, and has not been previously submitted for examination for any other award. I hereby give consent for my thesis, if accepted, to be available for photocopying and for inter-library loan, and for the title and summary to be made available to outside organisations. Some of the work that has formed parts of this thesis has been published in peer reviewed journals, as listed below:

1. **M. J. Taylor**, L. J. Durndell, M. A. Isaacs, C. M. A. Parlett, K. Wilson, A. F. Lee and G. Kyriakou, Highly selective hydrogenation of furfural over supported Pt nanoparticles under mild conditions, *Appl. Catal. B Environ*. 2016, **180**, 580–585. doi:10.1016/j.apcatb.2015.07.006.

2. **M. J. Taylor**, L. Jiang, J. Reichert, A. C. Papageorgiou, S. K. Beaumont, K. Wilson, A. F. Lee, J. V. Barth and G. Kyriakou, Catalytic hydrogenation and hydrodeoxygenation of furfural over Pt(111); a model system for the rational design and operation of practical biomass conversion catalysts, *J. Phys. Chem. C*, 2017, **121**, 8490-8497. doi: 10.1021/acs.jpcc.7b01744.

3. **M. J. Taylor**, M. A. Isaacs, C. M. A. Parlett, S. K. Beaumont, K. Wilson, A. F. Lee and G. Kyriakou, The effect of Cu in PtCu bimetallic and Single Atom Alloy catalysts for the selective hydrogenation of furfural, *ACS Catal*., **In preparation**

# Poster Presentations

1. **Title**: Pt-based heterogeneous catalysts for the selective hydrogenation of biomass derived molecules
   **Authors:** Martin J. Taylor and Georgios Kyriakou
   **Conference:** RSC Organic Division North East Regional meeting
   **Location:** University of Hull, Kingston upon Hull, United Kingdom
   **Date:** 9th April 2014

2. **Title**: Optimising Pt Based Heterogeneous Catalysts for the Hydrogenation of Biomass Derived Molecules
   **Authors:** Martin J. Taylor and Georgios Kyriakou
   **Conference:** Challenges in Catalysis for Pharmaceuticals and Fine Chemicals IV
   **Location:** Royal Society of Chemistry, Burlington House, London, United Kingdom
   **Date:** 5th November 2014

3. **Title**: Ultra-selective energy efficient Pt catalysts for the hydrogenation of biomass derivatives
   **Authors:** Martin J. Taylor and Georgios Kyriakou
   **Conference:** Hull University Student Research Colloquia
   **Location:** University of Hull, Kingston upon Hull, United Kingdom
   **Date:** 15th June 2015

4. **Title**: Highly selective supported nanoparticles for the hydrogenation of furfural under mild conditions
   **Authors:** Martin J. Taylor, Karen Wilson, Adam F. Lee and Georgios Kyriakou
   **Conference:** UK Catalysis Conference 2016
   **Location:** Loughborough University, Loughborough, United Kingdom
   **Date:** 6th - 8th January 2016

5. **Title**: Highly selective supported nanoparticles for the hydrogenation of furfural under mild conditions
   **Authors:** Martin J. Taylor, Karen Wilson, Adam F. Lee and Georgios Kyriakou
   **Conference:** Perspectives On Applied Catalyst Characterization
   **Location:** Royal Society of Chemistry, Burlington House, London, United Kingdom
   **Date:** 8th March 2016

6. **Title**: Highly selective supported nanoparticles for the hydrogenation of furfural under mild conditions
   **Authors:** Martin J. Taylor, Karen Wilson, Adam F. Lee and Georgios Kyriakou
   **Conference:** 16th International Congress on Catalysis (ICC 16)
   **Location:** China National Convention Centre**,** Beijing, BJ, China
   **Date:** 3rd - 8th July 2016

# Oral Presentations

1. **Title**: Highly selective platinum based catalysts for the hydrogenation of biomass derived molecules
   **Authors:** Martin J. Taylor and Georgios Kyriakou
   **Conference:** 4th Northern Sustainable Chemistry (NORSC) Post graduate symposium
   **Location:** Huddersfield University, Huddersfield, United Kingdom
   **Date:** 23rd October 2014

2. **Title**: Highly selective supported nanoparticles for the hydrogenation of furfural under mild conditions
   **Authors:** Martin J. Taylor, Karen Wilson, Adam F. Lee and Georgios Kyriakou
   **Conference:** UK Catalysis Conference 2017
   **Location:** Loughborough University, Loughborough, United Kingdom
   **Date:** 6th - 8th January 2017

## Tables of Figures

## Chapter 1 - Introduction



## Chapter 2 - Experimental

## Chapter 3 - The catalytic hydrogenation and HDO of furfural on a Pt extended surface

## Chapter 4 - Highly selective hydrogenation of furfural over supported Pt nanoparticles under mild conditions

## Chapter 5 - The effect of Cu in PtCu bimetallic particles and Single Atom Alloys for the transformation of furfural

## Chapter 6 - Conclusions and Future work

# Table of Contents

# Chapter 1 – Introduction

# 1.0 Introduction

## 1.1 Sustainable chemistry and catalytic systems

Dwindling resources and an imminent energy crisis are of global concern and must be tackled head on by exploiting sustainable resources. These include the use of biomass derived molecules that can be reclaimed from sustainable feedstocks, as well as green methods of achieving desired chemical compounds. A solution can very easily be achieved by utilizing catalytic systems which can be optimized to suit the chemistry at hand. Initially this asks the question, what is a catalyst? The answer to such an enquiry is that a 'catalyst is a substance that accelerates a reaction but does not undergo any chemical change'.[1] It works by lowering the activation energy required for the reaction to commence by providing an alternate reaction pathway at a lower energy. A diagram to illustrate this premise is seen in Figure 1. As a result of these changes in activation energy, more agreeable reaction conditions can be utilized. This involves a change in key reaction parameters such as temperature and pressure. However, many reactions are not straightforward and do not only produce a singular product. As activation barriers are altered and different reaction pathways are made available, this can invoke a broad scope for side reactions.[1,2]

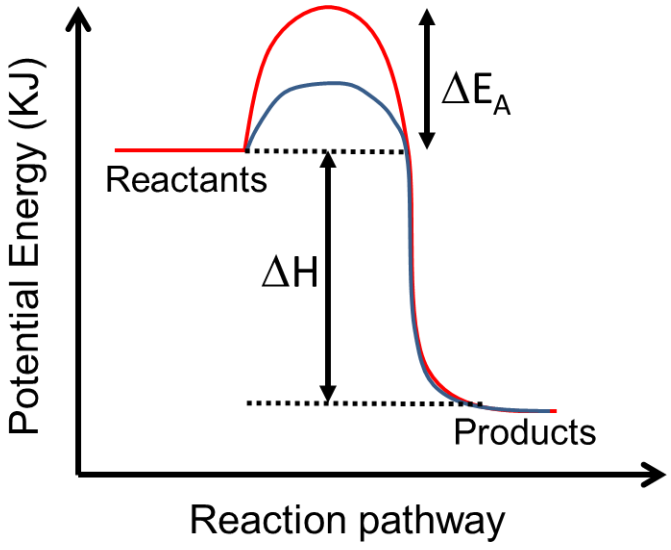


Figure 1 - Potential energy diagram for an exothermic reaction, an uncatalyzed reaction is shown by a solid red line and a catalyzed reaction by a solid blue line.

There are many different substances encapsulated in the term catalyst. Broadly, the area is separated into two distinct fields, heterogeneous and homogenous. From the Greek term 'genos' meaning kind and incorporating the English prefix of hetero (different) and homo (same). Examples of homogenous catalysts include organometallic complexes, enzymes and metal incorporated calixarenes.[3–6] Homogenous catalysts, although providing revolutionary breakthroughs in the pharmaceutical and fine chemicals industries they require vast quantities of chemicals and solvents to be effective. Not to mention arduous synthetic protocols and purification steps to generate a pure compound. Consequently, these materials can often be difficult to extract from the reaction mixtures.[7] On the other hand, heterogeneous catalysts can be very straightforward to synthesize, as well as recover from a chemical reaction (filter, centrifugation or even removal using magnetism[8]). Additionally, the active site of a heterogeneous catalyst can be highly customizable leading to size, shape and support induced interaction with the metallic species. Typically, due to the simple synthetic parameters and often high reusability, heterogeneous catalysts are seen as the greener, more environmentally friendly option. Albeit, precious metal content, the active site for a substantial amount of catalysts, is not sustainable. The growing demand to upgrade these existing materials by utilizing more abundant metals that can adopt similar activities and selectivities is highly desirable. However, heterogeneous catalysts can be prone to deactivation. This can be caused by substrate decomposition causing carbonaceous deposits to form on the surface, restricting molecular adsorption. In the case of nanomaterials this can be attributed to nanoparticle sintering caused by thermally unstable materials or reagents affecting changes to the nanoparticle morphology.[9–12]

## 1.2 Single Crystals - Well defined extended surfaces

Another form of heterogeneous systems is the study of molecular desorption from single crystals under Ultra-High Vacuum (UHV) conditions. These extended, well defined surfaces are formed with a single crystal plane. By eliminating any other crystallographic facets, a surface can be characterized to evaluate defects and potential contaminants, by means of Low Energy Electron Diffraction (LEED) or X-ray Diffraction.

### 1.2.1 The structure of a single surface

Although described as an extended single surface, this form of catalyst is not without defects and non-uniformity. A surface can be imaged using various techniques such as Scanning Tunnelling Microscopy (STM) as described in **Chapter 2, Section 2.6**. This method of analysis can provide us with the topographic detail of the extended surface, as shown in Figure 2. The surface is constructed of flat extended terraces which have inherent defects. Defects can include steps edges, which are shown in the diagram as a break in the flat surface where a second terrace meets the edge site at a different elevation. There is also the potential for edge site kinks, [13] although not included in the Figure 2. These are where the step edge is not linear, instead atoms are missing which form a slightly jagged edge. Another possibility is for point defects to exist, which consist of missing atoms in the terrace, creating vacancies. Alternatively, adatoms (additional atoms) can be added to the terrace to alter the chemical and electronic properties of the crystal, often forming self-assembled ensembles. In Figure 2, to differentiate between these and the terrace atoms, the adatom has been coloured in red.

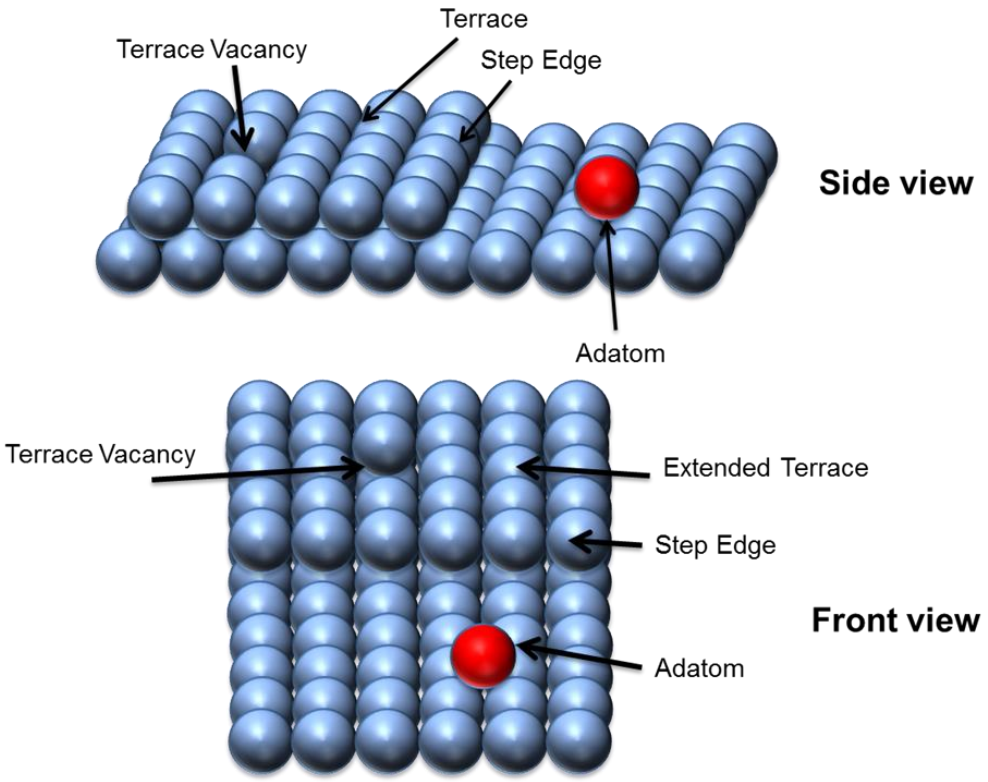


Figure 2 - Schematic representation of an extended surface (side view – (111) and top view (100)) with terrace and edge sites and other point defects (modified from reference[13]).

### 1.2.2 Miller Index

The Miller Index was introduced in 1839 and is the notation used in crystallography to indicate the specific crystal planes in the lattice structure.[13,14] Typically, low index faces are used as model surfaces, which contain the most basic atom arrangements. Figures 3 and 4 show three various atom arrangements, as well as the resulting crystal structures. A low index face is assigned through the Miller index where each system has integers {h, k and l}. These integers represent a point in space where an atom lays dependant on the Cartesian axis.

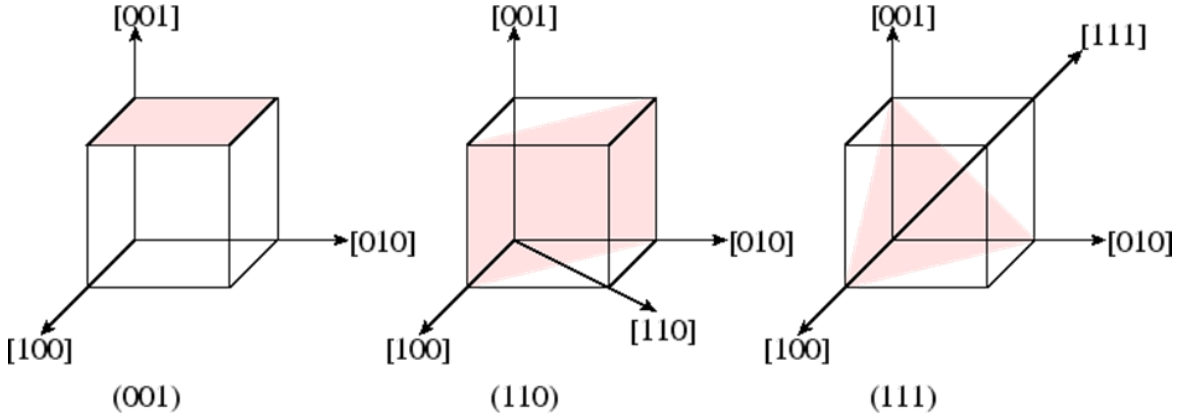


Figure 3 – The crystal planes of face centered cubic (FCC) crystals.[15]

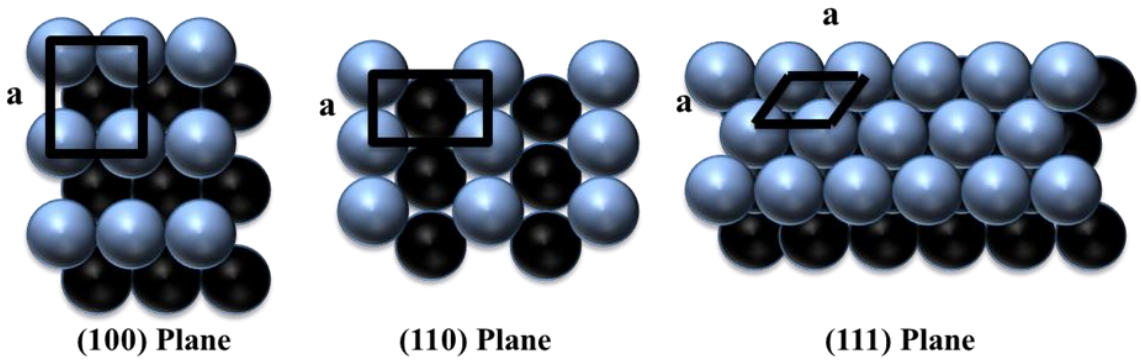


Figure 4 - Arrangement of atoms for various low index faces for a general lattice structure.

### 1.2.3 Customized surfaces

As mentioned above single crystal surfaces can be grown, checked with X-ray Diffraction techniques and cut to form a well-defined surface for ultra-high vacuum. A crystal can then be attached to a sample manipulator for a UHV chamber, as shown in **Chapter 2, section**

**2.4.1.1**. However, single crystal studies are not the only forms of catalysis which utilize ordered surfaces. Heterogeneous catalysis has recently undergone a boon through the development of nanoparticles; these materials are a collection of atoms which have been found to be catalytically active in comparison to bulk materials for some chemical reactions.[16,17] Synthesis of nanoparticles will create a multifaceted entity which possesses faces that can be identified by the Miller Index. These faces can be characterized in numerous ways; however, the most effective are by Powder X-ray Diffraction and by physically measuring the interplanar distances between lattices using Transmission Electron Microscopy (TEM). For materials generated in this work for the hydrogenation of biomass derived molecules, it was found that the Pt(111) and Cu(111) face were the most dominant when synthesized using wet chemical routes. Complementing these materials, a Pt(111) single crystal was used for ultra-high vacuum studies. Although experimental conditions are vastly different between the two systems, it is possible that molecular adsorption and geometry, as well as reaction selectivity, could provide similar results.

## 1.3 Hydrogen dissociation and bond activation

Specific metals have the ability to dissociate hydrogen; this is the separation of the H-H bond without bond activation, where the bond is subjected to sufficient energy to overcome its energy potential barrier.[18,19] Metals such as Pt, Pd, Ni, and Rh have the ability to dissociate molecular hydrogen without activating the covalent bond. It has been shown extensively that the Pd(100) facet is far more active than that of the Pd(111) and due to non-activating adsorption channels, hydrogen will spontaneously dissociate on the (100) surface.[20,21] The same conclusion has also been shown previously by Nørskov et al. when calculating the reactivity of the Cu(100) surface vs. Cu(111). They proved that there is around 0.1 eV difference in dissociation energy barriers between the two surfaces.[22,23] However, metals such as Cu,[24] Ag[25] and Au[26] cannot accomplish this process as they are not able to dissociate the bond without additional support via bond activation such as: high temperatures, being doped with a metal that can dissociate hydrogen (negate activation barrier)[24,25,27–31] or by supplying hydrogen at a sufficient pressure to ‘force’ hydrogen physically onto the surface of the metal.[24]

Hydrogen activation is the reason why noble metals are typically exploited for hydrogenation reactions. Obviously, each element possesses its own chemical and electronic characteristics which have an effect on the reaction at hand. It is the expense and lack of abundancy of precious metals, which is why research into cheaper alternatives with a greater availability is being carried out. It is also why consideration of nano-alloys that contain small quantities of precious metals is such a hot topic. Over the past decade, the materials frontier has been breached and isolated atomic entities have been found to be of high value for hydrogen dissociation on inert materials such as Cu and Ag.[27,28] Isolated atoms of Pt and Pd can rapidly dissociate molecular hydrogen, forcing a spillover effect onto the host material.[28,32] This practice has been extensively researched on single crystals under ultra-high vacuum and recently on physical catalysts for continuous flow reactors.[33]

### 1.4 Selective hydrogenation of organic molecules

Customizable materials are the ultimate aim of catalyst research. For this thesis the main goal is to synthesize highly selective hydrogenation catalysts. Hydrogenation is where a bond is reacted with a source of molecular hydrogen, which is usually completed to reduce the bond or otherwise saturate the bond. Generally, metallic species used for this reaction consist of Pt, Pd, Cu and Ni.[34–49] The term 'selective' is used as many systems have more than one point of unsaturation. A simple yet important example of this is the hydrogenation of ethene to ethane (Figure 5) where the molecule contains a single C=C bond. An application for such a process is the generation of margarines and utilizes a heterogeneous catalyst. This process has been completed extensively in the past using nickel, a very abundant and cheap metal that can readily dissociate hydrogen, making it ideal for this chemistry.[50–53] The reaction typically occurs at over 150 $^{o}$C by using supported nickel on a silica based support known as kieselguhr.[52] Although a material synthesized and tested more than 60 years ago, it is highly effective and still used in industry today. Conversely, to ensure high purity, other hydrogenation catalysts have been implemented such as palladium based materials.[54] Recent issues have indicated that nickel based materials could have toxic properties which has encouraged the development of newer, cleaner hydrogenation catalysts.[54]

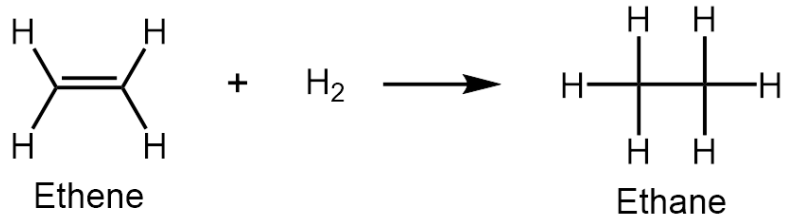


Figure 5 - The hydrogenation of ethene to ethane.

Other hydrogenated functional groups are carbonyls and the partial hydrogenation of alkynes. Often seen as a very easy bond to hydrogenate, the C=O (carbonyl group) can be found in many different positions generating aldehydes, carboxylic acids, ketones and amides.[55] However, when in conjunction with a second unsaturated system, there is competitive hydrogenation. This means that one of the functional groups or both will be saturated during the reaction. This is not always the favourable option and catalytic systems have been developed to omit the hydrogenation of certain groups; a process known as 'selective hydrogenation'.[56] The ability to control which areas of a molecule is reacted is very important as conjugation in a system, or unsaturated bonds in general, can change the chemical properties of a molecule completely, not to mention their usability in both industry and everyday life.

### 1.4.1 Furfural, a biomass derived platform molecule

Sustainable low carbon biofuels derived from lignocellulosic or oleochemical biomass sources are urgently sought[57–59] to address climate change and energy security issues arising from the availability of usable vs. unburnable[60] non-renewable fossil fuels. The quest for sustainable biofuels also impacts upon the broader chemicals industry, since the overwhelming proportion of carbon feedstocks employed today are obtained from petroleum and natural gas. In this respect, the development of the bio-refinery concept for the co-production of sustainable fuels and chemicals has the power to transform global energy and materials markets. However, this necessitates the development of new catalytic processes capable of selectively transforming biomass derived oxygenated organics into either alternative 'drop in' chemical intermediates and fuels, or entirely new compounds with novel applications.

A current hot topic in biomass utilization research is the upgrading of a very important platform molecule, furfural. A platform molecule, as the name would suggest, is a starting point which can be subtly altered to generate an array of other useful compounds.[59,61–64] Furfural is typically derived from the dehydration of xylose, which is formed through an acid-hydrolysis reaction with hemicellulose materials.[61,65] Furfural was initially isolated by Johann Wolfgang Döbereiner in 1821 in an attempt to synthesize formic acid.[66] Later, in 1840, it was found that the oily residue Döbereiner described previously could be extracted by simply reacting a variety of plant matter with sulphuric acid.[67] This process was later commercialized in 1922 by the Quaker Oats Company, in an effort to make better use of their large scale biomass waste material, namely corn husks.[67] It was rapidly understood that furfural could be utilized for a great many applications such as a process agent for generating lubricants and is also heavily used in the flavourings and perfume industries. By subtly altering the chemical structure, a wide range of flavourings and scents have been found.[63] Furfural and its derivatives are promising starting materials and building blocks from which to synthesize high volume products such as polyols, which find direct application as monomer precursors for the polyester industry. They can also be used to produce polyamides or polyurethenes via amination or oxidation respectively.[62,68] As a result large scale furfural production exists globally, with countries such as China, South Africa and the Dominican Republic contributing to a global production of >280000 tons per year.[61]

### 1.4.2 Furfural derivatives and their future potential

Figure 6 shows a wide range of potential furfural derivatives, many of which are possible through the further upgrading of subsequent molecules. The parent material can be readily decarbonylated to furan,[69,70] which is hydrogenated to tetrahydrofuran (THF),[71] a common laboratory solvent. It has also been recorded that further conversion of THF over Pt(111) can cause ring opening to butanol, followed by dehydration to propylene.[72] However, currently the most desired furfural transformation is via the selective hydrogenation to furfuryl alcohol. With over 68% of global furfural generated being hydrogenated, typically via non-environmentally friendly procedures.[62] Furfuryl alcohol, an intermediate for the

manufacture of lysine, ascorbic acid and numerous lubricants, represents a key synthetic transformation for furfural exploitation.[35,73]

The hydrogenolysis of furfuryl alcohol leads to 2-methyl furan, a molecule with a growing demand in the energy sector as this could have the potential as a fuel of the future, particularly in the haulage industries.[59,74–76] This molecule is obtained through the hydrogendeoxygenation (HDO) reaction pathway of furfuryl alcohol. This pathway has been studied in the past by many research groups across multiple catalytic systems and involves hydrogen being used to dehydrate the alcohol.[47,77–80] The production of methyl furan from furfural has been studied in a one pot system, where furfuryl alcohol is formed as an intermediate and then rapidly consumed. Furfuryl alcohol can be hydrogenated through the aromatic ring to form tetrahydrofurfuryl alcohol, the precursor for 1,5-pentandiol, a valuable molecule for the polymer industry (Figure 6).[81]

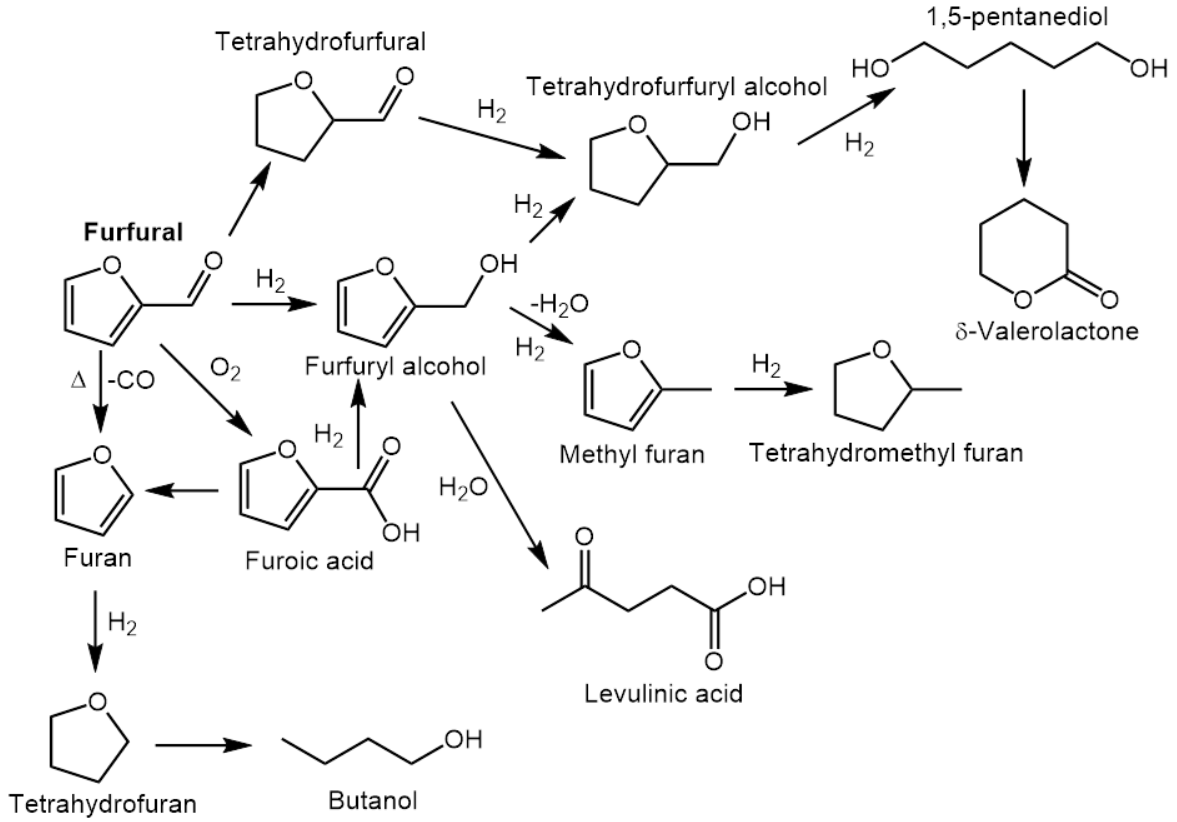


Figure 6 - Reaction scheme for the upgrading of furfural.[45,46,61,62,82–84]

### 1.4.3 Hydrogenation of furfural, past and present (liquid and vapour phase)

The typical industrial hydrogenation procedure involves using relatively high temperatures and pressures in addition to a well-established catalyst such as copper chromite, which is incredibly harmful both on the ecological scale and economically. This catalyst operates at high pressures (up to 30 bar) and high temperatures (around 200 $^{o}$C). Although presenting an acceptable selectivity towards furfuryl alcohol and reasonable activity, this material must be replaced due to rapid deactivation and evolution of toxic chromium compounds.[46,62,85] The use of toxic $Cr_2O_3$, whose disposal is prohibited in landfill sites, is highly undesirable, hence the drive to develop energy efficient alternative catalytic packages which can operate under milder temperatures and pressures, utilizing less toxic components.[36,86–88] A plethora of alternative metals have been used for the heterogeneous catalyzed hydrogenation of furfural to furfuryl alcohol. These include both monometallic and bimetallic supported nanoparticle systems used for liquid phase and vapour phase hydrogenation. Examples of metals used are Ni, Pd, Pt, Co, Cu, Rh, Ir and Ru.[43,46,83,84,89–92] To optimize systems specifically to a certain product or to reduce the costly precious metal content, a variety of bimetallic catalysts have also been explored such as PtSn, PtGe, RhSn, NiSn, CuCo, PdCu and PdRh.[77,78,92–94]

There are stark differences between the classical liquid phase reaction and that of the vapour phase. In the liquid phase, the substrate can be mixed with a ground catalyst both in the presence of a solvent or solvent free[64] and a source of hydrogen can be bubbled,[44] held in a static state[46] or pressurized.[44] Aliquots can be removed periodically and analyzed off line. In contrast, vapour phase reactions are typically self-contained systems, where a catalyst is placed in a quartz tube and positioned at the center of a furnace. Here the substrate is heated to its boiling point where the vapour, in combination with a hydrogen stream (typically around 1 bar), is passed through the catalyst bed. The continuous flow system produces a wide array of products due to the high temperature which is often very destructive, providing high levels of coke due to thermal decomposition pathways. Molecules are detected typically by an instrument online.[37,79,88,95,96]

### 1.4.4 Reactivity of furfural in the gas phase on model surfaces

The adsorption of unsaturated oxygenates has been studied over Cu, Ni, Pd and Pt(111) single crystal surfaces, as well as Zn adatom modified Pt(111)[97–110] and has been the focus of theoretical investigations. For furfural, reactively-formed furan (the decarbonylation product from furfural and furfuryl alcohol) behaves differently to molecular furan over Pd(111), the former being more prone to thermal decomposition to propylene.[104,111] Density Functional Theory (DFT) calculations have highlighted multiple reaction pathways for furfuryl alcohol hydrogenolysis over Pd(111) accompanied by the formation of adsorbed water. Calculations suggest that the latter by-product hinders furfural hydrogenation over Cu(111).[97] Furfural adsorption and decomposition over Pt(111) and Zn modified Pt(111) has been extensively investigated using Temperature Programmed Desorption (TPD) and High-Resolution Electron Energy Loss Spectroscopy (HREELS) by Shi and Vohs.[103] They report that furfural adsorbs at low temperatures through the aromatic ring on Pt(111) driving unselective decomposition to CO and $H_2$ upon heating. Surface modification with Zn adatoms favours furfural adsorption through the carbonyl carbon, and associated ring, tilting away from the Pt(111) surface.[103] This molecular re-orientation suppresses thermal decomposition and ring hydrogenation in favour of hydrodeoxygenation (HDO) of the C=O bond.

Although studied on its own, the co-adsorption of furfural in the presence of hydrogen has not been heavily explored, especially on a Pt extended surface. The hydrogenation reaction pathways have been studied theoretically on a Pd(111) simulated surface.[99] They have also been recently studied on Cu(111) and Ni(111),[112] where hydrogen was pre-dosed onto the clean surface and this was followed by exposing the crystal to furfural. Interestingly, neither surface produced hydrogenation related products. For Cu(111) this is not unusual as Cu is known for its inability to activate hydrogen. However, Ni has been used extensively in the past for such reactivity as a cheap metal for hydrogenation reactions. For the case of the single crystal reactions, the Cu(111) was able to generate furan through the decarbonylation reaction pathway. Ni(111) on the other hand was found to be very unselective and the converted furfural readily decomposed. When generating an alloyed surface of Ni/Cu(111) or Cu/Ni(111) and repeating the same experiments, there was

substantially less unselective decomposition; instead, there was a small yield of methyl furan at 300 K. This means that furfuryl alcohol was generated in an intermediate step. However, this was not reported as a detected molecule. When furfuryl alcohol was dosed onto the surface with the same hydrogen coverage, it was found that the pure Cu(111) surface once again did not produce any hydrogenation related products, whereas an alloyed surface of Ni on Cu(111) produced a very small amount of methyl furan, at a much higher desorption temperature than when formed from furfural, 382 K and 310 K respectively.

### 1.5 Why use Pt as an active metal site?

Throughout the literature numerous metallic active sites have been discussed mechanistically, theoretically and in physical reactions (liquid or gas phase). However, studies on platinum systems are not as extensive as materials such as Pd, Cu and Ni.[38,57,61,62,77,80,94,98,113,114] The literature tells us that Pt as an active site is typically able to operate at significantly lower reaction constraints than catalysts such as the toxic copper chromite or supported Pd and Cu.[46,62,82,92,93,115–117] It has also been shown that Pt is far more selective towards furfuryl alcohol than its counterparts. The reaction constraints involved consist of much lower temperatures (liquid phase systems) and pressures, both costly parameters on large scale operations. Although an expensive noble metal, platinum is able to dissociate hydrogen and therefore generating materials of low metal content would be of paramount importance. However, alternatives such as Cu are subject to deactivation over time,[78,89,113] as well as high selectivity towards methyl furan when high enough Cu loadings are used.[37,78,89,116–119] Palladium, as the active metal site, has also been shown to produce methyl furan, however accomplishing this task at much lower temperatures as compared with Cu.[47,77,116] Pd has been used extensively in hydrogenation reactions, both in homogeneous and heterogeneous catalysis and is often seen as the go to metal for such reactions. However, like Cu, although being far superior in terms of activity, it lacks the selectivity parameter which is required for the partial hydrogenation reaction, especially when used under low temperature and pressure constraints. Nickel has also been used for furfural hydrogenation both in a monometallic form and when alloyed with a second metal, typically copper or iron.[80,92,114,117,119] Ni has been found to be less active than Pd for the hydrogenation of furfural, however, the selectivity towards furfuryl alcohol is far higher.[117]

When high temperatures are used Ni loses hydrogenation product selectivity in favour of furfural decarbonylation pathways to furan.[80] Platinum in particular has drawn recent attention for the vapour phase hydrogenation of furfural over $SiO_2$, $Al_2O_3$, $TiO_2$, $Nb_2O_5$ and $Ta_2O_5$ mesoporous oxide supports which have been studied by Somorjai and co-workers.[79,120,121] Highlighting the importance of particle size effects; Pt nanoparticles <3 nm favoured furfural decarbonylation, whereas those between 3-7 nm promoted hydrogenation to furfuryl alcohol.[39,120] Sum frequency spectroscopy studies indicate that metal-support interactions are important for Pt nanoparticles on $TiO_2$, facilitating hydrogen spillover and the concomitant formation of a furfuryl-oxy intermediate over titania.[79,121] The influence of surface polarity upon the Pt catalyzed selective hydrogenation of allylic aldehydes was also reported over silica supports.[44] More recently the liquid phase hydrogenation of furfural has occurred over supports similar to those mentioned above as well as ZnO, $CeO_2$ and MgO.[46] By using monodisperse nanoparticles in the size range mentioned by Somorjai and co-workers,[120] furfuryl alcohol selectivity was maximised and furfural conversion was found to be very high while under near ambient hydrogen pressure at low temperature (50 $^{o}$C).[46] Platinum has also been supported at varying metal loadings on maple based bio-char, presenting relatively high furfuryl alcohol selectivity albeit operating at high temperature (210 $^{o}$C) and pressure (103 bar).[122]

### 1.6 The role of bimetallic species for the furfural reaction

With the ever dwindling stores of precious metals and therefore the rising cost for these elements, the drive towards sustainable materials is growing. At the time of writing this thesis the current price of platinum metal per gram is £25, whereas the price for other metals are; Cu (£0.006 per gram), Ni (£0.009 per gram) and Ag (£0.58 per gram). The price range between these metals is vast; which highlights the economic importance of using more sustainable materials. By utilizing the characteristic effects from one metal and alloying it with a second, the shared effects could prove to be beneficial. An example of this is steel, an alloy of iron and carbon. This mixture of elements has led to an extraordinary range of uses, from construction to early tools and weaponry, due to its high tensile strength and low cost. The material is generated by the high temperature incorporation of carbon into the iron unit cell. This form of alloy is called a solid solution.

However, not all alloy structures require vast temperatures to be formed, the literature shows that some alloys generated for catalytic uses can be synthesized in the liquid phase, purified and calcined at moderate temperatures.[123–127] Previously, bimetallic catalysts (two different metals, which can either be miscible or immiscible, represented as a bulk alloy)[128] have been explored for the hydrogenation of furfural. However, the majority of alloy research does not consider the reduction of precious metal content, purely an alloy effect promoted by relatively high loadings of both metals, creating a difference in reaction selectivity.[82,93,94,115,126] By combining two metals that each have their own characteristics, e.g. Pt/Pd/Ni and a second metal such as Cu, would form materials that in theory would allow Cu to be more active as a catalytic species, potentially through hydrogen spillover caused by the hydrogen activating metal.[28,129] A schematic of such a binary alloy is shown in Figure 7; where Pt and Cu could form a non-ordered alloyed structure.

Figure 7 - A schematic to show a proposed 50:50 ratio of metals on the face of a nanoparticle; atoms of Cu are represented as green and Pt as dark blue.

When Pt and Cu are alloyed together they have the potential to construct into one of three morphologies; depending on composition and synthetic procedure, these are $Pt_3Cu$, PtCu and $PtCu_3$.[130] However, the typical morphology for Pt and Cu alloying is $PtCu_3$. This structure has proven to be extremely effective for fuel cells and electrochemical materials research, both in an alloyed form and after dealloying at high temperatures.[130–137] The alloy surface structure is dependent on atom size, the molar ratios of the metals and the preparation used.[128,138] These can either be represented as a bulk homogenous structure or adopt other designs such as core-shell or a mixed aggregate. A very clear image to show the differences between the potential alloy formations is shown in Figure 8, as presented by Mavrikakis and co-workers.[138] This is where Pt and Ru form a mixed atom bulk particle, a core-shell structure where the Pt atoms are situated on the surface (exterior shell) and the Ru are situated in the core of the particle. Core-shell arrangements are seen to exhibit

different electronic effects to bulk alloys due to the positioning of the metal atoms. Finally, the linked nanoparticles are where two separate monometallic species are generated and are situated in very close proximity to one and other.

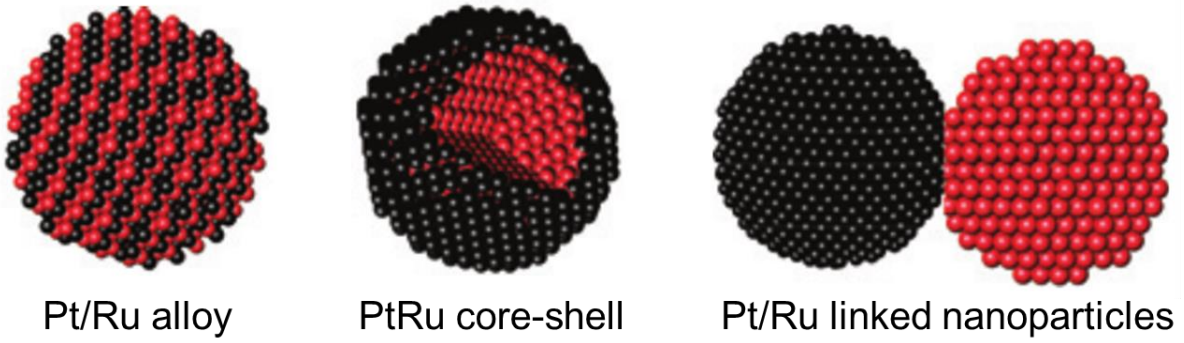


Figure 8 - The differences in alloy structure for Pt/Ru depending on preparation, where black balls are Pt and red are Ru. (Acquired from Alayoglu et al, Nat Mater, 2008, 7, 333-338.)[138]

### 1.7 The importance of dilute disperse noble metal systems

The dilution of noble metal atoms is of growing interest in the catalysis world, especially as most catalysis occurs on metal surfaces. The issue with this is that for the case of nanoparticles, only the exterior atoms play a role in the chemistry, atoms situated in the bulk are not accessible and ergo wasted in terms of active sites.[139] With this in mind, numerous chemical reactions have been seen to accommodate smaller nanoparticles to maximize the surface area to volume ratio, reducing atom wastage. The reduction of nanoparticle size has also been seen to alter the electronic effects of the metal itself, often impacting on reaction selectivities.[72,95] As a result, the literature for reducing nanoparticle size is diverse, where once large nanoparticles acquired though impregnation methods can now be synthesized via deposition precipitation or colloidal routes to form particles below 3 nm. Such particles were then found to change in size due to their interactions with reducible supports (Strong Metal Support Interactions, SMSI).[140–142] These interactions involve the strengthening of the chemical bonding between the metal particle and the support. This means that there is an electronic transfer between the two entities and can result in smaller metal particles, or lead to particle stabilization meaning that the

nanoparticle will not grow or agglomerate during the reaction or when subjected to thermal processing.[139,143]

Another method of particle size reduction and possibly the most favourable for precious metals, involves using dilute quantities of metal precursor. During the reduction process, by limiting the potential atoms in the system, one can reduce the chance of aggregation and subsequent agglomeration of atoms to clusters (2D and 3D), (an ensemble of atoms which have a size of <1 nm, typically consisting of less than 40 atoms as reported by Flytzani-Stephanopoulos, Gates and Boudart, shown in Figure 9)[142,144,145] and then from clusters to small nanoparticles.[139,144]

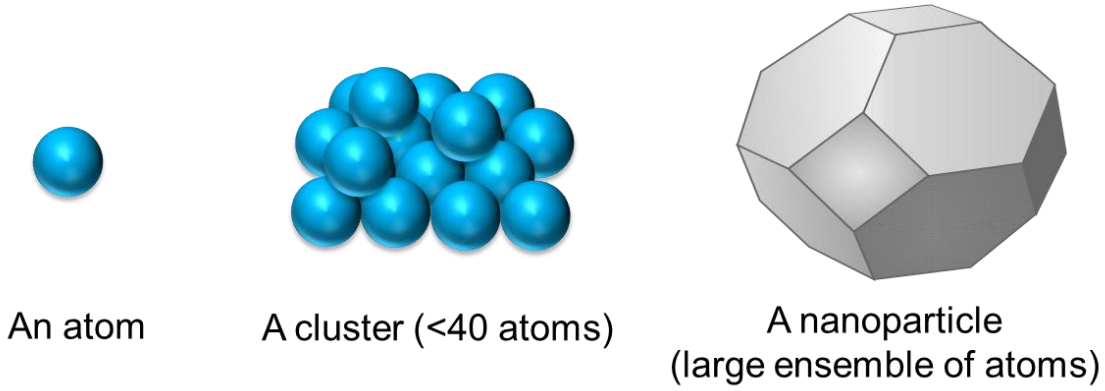


Figure 9 - Progression and classification of a single atom to a 3D cluster and finally to a nanoparticle.

Clusters can form naturally as atoms migrate to one and other, generally when the material is subjected to thermal treatment. However, clusters can be formed and stabilized by ligands when a mononuclear complex is reduced at a particular temperature. Specifically, the carbonyl based cluster has been extensively reviewed for metal clusters of iridium, rhodium and osmium,[144] where metal carbonyls are heated at high temperatures causing a decarbonylation reaction and a loss of the carbonyl functionality.

Metal clusters have been found to be very effective as heterogeneous catalysts for a variety of chemical reactions such as the water gas shift (oxidation of carbon monoxide in the presence of water) with a variety of sub nanometre clusters including Ni, Au, Pt, Pd and

Cu[146,147] and also a bimetallic cluster composed of Pt and Re.[148] Lambert and co-workers have conducted the selective oxidation of a model compound in the liquid phase very effectively with 55-atom clusters, generating nanoparticles.[149] Platinum clusters have also been found to be adept for the oxidation of CO in a rich $H_2$ stream.[150] On the other hand Pt based clusters have also been used for the selective reduction of NO by propylene for emission control purposes.[125]

### 1.7.1 Single Atom Catalysts

Even with the use of metal clusters there can still be a number of wasted atoms/potential reaction sites. To improve the overall atom efficiency of a material, clusters can be scaled down to generate true single site materials called Single Atom Catalysts (SAC). This class of metal supported catalysts was given its name by possessing isolated metal atomic sites to catalyze the desired chemical reaction. However, the chemical nature of this so called isolated atom site is debatable as it often depends on a number of positional effects such as its locality to other metal atoms and also its interaction with the support in question (charge transfer, similar to those seen for SMSIs). Although the name itself would suggest a material with 100% metal dispersion and an oxide support with random isolated atomic species (often noble metal), this is not the case. The term Single Atom Catalyst actually refers to a number of potential materials, especially as the single reaction site could occur on dimers, trimers or small aggregates of atoms to form very small clusters (either 2-dimensional or 3-dimensional, Figures 9 and 10) dependent on the nature of the atom itself or even the size of the molecule. A schematic of these species is shown in Figure 10.

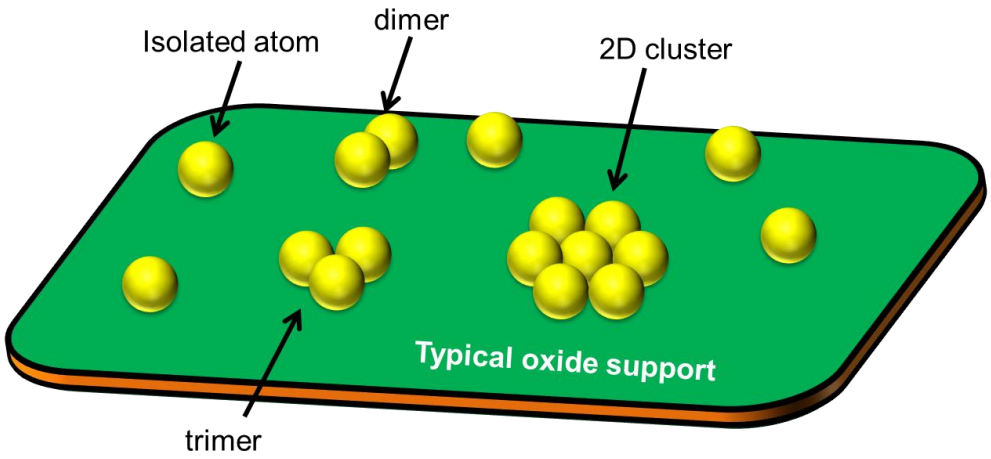


Figure 10 - Schematic of potential single site structures on a typical oxide support.

Depending on the arrangement of the atoms, the classification of the material has different nomenclature. The first is the true SAC, which is where there are no atomic structures present; this is strictly where only isolated species reside with no ordering amongst the atoms. This line of catalysts have had great success in the fields of CO oxidation/reduction,[151–153] hydrogenation of nitroarenes,[154] the selective hydrogenation of butadiene,[155] the production of hydrogen peroxide[156] and the water gas shift reaction mentioned previously for metal clusters,[157] these are just a small portion of the applications previously used for SACs. Atomic species used for the applications mentioned above have consisted of Pt, Ir and Au.

The next type of single atom based catalyst is known as the 'Single Site Heterogeneous Catalyst' (SSHC). This classification of materials uses 'single sites' containing multiple atoms which are spatially separated as discussed by Thomas et al; this is a major difference between the SSHC and SAC catalysts.[158,159] Each spatially separated atom in the SSHC possesses the same characteristics as the other atoms due to their partial isolation.[158]

Another type of SAC is likened to a combination of the true SAC and the SSHC where, although atomic entities are completely dispersed across the support, the atoms are not fully isolated. This is called the 'Atomically Dispersed Supported Metal Catalyst' (ADSMC).[139,142,160] The atoms begin to start forming surface structures such as dimers,

trimers and 2-dimensional clusters shown in Figure 10. Although this branch of Single Atom Catalysts can often prove to be very active, it is harder to distinguish and define the true active site responsible for the catalysis.

There is a large array of synthetic procedures already established to create SAC materials. Some are novel to the field, such as a method of laser ablation where the laser is focused at a rotating disk of the desired metal. The surface is heated, a vapor of the metal/carrier gas is generated, and this is then deposited on the oxide support. Due to the low kinetic energy of the atoms coming into contact with the support (<1 eV) this method of preparation is known as the 'Mass selected soft-landing'.[160,161] Another has been expertly carried out by the Flytzani-Stephanpoulos group where Au atoms are leeched from a larger Au based material by using high-pH conditions in the presence of sodium cyanide.[139,162] Although these sophisticated methods have been used to great effect in the past, it has been found that run-of-the-mill nanoparticle synthetic methodologies can be applied to create atomic species. Methods such as wetness impregnation[156,163,164] (using very low metal concentrations), albeit does lead to a variation in atomic morphologies. This is similar to the synthesis of nanoparticles, where sizes can deviate very widely and atoms can also aggregate to form the various arrays shown in Figures 9 and 10. Deposition precipitation methods have also been used where a metal complex is generated by a metal precursor reacting with a typical base.[165] This produces metal hydroxides that can often lead to cluster formation if metal concentrations are too high before interacting with the support material.[144] Another very interesting method for SAC synthesis is via 'co-precipitation', which is where the support material and the intended atomic component are reduced in situ. Generally, this method is used when FeOx is the intended support. During the reduction process, vacancies and defects occur in the iron oxide structure which are used as anchor sites for the atomic species.[151,152,154,157]

Although synthesized, to understand the structural properties and the presence of isolated single atomic entities, a number of characterization techniques can be applied that are sensitive enough, although in some cases destructive to detect or image the single atoms/cluster species. Chapter 5 shows some of these techniques in action as Pt single

atoms were both synthesized, imaged (HAADF-STEM) and the surface atomic loading was measured using XPS and EDX. Another tool for atomic site determination is by using a probe molecule such as CO for FTIR (Fourier-Transform Infrared Spectra), CO chemisorption.[27] These measurements allow the user to monitor specific CO binding modes. A nanoparticle can possess three different states, a-top, bridging and 3-fold. This is because the particles contain numerous atoms; a bridging CO will bind across two atoms and the 3-fold position can bind in three positions (Chapter 2). However, a single atom species should only show a single binding mode if it is truly isolated, the a-top position.[166] Other methods of analysis require synchrotron radiation for EXAFS. Extended X-ray Absorption Fine Structure is routinely used for nanoparticle analysis where metal-metal bonds are probed to determine the co-ordination number. XAS radiation can very easily depict the bonding between atoms and the support. If a metal-metal bond signal is missing and the metal presence is known, one can assume that only atoms are present. However, if there is a signal that appears to be larger than expected, there is a possibility that some aggregation has occurred (dimer/trimer) leading to small clusters.

### 1.7.2 Single Atom Alloys (UHV conditions)

Single Atom Alloys (SAA) are at the forefront of nanomaterials research. These materials epitomise the future of sustainability for heterogeneous catalysis as their composition utilizes critically low levels of precious metals. The principle of Single Atom Alloys has been explored very efficiently in ultra-high vacuum as well as used under practical conditions. The theory behind these materials for hydrogenation reactions in crude terms is to dope a metal species that is not able to activate the H-H bond with another metal that can dissociate the diatomic molecule. The resulting action should force rapid hydrogen spillover and therefore the material can successfully perform catalytic turnover. The novelty with these materials is that the ‘doping’ or even alloying nature is accomplished by supplying a single atomic entity that can alloy with a bulk surface.

While under UHV conditions, minute quantities of adatoms can be dispersed onto an extended surface (single crystal). An example of this is where Pd was added to a Cu(111) surface at 380 K.[28] The Pd atoms travelled over the surface in a random direction until they

reached a step edge position and alloy. Figure 11 shows a Cu(111) surface as produced by Kyriakou and co-workers by using an LTSTM (Low Temperature Scanning Tunneling Microscope)[28] with three different Pd surface quantities. The first is at the lowest quantity, 0.05 ML, (where 1 ML is 1 monolayer) and in conjunction with the high resolution inset image, single protrusions can be seen in the Cu(111) structure (Figure 11a). These larger components are isolated Pd adatoms and as the exposure is increased, the adatoms become less isolated and begin to aggregate (0.1 ML, Figure 11b) to a maximum of 1 ML where the Pd and Cu form distinct islands, no isolated atoms can be easily seen (Figure 11c) .

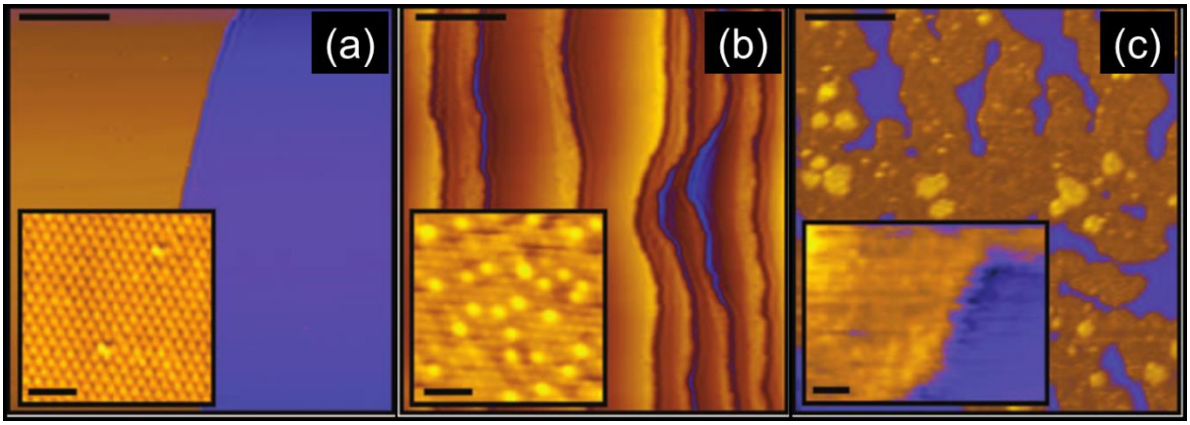


Figure 11 - STM array showing the morphology of Pd as a function of exposure on a Cu(111) where; (a) is 0.05 ML, (b) is 0.1 ML and (c) is 1 ML. The scale bars are 3 nm. (Acquired from Kyriakou et al, Science, 2012, 335, 1209-1212) - Reprinted with permission from AAAS[28]

To these constructed surfaces, hydrogen was supplied at varying exposures (1-200 L). It was found that the desorption profile of the hydrogen species changed dramatically depending on the surface coverage of Pd, as well as the desorption temperature. It was found that as more Pd was alloyed with the surface the temperature of desorption moved to a lower temperature (~175 K); this change is around 25 K lower than when the Cu(111) surface contained 0.01 ML of Pd forming the SAA surface. As the Pd content is increased, the $H_2$ (m/z 2) signal intensity is radically increased. It is understood that the reason for this rapid increase in intensity is due to the greater number of 'entrance and exit' routes allowing the hydrogen to adsorb on the alloyed surface as well as a degree of mobility before desorption. The desorption profile of the hydrogen also becomes much broader when 1 ML of Pd adatoms are used. This is because a number of the Pd atoms have begun

to generate multilayers of Pd on segregated islands (Figure 11c). Hydrogen desorption from the alloyed surface, Pd sites and Pd-Pd island sites, shifted to higher temperatures and revealed a very broad desorption range from ~175 K – 350 K.

With proof that the Pd/Cu(111) alloyed surface can cause hydrogen to spillover from Pd isolated sites onto the Cu extended surface, a probe molecule was also added to determine the reactivity on the SAA. The molecule of choice was styrene, with a terminal alkene group as well as an aromatic ring. It possesses two distinctly different unsaturated chemical environments, providing the possibility for numerous products. This probe molecule is very favourable for UHV studies as the aromaticity will cause strong $\pi$ interactions with the metal surface. Traditionally, Pd, as a majority metal, will readily decompose organic molecules under UHV and also when using practical catalysts in both liquid and gas phase reactors. This study does not demonstrate an exception to this trend as it shows that the styrene both hydrogenates to ethylbenzene but also generates a large quantity of surface carbon (~80% selectivity). A very similar scenario was observed when using a second probe molecule, acetylene. Surface carbon or coke is a real issue with practical catalysts as it is often construed as the reason for most catalyst deactivation due to poisoning. However, the reactivity of the SAA presents no decomposition of the parent molecule due to an absence of a high temperature hydrogen feature.

### 1.7.3 Single Atom Alloys (practical catalysis)

To truly use Single Atom Alloys for real world applications and generate atom efficient materials, the alloyed system must be supported. Typically, precious metal atoms are added to defected areas of a host, generally mildly active, nanoparticle which has displaced surface atoms.[24,25,109,137,167–169] A schematic of such an arrangement is shown in Figure 12 where Pt atoms have replaced Cu in a (111) structure. A method for generating these materials, as well as the reduction potentials for each metal, is shown in Chapter 2.

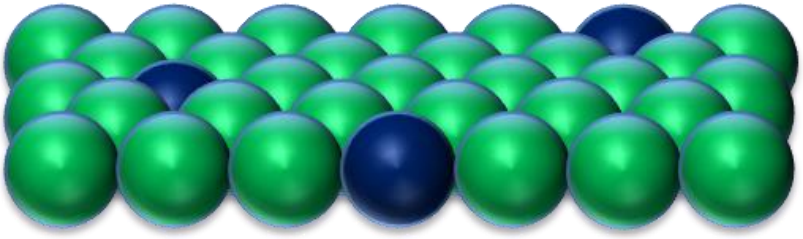

Figure 12 - A schematic to show the arrangement of atoms in a Cu (green) nanoparticle where isolated atoms are replaced by platinum (dark blue).

Palladium based Single Atom Alloy materials have already been shown to be highly active for a wide range of gas and vapour phase reactions such as the hydrogenation of alkyne based molecules.[25,27–29,31,33,169] Platinum as well as palladium has also been used in the partial hydrogenation of butadiene on a Cu host material as well as the dehydrogenation of formic acid using the same materials.[109,168] Although Pt itself will quickly poison in the presence of CO when used in the nanoparticle form or even on a single crystal, the poisoning on an isolated site could prove to be catastrophic when used in conjunction with a reaction which will undergo decarbonylation, generating CO.[46] This issue has been highlighted in the literature and has recently shown that the alloying with Cu will prevent CO from adsorbing onto Pt due to an electronic effect where electron density from the Cu will transfer to the noble metal, which was also shown to be the case for Pd sites.[94,109,167,170]

For many of the reactions listed above, the role of the Single Atom Alloy is not just the rate of hydrogen activation and subsequent spillover for hydrogenation reaction. It is the reaction selectivity that is brought from these materials, preventing the over hydrogenation pathways or decarbonylation typically seen when using bulk materials, subsequently leading to catalyst deactivation.[25,27–29] Generally to reduce the activity of a material, a poison is used to block reaction sites preventing over conversion reactions.[25] This poison can be anything from an additional element to carbonaceous deposits generated throughout the reaction naturally. As single atoms are smaller surfaces than bulk particles, this issue can be overcome. However, as a result, unless used in the correct chemistry or with a protective host material (electronic donation effects),[94] the single site will be blocked.[29] Currently in the literature there is no evidence of Single Atom Alloys being used for liquid phase hydrogenation reactions.

## 1.8 Thesis aims and objectives

The aims of this thesis are to:

- Investigate the reactivity of furfural on a Pt(111) single crystal, both on its own and in the presence of pre-adsorbed $H_2$ (0.4 ML) to develop the understanding of the surface reaction mechanism as well as changes in product selectivity with respect to molecular geometry. This will be studied in conjunction with Scanning Tunneling Microscopy to observe the furfural positioning on the Pt(111) at varying coverage.

- Optimise liquid phase furfural hydrogenation using dispersed monometallic Pt catalysts on various oxide supports, temperatures and solvents. This will be completed by maintaining a monodisperse particle size (~4 nm) and a constant Pt loading (2 wt%), while operating under mild temperature and minimal hydrogen pressure.

- Study the effect of Cu as a second metal to generate binary alloy nanoparticles with Pt on a $\gamma$-$Al_2O_3$ support. The molar ratios of the metals will be varied to determine the differences in activity, selectivity and surface protection from deactivation phenomena. Rates of reaction will also be considered across various hydrogen pressures to ascertain if an alloy effect is present and if this is beneficial to replace monometallic Pt catalysts.

- To generate Single Atom Alloy (SAA) catalysts by atom replacement techniques in a Cu host nanoparticle.[28–30,168,169] These cutting edge materials will then be probed as liquid phase hydrogenation catalysts, observing the effect of isolated noble metal entities on a Cu superstructure. These will then be compared with monometallic and bimetallic nanoparticles discussed at an earlier point of the thesis.

## 1.9 References


1 P. Atkins and J. de Paula, *Physical Chemistry*, Oxford University Press, 10th Editi., 2014.

2 M. Bowker, *The Basis and Applications of Heterogeneous Catalysis*, Oxford University Press, Oxford, 1997.

3 M. J. Walton, S. J. Lancaster and C. Redshaw, *ChemCatChem*, 2014, **6**, 1892–1898.

4 C. Gunanathan, Y. Ben-David and D. Milstein, *Science*, 2007, **317**, 790–2.

5 G. Sandoval, *Lipases and Phospholipases - Methods and Protocols*, Humana Press, 2009, vol. 531.

6 D. M. Homden and C. Redshaw, *Chem. Rev.*, 2008, **108**, 5086–5130.

7 D. J. Cole-Hamilton and R. P. Tooze, in *Catalyst Separation, Recovery and Recycling*, Springer Netherlands, 2006, pp. 1–8.

8 Z. Tai, M. A. Isaacs, C. M. A. Parlett, A. F. Lee and K. Wilson, *Catal. Commun.*, 2017, **92**, 56–60.

9 I. V. Yentekakis, G. Goula, P. Panagiotopoulou, S. Kampouri, M. J. Taylor, G. Kyriakou and R. M. Lambert, *Appl. Catal. B Environ.*, 2016, **192**, 357–364.

10 T. Tanabe, Y. Nagai, K. Dohmae, H. Sobukawa and H. Shinjoh, *J. Catal.*, 2008, **257**, 117–124.

11 L. D. Chen, M, Schmidt, *J. Catal.*, 1978, **55**, 348–360.

12 M. V. Twigg and M. S. Spencer, *Appl. Catal. A Gen.*, 2001, **212**, 161–174.

13 G. Attard and C. Barnes, *Surfaces*, OUP Oxford, Oxford, 1998.

14 L. E. Smart and E. A. Moore, *Solid State Chemistry: An Introduction*, Taylor & Francis, 3rd Editio., 2005.

15 S. Dhar, H. Kosina, V. Palankovski, S. E. Ungersboeck and S. Selberherr, *IEEE Trans. Electron Devices*, 2005, **52**, 527–533.

16 S. Eustis and M. A. El-Sayed, *Chem. Soc. Rev.*, 2006, **35**, 209–217.

17 E. Roduner, *Chem. Soc. Rev.*, 2006, **35**, 583–592.

18 J. Harris, *Langmiur*, 1991, **7**, 2528–2533.

19 M. Beye, H. Öberg, H. Xin, G. L. Dakovski, M. Dell'Angela, A. Föhlisch, J. Gladh, M. Hantschmann, F. Hieke, S. Kaya, D. Kühn, J. LaRue, G. Mercurio, M. P. Minitti, A. Mitra, S. P. Moeller, M. L. Ng, A. Nilsson, D. Nordlund, J. Nørskov, H. Öström,

H. Ogasawara, M. Persson, W. F. Schlotter, J. A. Sellberg, M. Wolf, F. Abild-Pedersen, L. G. M. Pettersson and W. Wurth, *J. Phys. Chem. Lett.*, 2016, **7**, 3647–3651.

20 A. T. Gee, B. E. Hayden, C. Mormiche and T. S. Nunney, *J. Chem. Phys.*, 2000, **112**, 7660–7668.

21 S. Wilke and M. Scheffler, *Phys. Rev. B*, 1996, **53**, 4926–4932.

22 B. Hammer, M. Scheffler, K. W. Jacobsen and J. K. Nørskov, *Phys. Rev. Lett.*, 1994, **73**, 1400–1403.

23 P. Kratzer, B. Hammer and J. K. Nørskov, *Surf. Sci.*, 1996, **359**, 45–53.

24 H. L. Tierney, A. E. Baber, J. R. Kitchin and E. C. H. Sykes, *Phys. Rev. Lett.*, 2009, **103**, 1–4.

25 P. Aich, H. Wei, B. Basan, A. J. Kropf, N. M. Schweitzer, C. L. Marshall, J. T. Miller and R. Meyer, *J. Phys. Chem. C*, 2015, **119**, 18140–18148.

26 T. Fujitani, I. Nakamura, T. Akita, M. Okumura and M. Haruta, *Angew. Chemie - Int. Ed.*, 2009, **48**, 9515–9518.

27 G. X. Pei, X. Y. Liu, A. Wang, A. F. Lee, M. A. Isaacs, L. Li, X. Pan, X. Yang, X. Wang, Z. Tai, K. Wilson and T. Zhang, *ACS Catal.*, 2015, **5**, 3717–3725.

28 G. Kyriakou, M. B. Boucher, A. D. Jewell, E. A. Lewis, T. J. Lawton, A. E. Baber, H. L. Tierney, M. Flytzani-Stephanopoulos and E. C. H. Sykes, *Science*, 2012, **335**, 1209–12.

29 M. D. Marcinkowski, A. D. Jewell, M. Stamatakis, M. B. Boucher, E. A. Lewis, C. J. Murphy, G. Kyriakou and E. C. H. Sykes, *Nat. Mater.*, 2013, **12**, 523–8.

30 G. Kyriakou, E. R. Davidson, G. Peng, L. T. Roling, S. Singh, M. B. Boucher, M. D. Marcinkowski, M. Mavrikakis, A. Michaelides and E. C. H. Sykes, *ACS Nano*, 2014, **8**, 4827–4835.

31 G. X. Pei, X. Y. Liu, A. Wang, L. Li, Y. Huang, T. Zhang, J. W. Lee, B. W. L. Jang and C.-Y. Mou, *New J. Chem.*, 2014, **38**, 2043–2051.

32 F. R. Lucci, M. D. Marcinkowski, T. J. Lawton and E. C. H. Sykes, *J. Phys. Chem. C*, 2015, **119**, 24351–24357.

33 G. Vilé, D. Albani, M. Nachtegaal, Z. Chen, D. Dontsova, M. Antonietti, N. López and J. Pérez-Ramírez, *Angew. Chemie - Int. Ed.*, 2015, **54**, 11265–11269.

34 N. Mahata, A. F. Cunha, J. J. M. Orfao and J. L. Figueiredo, *Appl. Catal. A Gen.*, 2008, **351**, 204–209.

35 H. Luo, H. Li and L. Zhuang, *Chem. Lett.*, 2001, 404–405.

36 L. Baijun, L. Lianhai, W. Bingchun, C. Tianxi and Katsuyoshi Iwatani, *Appl. Catal. A Gen.*, 1998, **171**, 117–122.

37 B. Nagaraja, A. Padmasri, B. Raju and K. Rama Rao, *J. Mol. Catal. A Chem.*, 2007, **265**, 90–97.

38 M. M. Villaverde, T. F. Garetto and A. J. Marchi, *Catal. Commun.*, 2015, **58**, 6–10.

39 S. Sitthisa, T. Sooknoi, Y. Ma, P. B. Balbuena and D. E. Resasco, *J. Catal.*, 2011, **277**, 1–13.

40 R. Malathi and R. P. Viswanath, *Appl. Catal. A Gen.*, 2001, **208**, 323–327.

41 S. Chytil, W. R. Glomm, I. Kvande, T. Zhao, J. C. Walmsley and E. A. Blekkan, *Top. Catal.*, 2007, **45**, 93–99.

42 D. Wang, F. Ammari, R. Touroude, D. S. Su and R. Schlögl, *Catal. Today*, 2009, **147**, 224–230.

43 S. Bhogeswararao and D. Srinivas, *J. Catal.*, 2015, **327**, 65–77.

44 L. J. Durndell, C. M. A. Parlett, N. S. Hondow, M. A. Isaacs, K. Wilson and A. F. Lee, *Sci. Rep.*, 2015, **5**, 9425.

45 X. Chen, L. Zhang, B. Zhang, X. Guo and X. Mu, *Sci. Rep.*, 2016, **6**, 28558.

46 M. J. Taylor, L. J. Durndell, M. A. Isaacs, C. M. A. Parlett, K. Wilson, A. F. Lee and G. Kyriakou, *Appl. Catal. B Environ.*, 2016, **180**, 580–585.

47 S. Iqbal, X. Liu, O. F. Aldosari, P. J. Miedziak, J. K. Edwards, G. L. Brett, A. Akram, G. M. King, T. E. Davies, D. J. Morgan, D. K. Knight and G. J. Hutchings, *Catal. Sci. Technol.*, 2014, **4**, 2280.

48 A. Sachse, N. Linares, P. Barbaro, F. Fajula and A. Galarneau, *Dalt. Trans.*, 2013, **42**, 1378–1384.

49 J. Mitra, X. Zhou and T. Rauchfuss, *Green Chem.*, 2015, **17**, 307–313.

50 J. W. E. Coenen, *Ind. Eng. Chem. Fundam.*, 1986, **25**, 43–52.

51 D. Jovanovic, R. Radovic and L. Mares, *J. Agric. Food Chem.*, 1998, **43**, 21–28.

52 G. H. Twigg, *Discuss. Faraday Soc.*, 1950, **8**, 152.

53 G. L. Hasenhuettl and R. W. Hartel, *Food emulsifiers and their applications: Second*

*edition*, 2008.

54 B. V. I. Savchenko and I. A. Makaryan, *Platin. Met. Rev.*, 1999, **43**, 74–82.

55 J. Clayden, N. Greeves, S. Warren and P. Wothers, *Organic Chemistry*, OUP Oxford, Oxford, 2001.

56 T. Renner, H. A. Favre and W. H. Powell, *Nomenclature of Organic Chemistry*, Royal Society of Chemistry, 2013.

57 D. Bulushev and J. R. Ross, *Catal. Today*, 2011, **171**, 1–13.

58 D. A. Simonetti and J. A. Dumesic, *ChemSusChem*, 2008, **1**, 725–733.

59 M. J. Climent, A. Corma and S. Iborra, *Green Chem.*, 2014, **16**, 516–547.

60 C. McGlade and P. Ekins, *Nature*, 2015, **517**, 187–190.

61 G. Machado, S. Leon, F. Santos, R. Lourega, J. Dullius, M. E. Mollmann and P. Eichler, *Nat. Resour.*, 2016, **7**, 115–129.

62 A. Mandalika, L. Qin, T. K. Sato and T. Runge, *Green Chem.*, 2014, **16**, 2480–2489.

63 P. Gallezot, *Chem. Soc. Rev.*, 2012, **41**, 1538–58.

64 M. Besson, P. Gallezot and C. Pinel, *Chem. Rev.*, 2014, **114**, 1827–1870.

65 X. Hu, C. Lievens and C. Z. Li, *ChemSusChem*, 2012, **5**, 1427–1434.

66 J. W. Döbereiner, *Ann. der Pharm.*, 1832, **32**, 141–146.

67 S. L. Suib, *New and Future Developments in Catalysis: Catalytic Biomass Conversion*, Elsevier Ltd, 2013.

68 M. Chatterjee, H. Kawanami, T. Ishizaka, M. Sato, T. Suzuki and A. Suzuki, *Catal. Sci. Technol.*, 2011, **1**, 1466–1471.

69 P. Lejemble, A. Gaset and P. Kalck, *Biomass*, 1984, **4**, 263–273.

70 C. D. Hund, A. R. Goldsby and E. N. Osborne, *J. Am. Chem. Soc.*, 1932, **54**, 2532–2536.

71 D. S. Jackson, A. S. Canning, E. M. Vass and S. R. Watson, *Ind. Eng. Chem.*, 2003, **42**, 5489–5494.

72 C. J. Kliewer, C. Aliaga, M. Bieri, W. Huang, C.-K. Tsung, J. B. Wood, K. Komvopoulos and G. A. Somorjai, *J. Am. Chem. Soc.*, 2010, **132**, 13088–95.

73 A. Halilu, T. H. Ali, A. Y. Atta, P. Sudarsanam, S. K. Bhargava and S. B. Abd Hamid, *Energy & Fuels*, 2016, **30**, 2216-2226.

74 C. Wang, H. Xu, R. Daniel, A. Ghafourian, J. M. Herreros, S. Shuai and X. Ma,

*Fuel*, 2013, **103**, 200–211.

75 H. Wei, D. Feng, G. Shu, M. Pan, Y. Guo, D. Gao and W. Li, *Appl. Energy*, 2014, **132**, 317–324.

76 G. Li, N. Li, S. Li, A. Wang, Y. Cong, X. Wang and T. Zhang, *Chem. Commun.*, 2013, **49**, 5727–9.

77 O. F. Aldosari, S. Iqbal, P. J. Miedziak, G. L. Brett, D. R. Jones, X. Liu, J. K. Edwards, D. J. Morgan, D. K. Knight and G. J. Hutchings, *Catal. Sci. Technol.*, 2016, **6**, 234–242.

78 S. Srivastava, G. C. Jadeja and J. Parikh, *RSC Adv.*, 2016, **6**, 1649–1658.

79 K. An, N. Musselwhite, G. Kennedy, V. V Pushkarev, L. R. Baker and G. A. Somorjai, *J. Colloid Interface Sci.*, 2013, **392**, 122–8.

80 S. Sitthisa, W. An and D. E. Resasco, *J. Catal.*, 2011, **284**, 90–101.

81 Y. Nakagawa and K. Tomishige, *Catal. Today*, 2012, **195**, 136–143.

82 A. B. Merlo, V. Vetere, J. F. Ruggera and M. L. Casella, *Catal. Commun.*, 2009, **10**, 1665–1669.

83 M. Audemar, C. Ciotonea, K. De Oliveira Vigier, S. Royer, A. Ungureanu, B. Dragoi, E. Dumitriu and F. Jérôme, *ChemSusChem*, 2015, **8**, 1885–1891.

84 M. M. Villaverde, N. M. Bertero, T. F. Garetto and A. J. Marchi, *Catal. Today*, 2013, **213**, 87–92.

85 B. H. Wojcik, *Ind. Eng. Chem.*, 1948, **20**, 210–216.

86 K. Egeblad, J. Rass-Hansen, C. Marsden, E. Taarning and C. Hviid, in *Catalysis: Volume 21*, Royal Society Of Chemistry, 2008, pp. 13–50.

87 A. S. Gowda, S. Parkin and F. T. Ladipo, *Appl. Organomet. Chemsitry*, 2012, **26**, 86–93.

88 B. M. Nagaraja, V. Siva Kumar, V. Shasikala, A. H. Padmasri, B. Sreedhar, B. David Raju and K. S. Rama Rao, *Catal. Commun.*, 2003, **4**, 287–293.

89 D. Vargas-Hernández, J. M. Rubio-Caballero, J. Santamaría-González, R. Moreno-Tost, J. M. Mérida-Robles, M. A. Pérez-Cruz, A. Jiménez-López, R. Hernández-Huesca and P. Maireles-Torres, *J. Mol. Catal. A Chem.*, 2014, **383**–**384**, 106–113.

90 R. M. Mironenko, O. B. Belskaya, T. I. Gulyaeva, A. I. Nizovskii, A. V. Kalinkin, V. I. Bukhtiyarov, A. V. Lavrenov and V. A. Likholobov, *Catal. Today*, 2015, **249**,

145–152.

91 P. Reyes, D. Salinas, C. Campos and M. Oportus, *Quim. Nova*, 2010, **33**, 777–780.

92 V. Vetere, A. B. Merlo, J. Ruggera and M. L. Casella, *J. Braz. Chem. Soc.*, 2010, **21**, 914–920.

93 A. B. Merlo, V. Vetere, J. M. Ramallo-López, F. G. Requejo and M. L. Casella, *React. Kinet. Mech. Catal.*, 2011, **104**, 467–482.

94 K. Fulajtárova, T. Soták, M. Hronec, I. Vávra, E. Dobročka and M. Omastová, *Appl. Catal. A Gen.*, 2015, **502**, 78–85.

95 C.-K. Tsung, J. N. Kuhn, W. Huang, C. Aliaga, L.-I. Hung, G. A. Somorjai and P. Yang, *J. Am. Chem. Soc.*, 2009, **131**, 5816–22.

96 W.-S. Lee, Z. Wang, W. Zheng, D. G. Vlachos and A. Bhan, *Catal. Sci. Technol.*, 2014, **4**, 2340.

97 Y. Shi, Y. Zhu, Y. Yang, Y. W. Li and H. Jiao, *ACS Catal.*, 2015, **5**, 4020–4032.

98 V. Vorotnikov, G. Mpourmpakis and D. G. Vlachos, *ACS Catal.*, 2012, **2**, 2496–2504.

99 S. Wang, V. Vorotnikov and D. G. Vlachos, *ACS Catal.*, 2015, **5**, 104–112.

100 S. Wang, V. Vorotnikov, J. E. Sutton and D. G. Vlachos, *ACS Catal.*, 2014, **4**, 604–612.

101 B. Liu, L. Cheng, L. Curtiss and J. Greeley, *Surf. Sci.*, 2014, **622**, 51–59.

102 S. H. Pang, C. A. Schoenbaum, D. K. Schwartz and J. W. Medlin, *ACS Catal.*, 2014, **4**, 3123–3131.

103 D. Shi and J. M. Vohs, *ACS Catal.*, 2015, **5**, 2177–2183.

104 S. H. Pang and J. W. Medlin, *ACS Catal.*, 2011, **1**, 1272–1283.

105 K. E. Wilson and C. J. Baddeley, *J. Phys. Chem. C*, 2009, **113**, 10706–10711.

106 J. Hong, K. E. Djernes, I. Lee, R. J. Hooley and F. Zaera, *ACS Catal.*, 2013, **3**, 2154–2157.

107 G. Goubert, M. N. Groves, Y. Dong, J.-C. Lemay, P. H. McBreen and B. Hammer, *J. Phys. Chem. C*, 2015, **119**, 7319–7326.

108 T. J. Lawton, V. Pushkarev, D. Wei, F. R. Lucci, D. S. Sholl, A. J. Gellman and E. C. H. Sykes, *J. Phys. Chem. C*, 2013, **117**, 22290–22297.

109 M. D. Marcinkowski, J. Liu, C. J. Murphy, M. L. Liriano, N. A. Wasio, F. R. Lucci,

M. Flytzani-Stephanopoulos and E. C. H. Sykes, *ACS Catal.*, 2017, **7**, 413–420.

110 M. J. Taylor, L. Jiang, J. Reichert, A. C. Papageorgiou, S. K. Beaumont, K. Wilson, A. F. Lee, J. V Barth and G. Kyriakou, *J. Phys. Chem. C*, 2017, **121**, 8490–8497.

111 R. M. Ormerod, C. J. Baddeley, C. Hardacre and R. M. Lambert, *Surf. Sci.*, 1996, **360**, 1–9.

112 K. Xiong, W. Wan and J. G. Chen, *Surf. Sci.*, 2016, **652**, 91–97.

113 R. Rao, R. Baker and M. Vannice, *Catal. Letters*, 1999, **60**, 51–57.

114 J. Wu, G. Gao, J. Li, P. Sun, X. Long and F. Li, *Appl. Catal. B Environ.*, 2017, **203**, 227–236.

115 S. T. Thompson and H. H. Lamb, *ACS Catal.*, 2016, **6**, 7438–7447.

116 C. Sun, P. Zeng, M. He, X. He and X. Xie, *Catal. Commun.*, 2016, **86**, 5–8.

117 C. Zhang, Q. Lai and J. H. Holles, *Catal. Commun.*, 2017, **89**, 77–80.

118 S. Sitthisa and D. E. Resasco, *Catal. Letters*, 2011, **141**, 784–791.

119 O'Driscoll, J. J. Leahy and T. Curtin, *Catal. Today*, 2017, **279**, 194–201.

120 V. V Pushkarev, N. Musselwhite, K. An, S. Alayoglu and G. A. Somorjai, *Nano Lett.*, 2012, **12**, 5196–201.

121 L. R. Baker, G. Kennedy, M. Van Spronsen, A. Hervier, X. Cai, S. Chen, L.-W. Wang and G. A. Somorjai, *J. Am. Chem. Soc.*, 2012, **134**, 14208–16.

122 A. Fuente-Hernandez, R. Lee, N. Beland, I. Zamboni and J. M. Lavoie, *Energies*, 2017, **10**, 286.

123 J. Lee, Y. T. Kim and G. W. Huber, *Green Chem.*, 2014, **16**, 708.

124 A. B. Merlo, V. Vetere, J. F. Ruggera and M. L. Casella, *Catal. Commun.*, 2009, **10**, 1665–1669.

125 C. Mihut, B. D. Chandler and M. D. Amiridis, *Catal. Commun.*, 2002, **3**, 91–97.

126 B. Chen, F. Li, Z. Huang and G. Yuan, *Appl. Catal. A Gen.*, 2015, **500**, 23–29.

127 E. Rubinov, M. Diab, M. Volokh and T. Mokari, *CrystEngComm*, 2014, **16**, 9493–9500.

128 O. Deutschmann, H. Knözinger, K. Kochloefl and T. Turek, *Heterogeneous Catalysis and Solid Catalysts*, Wiley-VCH Verlag GmbH & Co. KGaA, 2009.

129 S. Sitthisa, T. Pham, T. Prasomsri, T. Sooknoi, R. G. Mallinson and D. E. Resasco, *J. Catal.*, 2011, **280**, 17–27.

130 M. Oezaslan, F. Hasche and P. Strasser, *J. Electrochem. Soc.*, 2012, **159**, 444–454.

131 M. Oezaslan and P. Strasser, *J. Power Sources*, 2011, **196**, 5240–5249.

132 Y. Jia, Y. Jiang, J. Zhang, L. Zhang, Q. Chen, Z. Xie and L. Zheng, *J. Am. Chem. Soc.*, 2014, **136**, 3748–3751.

133 R. Yang, J. Leisch, P. Strasser and M. F. Toney, *Chem. Mater.*, 2010, **22**, 4712–4720.

134 Y. Jia, J. Su, Z. Chen, K. Tan, Q. Chen, Z. Cao, Y. Jiang, Z. Xie and L. Zheng, *RSC Adv.*, 2015, **5**, 18153–18158.

135 N. Hodnik, C. Jeyabharathi, J. C. Meier, A. Kostka, K. L. Phani, A. Rečnik, M. Bele, S. Hočevar, M. Gaberšček and K. J. J. Mayrhofer, *Phys. Chem. Chem. Phys.*, 2014, **16**, 13610.

136 L. Han, H. Liu, P. Cui, Z. Peng, S. Zhang and J. Yang, *Sci. Rep.*, 2014, **4**, 6414.

137 Y. Xiong, Y. Ma, Z. Lin, Q. Xu, Y. Yan, H. Zhang, J. Wu and D. Yang, *CrystEngComm*, 2016, **18**, 7823–7830.

138 S. Alayoglu, A. U. Nilekar, M. Mavrikakis and B. Eichhorn, *Nat. Mater.*, 2008, **7**, 333–338.

139 J. Liu, *ACS Catal.*, 2016, **7**, 34–59.

140 F. Jiang, J. Cai, B. Liu, Y. Xu and X. Liu, *RSC Adv.*, 2016, **6**, 75541–75551.

141 M. Abid, V. Paul-Boncour and R. Touroude, *Appl. Catal. A Gen.*, 2006, **297**, 48–59.

142 M. Flytzani-Stephanopoulos and B. C. Gates, *Annu. Rev. Chem. Biomol. Eng.*, 2012, **3**, 545–574.

143 S. J. Tauster, S. C. Fung, R. T. Baker and J. A. Horsley, *Science*, 1981, **211**, 4487.

144 B. C. Gates, *Chem. Rev.*, 1995, **95**, 511–522.

145 M. Boudart, *J. Mol. Catal.*, 1985, **30**, 27–38.

146 Y. Li, Q. Fu and M. Flytzani-Stephanopoulos, *Appl. Catal. B Environ.*, 2000, **27**, 179–191.

147 C. Wen, Y. Zhu, Y. Ye, S. Zhang, F. Cheng, Y. Liu, P. Wang and F. Tao, *ACS Nano*, 2012, **6**, 9305–9313.

148 A. S. Duke, K. Xie, A. J. Brandt, T. D. Maddumapatabandi, S. C. Ammal, A. Heyden, J. R. Monnier and D. A. Chen, *ACS Catal.*, 2017, **7**, 2597–2606.

149 M. Turner, V. B. Golovko, O. P. H. Vaughan, P. Abdulkin, A. Berenguer-Murcia,

M. S. Tikhov, B. F. G. Johnson and R. M. Lambert, *Nature*, 2008, **454**, 981–983.

150 B. Qiao, A. Wang, L. Li, Q. Lin, H. Wei, J. Liu and T. Zhang, *ACS Catal.*, 2014, **4**, 2113–2117.

151 B. Qiao, A. Wang, X. Yang, L. F. Allard, Z. Jiang, Y. Cui, J. Liu, J. Li and T. Zhang, *Nat. Chem.*, 2011, **3**, 634–641.

152 B. Qiao, J. X. Liang, A. Wang, C. Q. Xu, J. Li, T. Zhang and J. J. Liu, *Nano Res.*, 2015, **8**, 2913–2924.

153 S. Back, J. Lim, N.-Y. Kim, Y.-H. Kim and Y. Jung, *Chem. Sci.*, 2017, **594**, 1–19.

154 H. Wei, X. Liu, A. Wang, L. Zhang, B. Qiao, X. Yang, Y. Huang, S. Miao, J. Liu and T. Zhang, *Nat. Commun.*, 2014, **5**, 1–8.

155 H. Yan, H. Cheng, H. Yi, Y. Lin, T. Yao, C. Wang, J. Li, S. Wei and J. Lu, *J. Am. Chem. Soc.*, 2015, **137**, 10484–10487.

156 S. Yang, Y. J. Tak, J. Kim, A. Soon and H. Lee, *ACS Catal.*, 2016, **7**, 1301–1307.

157 J. Lin, A. Wang, B. Qiao, X. Liu, X. Yang, X. Wang, J. Liang, J. Li, J. Liu and T. Zhang, *J. Am. Chem. Soc.*, 2013, **135**, 15314–15317.

158 J. M. Thomas, R. Raja and D. W. Lewis, *Angew. Chemie - Int. Ed.*, 2005, **44**, 6456–6482.

159 J. M. Thomas, *Proc. R. Soc. A Math. Phys. Eng. Sci.*, 2012, **468**, 1884–1903.

160 J. H. Kwak, L. Kovarik and J. Szanyi, *ACS Catal.*, 2013, **3**, 2094–2100.

161 Y.-X. Zhao, Z.-Y. Li, Z. Yuan, X.-N. Li and S.-G. He, *Angew. Chem. Int. Ed. Engl.*, 2014, **53**, 9482–6.

162 Q. Fu, H. Saltsburg and M. Flytzani-Stephanopoulos, *Science*, 2003, **301**, 935–938.

163 C. H. Choi, M. Kim, H. C. Kwon, S. J. Cho, S. Yun, H.-T. Kim, K. J. J. Mayrhofer, H. Kim and M. Choi, *Nat. Commun.*, 2016, **7**, 10922.

164 S. Yang, J. Kim, Y. J. Tak, A. Soon and H. Lee, *Angew. Chemie - Int. Ed.*, 2016, **55**, 2058–2062.

165 X.-K. Gu, B. Qiao, C.-Q. Huang, W.-C. Ding, K. Sun, E. Zhan, T. Zhang, J. Liu and W.-X. Li, *ACS Catal.*, 2014, **4**, 3886–3890.

166 J. C. Matsubu, V. N. Yang and P. Christopher, *J. Am. Chem. Soc.*, 2015, **137**, 3076–3084.

167 J. Liu, F. R. Lucci, M. Yang, S. Lee, M. D. Marcinkowski, A. J. Therrien, C. T.

Williams, E. C. H. Sykes and M. Flytzani-Stephanopoulos, *J. Am. Chem. Soc.*, 2016, **138**, 6396–6399.

168 F. R. Lucci, J. Liu, M. D. Marcinkowski, M. Yang, L. F. Allard, M. Flytzani-Stephanopoulos and E. C. H. Sykes, *Nat. Commun.*, 2015, **6**, 8550.

169 M. B. Boucher, B. Zugic, G. Cladaras, J. Kammert, M. D. Marcinkowski, T. J. Lawton, E. C. H. Sykes and M. Flytzani-Stephanopoulos, *Phys. Chem. Chem. Phys.*, 2013, **15**, 12187–96.

170 K. Yuge, Y. Koyama, A. Kuwabara and I. Tanaka, *J. Phys. Condens. Matter*, 2014, **26**, 355006.

# Chapter 2 – Experimental

## 2.1 Catalyst Preparation

### 2.1.1 Monometallic Pt Supported Catalysts

Colloidal Pt nanoparticles were prepared by adapting the method of Koebel and co-workers[1], employing a $H_2PtCl_6.H_2O$ precursor, since residual chlorine has been found to have a promotional effect in the selective hydrogenation of α,β-unsaturated aldehydes.[2] To a stirred 10 mL aliquot of ethylene glycol (Fisher >99%) at 120 °C, 50 μL of 0.1 M aqueous sodium hydroxide solution was added to promote nucleation. To the hot glycol, a solution of $H_2PtCl_6.H_2O$ (10.6 mM, Alfa Aesar, 99.9%) and polyvinylpyrrolidone (PVP) (91 mM, Alfa Aesar) in a 9:1 per volume ethylene glycol:water mixture was added slowly over the course of an hour resulting in a colour change from light brown to black. The reaction mixture was stirred for an additional 20 min and then cooled to room temperature. Nanoparticles were isolated by the addition of acetone (three times the reaction volume) followed by subsequent centrifugation at 3500 rpm; the role of the acetone is to cause a switch in the polarity of the mixture, causing the nanoparticle to drop out of solution. This process was repeated three times and the reclaimed pellet was then dispersed in ethanol before supporting on the following oxides: $SiO_2$ (Alfa Aesar amorphous fumed, 175-225 $m^2\ g^{-1}$), γ-$Al_2O_3$ (Alfa Aesar 99.5 %, 32-40 $m^2.g^{-1}$), $CeO_2$ (Alfa Aesar 99.5 %, 3 $m^2\ g^{-1}$), MgO (Alfa Aesar, 99+ %, >7 $m^2\ g^{-1}$) and ZnO (Alfa Aesar, 99.9 %, 10 $m^2\ g^{-1}$). The suspension was added to 1 g of oxide support and mixed for 20 minutes before transferring to a rotary evaporator; the solvent was removed under vacuo at 40 $^oC$. Supports were not pre-treated prior to platinum deposition. The resulting slurries were slowly dried in vacuo, and the dried powders were then transferred to a tube furnace and heated at 3 °C $min^{-1}$ under flowing air (60 $cm^3\ min^{-1}$) to 300 °C for 4 h to remove the PVP stabilizer and immobilize the Pt nanoparticles. The resulting materials were reduced at 200 °C in flowing 10 % $H_2/N_2$ for 1 h, cooled and stored in air.

### 2.1.2 Bimetallic Pt Supported Catalysts

Colloidal Pt, Cu and PtCu nanoparticles were synthesized using a similar method to that mentioned above.[1,3,4] Ethylene glycol (10 mL, Fisher >99%) was stirred at 140 °C in the presence of aqueous sodium hydroxide (1 mL, 1 M) to promote nucleation. To ensure the synthesized particles were bimetallic, subtle modifications were made to allow for a slow

addition of metal precursors. Using $H_2PtCl_6.H_2O$ (Alfa Aesar, 99.9%), $Cu(NO_3)_2.3H_2O$ (Acros, 99%) and $CuSO_4.5H_2O$ (Aldrich, ≥98.0%) as precursors, the Pt and Cu precursors, as well as polyvinylpyrrolidone (PVP) (91 mM, Alfa Aesar), were added to a 9:2 mixture of ethylene glycol and water. The ratios of Pt:Cu were altered to ensure molar ratios of 50:50 and 25:75 respectively. The mixture was briefly sonicated for 5 min to ensure the solution was homogenous. The combined precursor solution was then delivered dropwise into the warm ethylene glycol solution via syringe pump (World Precision Instruments, AL-4000 Programmable Syringe Pump – Figure 1) at 5 mL $h^{-1}$. Slowly, the colour of the solution turned from light brown to black for Pt and PtCu solutions, whereas the Cu solution changed from a light blue to brown. Upon successive centrifugation (isolated and washed with acetone three times in a 3:1 ratio), the nanoparticles were suspended in ethanol and supported on γ-$Al_2O_3$ (Alfa Aesar 99.5%, 32–40 $m^2$ $g^{-1}$). The support was not pre-treated prior to nanoparticle deposition. Catalysts were dried under vacuo, and then further dried in an oven at 60 $^oC$ overnight. The powders were then transferred to a muffle furnace and heated at 3 $^oC$ $min^{-1}$ under air to 300 $^oC$ for 4 h to remove the PVP stabilizer.[5] Synthesized alloyed particles are given the following notation (N) for $Cu(NO_3)_2$ and (S) for $CuSO_4$ containing materials.


Figure 13 - Bimetallic nanoparticle synthesis set up (Cu particle synthesis) precursor solution added at 5 mL $h^{-1}$.

### 2.1.3 Pt Single Atom Alloy Catalysts

Atom efficient catalysts were synthesized by adopting a method of galvanic replacement previously reported by Lucci.[6] Initially, a monometallic 1% Cu/$\gamma$-$Al_2O_3$ catalyst was generated by the same process as reported in **Section 2.1.2** using $Cu(NO_3)_2.3H_2O$ as a precursor, once the PVP stabilizer was removed and the powder was reduced under $H_2$ flow at 300 $^oC$ (5 $^oC$ $min^{-1}$) for 3 h. The resulting material was immediately added to 50 mL of HCl (2 mM) while under nitrogen protection. Galvanic replacement, the process where surface Cu atoms are replaced by Pt atoms, was completed under constant stirring and refluxing at 100 °C. To generate single atom entities, intended Pt metal loadings of 0.05% and 0.005% were used to create atomic ratios of $Pt_{0.2}Cu_{12}$ and $Pt_{0.2}Cu_{50}$ where for every single Pt atom there are 60 and 250 Cu atoms respectively. The Pt precursor, $H_2PtCl_6.H_2O$ (Alfa Aesar, 99.9%) was added to 2 mL HCl (2 mM) and then delivered to the refluxing Cu containing suspension, where the $Cu^0$ is known to reduce the Pt salt; the reduction potential schematic is shown below. After 20 min, the resulting material was centrifuged and washed multiple times with deionized water (~300 mL), the reclaimed pellet was then transferred to an oven where it was dried at 60 $^oC$ overnight.

$$PtCl_6^{2-} + 4\ e^- \rightarrow Pt + 6\ Cl^- \ \mathbf{(\Delta E° = 0.74\ V)}$$

$$Cu \rightarrow Cu^{2+} + 2\ e^- \ \mathbf{(\Delta E° = -0.34\ V)}$$

Due to the difference in reduction potentials, the Cu can readily reduce the Pt precursor when fully reduced itself. In this respect the nano-copper component acts as a sacrificial template for the metal exchange process.[5–8] The overall reduction reaction is favourable due to the difference in reduction potentials; the displacement reaction for this is seen below.[9,10]

$$2Cu + Pt^{4+} \rightarrow 2Cu^{2+} + Pt \ \mathbf{(\Delta E° = 0.40\ V)}$$

## 2.2 Catalyst Characterization

### 2.2.1 Inductive Coupled Plasma Optical Emission Spectroscopy

Bulk metal contents of all catalysts were measured by Inductively Coupled Plasma Optical Emission Spectroscopy using either a PerkinElmer Optical Emission Spectrometer Optima 5300 DV or a Thermo Scientific iCAP 7400 duo.

ICP is where a liquid sample is carried to a nebulizer in conjunction with a carrier gas (argon) and enters a spray chamber (Figure 2). The resulting aerosol is carried to the plasma torch where it is ionized. The resulting ions recombine repeatedly, producing an electromagnetic signal.[11] This radiation has a characteristic wavelength, which is then analyzed and a ppm value is generated according to an array of calibration standards created. Typically, due to elemental overlap, at least 3 separate wavelengths are compared for each sample.

For each system, samples were digested via a CEM–MARS microwave reactor using 2 mL $HNO_3$ (Romil SPA grade 70%) and 2 mL HCl (Romil SPA grade 60%). In the case of the Perkin Elmer system and depending on the oxide support, 2 mL HF (Romil SPA grade 40%) is added and then heated to 200 $^{o}$C followed by aqueous dilution. For the Thermo Scientific ICP, samples were digested in 5 mL $HNO_3$ (Fisher, 70%) and 100 mg $NH_4F$ (Sigma Aldrich, ≥98.0%) at 190 $^{o}$C. The solutions were then neutralized by adding 1 mL boric acid solution (Aldrich, 3%) and 1 mL HCl (Fisher, 37%) followed by heating in the microwave to 150 $^{o}$C. Samples were subsequently diluted in 10% $HNO_3$ solution and analyzed. A typical ICP-OES schematic is shown in Figure 2.

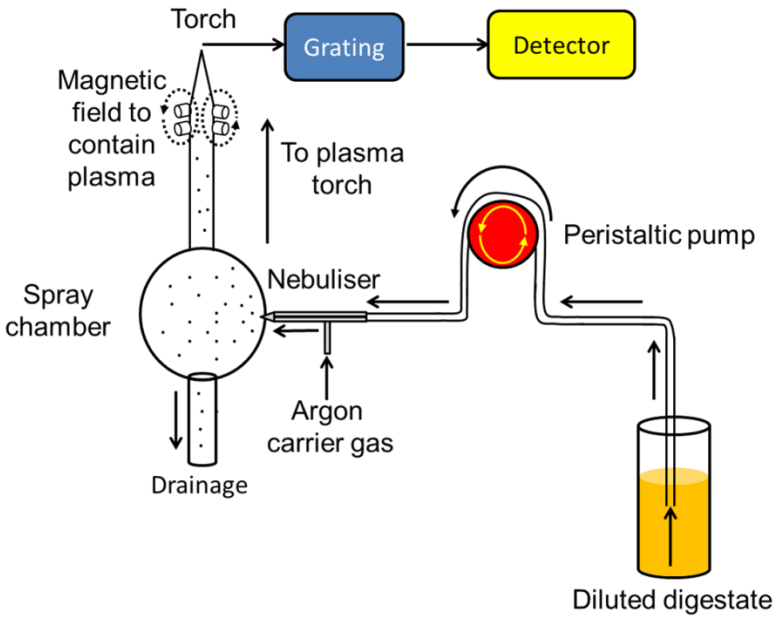


Figure 2 - Typical ICP-OES schematic showing the process of the digestate reaching the plasma torch.

### 2.2.2 Transmission Electron Microscopy

Microscopy was completed on two instruments; a JEOL 2010 Transmission Electron Microscope (TEM) operated at 200 kV and a Scanning Transmission Electron Microscope (STEM) utilizing a Cs aberration-corrected JEOL 2100F microscope at 200 kV. Images were collected using a Gatan Ultrascan 4000 digital camera operated by Digital Micrograph software. Samples were dispersed in ethanol and deposited on 300-mesh carbon-supported copper grids or carbon-supported nickel grids (Cu, PtCu and Pt Single Atom Alloys) and were then dried under ambient conditions. Images were processed using both the Gatan Ultrascan software and by ImageJ version 1.41 software.

In electron microscopy a beam of electrons is passed through a thin layer of sample deposited on a carbon coated grid. Resulting electron absorption leads to an image shown on a fluorescent screen; this image can then be magnified and focused like a conventional microscope. A significant difference between the two instruments used in this study is that the STEM has the ability to focus the beam into a very narrow stream; this then sweeps the sample line by line, providing much better resolution than conventional TEM. The instrument is also fitted with dark field imaging; this makes the resolution of nanoparticles

in particular easier to measure if they exhibit a similar Z contrast to the support they are measured against. The Z contrast of a material is directly proportional to the atomic number of said metal e.g. Pt - 78 will image much more strongly than Cu - 29. With this in mind, to be sure of the presence of Cu nanoparticles, one must focus the image sufficiently to observe atomically resolved images; this is where the interplanar distance can be measured. This is the distance between the lattices of the metal particle.

A limitation of this form of microscopy is the electron beam itself. If it is held in position for an extended period of time, it leads to the sintering, agglomeration or general deformation of sample material.[12] Additionally, the STEM is much more susceptible to image contamination if there is any carbon present on the sample when at high magnification. To eliminate surface contamination, the sample is subjected to a defocused beam at a magnification of ~50 000 times where it is physically moved to a higher position in the instrument.[13] The 'beam shower' procedure is not known to damage the sample and proved to be invaluable when imaging all catalysts synthesized using ethylene glycol and PVP, as residual carbon material appeared to cause contamination very quickly.

A general schematic for electron microscopy, in comparison with standard optical microscopy, is shown in Figure 3.


Figure 3 - A general schematic of electron microscopy compared with a light microscope.[14]

### 2.2.2.1 Energy Dispersive X-ray Spectroscopy

Bimetallic samples were analyzed by Energy Dispersive X-ray spectroscopy (EDX), similar to the photoelectron effect as explained by Albert Einstein.[15] The sample is irradiated with an x-ray source, where a photon excites a core electron causing it to be ejected from the shell that it resides in. The hole created by an excited electron is then filled by an electron demoting from an outer shell. This change in energy can be emitted as an x-ray itself and, dependent on the number and intensity of the emission, the analyzer can differentiate elements. Relative intensity of the signal can then be integrated to determine the sample composition. This process is invaluable when determining atomic ratios in a sample, especially if signal overlap is apparent for XPS analysis. A typical emission spectrum for a PtCu/$\gamma$-$Al_2O_3$ bimetallic nanoparticle is seen below in Figure 4. Energy Dispersive X-ray Spectroscopy was conducted using an Oxford Instruments INCA EDS system.

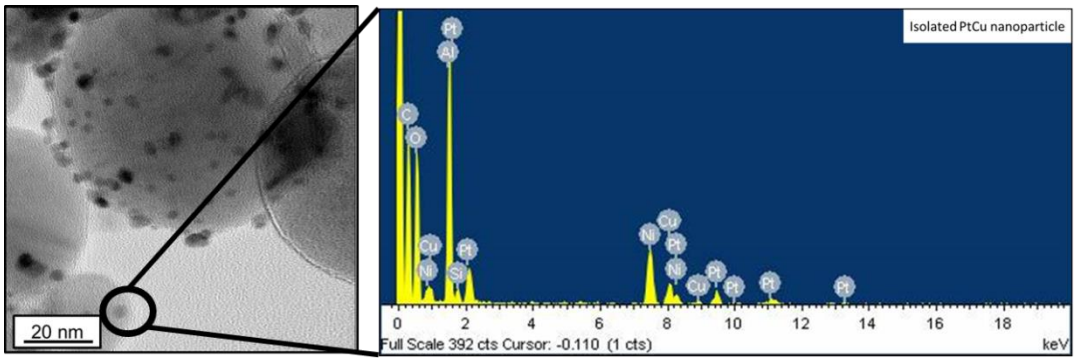


Figure 4 - Typical EDX spectrum from a $Pt_{65}Cu_{35}$/$\gamma$-$Al_2O_3$ sample after calcination (300 $^{o}$C) and reduction (200 $^{o}$C).

### 2.2.3 Powder X-ray Diffraction

X-ray diffractograms, for all powder catalysts, were collected on a Bruker D8 Advance diffractometer using monochromated Cu K$\alpha$1 radiation ($\lambda$ = 0.1542 nm). Subsequent peak assignment was based on the ICDD's PDF-2 2012 database. X-ray diffraction is seen to be a non-destructive analysis technique where the sample has been scanned; it can be reclaimed for further characterization or catalysis. The x-ray source, specifically Cu radiation for all powder characterization in this thesis, involves photoemission similar to EDX mentioned previously. A vacancy or hole is generated in the core electron level and this is filled by an electron in a higher shell; this energy change produces an x-ray. The

resulting radiation is angled towards the sample through a monochromator. The powder used should be finely ground and a smooth surface is essential, a schematic for an X-ray diffraction experiment is shown in Figure 5. Although by eye the powder will be of homogenous size, in reality there will be a range of mesh sizes in the ground material. However, there will be a large array of crystallites of the correct orientation to allow for constructive interference with the incident rays, which gives rise to the displayed diffraction pattern of the crystalline or amorphous material scanned. Constructive interference can be understood by Bragg's Law, where refraction angles are observed only if the interplanar distance is equal to an integer multiplied by the x-ray wavelength.[16]

$$n\lambda = 2d\sin\theta$$ Equation 1 – Bragg's Law

where:

- $\lambda$ is the wavelength of the x-ray
- n is the multiplication integer (order of reflection)
- d is the interplanar distance
- $\theta$ is the diffraction angle at which the peak is associated

As well as providing diffraction patterns of the support material, if the active metal is of high enough loading and crystallite size, nanoparticles can be depicted from the diffractogram. A Miller index can be assigned to the reflection seen, as well as a crystallite size estimate, as calculated by the Scherrer equation.[17] This information is useful as it can provide an early indication of particle size before advanced characterization such as Transmission Electron Microscopy. This being said, there is a limitation to crystallite detection. Depending on crystallinity of the supporting material and if the particles present are $\leq$3 nm, the peak will begin to broaden and lose its shape. The broadening of such peaks is due to destructive interference not being removed from the signal which diminishes any constructive interference leading to the peak. This issue can be overcome by monitoring multiple crystal planes and averaging the crystallite size.[17]

$$\tau = \frac{K\lambda}{\beta\cos\theta}$$ Equation 2 - Scherrer equation to determine crystallite size[17]

where:

- $\tau$ is the mean crystallite size
- K is a dimensionless shape factor (0.89)
- $\lambda$ is the wavelength of the radiation used (Cu - 0.1542 nm)
- $\beta$ is the Full Width at Half Maximum (FWHM) as calculated by the instrument or by manual integration
- $\theta$ is the diffraction angle at which the peak is associated

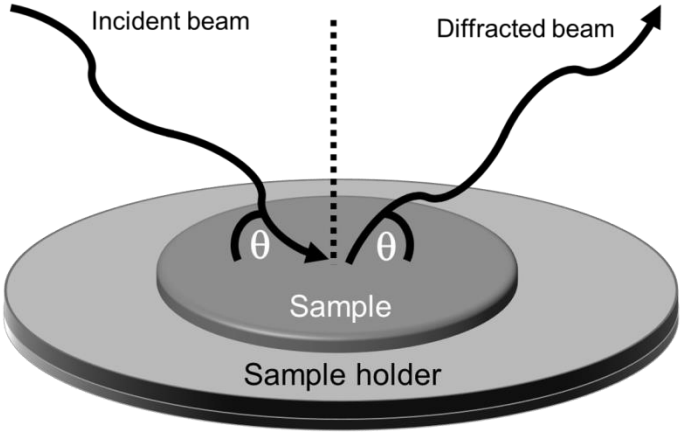


Figure 5 – General schematic for X-ray Diffraction on a typical sample in sample holder.

### 2.2.4 X-ray Photoelectron Spectroscopy

X-ray Photoelectron Spectroscopy (XPS) is a surface sensitive technique that can provide valuable information about oxidation state, surface population and trace elemental content in materials. Typically, XPS instruments are equipped with 2 separate anodes where Mg K$\alpha$ (1253.6 eV) and Al K$\alpha$ (1486.6 eV) monochromated radiation can be used to irradiate samples. This relatively low energy technique is classified as 'soft x-rays' as opposed to 'hard x-rays' which require synchrotron radiation which has an energy around 1 million times higher (1-6 GeV). As previously stated, XPS is a surface sensitive technique; this is due to the small distance that an electron can escape (1-3 nm).[18] This is the opposite to the penetration depth of the x-rays themselves which are known to be able to pass deep into a material. When the material has been irradiated, there is a subsequent ejection of a core electron if the appropriate energy is supplied. Upon emission, the core hole is left in an

excited state and the overall electronic configuration is temporarily in an unstable state. As a result, outer electrons are demoted to fill the core hole and the atom is returned to a stable state. This premise is depicted in Figure 6.

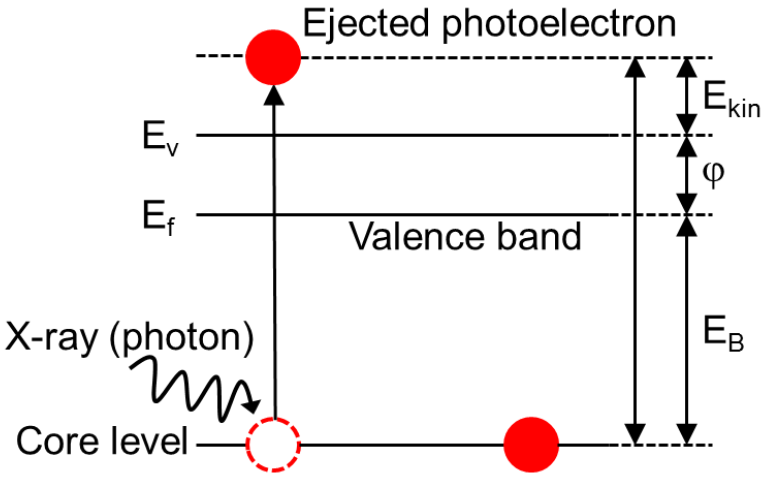


Figure 6 - Schematic depiction of photoionization ($E_{kin}$ = Photoelectron kinetic energy, $E_B$ = electron binding energy; φ = work function; $E_f$ = Fermi level; $E_v$ = vacuum level.

The photoemission possesses a specific kinetic energy ($E_{kin}$) which is characteristic of the element and its chemical nature. The binding energy ($E_B$) is the energy required to promote an electron to the Fermi level ($E_f$) and this energy is also unique to the element in question. As a result of the energy and position of the photoelectron, an XP spectrum can be acquired. The binding energy of the electron can be obtained by subtracting $E_{kin}$ and the spectrometer work function from the incident photon energy. This is summarized in the equation deduced from the work of Ernest Rutherford (equation 3). Where hv is the photon energy and h is Planck's constant ($6.626 \times 10^{-34}$ $m^2$ kg $s^{-1}$).

$$E_{kin} = h\nu - E_B - \varphi$$ Equation 3 – Kinetic energy

The spectrometer work function relates to the ejection energy from the $E_F$ to the vacuum ($E_V$). However, surface charging can occur which can cause deformation to peak shape and also shift binding energies. As a result charge neutralizers are used to dampen this effect and sharpen resolution. However, for some materials the charging phenomenon is not

easily overcome. As a result a reference material is used as a correction factor; this is typically the C 1s peak originating from the carbon tape that the sample is adhered to.

X-ray Photoelectron spectra were acquired on a Kratos AXIS HSi spectrometer equipped with a charge neutralizer and monochromated Al Kα excitation source (1486.7 eV), with energies referenced to adventitious carbon at 284.6 eV. Spectral fitting was performed using CasaXPS version 2.3.15. For the case of monometallic Pt (Chapter 4), Pt 4f peaks were fitted using a common asymmetric peak shape. Errors were estimated by varying the Shirley background subtraction procedure across reasonable limits. However, bimetallic and Single Atom Alloys synthesized and tested in Chapter 5 utilize the Pt 4d region (limited signal due to building upon a C 1s satellite) due to Pt 4f peak overlap with the Al 2p region originating from the catalyst support. Copper oxidation states were investigated by monitoring the Cu LMM region with a Mg source, specifically the broadening of the $L_3VV$ peak.

### 2.2.5 Nitrogen physisorption measurements

High surface area materials are critically acclaimed as superior performing materials in the realm of catalysis. This is seen to be the case as gas and product diffusion is enhanced leading potentially to a higher rate of reaction. However, many commercially bought oxides that are typically used as catalyst supports are of a wide range of surface areas. This leads to varying metal dispersions and potentially different rates of reactions. Additionally, metal support interactions and chemical environments have a bearing on reaction rate as well as surface area. The majority of oxide supports used for the liquid phase reactions in this thesis are relatively low, as compared to materials such as ordered porous materials and some nano-supports.[19–22] Surface area is calculated by the Brunauer–Emmett–Teller (BET) equation (equation 4 and 4b).

$$\frac{P}{V_a(P_0 - P)} = \frac{1}{V_m C} + \frac{C - 1}{V_m C}\left(\frac{P}{P_0}\right) \qquad \text{Equation 4 – BET (linear)}$$

Where:

- P = pressure
- $P_0$ = saturation pressure
- $V_a$ = volume adsorbed
- $V_m$ = monolayer volume
- C = multilayer adsorption parameter

Nitrogen physisorption occurs at a constant temperature (77.5 K) and pressure where surface area measurements are conducted by the physical adsorption of a gas (nitrogen) on to the surface. The amount of surface bound $N_2$ is then calculated to determine monolayer coverage. The interaction between the nitrogen molecules and the material in question is based upon relatively weak intermolecular forces (van der Waals forces). The nitrogen pressure is gradually increased across the analysis where an equilibrium between adsorption and desorption is assumed. Due to the low analysis temperature, nitrogen multilayers occur, which is where nitrogen interacts with other nitrogen molecules instead of the adsorbate.

The theory of nitrogen physisorption to determine surface area was developed by slightly modifying the original Langmuir theory. As the Langmuir theory does not take $N_2$ multilayer formation into consideration the constant C was established to account for interactions between adlayers of $N_2$. The specific surface area is calculated from the linear region of the BET plot, which indicates monolayer coverage assuming the packing between nitrogen molecules is 0.162 $nm^2$. The parameters of this process are expressed in equations 4a and 4b which determine both the multilayer interaction constant and the true surface area calculation assuming equal spacing between nitrogen molecules.

$$C \propto \exp \frac{E_1 - E_L}{RT}$$

Equation 4a – Definition of constant C

Where:

- C - multilayer adsorption parameter
- $E_1$ – the heat of adsorption for the first layer (kJ $mol^{-1}$)
- $E_L$ – the heat of adsorption for the second subsequent $N_2$ layers (kJ $mol^{-1}$)
- R – Universal gas constant (8.314 J $mol^{-1}$ $K^{-1}$)
- T – Analysis temperature (K)

$$SA = \frac{V_m \sigma N_a}{mv}$$ Equation 4b – BET surface area calculation

Where:

- SA – BET specific surface area
- $V_m$ - monolayer volume
- σ - $N_2$ packing value (0.162 $nm^2$)
- Na - Avogadro number
- T – Analysis temperature
- m - sample mass
- v - gas molar volume

The surface area of the monometallic Pt supported materials used in Chapter 4 were determined using a Micromeritics TriStar porosimeter by initially degassing under sustained helium flow at 60 $^oC$ for 4 hours.

Bimetallic catalysts and Single Atom Alloy surface areas were measured using a Quantachrome Nova 1200 porosimeter and NovaWin v2.2 analysis software. Samples were degassed at 120 °C under vacuum for 1 h prior to $N_2$ adsorption. In contrast to other surface area measurements acquired when using the Micromeritics TriStar porosimeter, the degas process uses a vacuum station opposed to flowing helium through the material. By degassing materials at an elevated temperature to ensure water removal, the surface area measurements were found to be comparable.

### 2.2.6 Carbon monoxide pulse chemisorption

Monometallic and bimetallic nanoparticle dispersions were obtained by CO chemisorption using a Quantachrome ChemBET 3000 (Instrument used as well as in house built gas delivery system is shown in Figure 7). To be compatible with catalysis testing procedures, all thermal processing before chemical analysis was identical. This involved purging the material with flowing He (~30 $cm^3$ $min^{-1}$) for 30 min. Reduction was completed under flowing $H_2$ (20 $cm^3$ $min^{-1}$ – regulated by mass flow controller), heating up to 300 $^oC$ and held for 30 min. This was then followed by sustained He flow at 300 $^oC$ to remove surface bound $H_2$ (30 min). The sample was then cooled to room temperature before CO titration.

Carbon monoxide was injected (50 μl) into a carrier He stream (~60 $cm^3$ $min^{-1}$) which passed over the sample. The injection process was repeated numerous times (at least 5 cycles) until there were 3 concordant results showing no further CO adsorption onto the surface of the catalyst.

The covalent bond strength between CO and metal surfaces such as Pt is far stronger than that seen for organometallic complexes.[23] As the bond strength is so strong, there is a large thermal stability meaning that the substrate does not need to be at cryogenic temperatures, as the CO will readily adsorb at room temperature. This in turn means that the CO will stay on the metal surface rather than migrate off and into the gas phase. The TEM images from the monometallic Pt nanoparticles have shown that the dominant facet formed is the Pt(111). This face is the primary adsorption site for CO due to an interaction between the non-bonding 5σ molecular orbital and the Pt $d_z^2$ orbital, creating two alternate bonding and antibonding sigma orbitals. This is shown in Figure 8 where the generated orbitals 5σ~ and 5σ lie well below the Fermi level; this means that they are more prone to electron addition.[24,25]

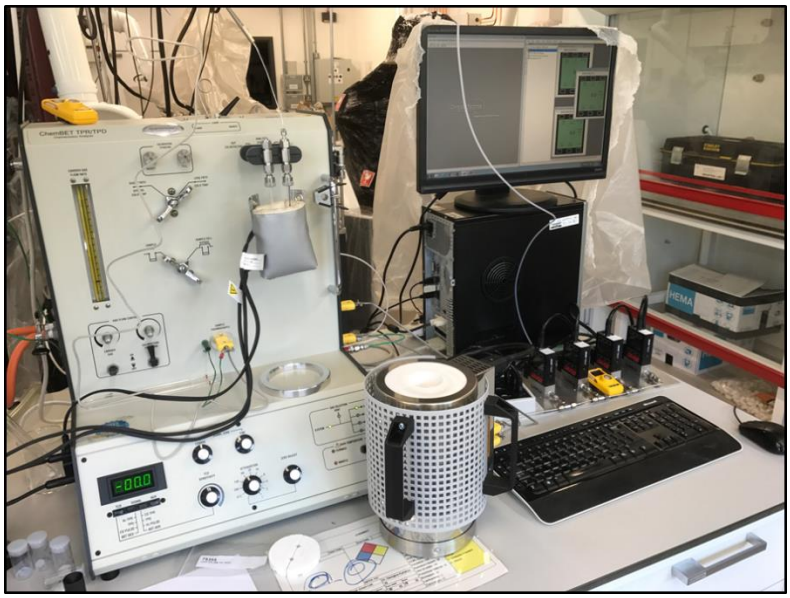

Figure 7 – Image of the Quantachrome ChemBET used for CO chemisorption measurements equipped with an in house mass flow controller system.

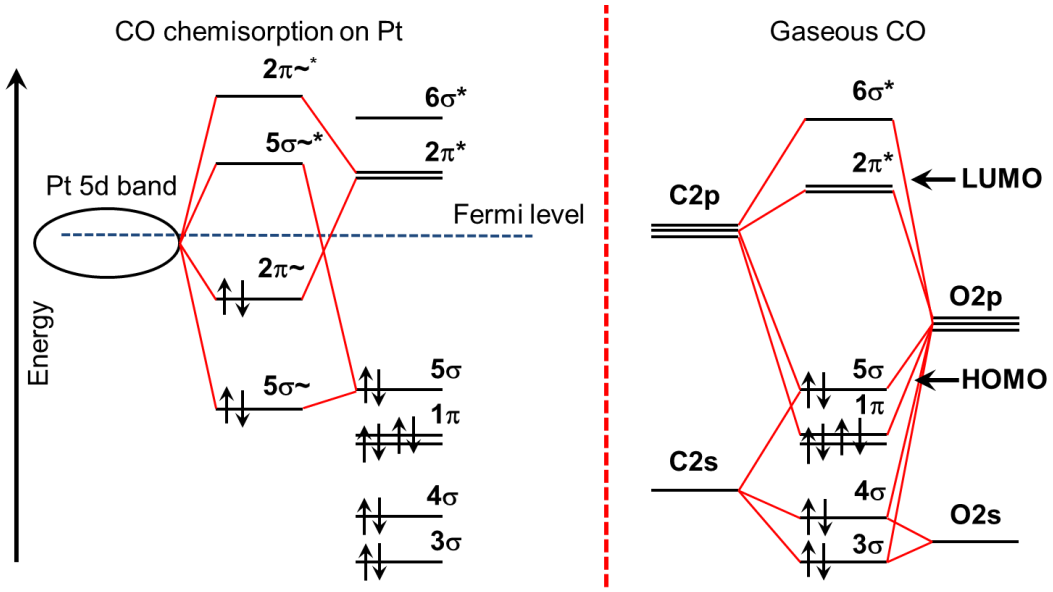


Figure 8 - Molecular orbital diagrams for CO on Pt and free gaseous CO.

Orbital positioning near the Fermi level determines the overall CO bond strength. Due to Pt possessing 5d valence orbitals, it can experience greater electron mobility between the d orbital and its lower energy 6s orbital. The movement of electrons between these orbitals strengthens the Pt-CO bond as the CO will donate charge to the surface.

All CO titrations were carried out at room temperature (18 $^{o}$C) and assuming that the CO:$Pt_{surface}$ stoichiometry is 0.68, it reaches a maximum surface coverage of 0.7 ML, as a full monolayer is seen to be energetically not favoured at these conditions. It is assumed that the 0.7 ML is reached upon successive CO injections until no peak height increase is seen.[26,27] Using this technique of titration, both particle surface dispersion and Pt particle size can be calculated using equations 5 and 6.[25,28] However, particle size analysis via this method is possibly less trustworthy compared to other characterization techniques, such as TEM and PXRD, as it takes into consideration a shape factor which is dependent on the particle/support protrusion, revealing a specific surface area for CO adsorption. This shape factor can be likened to the wettability of a droplet on a surface depending on the hydrophobicity of the particle to the surface. A metallic particle can reside on the surface as a whole shape or begin to enter the surface where only a fraction is free for adsorption.

$$D_m = \left(\frac{mol_{COads}\, S_{av}}{mol_{Pt}}\right) \times 100$$ Equation 5: Pt surface dispersion

Where:

- $D_m$ – metal dispersion
- $mol_{COads}$ – moles of CO adsorbed
- $S_{av}$ – CO:Pt stoichiometry
- $mol_{Pt}$ = number of moles of Pt in sample

$$PS_{ave} = \left(\frac{5C_m f_m}{2.7x10^{12} \times S_{av} d_m V_g}\right)$$ Equation 6: Average particle size

Where:

- $PS_{ave}$ – particle size (nm)
- $C_m$ – metal surface density (atom $cm^{-1}$)
- $f_m$ – metal loading (mass of metal (g) /mass of catalyst (g))
- $S_{av}$ - CO:Pt stoichiometry
- $d_m$ – metal density ($g_{met}/cm^3$)
- $V_g$ - chemisorbed gas volume ($cm^3/g_{cat}$)

### 2.2.7 Diffuse Reflection Infra-red Fourier Transform Spectroscopy

Diffuse Reflection Infra-red Fourier Transform Spectroscopy (DRIFTS) is a technique which utilizes the infra-red section of the electromagnetic spectrum. This form of spectroscopy is used to ascertain the bonding mode of a surface bound species. This is achieved by IR radiation absorbing, and subsequently causing excitation of the vibrational modes of the surface bound functional groups. Such vibrational modes are represented in either bond stretching or bending, through the absorption of photons at a specific energy. This absorption generates a dipole moment which has its own specific wavenumber depending on the bond. The relationship between the frequency ($\bar{\upsilon}$) of the vibration with the force constant (k) and the reduced mass of the system ($\mu$) can be found by applying Hooke's law, as shown in equation 7.

$$\bar{\upsilon} = \frac{1}{2\pi}\sqrt{\frac{\kappa}{\mu}}$$ Equation 7 – Hooke's law[29]

Due to the fact that photons can either be transmitted through the sample or scattered, generating a large noise to signal ratio, a parabolic mirror is used to focus the reflected

beam. This increases both the sensitivity and signal to noise ratio dramatically. A schematic of such an operation is presented in Figure 9.

In situ, CO adsorption experiments were conducted using a Thermo Scientific Nicolet iS50 FT-IR with Smart Collector accessory, mid/near infrared source and mercury cadmium telluride (MCT) photon detector cooled to -196 °C (Figure 9). A temperature programmable, gold-coated in situ cell, interfaced to mass flow controllers via a gas manifold permitted the following treatment. Pure samples were purged with flowing He (20 $cm^3$ $min^{-1}$) for 30 min and reduced at 300 $^oC$ under flowing $H_2$ (10 $cm^3$ $min^{-1}$) for 30 min. While at this temperature, the gas treatment was switched to He (20 $cm^3$ $min^{-1}$) to remove adsorbed $H_2$ and to purge the cell. The sample was then water cooled to 20 $^oC$. CO adsorption was conducted under flowing CO (10 $cm^3$ $min^{-1}$) at 20 °C until the gas phase peaks indicated the cell was saturated. Spectra readings were obtained every 2 minutes until concordant saturation spectra were observed. The cell was subsequently purged with He and once again spectra were recorded every 2 minutes to determine whether or not CO had bound to the surface. Spectra were measured from 4000 to 400 $cm^{-1}$ wavenumbers with a resolution of 4 (Resolution being degree of fineness for the data, units of $cm^{-1}$).

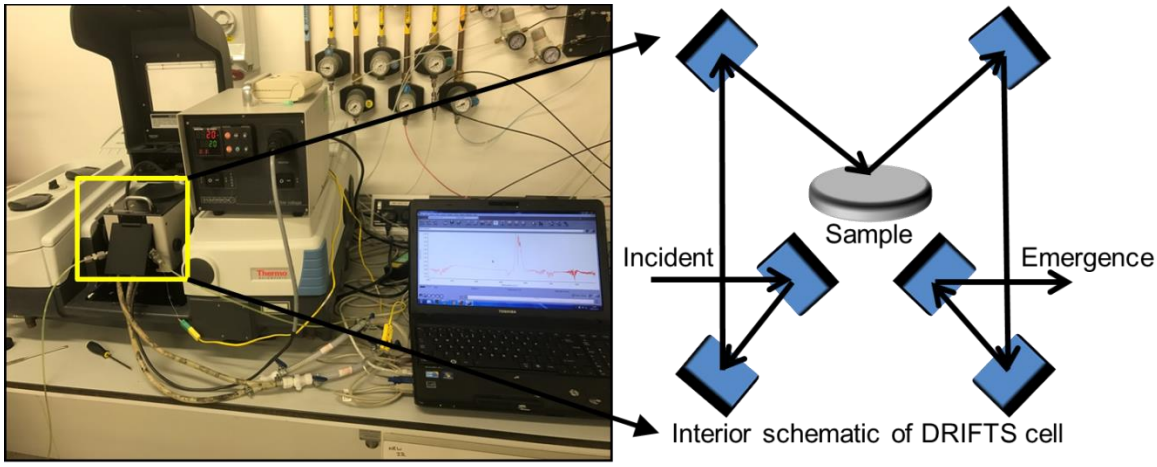


Figure 9 – Infrared spectrometer experimental setup and interior schematic.

The CO adsorption on metallic sites can vary depending on the facet, which is represented by different bonding types. These are observed by shifts in the carbon-oxygen stretching frequency. Increasing electron back donation shows a shift to lower wavenumbers.

Potential bonding modes are; atop, bridging and 3-fold, which are shown in Figure 10. Changes in surface coverage shifts C=O stretching frequencies to higher numbers due to a decrease in electron back donation, which can often be observed by a change in the preferred CO bonding mode from 3-fold to bridging.

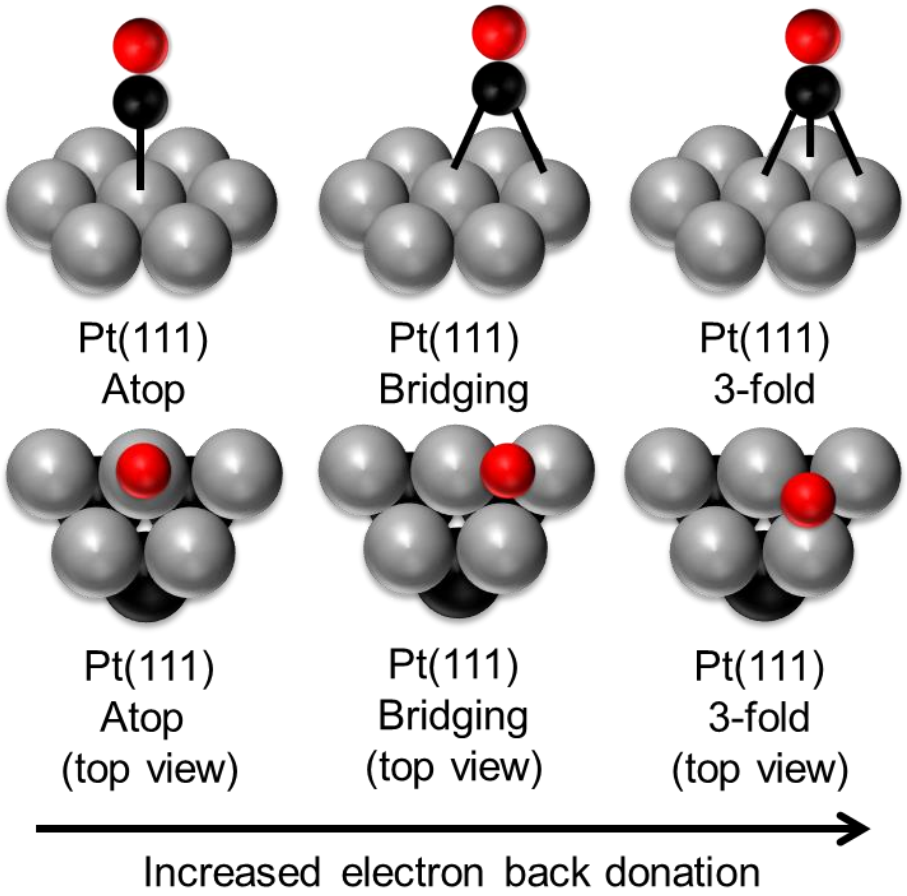


Figure 10 - Possible CO (black ball representing carbon and red ball representing oxygen) adsorption orientations; atop, bridging and 3-fold on Pt(111). For clarity a top view was generated and only the oxygen atom is shown (red).

## 2.3 Catalyst testing

### 2.3.1 Ambient pressure hydrogenation of furfural with monometallic Pt catalysts

Catalytic hydrogenation was performed using a 12-port Radleys Plus Reaction Station (Figure 11). Reaction tubes were first evacuated and purged with hydrogen (Energas 99.99%) three times to ensure that the system was air-free; hydrogen was supplied via 2 balloons pressurized to 1.02 atm, as measured by a Measurement SpecialtiesTM XP5

pressure sensor. The first balloon acted as a hydrogen reservoir to purge the reaction tubes and the second as a reaction gas supply. In a typical run, 10 mL of solvent (MeOH, EtOH, n-BuOH, toluene or hexane), 16.5 μL (approximately 0.2 mmols) of furfural and 20 mg of catalyst were mixed at 600 rpm at various temperatures (30, 50 or 70 $^{o}$C). The reaction mixture was sampled (0.2 mL) at measured time intervals with quantification via an external dodecane standard (50 μL from a 0.02 M standard) or decane as an internal standard for high pressure reactions. These were analyzed on a Bruker Scion 456-GC equipped with a flame ionization detector and a Zebron ZB-5 (5%-phenyl-95%-dimethylpolysiloxane) capillary column (Figure 12). GC–MS was performed using an Agilent 6890 GC equipped with an Agilent 5973N Quadrupole mass spectrometer and an RXI-5MS (5%-phenyl-95%-dimethylpolysiloxane) capillary column.


Figure 11 - 12-port Radleys Plus Reaction Station with hydrogen filled balloon.


Figure 12 - Bruker Scion-456 GC used for all reaction quantification.

#### 2.3.1.1 Column heating and product retention.

To ensure clear peak separation with Gaussian shaped peaks, the method used started with a cool column (30 $^{o}$C) so that there was a clear separation between the solvent and furan. Gradually heating at 20 $^{o}$C min$^{-1}$ to 200 $^{o}$C and holding for an additional 3 minutes (isocratic period) ensured that all potential products and impurities had fully eluted. A typical chromatograph for data shown in Chapters 4 and 5 is presented in Figure 13. The wider diffractogram is split into two sections, the first for solvent and furan retention and the latter with furfural and furfural hydrogenation.

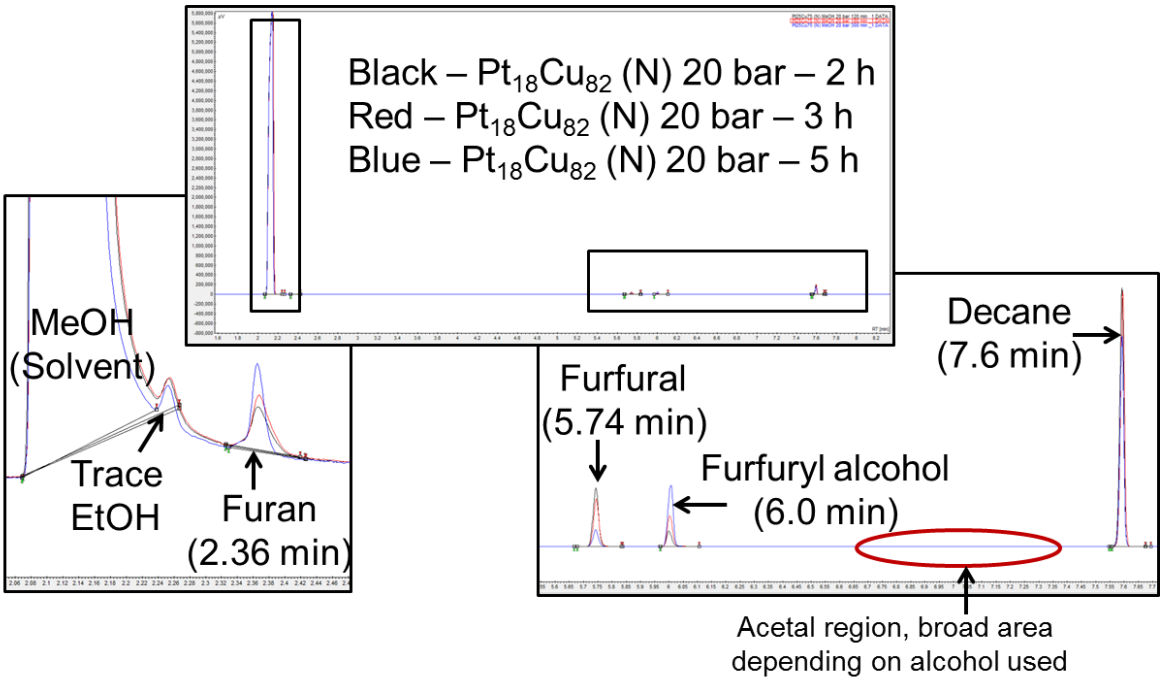


Figure 13 - A typical GC chromatograph showing the peak separation for a typical furfural hydrogenation reaction ($Pt_{18}Cu_{82}$ (N)) completed in Chapter 5.

#### 2.3.1.2 Reusability of monometallic Pt catalysts

The reusability of supported monodisperse Pt nanoparticles was completed by separating the catalyst powder from the reaction mixture by centrifugation and washing three times with methanol. The powders were then dried at 50 $^{o}$C overnight and then reused.

### 2.3.2 In situ reduction and high pressure hydrogenation reactions

In situ reduction and catalysis were carried out in a HEL multi-reactor high pressure platform, housing a bank of three 50 mL stainless steel reactor vessels (Figure 14). The catalysts of mass ~30 mg were heated under flowing $H_2$ to 300 $^{o}$C at 5 $^{o}$C min$^{-1}$ and held for 0.5 h. Upon cooling under flowing $H_2$, the autoclaves were sealed and purged with He to prevent catalyst oxidation. While He is flowing, the reaction mixture consisting of methanol (10 mL, Fisher Scientific, 99.99%), furfural (16.5 μL, 0.02 M, Sigma Aldrich) and decane (38 μL, 0.02 M, Sigma Aldrich) was injected into each reactor. The mixture was degassed for a period of 10 minutes before pressurizing under $H_2$ (1.5, 10 and 20 bar, BOC, 99.995%), heating to 50 $^{o}$C and stirred at 600 rpm. The reaction was run for 7 h and sampled periodically (~0.2 mL) by slowly depressurizing to atmospheric pressure and then

repressurizing. Samples were analyzed on a Bruker Scion 456-GC equipped with a flame ionization detector and fitted with a Zebron ZB-5 (5%-phenyl-95%-dimethylpolysiloxane) capillary column.

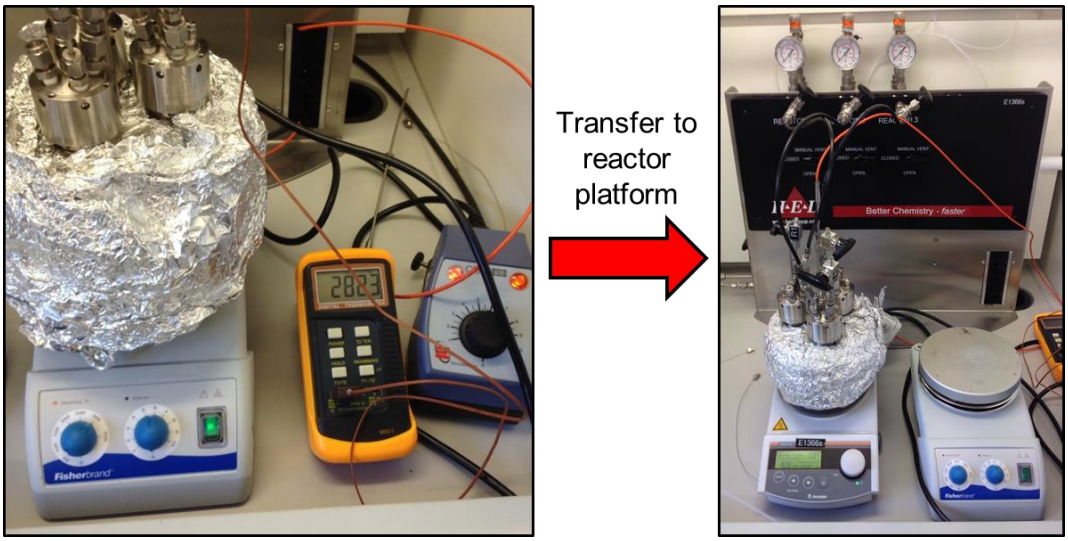


Figure 14 - The reactor set up for in-situ reduction/reaction.

## 2.4 Ultra-high vacuum systems and crystal preparation

### 2.4.1 UHV TPR chamber system set up

Temperature Programmed Reaction/Desorption (TPR/TPD) experiments were conducted in a stainless steel chamber pumped by a Varian Turbo-V 300HT turbomolecular pump with an operating speed of 56 krpm and an Edwards RV5 rotary pump. This provided an operational base pressure of $3\times10^{-10}$ mbar. A second rotary pump (Edwards RV2) was also used to achieve a high-vacuum in the gas lines. The system was equipped with an Omicron 4 grid retarding field analyser for LEED/AES analysis and a VG 300 quadrupole mass spectrometer whose ionizer was positioned 6 mm from the front face of the sample. The chamber was also equipped with a Thermo Scientific VG ion gun for $Ar^+$ sputtering.

#### 2.4.1.1 Mounting of the single crystal

The Pt(111) (Surface Preparation Laboratory, The Netherlands, oriented within 0.2 degrees) sample was mounted on the manipulator of the UHV system via four 0.25 mm tantalum wires (Advent Research Materials Ltd, 99.9%), threaded through four holes on

the sides of the crystal edge and spot welded to two molybdenum rods (Figure 15). The Pt(111) single crystal was cooled by liquid nitrogen to 140 K and heated resistively to 1000 K, which was monitored by a $T_1T_2$ K-type thermocouple spot-welded directly to the top edge of the sample.

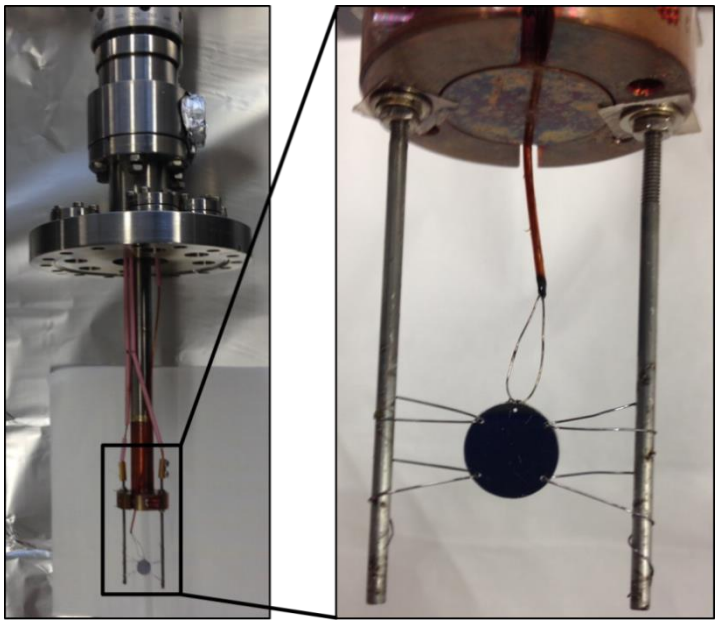

Figure 15 - Mounting of the Pt(111) sample onto the manipulator

### 2.4.1.2 Sample preparation

Platinum readily adsorbs carbon monoxide[23] and this, as well as carbonaceous deposits formed via thermal decomposition of organic material, were removed by repeated cycles of $Ar^+$ (99.999% Messer) sputtering (1 keV, 5 μA) for a period of 40 min followed by annealing at 1000 K (Figure 16). This process was followed by exposing the sample to $5.5\times10^{-8}$ mbar $O_2$ (Energas, 99.95%) for 25 min at 815 K. The sample was finally annealed to 1000 K and the desorption products released through the TPD were monitored by QMS (Quadrupolar Mass Spectrometry). The following molecules and their mass fragments were observed: CO (*m/z* 28), $H_2O$ (*m/z* 18), $CO_2$ (*m/z* 48), $O_2$ (*m/z* 32) and O (*m/z* 16). The sample was known to be clean upon successful desorption of molecular oxygen instead of CO.

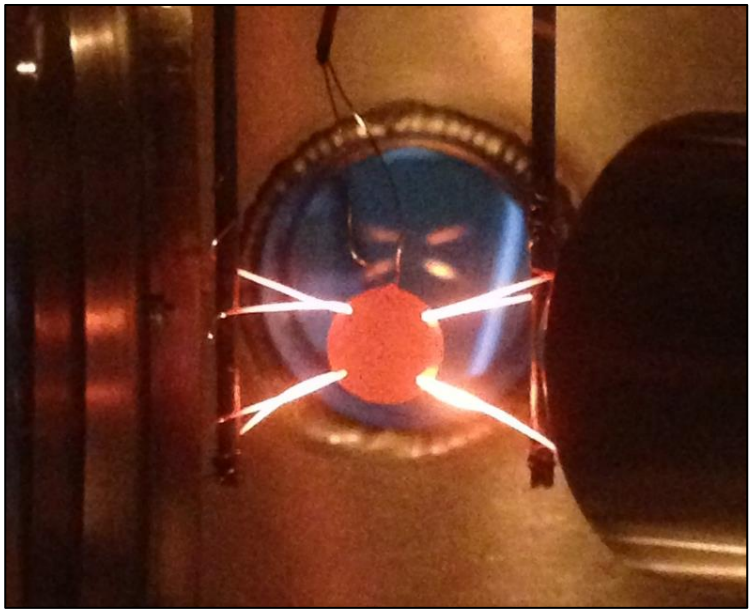

Figure 16 - Annealing of the Pt(111) at 1000 K

#### 2.4.1.3 Reagent exposure

Both gases; $H_2$ (Energas, 99.99%) and $O_2$ (Energas, 99.999%) as well as the organic molecules; furfural (Sigma Aldrich, 99%), furan (Sigma Aldrich, ≥ 99%), 2-methyl furan (Sigma Aldrich, 99%) and furfuryl alcohol (Sigma Aldrich, 98%) were purified by several freeze-pump-thaw cycles and dosed onto the Pt(111) surface by backfilling the chamber to the required pressure.

## 2.5 Temperature Programmed Desorption and Reaction (TPD/TPR)

TPD and TPR measurements were performed with a linear heating ramp of 9.9 K $s^{-1}$. Selectivity calculations (Equation 8) from the mass spectrometry data include corrections for mass spectrometer sensitivity and molecular ionization cross section achieved by admitting a known pressure of each molecule into the vacuum system measuring the intensity of the mass fragments and correcting the pressure gauge reading based on the theoretical ionization cross section. Mass fragments for molecular identification were as follows; furfural (m/z 96 and 39), furan (m/z 68 and 39), furfuryl alcohol (m/z 98, 81 and 39) and methyl furan (m/z 82, 53 and 39). Additional ions were also monitored to identify potential products tetrahydrofuran (m/z 72), tetrahydrofurfuryl alcohol (m/z 102), 2-methyltetrahydrofuran (m/z 82) and propene (m/z 42) however none of these latter

molecules were detected from furfural with and without co-adsorbed $H_2$. Exposures are quoted in Langmuirs (L), where 1 L is $1\times10^{-6}$ Torr $s^{-1}$ and have been corrected for ion gauge sensitivity.

$$S_{FFA}(\%) = \left(\frac{A_{FFA}}{A_{FFA} + A_{Furan} + A_{MF} + C}\right) \times 100$$ Equation 1 - Reaction selectivity

Where:

FFA – Furfuryl alcohol

MF – Methyl furan

C – Surface carbon

S – Selectivity of a specific product (%)

A– Desorption peak area

The resulting desorption of the molecules entering the gas phase is monitored by the mass spectrometer positioned 6 mm from the front of the crystal. This process is known as a Temperature Programmed Desorption (TPD). However, when the reactant desorbing from the surface has reacted with a co-dosed molecule or has altered its chemical structure, the process is known as a Temperature Programmed Reaction (TPR). Such a process can reveal important structural information such as; molecular geometry,[30–33] enthalpy changes such as adsorption, desorption and activation energies, as well as bond strengths. TPD profiles can also give information about the relative coverage of the adsorbed material on the surface. The theory behind adsorption-desorption can be described by a set of rate equations leading to the Polanyi-Wigner equation which describes the rate of desorption as a function of temperature T and surface coverage θ with order of desorption being n and energy of desorption $E_d$.[34,35]

$$r_{des} = -\frac{\Delta\theta}{\Delta t} = k_n \cdot \theta^n$$ Equation 9 – Description for the rate of desorption

It can then be inferred that the rate constant ($k_n$) is described by the Arrhenius equation where A is the pre-exponential factor which is assumed to be the same as the molecular vibrational frequency, typically $10^{13}$ $s^{-1}$. However, larger molecules have different vibrational frequencies and other pre-exponential factors have to be used.[36] This can be problematic as the function can change significantly by many orders of magnitude.[37] Also represented in the equation is the universal gas constant, R.

$$k_n = A \,.\, \exp\left(-\frac{\Delta E_{des}^{PW}}{RT}\right)$$ Equation 10 – The Arrhenius equation

By combining both equations we can see that the rate of desorption is as described above, a function of temperature, surface coverage and desorption energy $\left(\Delta E_{des}^{PW}\right)$.

$$r_{des} = -\frac{\Delta\theta}{\Delta t} = A \,.\, \exp\left(-\frac{\Delta E_{des}^{PW}}{RT}\right) \,.\, \theta^n$$ Equation 11 – The Polanyi-Wigner equation[34]

The process of a TPD measurement involves a linear heating ramp, which is represented as β and is calculated by the change in temperature over the change of time ($\Delta T/\Delta t$). By incorporating this factor into the Polanyi-Wigner equation we can begin to derive reaction order directly from the TPD data.

$$r_{des} = -\frac{\Delta\theta}{\Delta T} = \frac{A\theta^n}{\beta} \,.\, \exp\left(-\frac{\Delta E_{des}^{PW}}{RT}\right)$$ Equation 12 – Adapted PW equation[24,35]

When the heating ramp is started the adsorbed material, whether it be gas or organic, is desorbed during the TPD sweep. There is no universal heating rate used as it can be very high or very slow depending on requirement. An example of this is heating for an STM stage which is generally very slow. The heating ramp for the work completed in this thesis is ~10 K $s^{-1}$. Upon desorption the peak observed from the QMS at varying molecule exposure can give a good idea of the order of reaction due to peak shape, symmetry and additional features.[24,37]

### 2.5.1 Zero-order desorption

Zero order desorption (n = 0) is where a molecule will desorb at a specific temperature and increasing exposure will cause the growth of a monolayer up to a maximum. At this point the molecule will begin to layer on top of the monolayer generating a multilayer species. This multilayer peak is at a slightly lower temperature due to less energy required to desorb adsorbate-adsorbate than adsorbate-surface.[24,37,38] This is represented by the following equation:

$$-\frac{\Delta\theta}{\Delta t} = \frac{A}{\beta} \cdot \exp\left(-\frac{\Delta E_{des}^{PW}}{RT}\right)$$ Equation 13 – Zero order desorption

### 2.5.2 First-order desorption

First order desorption (n = 1) is coverage dependent, which is where a peak will grow linearly with coverage, the shape will begin to widen and the leading edge will slowly move to a lower temperature as the surface becomes saturated. A classic example of this is the desorption of molecular hydrogen on the Pt(111) surface presented in this thesis. Up to a maximum (0.8 ML) the peak widens and increases in intensity as a function of coverage. Redhead[35] has also shown that for first order desorption the enthalpy of desorption ($E_{des}$) can be calculated. However, this can only be seen as an approximation as there are numerous parameters which can lead to errors such as; the pre-exponential factor, heating ramp and desorption temperature.

$$-\frac{\Delta\theta}{\Delta t} = \theta\frac{A}{\beta} \cdot \exp\left(-\frac{\Delta E_{des}^{PW}}{RT}\right)$$ Equation 14 – First order desorption

$$E_{des} = RT_{max}\left[\ln\left[\frac{AT_{max}}{\beta}\right] - 3.46\right]$$ Equation 15 – The Redhead equation[35]

### 2.5.3 Second-order desorption

Second order desorption (n = 2) is where the desorption profiles in the TPR sweep are asymmetric about $T_{max}$. This desorption is observed when two adsorbed species can react (combine) on the surface and then desorb as a different molecule. As previously seen for

first order desorption, there is a second Redhead equation to determine the activation energy. However, for this to be accurate the peak must be of high resolution.

$$-\frac{\Delta\theta}{\Delta t} = \theta^2 \frac{A}{\beta} \cdot \exp\left(-\frac{\Delta E_{des}^{PW}}{RT}\right)$$

$$\frac{E_{des}}{RT_{max}^2} = \frac{A}{\beta} 2\theta \cdot \exp\left(-\frac{E_{des}}{RT_{max}}\right)$$ Equation 16 – Equation for activation energy

## 2.6 Scanning Tunneling Microscopy

Colleagues from the Technical University of Munich provided high resolution STM measurements. These were obtained by utilizing a custom built UHV system (base pressure low $10^{-10}$ mbar) with a commercial STM Aarhus 150 supplied by SPECS using a chemically etched tungsten tip held at 293 K. Furfural molecules were dosed in situ. The tunneling bias ($V_t$) is applied to the sample. The STM micrographs were processed using the WSxM software.[39,40]

STM can produce atomically resolved images of a solid surface; this is where a sharp tip (typically tungsten) is positioned at a distance (d) of a few nm from the surface. As a potential is placed between the tip and the surface in question, a flow of electrons will travel between the two entities. The current in question is between a range of pA – nA and is known as the tunneling current ($I_T$). Although it sounds as if the current is destructive as it travels through the material, this is not the case as the process is a quantum mechanical effect where the flow of electrons can pass from the tip and penetrate through into the second metal.

To allow for pin point accuracy, the tip is attached to a piezoelectrically driven support, which is controlled by a computer which can move the slider in horizontal and vertical axes.[41] This allows for the tip to move across the sample and also decreases the distance between the surface and the tip to allow for tunneling to occur, as the electron energy barrier diminishes as the distance between the tip and surface decreases.

STM experiments are generally conducted in one of two scanning modes, these are; constant-height and constant-current modes.[42–44]

Constant-current mode is where the tip is vertically adjusted so that the current remains constant (no change in elevation). It is maintained by using a feedback loop which provides a correction voltage to the piezodrive. This subtle correction will adjust the height in such a way that the current remains the same when traversing a protrusion in the surface. Recording the voltage differences during the scanning process creates a surface contour plot.

Constant-height mode is where the tip is fixed at a constant distance above the surface. As the piezodrive moves, the height is restricted by a slow or disabled feedback current. This method of imaging is only useful for atomically flat surfaces as the tip could crash. The major advantage of this method is the high scanning frequencies (up to 10 kHz) whereas the constant-current mode is much slower. All STM images obtained and used in this thesis were acquired using the constant-current mode.

An image of the atomically clean Pt(111) surface used for STM images in Chapter 3 is shown in Figure 17. This was achieved after extensively cleaning of the crystal by argon sputtering followed by annealing.

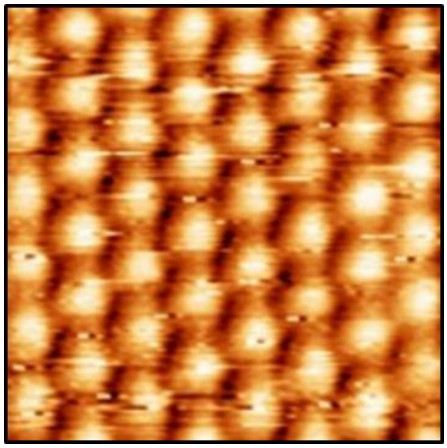

Figure 17 – Magnified STM image of atomically clean Pt(111). (1.8×1.8 $nm^2$, T = 293 K, $V_t$ = 0.42 V, $I_t$ = 16.70 nA)

## 2.7 References


1 M. M. Koebel, L. C. Jones and G. A. Somorjai, *J. Nanoparticle Res.*, 2008, **10**, 1063–1069.

2 D. Wang, F. Ammari, R. Touroude, D. S. Su and R. Schlögl, *Catal. Today*, 2009, **147**, 224–230.

3 M. J. Taylor, L. J. Durndell, M. A. Isaacs, C. M. A. Parlett, K. Wilson, A. F. Lee and G. Kyriakou, *Appl. Catal. B Environ.*, 2016, **180**, 580–585.

4 E. Rubinov, M. Diab, M. Volokh and T. Mokari, *CrystEngComm*, 2014, **16**, 9493–9500.

5 M. B. Boucher, B. Zugic, G. Cladaras, J. Kammert, M. D. Marcinkowski, T. J. Lawton, E. C. H. Sykes and M. Flytzani-Stephanopoulos, *Phys. Chem. Chem. Phys.*, 2013, **15**, 12187–96.

6 F. R. Lucci, J. Liu, M. D. Marcinkowski, M. Yang, L. F. Allard, M. Flytzani-Stephanopoulos and E. C. H. Sykes, *Nat. Commun.*, 2015, **6**, 8550.

7 M. D. Marcinkowski, J. Liu, C. J. Murphy, M. L. Liriano, N. A. Wasio, F. R. Lucci, M. Flytzani-Stephanopoulos and E. C. H. Sykes, *ACS Catal.*, 2017, **7**, 413–420.

8 Z. Sun, J. Masa, W. Xia, D. König, A. Ludwig, Z. A. Li, M. Farle, W. Schuhmann and M. Muhler, *ACS Catal.*, 2012, **2**, 1647–1653.

9 I. Mintsouli, J. Georgieva, S. Armyanov, E. Valova, G. Avdeev, A. Hubin, O. Steenhaut, J. Dille, D. Tsiplakides, S. Balomenou and S. Sotiropoulos, *Appl. Catal. B Environ.*, 2013, **136**–**137**, 160–167.

10 Y. Xiong, Y. Ma, Z. Lin, Q. Xu, Y. Yan, H. Zhang, J. Wu and D. Yang, *CrystEngComm*, 2016, **18**, 7823–7830.

11 A. Montaser and D. Golightly, *Inductively coupled plasmas in analytical atomic spectrometry*, VCH Publishers, New York, 2nd edn., 1992.

12 S. B. Simonsen, I. Chorkendorff, S. Dahl, M. Skoglundh, J. Sehested and S. Helveg, *J. Am. Chem. Soc.*, 2010, **132**, 7968–7975.

13 R. Ramachandra, H. Demers and N. De Jonge, *Appl. Phys. Lett.*, 2011, **98**, 1–3.

14 Radboud University Nijmegen, *F. Emiss. Scanning Electron Microsc. Freq. Asked Quest.*, 2012, Accessed-10/05/2017.

15 A. Einstein, *Ann. Phys.*, 1905, **17**, 132–148.

16 L. E. Smart and E. A. Moore, *Solid State Chemistry: An Introduction*, Taylor & Francis, 3rd Editio., 2005.

17 A. L. Patterson, *Phys. Rev.*, 1939, **56**, 978–982.

18 I. Chorkendorff and J. W. Niemantsverdriet, *Concepts of Modern Catalysis and Kinetics*, Wiley-VCH, 2007.

19 L. J. Durndell, C. M. A. Parlett, N. S. Hondow, M. A. Isaacs, K. Wilson and A. F. Lee, *Sci. Rep.*, 2015, **5**, 9425.

20 C. M. A. Parlett, M. A. Isaacs, S. K. Beaumont, L. M. Bingham, N. S. Hondow, K. Wilson and A. F. Lee, *Nat. Mater.*, 2015, **15**, 178–182.

21 Y. Deng, Y. Cai, Z. Sun, J. Liu, C. Liu, J. Wei, W. Li, C. Liu, Y. Wang and D. Zhao, *J. Am. Chem. Soc.*, 2010, **132**, 8466–8473.

22 C. Huo, J. Ouyang and H. Yang, *Sci. Rep.*, 2014, **4**, 3682.

23 G. Bond, *Platin. Met. Rev.*, 2000, **44**, 146–155.

24 J. W. Niemantsverdriet, *Spectroscopy in catalysis: An introduction*, Wiley-VCH Verlag GmbH & Co. KGaA, Weinheim, Germany, 2nd Editio., 2007.

25 G. A. Somorjai and Y. Li, *Introduction to Surface Chemistry and Catalysis*, Wiley-Blackwell, 2nd Editio., 2010.

26 R. Chen, Z. Chen, B. Ma, X. Hao, N. Kapur, J. Hyun, K. Cho and B. Shan, *Comput. Theor. Chem.*, 2012, **987**, 77–83.

27 R. Toyoshima, M. Yoshida, Y. Monya, K. Suzuki, K. Amemiya, K. Mase, B. S. Mun and H. Kondoh, *Phys. Chem. Chem. Phys.*, 2014, **16**, 23564–23567.

28 N. Pernicone, *CATTECH*, 2003, **7**, 196–204.

29 J. T. Burke, *J. Chem. Educ.*, 1997, **74**, 1213.

30 A. Mulligan, S. M. Johnston, G. Miller, V. Dhanak and M. Kadodwala, *Surf. Sci.*, 2003, **541**, 3–13.

31 B. A. Sexton, *Surf. Sci.*, 1985, **163**, 99–113.

32 M. J. Taylor, L. Jiang, J. Reichert, A. C. Papageorgiou, S. K. Beaumont, K. Wilson, A. F. Lee, J. V Barth and G. Kyriakou, *J. Phys. Chem. C*, 2017, **121**, 8490–8497.

33 N. Orozco, G. Kyriakou, S. K. Beaumont, J. Fernandez, J. P. Holgado, M. J. Taylor, J. P. Espinos, M. Márquez, Antonio, D. J. Watson, A. R. Gonzalez-elipe and R. M. Lambert, *ACS Catal.*, 2017, **7**, 3113–3120.

34 S. Schroeder and M. Gottfried, *Temperature-Programmed Desorption (TPD) Thermal Desorption Spectroscopy (TDS)*, Advanced Physical Chemistry Laboratory, Berlin, 2002.

35 P. A. Redhead, *Vacuum*, 1962, **12**, 203–211.

36 G. E. Gdowski, J. A. Fair and R. J. Madix, *Surf. Sci.*, 1983, **127**, 541–554.

37 D. P. Woodruff and T. A. Delchar, *Modern techniques of surface science*, Cambridge University Press, Cambridge, Illustrate., 1994.

38 G. Attard and C. Barnes, *Surfaces*, OUP Oxford, Oxford, 1998.

39 C. Romero-Muñiz, A. Martín-Recio, P. Pou, J. M. Gómez-Rodríguez and R. Pérez, *Carbon N. Y.*, 2016, **101**, 129–134.

40 I. Horcas, R. Fernández, J. M. Gómez-Rodríguez, J. Colchero, J. Gómez-Herrero and A. M. Baro, *Rev. Sci. Instrum.*, 2007, **78**, 013705–013712.

41 S. C. Kim and S. H. Kim, *Mechatronics*, 2001, **11**, 969–985.

42 J. Y. Park, *Scanning Tunneling Microscopy, Characterization of Materials*, John Wiley & Sons, 2nd Editio., 2012.

43 H. J. Guntherodt and R. Wiesendanger, *Springer Series in Surface Sciences*, Springer, Berlin, 2nd Editio., 1994.

44 E. Burstein and S. Lundqvist, *Tunneling Phenomena in Solids*, Springer US, Denmark, 1969.

# Chapter 3 - The catalytic hydrogenation and HDO of furfural on a Pt(111) single crystal

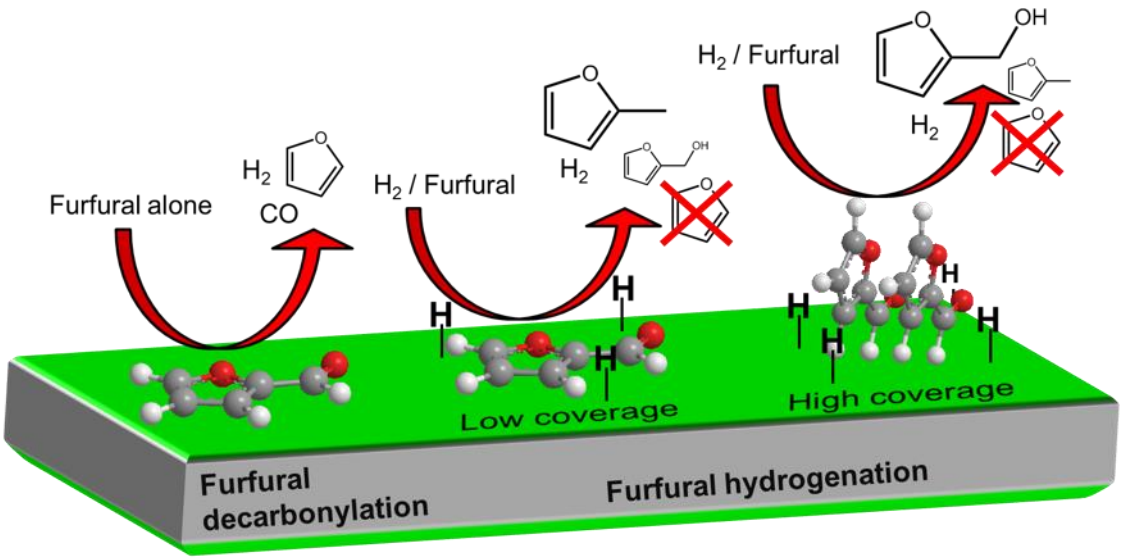

## 3.1 Introduction

Adsorption of unsaturated oxygenates over Cu, Ni, Pd and Pt(111) single crystal surfaces, and Zn adatom modified Pt(111)[1–14] has been the focus of both experimental and theoretical investigations. For furfural, reactively-formed furan (a decarbonylation product from furfural and furanoic acid) behaves differently to molecular furan over Pd(111), the former being more prone to thermal decomposition to propylene.[8,15] Density Functional Theory (DFT) calculations have highlighted multiple reaction pathways for furfuryl alcohol hydrogenolysis over Pd(111) accompanied by the formation of adsorbed water; calculations suggest that the latter by-product hinders furfural hydrogenation over Cu(111).[1] Furfural adsorption and decomposition over Pt(111) and Zn modified Pt(111) have been extensively investigated using Temperature Programmed Desorption (TPD) and high-resolution electron energy loss spectroscopy by Shi and Vohs.[7] They report that furfural adsorbs at low temperatures through the aromatic ring on Pt(111) driving unselective decomposition to CO and $H_2$ upon heating. Surface modification with Zn adatoms favors furfural adsorption through the carbonyl carbon, and associated ring tilting away from the Pt(111) surface.[7] This molecular re-orientation suppresses thermal decomposition and ring hydrogenation in favour of hydrodeoxygenation (HDO) of the C=O bond.

Here we utilize Temperature Programmed Reaction Spectrometry (TPRS) and Scanning Tunneling Microscopy (STM) to elucidate salient features of furfural's adsorption and hydrogenation over Pt(111), and correlate coverage dependent orientation and self-assembly with selectivity towards hydrogenation vs. decomposition pathways. Furfural adsorbs in a hydrogen bonded planar network at low coverage, adopting a tilted geometry for a densely packed furfural adlayer. Adsorption geometry and hydrogen co-adsorption influence selectivity towards both evolved products and surface carbon. Pre-adsorbed hydrogen promotes hydrogenation to furfuryl alcohol over decarbonylation to furan, and passivates Pt(111) towards molecular decomposition. These results specifically allow us to discuss the fundamental surface behaviour of furfural that leads to the selectivity of platinum vs. other precious metal catalysts, such as palladium, in this important hydrogenation reaction. They also identify the critical importance of surface hydrogen

concentration in both selectivity and deactivation as a result of surface coking by carbon. In consequence, the present findings help pave the way toward replacement catalysts for the undesirable copper chromite catalyst packages currently employed.

## 3.2 Results and discussion

### 3.2.1 Adsorption and reactivity of furfural on Pt(111)

Figure 1 shows TPRS acquired after clean Pt(111) was exposed to 0.15 L of furfural at 140 K. The evolved products were unreacted furfural (m/z 96) and reactively-formed furan (m/z 68), CO (m/z 28), $H_2$ (m/z 2) and $H_2O$ (m/z 18). 72% of the adsorbed furfural desorbed intact (main peak at 227 K with a smaller more strongly bound feature at 280 K) while ~22% reacted to furan which desorbed at 291 K. Note that furfural multilayer peaks on Pt(111) appear at 190 K (Figure 2). The remainder formed surface carbon (see below), CO and $H_2$. Note that the 227 K peak in the furan desorption corresponds to furfural which shares a m/z 68 fragment with furan. This m/z 68 fragment is sufficiently weak that we can be confident it is not the main contributor to the furan desorption at 291 K, and indeed the 280 K furfural peak is clearly offset in temperature from the former confirming their different chemical origins. Use of the parent ion and ionization fragments in this study enables molecular identification, whereas previous work[7] only followed the low molecular mass m/z 39 fragment in common between furfural and furan leading to the attribution of both these desorption features to furfural. Carbon monoxide desorption due to furfural decarbonylation occurred at 384 K, coincident with the temperature for chemisorbed CO desorption over Pt(111), indicating the former's appearance was desorption-rate limited and hence decarbonylation occurs below 384 K. $H_2$ desorption from furfural decomposition occurred at 415 K, 488 K and 604 K: all three $H_2$ desorption peak temperatures are higher than that of chemisorbed $H_2$ over clean Pt(111), and hence their appearance was reaction-rate limited (see Figures 1, 9 and 17).

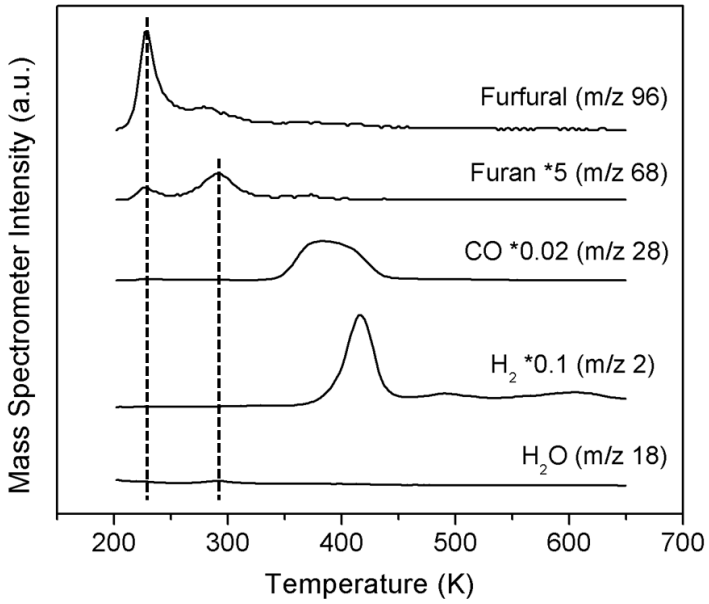


Figure 1 - Raw data showing the desorption products of furfural (0.15 L) on clean Pt(111).

Liberation of surface atomic hydrogen from furfural decomposition (Figure 1) does not lead to any self-hydrogenation products, presumably since the temperature for surface hydrogen formation is higher than the desorption temperature of furfuryl alcohol (Figure 13a). The hydrogen desorption peak area can be used to estimate the amount of residual carbon on Pt(111) following the temperature ramp as described below. We estimate ~6% of the total adsorbed furfural adlayer remains as carbonaceous deposits.

Surface carbon was calculated as follows:

$$C = \frac{\left(\frac{H_2 des}{H_2 correction}\right)}{H{:}C\ ratio}$$

Where:
$H_2$des – Area of hydrogen desorption peaks (3 components)
$H_2$correction – Correction for QMS sensitivity and $H_2$ ionization cross-section
H:C ratio – The ratio of hydrogen to carbon QMS sensitivity

Figure 2 presents the total furfural conversion and product selectivity as a function of exposure, revealing lower reactivity over crowded surfaces (conversion decreasing from 28% to 9%), while furan selectivity (and the amount of residual carbon) were coverage independent. This fall in furfural conversion and subsequent plateau occurs around 0.45 L,

coinciding with saturation of the furfural monolayer (Figure 3). This saturation exposure is similar to that of 0.6 L reported by Shi and Vohs,[7] with higher exposure rapidly populating multilayers.

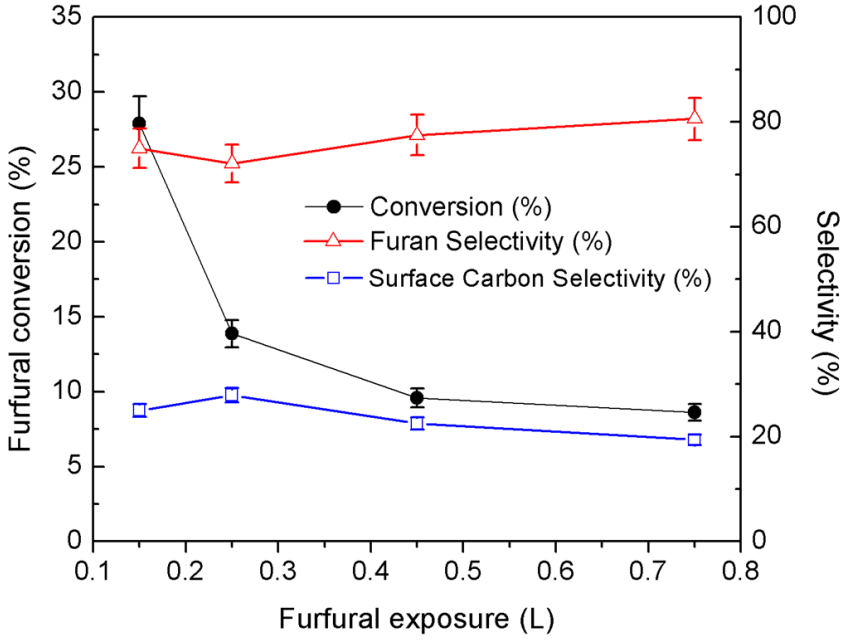


Figure 2 - The reactivity of the Pt(111) at varying furfural exposure.

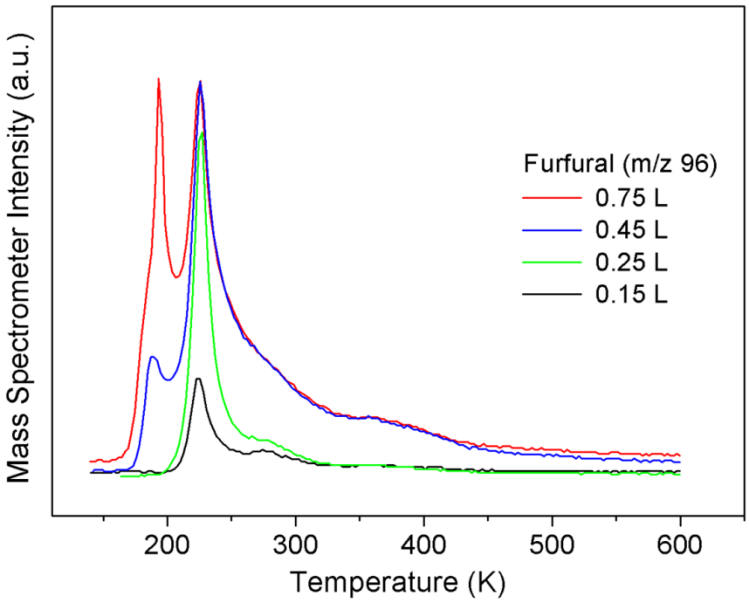


Figure 3 - The desorption of furfural at varying exposures off clean Pt(111).

A microscopic view of furfural on Pt(111) at two different coverages was obtained by STM (Figures 4 and 5). Figure 4 shows a representative image for ~0.5 ML furfural, whereas Figure 5 shows a saturated furfural adlayer and may also feature some multilayer patches. Individual furfural molecules (outlined in blue) are observed to self-assemble in Figure 4, presumably due to attractive adsorbate-adsorbate interactions. Considering the optimal furfural adsorption geometry calculated by DFT[5] and the assignment of the bright, protrusions in Figure 4 to individual furfural molecules, we propose that this self-assembly is driven by weak hydrogen bonding between aromatic and the carbonyl oxygen: aromatic-C-H···O=C-.[16] At high coverage (Figure 5) these bright features change appearance, forming narrow, anisotropic protrusions (example outlined in purple) ~0.3 nm apart, much closer than the molecular footprint of a planar furfural molecule. The packing density of furfural here is ~3 molecules per $nm^2$ vs. a maximum density of ~2 molecule per $nm^2$ observed in the submonolayer surface (Figure 4). We can attribute this to a change in the adsorption geometry towards a strongly tilted molecule driven by the maximization of the number of molecules in contact with the metal surface.

The preceding STM data aid interpretation of the TPRS results. Furfural within the monolayer exhibits two distinct molecular desorption states (Figure 1), a dominant one at 227 K, and a minor, more strongly bound state around 280 K. This desorption spectrum was obtained for a furfural exposure of 0.15 L, and hence at a similar density of furfural molecules as imaged in Figure 4 (corresponding to an exposure of ~0.1 L). We suggest that the lower temperature furfural desorption is associated with isolated adsorbates, while the minority higher temperature furfural desorption is associated with molecules present within hydrogen bonded networks. This hypothesis is supported by the increase in high temperature furfural desorption with increasing exposure, consistent with a greater population of hydrogen-bonded furfural (whether flat-lying or tilted).

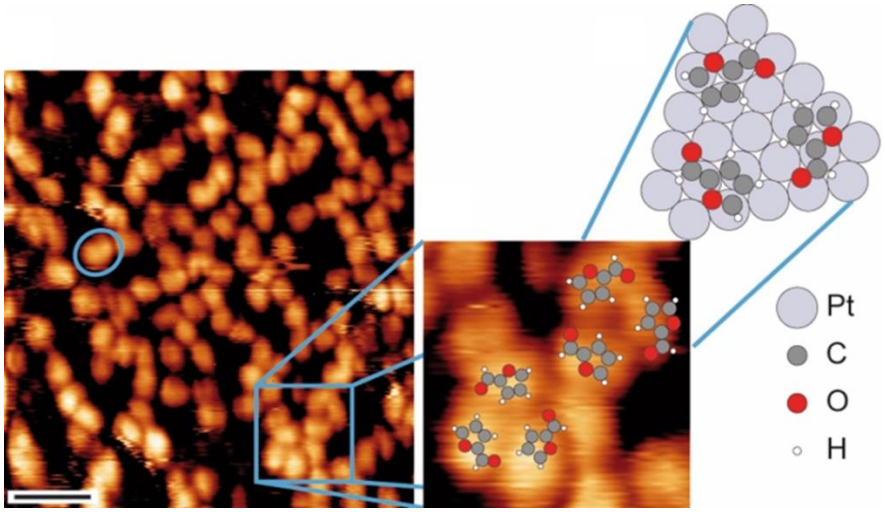


Figure 4 - STM images of different furfural coverages on Pt(111). Furfural molecules were dosed to a Pt(111) surface kept at 95 K - At submonolayer coverage furfural adopts a planar geometry as indicated in the magnified image. A single furfural molecule is indicated by the blue circle on the STM image. (T = 145 K, $V_t$ = 1.28 V, $I_t$ = 0.12 nA). A plausible atomistic scale model is displayed for two selected circular hydrogen bonded supramolecules in the magnified image.

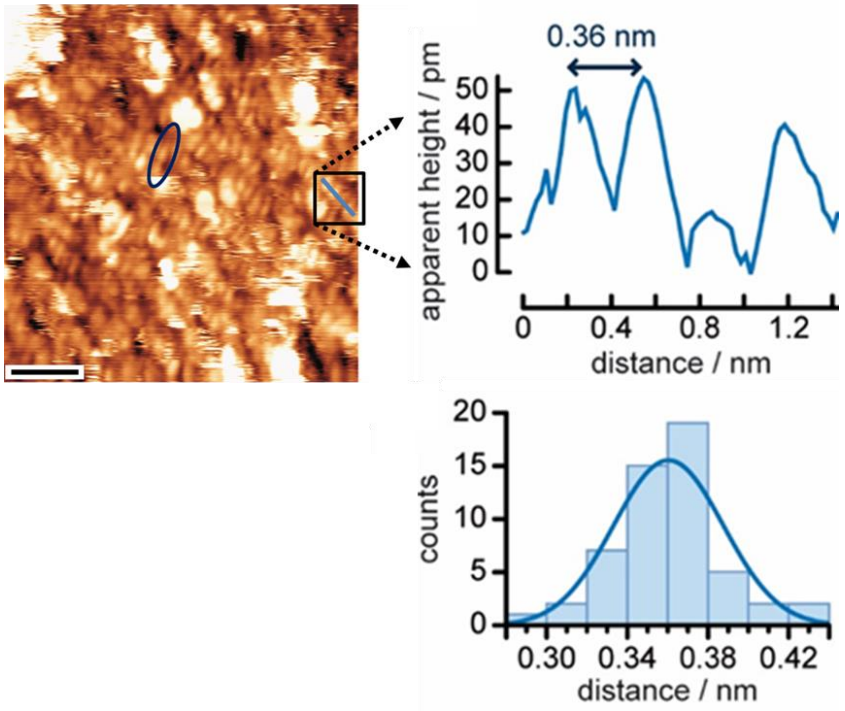


Figure 5 - At coverages without any bare Pt the line profile (right) across the line (highlighted by a square) indicated on the STM image (T = 125 K, $V_t$ = -1.58 V, $I_t$ = 0.16 nA) in the same colour shows that the molecular features (example outlined in purple) are separated by ~ 0.36 nm. The scale bar (black line) in both images is 2 nm.

At 244 K (above the main desorption peak of unreactive furfural), the STM reveals that at submonolayer coverages, some of the structures identified as single furfural molecules packing in the hydrogen-bonded networks are less discernible (Figure 6). Flat-lying furfural is indicated within a solid blue circle, accompanied by additional, smaller rounded protrusions enclosed within dotted blue circles whose dimensions are consistent with furan. At 263 K, above the temperature for furfural desorption and coincident with that for reactively-formed furan desorption, Figure 7 shows a decrease in the surface coverage of adsorbates and disruption of the hydrogen-bonded structures. We attribute this to decarbonylation and decomposition of the initial furfural adlayer.

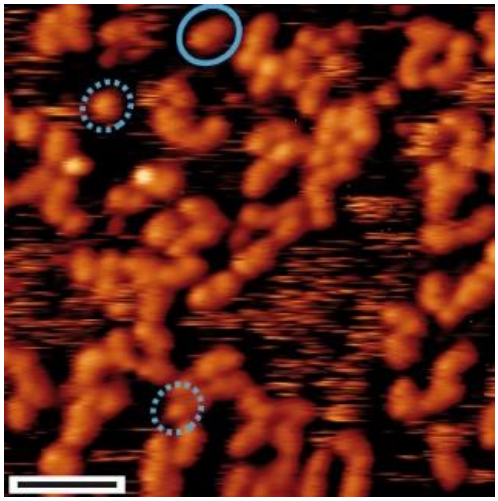

Figure 6 - Temperature dependent STM images of the molecular layer on Pt(111) after dosing ~0.1 L furfural at 157 K. At 244 K, molecular species consistent with both furan, such as the ones in dotted circles and furfural (example outlined with a blue solid line) can be found ($V_t$ = 1.06 V, $I_t$ = 0.10 nA).

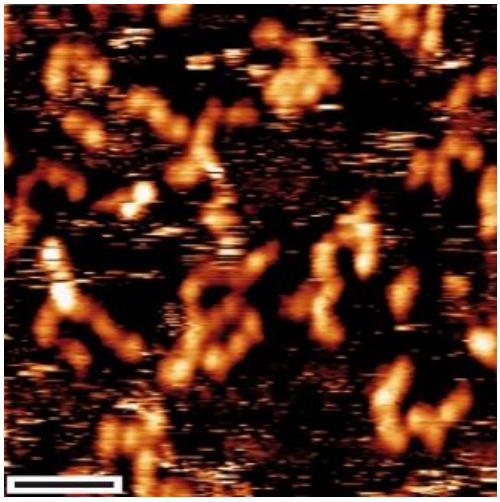

Figure 7 - Temperature dependent STM images of the molecular layer on Pt(111) after dosing ~0.1 L furfural at 157 K. At 263 K furfural molecules desorb and the self-assembly is no longer mediated by –C=O···H–C– ($V_t$ = -0.45 V, $I_t$ = 0.07 nA) The scale bar is 2 nm.

### 3.2.2 Investigation of furan reaction product on Pt(111)

Figure 8 shows TPR spectra of furan from a clean Pt(111) surface as a function of exposure (0.2, 0.3, and 0.9 L). Two very distinct peaks are seen (labelled α –299 K and β – 249 K), which based on the literature are available on other substrates such as Cu(111) and Cu(100) or Si(111)-7x7, can likely be ascribed to the desorption of molecules in different adsorption geometries.[17,18] The small shoulder at ~350 K is suggested, on the basis of similar features on copper substrates, to be ascribed to defects on the crystal surface.[17] At higher exposures a new peak develops at 194 K which corresponds to multilayer formation. Similar desorption trends of furan have been previously observed by Mulligan and Sexton when utilizing Cu(111) and Cu(100) surfaces under UHV.[17,18] They found, by TPR and Electron Energy Loss Spectroscopy, that furan desorbs in two main desorption states at 140 K and 156 K resulting from two different modes of adsorption of furan on the surface. The lower temperature desorption peak (β) they assigned to furan molecules adsorbed with the ring in an upright or perpendicular geometry, leading to a weaker interaction with the surface, while the higher temperature desorption peak (α) corresponds to an adsorption geometry with the ring lying flat or parallel to the surface. The first is through a surface π–interaction which is comparable with the α-state seen for Cu single crystals and the second via a σ–interaction, where there is bonding through the oxygen to the metal surface (like the β-

state).[17,19] In the present case the reactively-formed furan due to the decarbonylation of furfural shown in Figure 1 appears at 291 K, that is similar to the temperature of the α-state desorption of furan, which as explained above is ascribed to the flat lying conformation of the molecule on the surface.[15,17] The coincidence in temperature of reactively-formed furan with this α-state desorption that is seen if the furan molecules are adsorbed independently, strongly suggests that the furan formed by decarbonylation of furfural has formed below this temperature and so desorbs in the same way as the low coverage furan species.

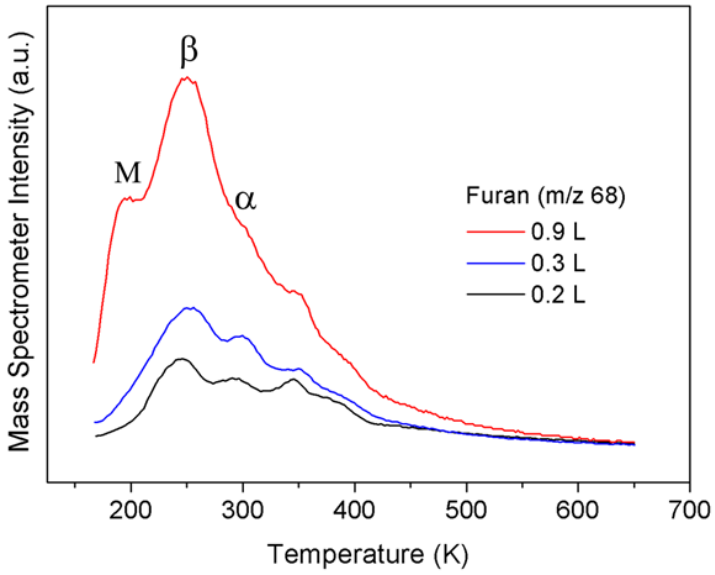


Figure 8 - The desorption of furan on a Pt(111) surface as a function of temperature at exposures of 0.2, 0.3 and 0.9 L.
M – Multilayer, β – σ-interaction and α – π-interaction.

### 3.2.3 Desorption enthalpies for furfural and furan on Pt(111)

Enthalpies of furfural and furan desorption from Pt(111) were determined from a Redhead analysis,[20] assuming a common pre-exponential factor of $10^{13}$ $s^{-1}$ as widely adopted for organic adsorbates including phenol,[21] benzene[22] and naphthalene.[23] The desorption enthalpy of chemisorbed furfural in the main desorption peak at 227 K was ~56 kJ $mol^{-1}$. This value appears to be close to the value calculated for the desorption of phenol (57 kJ $mol^{-1}$) and cyclopentane (58 kJ $mol^{-1}$) on similar Pt(111) surfaces.[22,24] Furfural desorption from Pd(111) occurs at a far higher temperature, 365 K,[8] and hence must be associated with a far greater activation barrier. DFT calculations for furfural on

precious metals[5,8,25] have produced disparate values for the adsorption strength and are sensitive to the inclusion of dispersive interactions.[5] A comparative study suggested that furfural adopts both C=C ring and C=O bonding motifs over Pd, whereas on Pt adsorption only occurs through the C=C ring. The latter adsorption geometry is consistent with the ability of furfural to form the hydrogen-bonded networks described above. The DFT calculated binding energies (PW91functional) of furfural on Pt(111) and Pd(111) were reported as -1.14 eV and -0.90 eV respectively.[5] Note that the experimental order of desorption energies for Pd(111) > Pt(111) derived from Temperature Programmed Desorption is inconsistent with that from DFT calculations, possibly as a result of the hydrogen-bonding networks proposed above.

The stronger adsorption of furfural over Pd(111) versus Pt(111) undoubtedly underpins their different reactivity: furfural evolves furan (365 K), CO (460 K) and $H_2$ (330 K and 410 K) over Pd(111), but also undergoes extensive ring decomposition leading to propylene (385 K).[6,8] In contrast, propylene was not observed over Pt(111) in this work. Redhead analysis for reactively-formed furan from flat laying furan (Figure 8) reveals a desorption enthalpy of ~73 kJ $mol^{-1}$, close to that of unsubstituted aromatics such as benzene with 68 kJ $mol^{-1}$ over Pt(111).[22]

### 3.2.4 Investigation and quantification of surface carbon product during furfural desorption from Pt(111)

As discussed above, furfural adsorption over Pt results in carbon deposition, presenting a major technological drawback to utilizing Pt for large scale furfural hydrogenation. Figures 9 and 10 show consecutive TPRS profiles following a 0.25 L furfural exposure over Pt(111), without cleaning the surface each cycle. Figure 9 shows a 47% drop in furfural desorption intensity between the first and second cycle, with the amount of reactively-formed hydrogen (Figure 10) reduced by a similar amount (40%). However, between the second and third exposure the furfural and hydrogen desorption intensities only decrease by a further 5% and 3% respectively. These observations demonstrate that the number of available adsorption sites has decreased significantly, indicating the accumulation of significant (carbonaceous) residues. Furthermore, the initial decrease in

furfural desorption of ~47% between cycles one and two is significantly greater than the proportion of adsorbed furfural calculated to decompose to carbon (~20% from Figure 2). This suggests that any carbon deposits are likely uniformly distributed across the Pt(111) surface, and hence block a large number of furfural adsorption sites. The formation of carbonaceous deposits from furfural is reportedly favoured at 377 K - 385 K over Pt catalysts during gas phase hydrogenation,[26,27]comparable to the desorption temperature for reactively-formed hydrogen (indicative of hydrocarbon decomposition) from furfural over Pt(111) shown in Figure 1. High furan yields during liquid phase hydrogenation of furfural over Pt nanoparticles is also reported around 343 K,[28] in good agreement with that for the desorption of reactively-formed furan from Pt(111) in this work of 323 K. CO formed through furfural decarbonylation to furan may also be responsible for site-blocking and poisoning of Pt catalysts at temperatures below that necessary for desorption of the former.[28] Poisoning by carbon laydown typically requires catalyst reactivation (e.g. through calcination) and concomitant loss in metal surface area or changes in particle morphology and hence is often considered irreversible. In contrast, reversible CO poisoning may be mitigated by higher temperature operation.

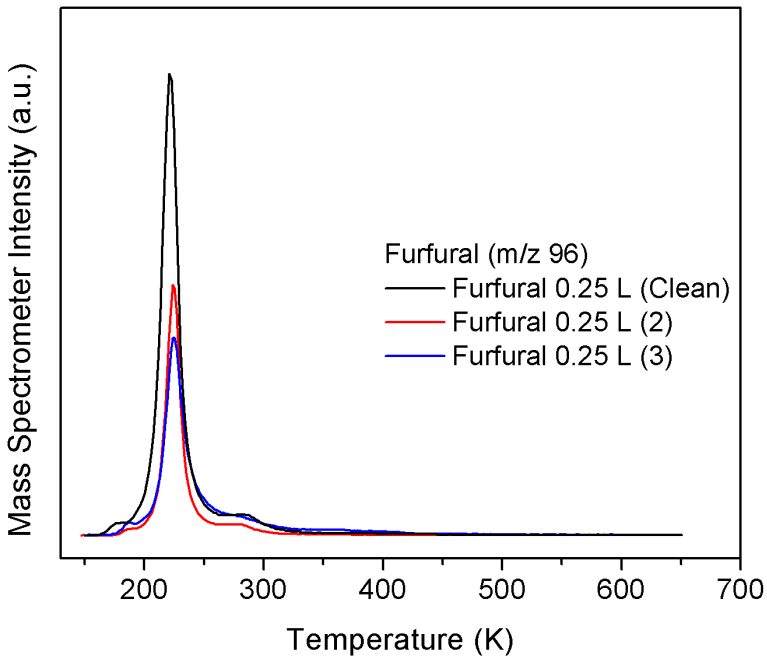


Figure 9 - Repeated exposure of furfural (0.25 L), followed by desorption, without surface cleaning in between cycles, showing diminished overall monolayer adsorption feature intensity at 222 K, indicating site blocking by carbon deposits.

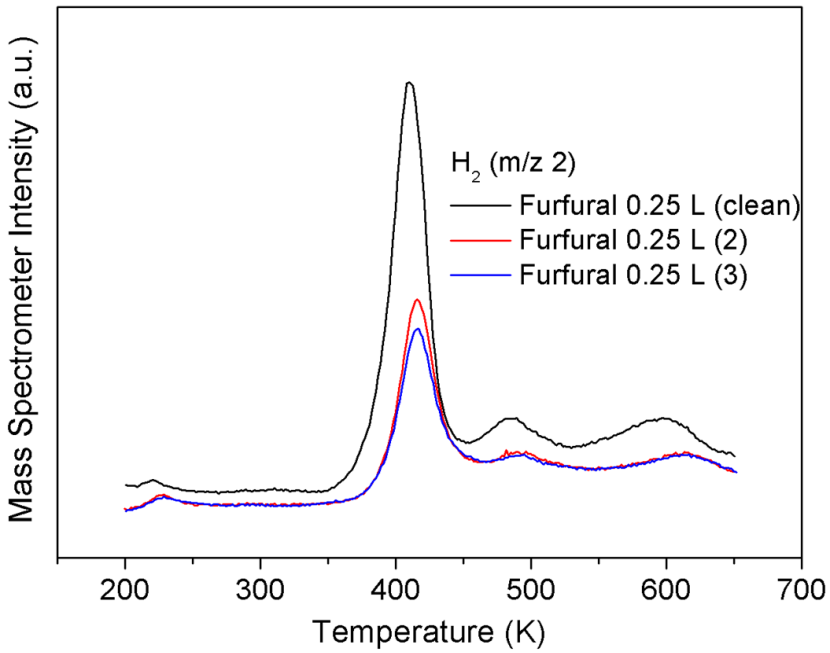


Figure 10 - Corresponding decrease in $H_2$ signal during adsorption/desorption cycles showing a decrease in reactive furfural due to carbonaceous deposits.

### 3.2.5 Furfural hydrogenation on Pt(111)

Hydrogen adsorption over clean Pt(111) was first studied by TPRS (Figure 11) as a function of exposure. The desorption temperature of molecular hydrogen decreased with increasing $H_2$ exposure in accordance with the expected second order kinetics reported by Gebhardt and Koel.[29] Hydrogen coverages were calculated according to the work of Ertl and co-workers wherein $\theta H_{sat}$ was 0.8 ML.[30] Furfural and hydrogen were co-dosed employing a $H_2$ exposure of 100 L (corresponding to ~0.4 ML) to ensure vacant Pt sites were available for furfural adsorption.

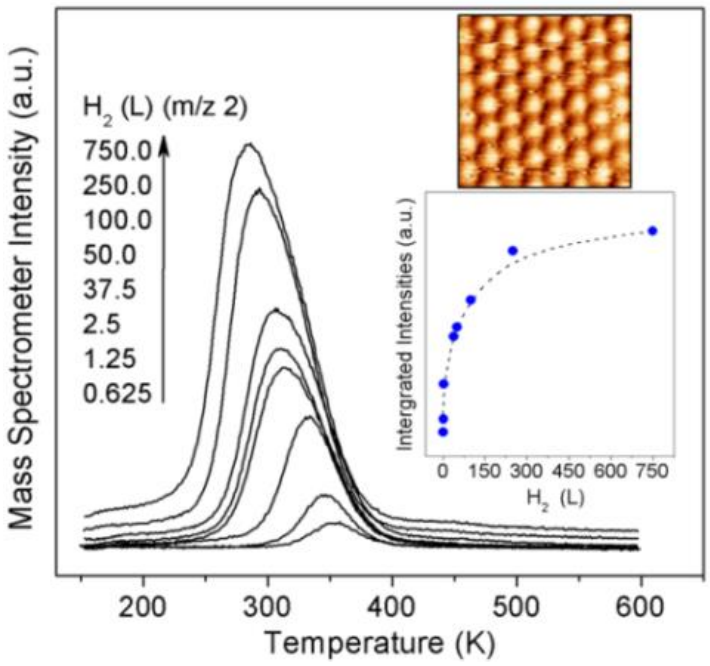


Figure 11 - The uptake of $H_2$ on the Pt (111) at various exposures. Insets: (bottom) the integrated desorption areas to map uptake; (top) STM image (1.8×1.8 $nm^2$, T = 293 K, $V_t$ = 0.42 V, $I_t$ = 16.70 nA) with the atomic resolution on the planar Pt(111) surface.

Figure 12 shows data from TPRS of a 100 L $H_2$ exposure and subsequent 0.35 L furfural exposure at 140 K over Pt(111). Furfural exhibits a multilayer desorption peak ~190 K, and a monolayer desorption at 227 K. Similar total yields of reactively-formed furfuryl alcohol (m/z 98) and methyl furan (m/z 82) were observed at 240 K and 360 K respectively, however, no furan desorption was observed. Note that furan, furfuryl alcohol and methyl furan desorptions contain a contribution from furfural (which also exhibits mass fragments at m/z 68, 82 and 98) however, the desorption temperatures of reactively-formed furfuryl alcohol and methyl furan differ from that of furfural, but are in close agreement to those observed from their respective molecularly adsorbed species (Figure 13) indicating that their appearance is desorption-rate limited. Figure 17 shows the appearance of a low temperature $H_2$ desorption peak around 306 K characteristic of the recombinative desorption of molecularly adsorbed hydrogen (Figure 11). Additional hydrogen desorption must arise from the co-adsorbed furfural and indeed are identical to those observed following furfural adsorption over clean Pt(111) at 415 K, 488 K and 604 K (Figure 1). As noted in an earlier section furfural auto-hydrogenation over Pt(111) does not occur (Figure 1). However, the observation of furfuryl alcohol in the presence of co-adsorbed

hydrogen evidences that furfural hydrogenation is possible over Pt(111) under UHV, providing that a high concentration of hydrogen adatoms is available at a relatively low surface temperature.

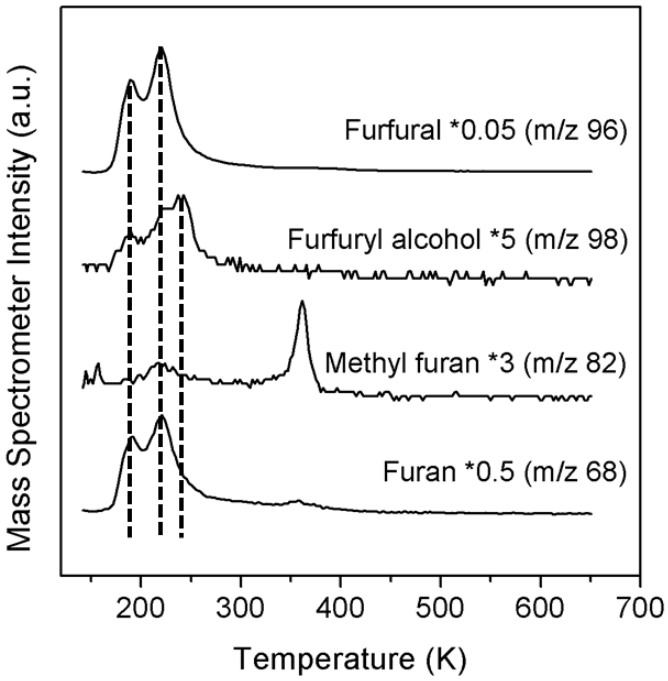


Figure 12 - TPRS for Pt(111) exposed to 100 L $H_2$ followed by 0.35 L furfural.

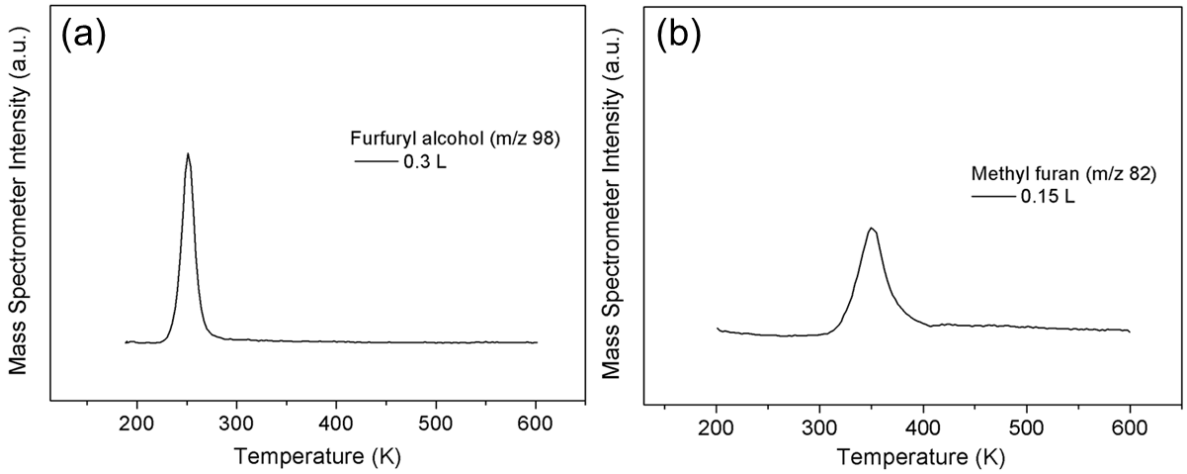


Figure 13 - TPD spectra of (a) furfuryl alcohol and (b) methyl furan at low exposure showing desorption temperatures of 251 K and 350 K respectively.

Pre-adsorbing hydrogen onto the Pt(111) surface will restrict furfural adsorption. This is shown in Figure 14 where multilayer formation is observed much more quickly than when a clean surface is exposed to furfural.

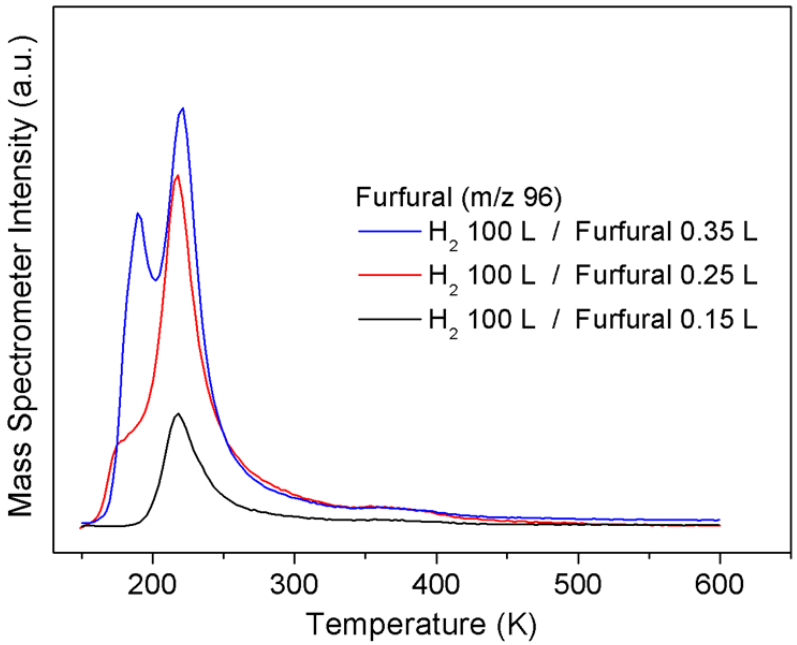


Figure 14 - The desorption of furfural when co-dosed with 100 L $H_2$.

Figure 15 shows furfural conversion and selectivity as a function of furfural exposure over Pt(111) pre-covered with 100 L $H_2$. Reversing the dosing sequence, such that Pt(111) was first exposed to 0.25 L furfural followed by 100 L $H_2$, suppressed hydrogenation pathways to both furfuryl alcohol and methyl furan (Figure 16), affording a similar conversion and selectivity to that seen over clean Pt(111). The results are in excellent agreement with the reaction pathways proposed, both in the literature and the reaction scheme for furfural transformation shown in Chapter 1. At low furfural exposures (corresponding to a high ratio of surface H(a):furfural) the stepwise hydrogenation of furfural to furfuryl alcohol, and its subsequent HDO to methyl furan, is favoured. At high furfural exposures (a low surface H(a):furfural ratio), insufficient surface hydrogen is available to further hydrogenate reactively-formed furfuryl alcohol, which hence becomes the dominant product, albeit in the latter scenario more furfural desorbs molecularly. As a result of

hydrogenation instead of decarbonylation when hydrogen is pre-adsorbed to the surface, Figure 18 shows the instances where furan is observed; these are on the clean Pt(111) and when hydrogen is dosed second.

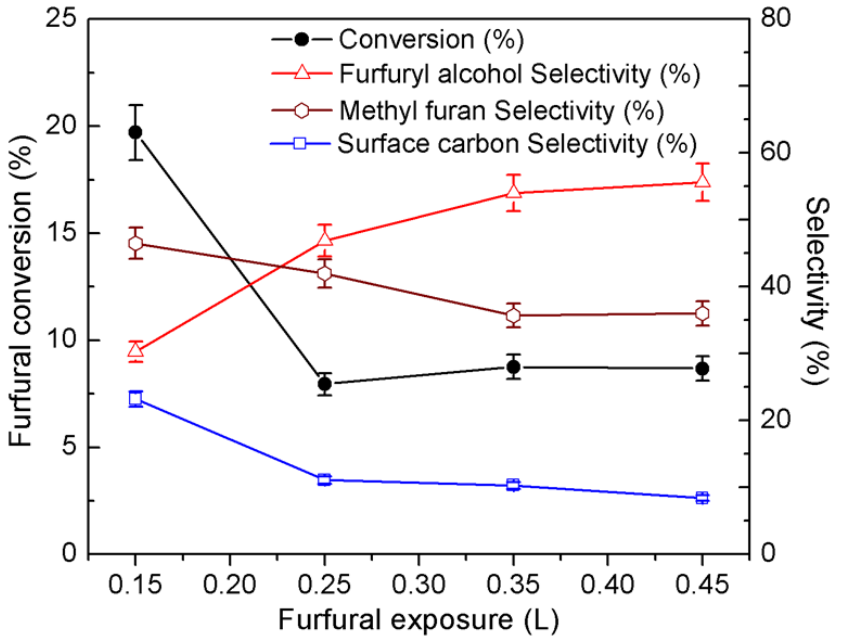


Figure 15 - Furfural reactivity over Pt(111) pre-exposed to 100 L $H_2$ as a function of furfural exposure. Molecular adsorption was performed at 140 K in all cases.

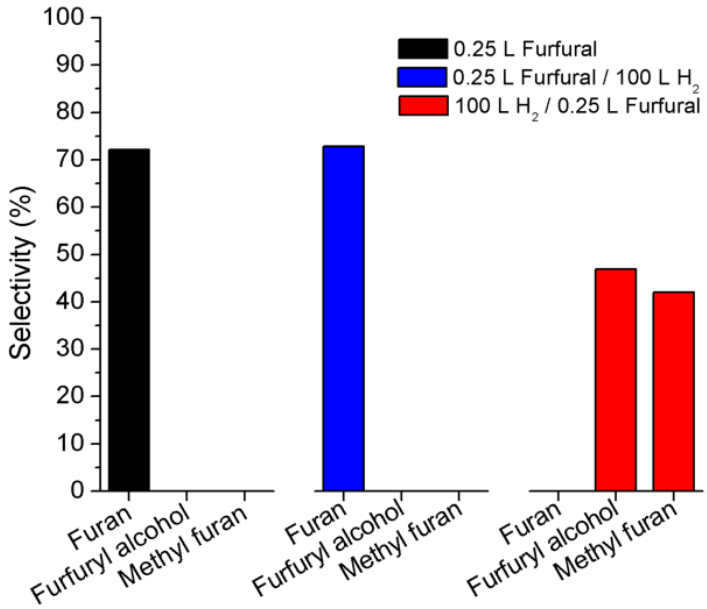


Figure 16 - Gas phase selectivities to molecular products for furfural with and without $H_2$ and for different orders of exposure to the two reactants.

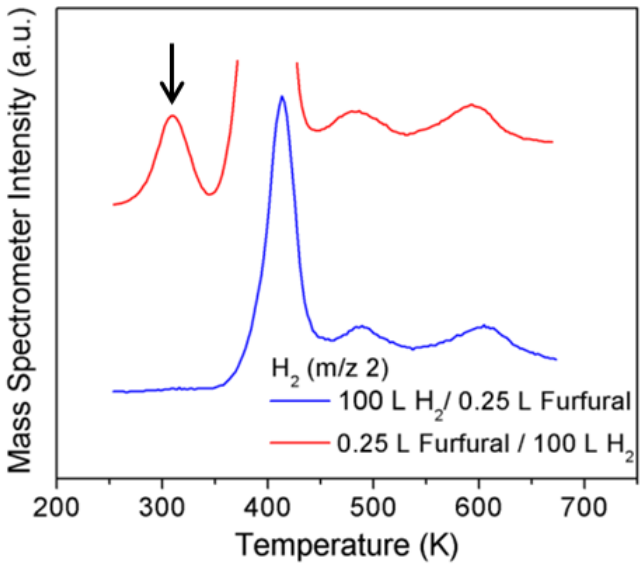


Figure 17 - Comparative hydrogen desorptions from furfural over Pt(111) surfaces, an arrow is used to indicate molecular hydrogen desorption.

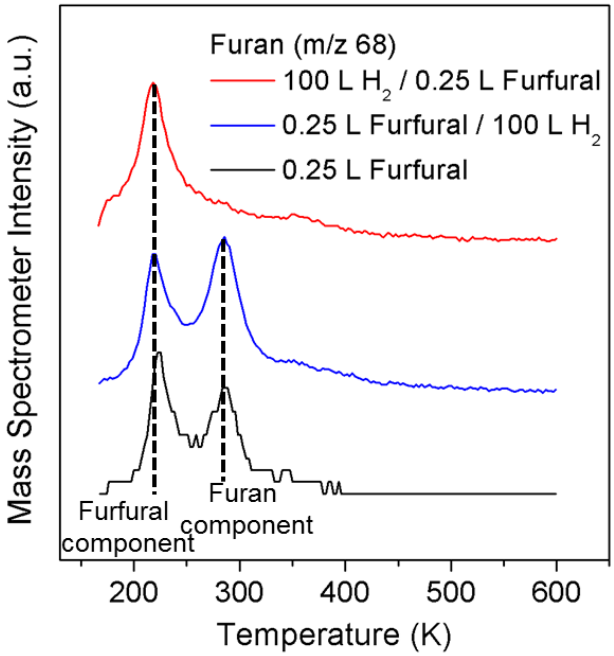


Figure 18 - Reactively-formed furan production from furfural over Pt(111) surfaces.

The preceding insight enables us to predict the selectivity to furfuryl alcohol during furfural hydrogenation; higher surface hydrogen concentrations encountered in gas phase furfural hydrogenation are expected to favour methyl furan relative to furfuryl alcohol,

whereas the latter should be favoured in the liquid phase. This is precisely as reported in the literature.[26,28,31,32]

## 3.3 Conclusions

The hydrogenation of furfural on Pt(111) was found to be highly sensitive to the conditions used to carry out the catalytic reaction, in particular surface crowding and associated changes in the adsorption geometry. On clean Pt(111), furfural adopts a planar motif at low coverages and a more tilted geometry as the coverage is increased. The extent of decarbonylation to furan was found to depend strongly on the coverage (and therefore adsorption geometry): at low coverage the planar motif results in a much greater conversion to furan than occurs in the higher coverage tilted molecules. The formation of surface carbon and possible consequences for practical catalyst deactivation processes have also been investigated and discussed.

Control of the reactant adsorption geometry on the surface is critical to the reaction selectivity, with hydrogenation and hydrogenolysis being possible in either motif. A strong correlation between the reactivity of the Pt(111) surface with that of Pt dispersed systems was observed, which enables the prediction of the activity and selectivity of Pt based catalysts under practical conditions in the liquid and the gas phase. The order in which the surface encounters hydrogen and furfural is critically important. When furfural encounters a bare surface, it hinders the subsequent dissociative chemisorption of hydrogen and resulting hydrogenation activity. In contrast, when furfural encounters pre-adsorbed atomic hydrogen, furfuryl alcohol and methyl furan are produced; the former a product of direct furfural hydrogenation, and the latter a secondary product arising from the HDO of furfuryl alcohol (requiring a high ratio of surface H(a):furfural). At a low surface H(a):furfural ratio, insufficient surface hydrogen is available to further hydrogenate reactively-formed furfuryl alcohol, which hence becomes the dominant product. Our results indicate that control over the furfural adsorption geometry, and surface hydrogen concentration, are key considerations for the design and operation of practical Pt catalysts for this important bio-economy transformation.

## 3.4 References


1 Y. Shi, Y. Zhu, Y. Yang, Y. W. Li and H. Jiao, *ACS Catal.*, 2015, **5**, 4020–4032.

2 V. Vorotnikov, G. Mpourmpakis and D. G. Vlachos, *ACS Catal.*, 2012, **2**, 2496–2504.

3 S. Wang, V. Vorotnikov, J. E. Sutton and D. G. Vlachos, *ACS Catal.*, 2014, **4**, 604–612.

4 S. Wang, V. Vorotnikov and D. G. Vlachos, *ACS Catal.*, 2015, **5**, 104–112.

5 B. Liu, L. Cheng, L. Curtiss and J. Greeley, *Surf. Sci.*, 2014, **622**, 51–59.

6 R. Williams and J. Medlin, *J. Phys. Chem. C*, 2014, **118**, 27933–27943.

7 D. Shi and J. M. Vohs, *ACS Catal.*, 2015, **5**, 2177–2183.

8 S. H. Pang and J. W. Medlin, *ACS Catal.*, 2011, **1**, 1272–1283.

9 K. E. Wilson and C. J. Baddeley, *J. Phys. Chem. C*, 2009, **113**, 10706–10711.

10 Y. Yao and F. Zaera, *Surf. Sci.*, 2016, **646**, 37–44.

11 G. Goubert, M. N. Groves, Y. Dong, J.-C. Lemay, P. H. McBreen and B. Hammer, *J. Phys. Chem. C*, 2015, **119**, 7319–7326.

12 T. J. Lawton, V. Pushkarev, D. Wei, F. R. Lucci, D. S. Sholl, A. J. Gellman and E. C. H. Sykes, *J. Phys. Chem. C*, 2013, **117**, 22290–22297.

13 M. D. Marcinkowski, J. Liu, C. J. Murphy, M. L. Liriano, N. A. Wasio, F. R. Lucci, M. Flytzani-Stephanopoulos and E. C. H. Sykes, *ACS Catal.*, 2017, **7**, 413–420.

14 M. J. Taylor, L. Jiang, J. Reichert, A. C. Papageorgiou, S. K. Beaumont, K. Wilson, A. F. Lee, J. V Barth and G. Kyriakou, *J. Phys. Chem. C*, 2017, **121**, 8490–8497.

15 R. M. Ormerod, C. J. Baddeley, C. Hardacre and R. M. Lambert, *Surf. Sci.*, 1996, **360**, 1–9.

16 S. Lavoie and P. H. McBreen, *J. Phys. Chem. B*, 2005, **109**, 11986–11990.

17 A. Mulligan, S. M. Johnston, G. Miller, V. Dhanak and M. Kadodwala, *Surf. Sci.*, 2003, **541**, 3–13.

18 B. A. Sexton, *Surf. Sci.*, 1985, **163**, 99–113.

19 S. Letarte, A. Adnot and D. Roy, *Surf. Sci.*, 2000, **448**, 212–218.

20 P. A. Redhead, *Vacuum*, 1962, **12**, 203–211.

21 H. Ihm and J. M. White, *J. Phys. Chem. B*, 2000, **104**, 6202–6211.

22 H. Ihm, H. M. Ajo, J. M. Gottfried, P. Bera and C. T. Campbell, *J. Phys. Chem. B*,

2004, **108**, 14627–14633.

23 J. M. Gottfried, E. K. Vestergaard, P. Bera and C. T. Campbell, *J. Phys. Chem. B*, 2006, **110**, 17539–17545.

24 N. R. Avery, *Surf. Sci.*, 1985, **163**, 357–368.

25 S. M. Rogers, C. R. A. Catlow, C. E. Chan-Thaw, A. Chutia, N. Jian, R. E. Palmer, M. Perdjon, A. Thetford, N. Dimitratos, A. Villa and P. P. Wells, *ACS Catal.*, 2017, **7**, 2266–2274.

26 V. V Pushkarev, N. Musselwhite, K. An, S. Alayoglu and G. A. Somorjai, *Nano Lett.*, 2012, **12**, 5196–201.

27 L. R. Baker, G. Kennedy, M. Van Spronsen, A. Hervier, X. Cai, S. Chen, L.-W. Wang and G. A. Somorjai, *J. Am. Chem. Soc.*, 2012, **134**, 14208–16.

28 M. J. Taylor, L. J. Durndell, M. A. Isaacs, C. M. A. Parlett, K. Wilson, A. F. Lee and G. Kyriakou, *Appl. Catal. B Environ.*, 2016, **180**, 580–585.

29 S. C. Gebhardt and B. E. Koel, *J. Phys. Chem.*, 1992, **95**, 7056–7063.

30 K. Christmann, G. Ertl and T. Pignet, *Surf. Sci.*, 1976, **54**, 365–392.

31 X. Chen, L. Zhang, B. Zhang, X. Guo and X. Mu, *Sci. Rep.*, 2016, **6**, 28558.

32 K. An, N. Musselwhite, G. Kennedy, V. V Pushkarev, L. R. Baker and G. A. Somorjai, *J. Colloid Interface Sci.*, 2013, **392**, 122–8.

# Chapter 4 – The highly selective hydrogenation of furfural over supported Pt nanoparticles under mild conditions

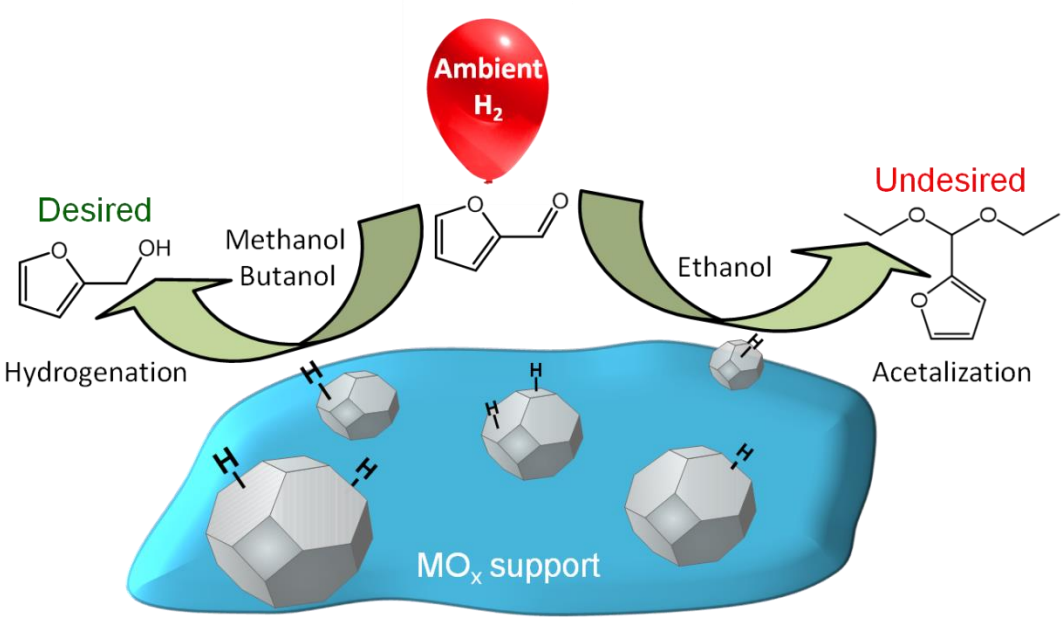

## 4.1 Introduction

With the growing environmental concerns arising from the use of copper chromite and the imminent energy crisis, cleaner and more energy efficient systems must be established. Dispersed platinum nanoparticles have been shown in the past to be effective for the hydrogenation of furfural, both in the liquid and gas phase.[1–7] The adsorption of furfural has also been previously studied on Pt(111) single crystal surfaces and Zn adatom modified Pt(111) under UHV conditions. As shown in Chapter 3, furfural can be hydrogenated and reacted further by hydrogendeoxygenation reaction pathways (Figure 1).[8,9]

A variety of precious metal catalysts have been investigated for the gas phase and liquid phase hydrogenation of furfural, including Ni, Ru, Re, Pd, Ir, Mo, Co, Cu and Pt.[10–21] Platinum in particular has drawn recent attention for the vapour phase hydrogenation of furfural by Somorjai and co-workers over $SiO_2$, $Al_2O_3$, $TiO_2$, $Nb_2O_5$ and $Ta_2O_5$ mesoporous oxide supports, [5,22,23] highlighting the importance of particle size effects. Pt nanoparticles <3 nm favoured furfural decarbonylation to furan, whereas those between 3-7 nm promoted hydrogenation to furfuryl alcohol.[1,5,13,14,24,25] Sum frequency spectroscopy studies also indicate that metal-support interactions are important for Pt nanoparticles on $TiO_2$, facilitating hydrogen spillover and the concomitant formation of a furfuryl-oxy intermediate over titania.[5,22] The influence of surface polarity upon the Pt catalyzed selective hydrogenation of allylic aldehydes was also recently reported over silica supports.[26]

This chapter probes the selective hydrogenation of furfural to furfuryl alcohol under extremely mild reaction conditions over Pt nanoparticles immobilized on $SiO_2$, ZnO, γ-$Al_2O_3$, $CeO_2$ and MgO. Strong support and solvent dependencies were observed, with methanol and n-butanol proving excellent solvents for promoting high furfuryl alcohol yields over uniformly dispersed Pt nanoparticles when using MgO, $CeO_2$ and γ-$Al_2O_3$ at 50 °C and atmospheric hydrogen pressure. In contrast, non-polar solvents conferred poor furfural conversion, while ethanol favoured acetal by-product formation, as commonly reported in the literature (Figure 1).[3,12,27–31]

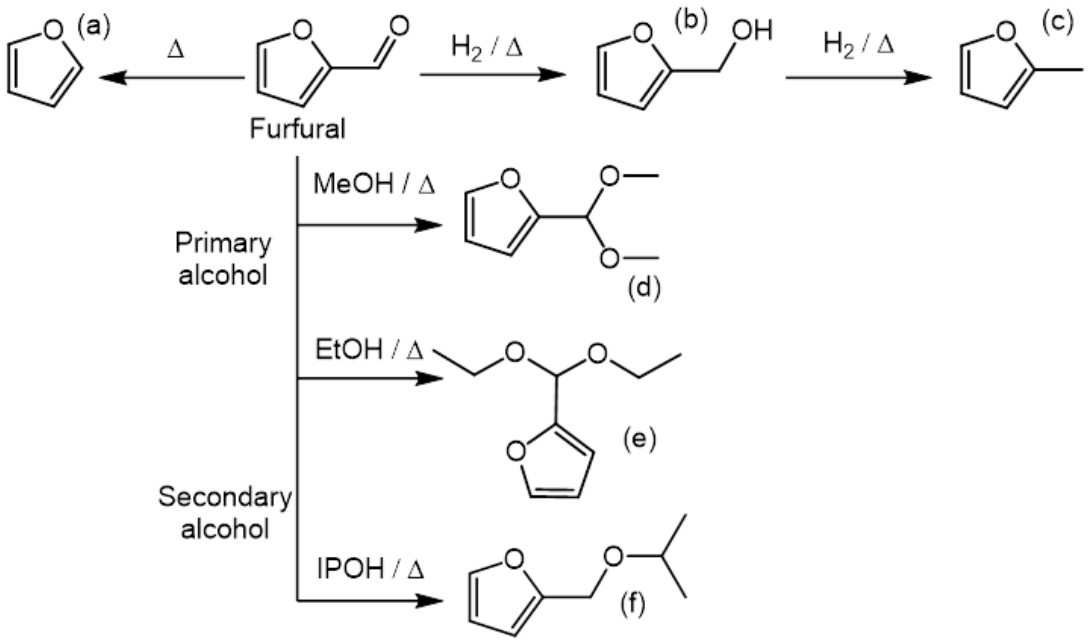


Figure 1 - Furfural reaction scheme containing both hydrogenation and coupling reactions occurring with alcohol based solvents, both primary and secondary. (a) furan, (b) furfuryl alcohol, (c) methyl furan, (d) 2-furaldehyde dimethyl acetal, (e) 2-furaldehyde diethyl acetal and (f) 2-(isopropoxymethyl)furan.

Furfural coupling with the liquid phase medium is a serious concern throughout the literature.[1,29,32,33] There are numerous methods established to overcome this reaction, ranging from the addition of base,[34] water to force the back reaction[29] or simply, as found, lower the reaction temperature as this coupling reaction is thermally driven.[1] It was also shown that short chain alcohols promote the hydrogenation pathway and passivate acetal side reactions as they are thermodynamically unfavourable. Acetal selectivities were found to be substantially lower when using methanol over solvents such as ethanol or isopropanol, often used in the literature.[1,4,32] The reaction mechanism for acetal formation is shown in Figure 2, where R is substitutable for the carbon chain length of a primary alcohol.

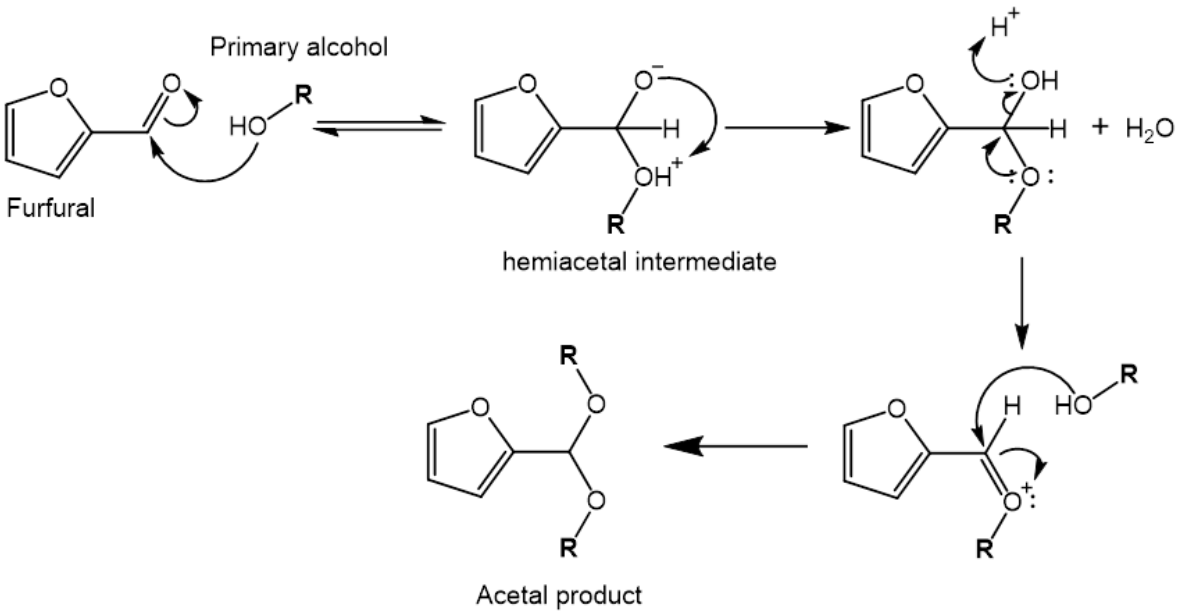


Figure 2 - Reaction mechanism for acetal formation with furfural and a primary alcohol.

## 4.2 Catalyst Characterization

### 4.2.1 ICP and Surface Area Analysis

Table 1 shows elemental analysis and surface area measurements for the five supported Pt catalysts after calcination and reduction, from which it is apparent that the Pt content was close to the nominal 2 wt% over $SiO_2$, $\gamma$-$Al_2O_3$ and ZnO supports, and only deviated slightly from this for the $CeO_2$ and MgO supports. Although the surface areas of the parent supports spanned a wide range, there was minimal change for any of the five catalysts following particle deposition, calcination and reduction treatments relative to the parent value.

Table 1 - Bulk elemental analysis and surface area measurements of Pt catalysts.

| Catalyst | Pt loading[a] / wt % | Surface area[b] / $m^2.g^{-1}$ |
|---|---|---|
| $Pt/CeO_2$ | 1.4 | 5 |
| Pt/ZnO | 1.9 | 7 |
| Pt/MgO | 2.3 | 12 |
| $Pt/SiO_2$ | 2.0 | 181 |
| $Pt/\gamma$-$Al_2O_3$ | 1.9 | 34 |

[a]Determined by ICP-OES; [b]BET surface area from $N_2$ porosimetry.

### 4.2.2 Powder X-ray Diffraction

Powder X-ray Diffraction was also performed on all Pt catalysts (Figure 3). The samples show no evidence of Pt particles due to both the low metal loading and small particle size, with the exception of $Pt/SiO_2$ which shows the Pt(200) reflection. Due to the low signal to noise ratio and peak broadness the FWHM (full width half maximum) obtained through integration and subsequent analysis by the Scherrer equation estimates a slightly larger average crystallite size than that measured by TEM (shown later) at 8.1 nm. However, this does show that on the whole the catalyst thermal processing in both air and dilute hydrogen has no effect on the morphology of the oxide supports, which present the expected diffraction pattern. The diffractogram of $\gamma$-$Al_2O_3$ shows trace amounts of $\delta$-$Al_2O_3$ impurities (34.5° and 36.5°) and the $SiO_2$ support appears to be amorphous in nature.

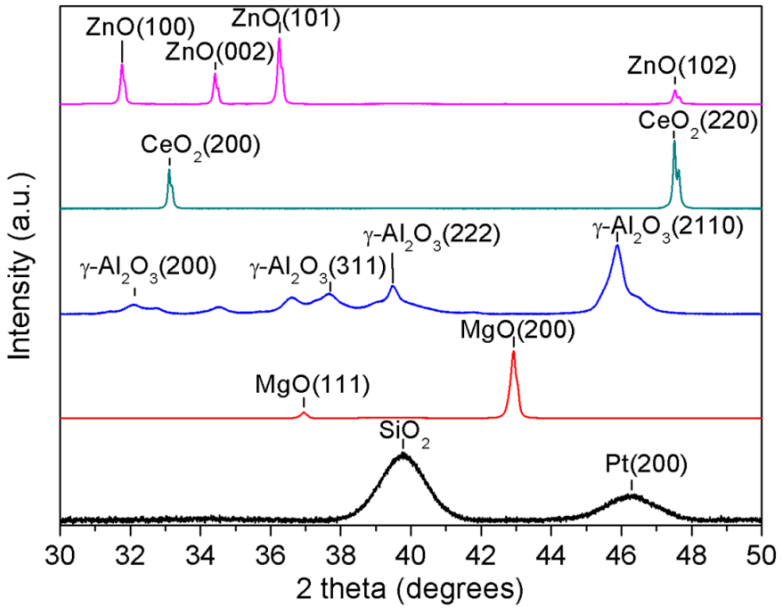


Figure 3 - Powder X-ray Diffractograms of 2 wt% Pt containing catalysts. Reflections are assigned based on the ICDD's PDF-2 2012 database.

### 4.2.3 X-ray Photoelectron Spectroscopy

Table 2 shows the XPS derived Pt surface loading and metal content. The Pt 4f spectra are shown in Figure 4. The observed surface Pt loading (calculated by equation 1) was inversely proportional to the support surface area, reflecting a greater proportion of nanoparticles dispersed over the external surface of (largely non-porous) MgO, $CeO_2$ and

ZnO. Figure 10 shows bright field TEM images of $Pt/SiO_2$ highlighting the low density of nanoparticles across the higher area support, in contrast to $Pt/CeO_2$ (Figure 7) wherein the high surface Pt loading (48.7 wt%) from XPS is consistent with a higher surface density of Pt nanoparticles (Table 2). In all cases the as-prepared catalysts contained a high proportion of metallic platinum following reductive pre-treatment as expected.

$$\text{Surface Pt loading} = \frac{\text{Pt 4f doublet peak area}}{\text{MO}_x \text{ peak area}} \times 100 \quad \text{Equation 1 – Surface Pt loading (wt\%)}$$

Where:

$MO_x$ – (Typically) Metal oxide support

Table 2 - Surface Pt metal concentration and Pt loading from XPS.

| Sample | $Pt^0$ / % | Surface Pt loading / wt% |
|---|---|---|
| 1.4% $Pt/CeO_2$ | 85.0 | 48.7 |
| 1.9% Pt/ZnO | 96.2 | 32.1 |
| 2.3% Pt/MgO | 71.7 | 10.3 |
| 2.0% $Pt/SiO_2$ | 61.3 | 0.9 |
| 1.9% $Pt/\gamma\text{-}Al_2O_3$ | 72.6 | 14.3 |

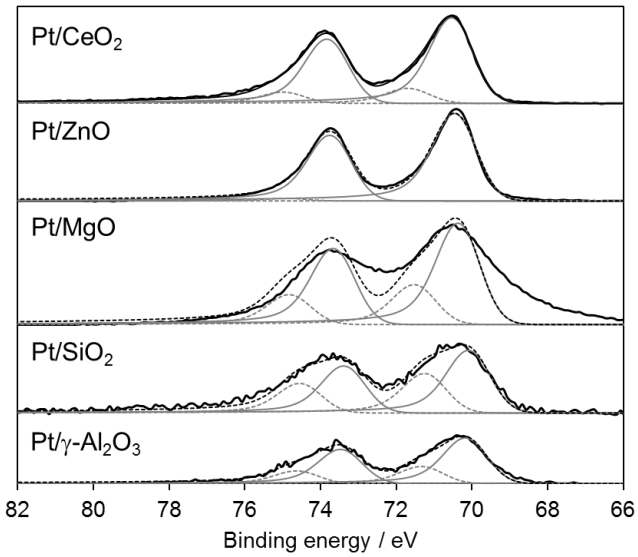


Figure 4 - Pt 4f XP spectra and fits of 2 wt% Pt containing catalysts. Grey dotted lines correspond to $Pt^{4+}$ and grey solid lines to $Pt^0$ chemical states.

### 4.2.4 Transmission Electron Microscopy

Figures 5-10 show TEM images and corresponding particle size distributions for the unsupported, PVP-stabilized Pt nanoparticles, and oxide supported analogues following thermal processing. The unsupported Pt-PVP nanoparticles exhibited mean particle diameters of 3.9 ± 0.8 nm. Similar dimensions were observed for the thermally processed, supported Pt nanoparticles on $\gamma$-$Al_2O_3$ (4.0 ± 0.5 nm), $CeO_2$ (4.2 ± 0.6 nm) and MgO (3.9 ± 0.5 nm).

#### 4.2.4.1 Unsupported Pt-PVP nanoparticles

Figure 5 shows unsupported Pt-PVP nanoparticles over various areas on the TEM grid imaged by regular TEM. A highly focused image of a particle with visible interplanar spacing is present in Figure 5a; these were measured and found to be 0.22 nm, which is characteristic of the Pt(111) facet. Figure 5b shows the particle size histogram for the unsupported nanoparticles.

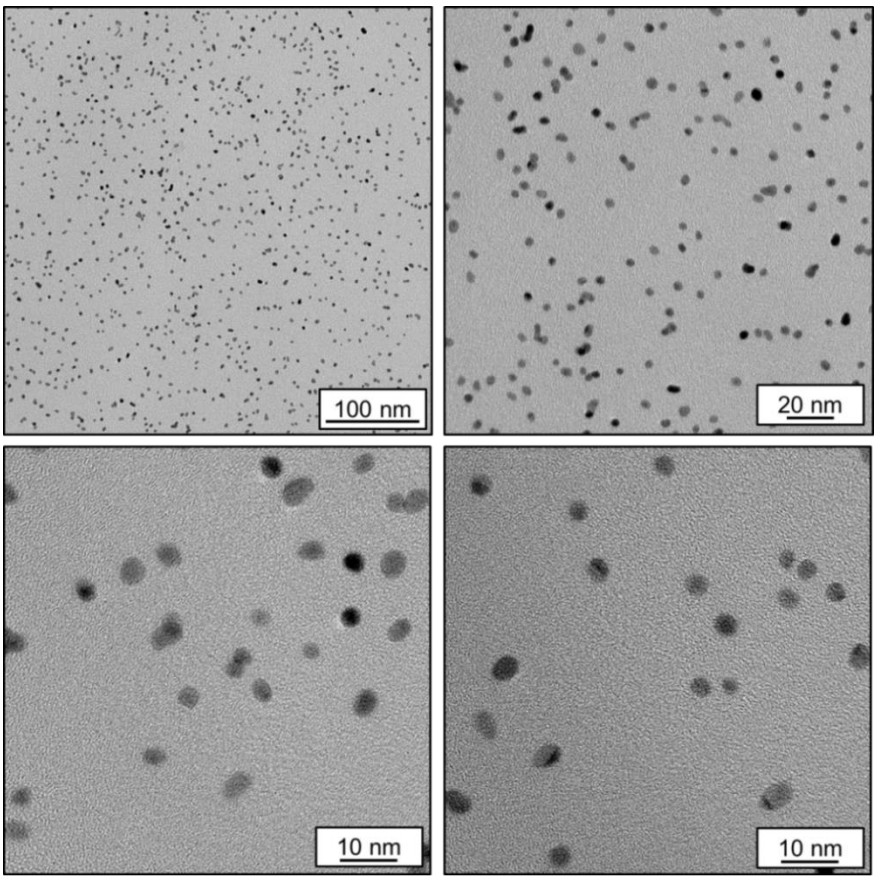


Figure 5 – Unsupported Pt-PVP nanoparticles over various areas on the grid.

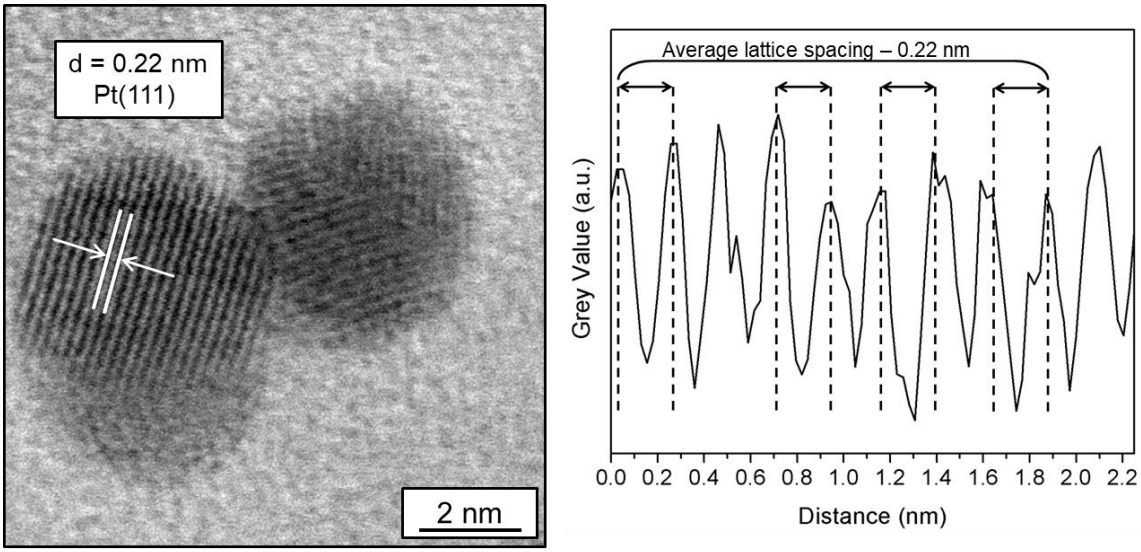


Figure 5 a - Unsupported Pt nanoparticle measured by STEM, showing visible lattice spacings and profile plot.

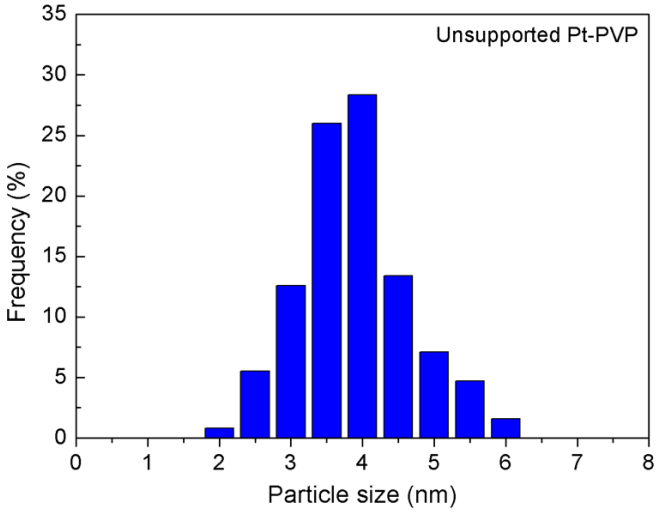


Figure 5 b – Unsupported Pt-PVP particle size histogram.

Figure 6 shows a series of images of Pt nanoparticles supported on $\gamma$-$Al_2O_3$. This support had the second largest surface area of 34 $m^2$ $g^{-1}$. The images highlight a series of positions on the TEM grid and demonstrate that the particles are very much monodisperse in nature and are clearly immobilized on the support. Figure 6a shows the particle size distribution for this catalyst.

#### 4.2.4.2 Supported Pt/γ-$Al_2O_3$

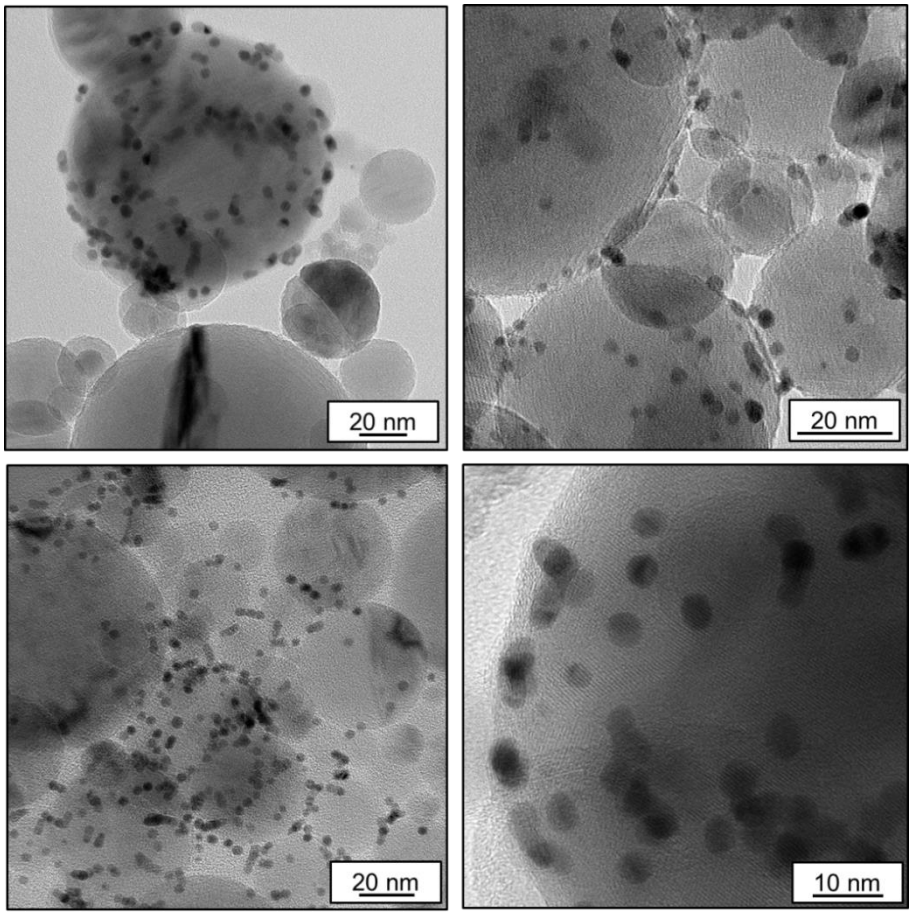


Figure 6 - Supported Pt nanoparticles on γ-$Al_2O_3$ from various areas on the TEM grid.

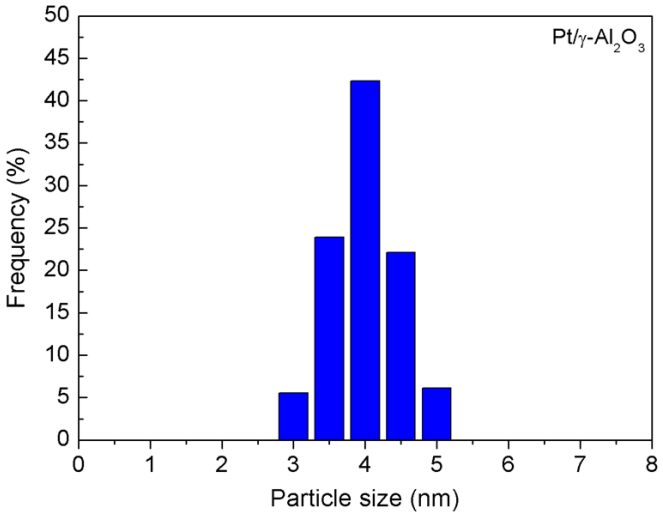


Figure 6 a - Particle size distribution for Pt/γ-$Al_2O_3$.

Figure 7 shows various TEM images of $Pt/CeO_2$. Once again, the Pt nanoparticles are very monodisperse on the support and show a high concentration of Pt nanoparticles over the support. XPS showed that this catalyst had the greatest amount of surface Pt loading 48.7 wt% (Table 2). This is followed by the particle size histogram in Figure 7a.

#### 4.2.4.3 Supported $Pt/CeO_2$

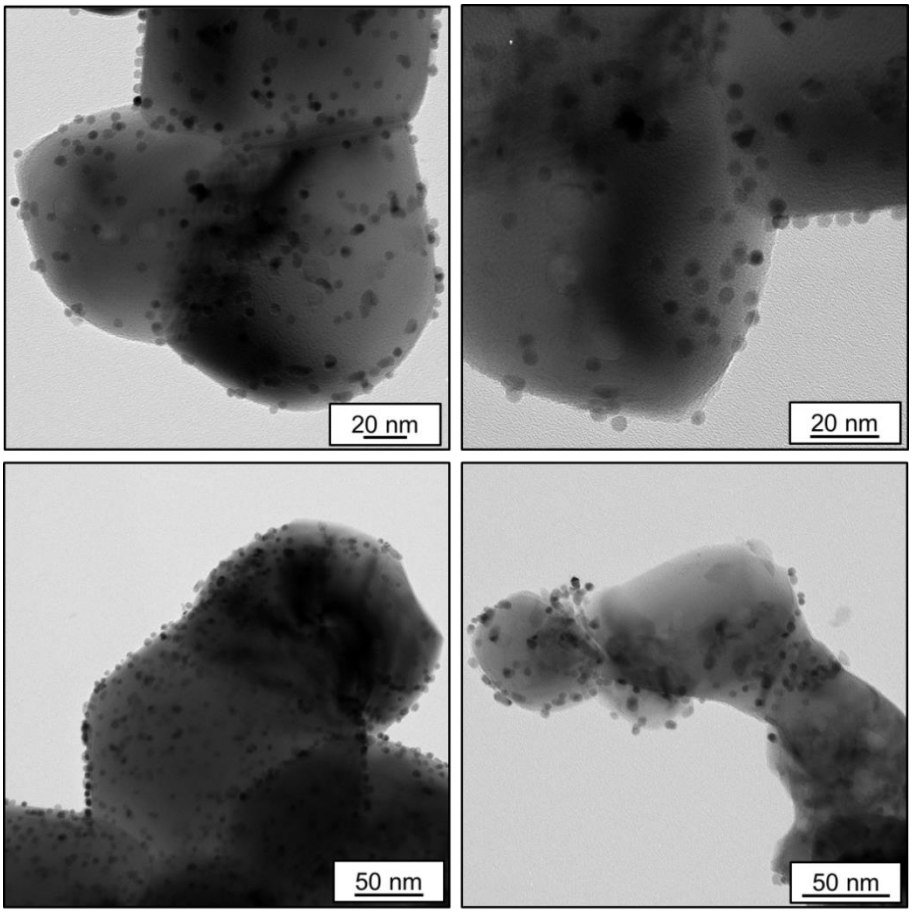


Figure 7 - Arrangement of $Pt/CeO_2$ TEM images from various areas of the grid.

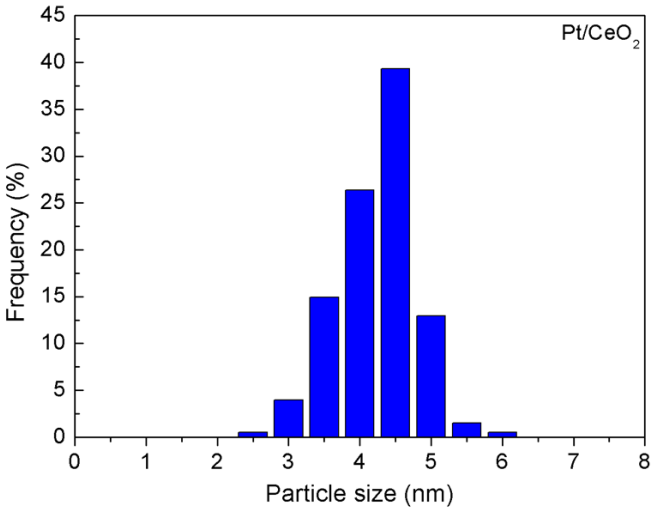


Figure 7 a - Particle size distribution for $Pt/CeO_2$.

Figure 8 shows an array of TEM images of supported Pt nanoparticles on MgO, with Figure 8a highlighting the particle size distribution. Like the other supports, this metal oxide does not have a high surface area. XPS shows that the surface Pt loading is very similar to $\gamma$-$Al_2O_3$.

#### 4.2.4.4 Supported Pt/MgO

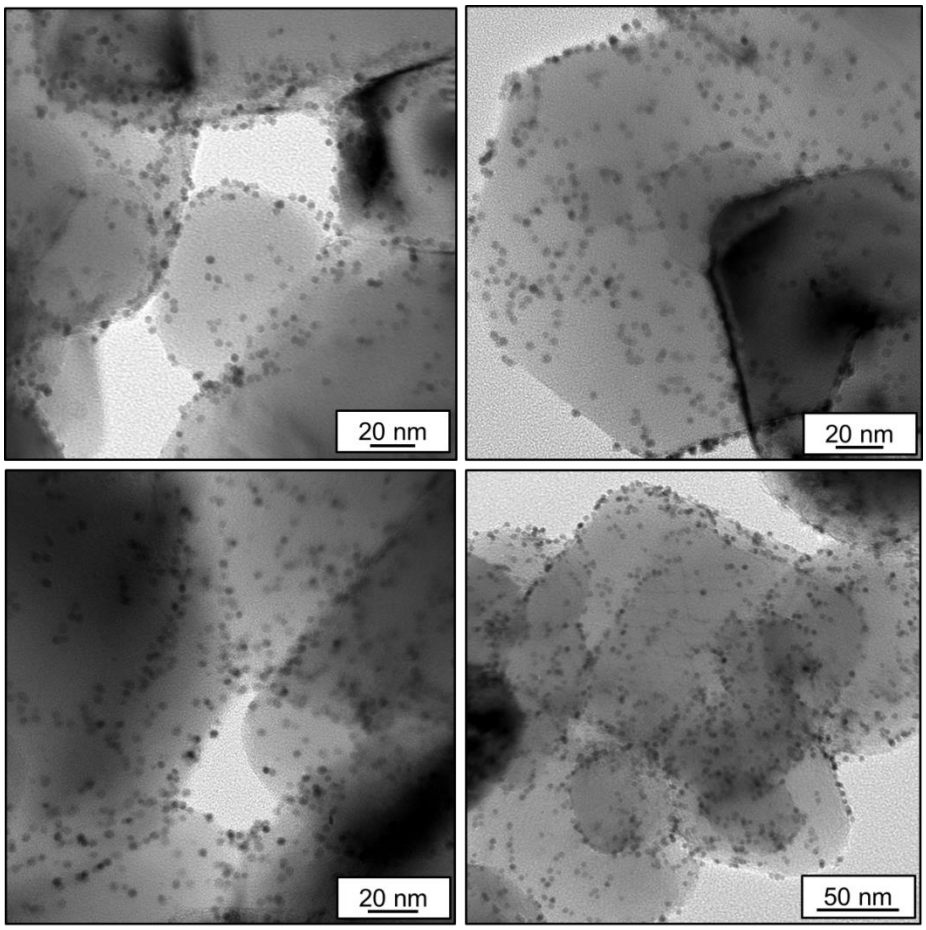


Figure 8 - TEM images of Pt/MgO at different areas on the grid.

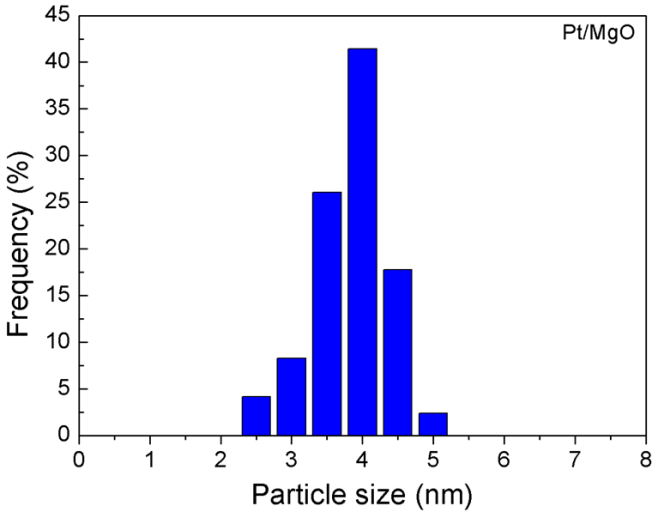


Figure 8 a - Particle size distribution for Pt/MgO.

For Pt/ZnO, the Pt nanoparticles do not follow the same monodisperse trend shown by the previous catalysts (Figures 5-8), where the average particle size is overall smaller. Images for this material are displayed in Figure 9 as well as the corresponding size distribution profile (Figure 9a).

This is then followed by the final monometallic Pt catalyst, $Pt/SiO_2$ (Figure 10). In Figure 10a the particle size distribution is shown and similarly to Pt/ZnO does not correlate completely with the monodisperse nature of the other materials. For this sample there are areas of slight particle agglomeration leading to nanoparticles of 6-8 nm.

#### 4.2.4.5 Supported Pt/ZnO

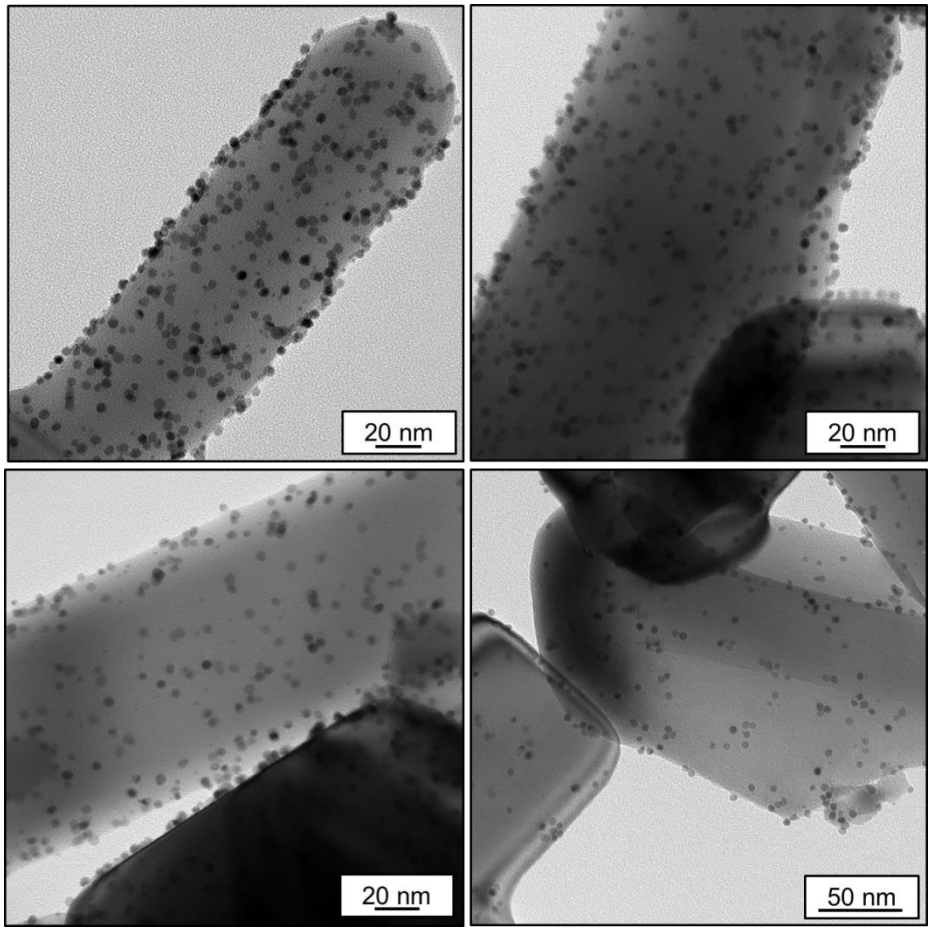


Figure 9 - TEM images of Pt/ZnO at different areas on the grid.

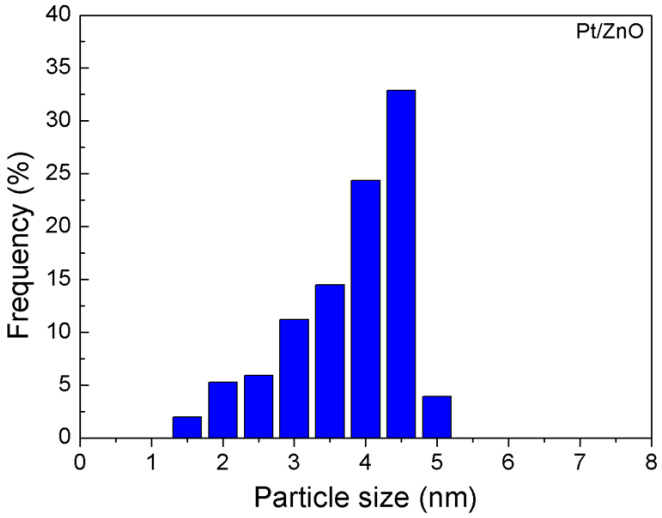


Figure 9 a - Particle size distribution for Pt/ZnO.

#### 4.2.4.6 Supported $Pt/SiO_2$

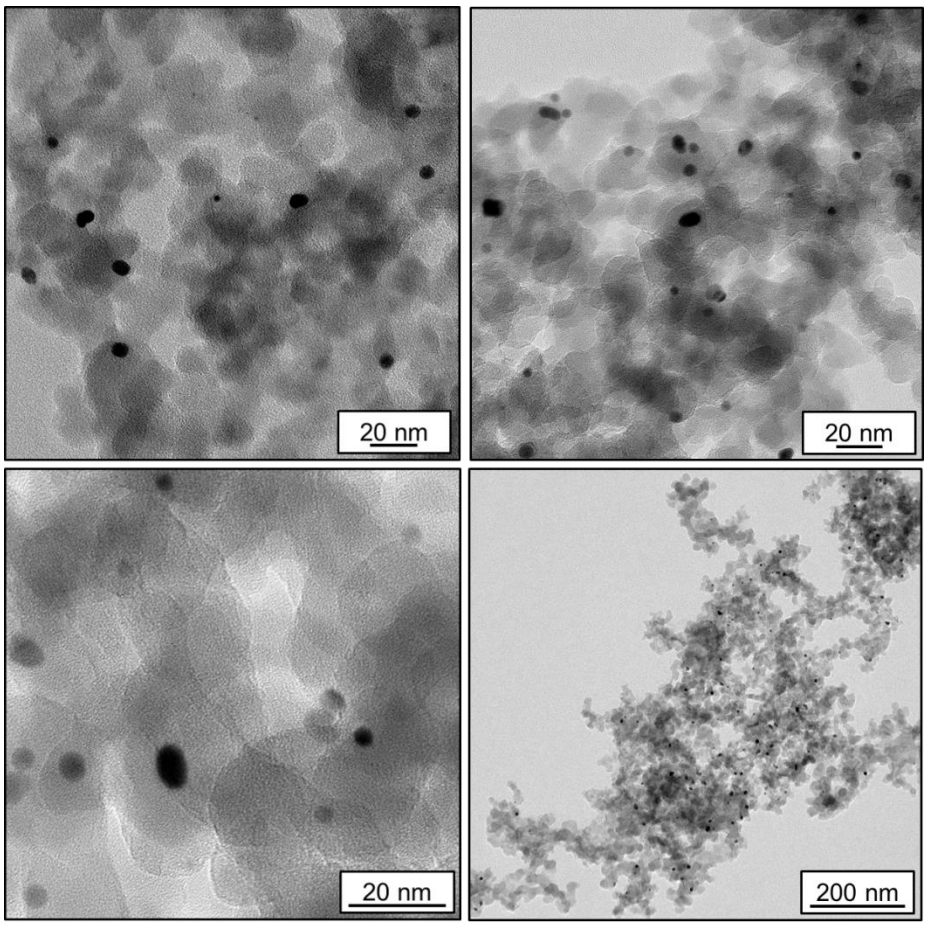


Figure 10 - TEM images of $Pt/SiO_2$ at different areas on the TEM grid.

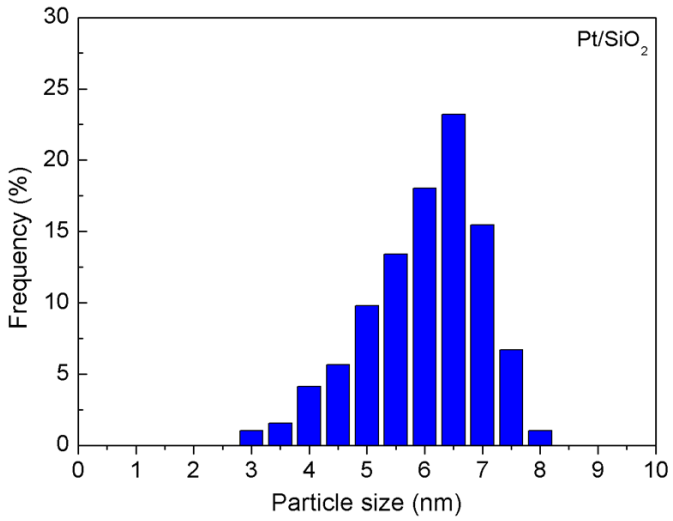


Figure 10 a - Particle size distribution for $Pt/SiO_2$.

The size distribution diagrams shown in Figures 5b, 6a, 7a, 8a, 9a and 10a show that the overall distributions are fairly tight and that the particles are relatively homogeneously distributed. The Pt particle size distribution on $SiO_2$ was substantially broader with a larger mean diameter of 6.0 ± 1.0 nm, which likely reflects a weaker interaction with the silica support and resultant mild sintering.[35–37] For the Pt/ZnO catalyst, the particle size distribution was also centred around 3.8 nm (± 0.9 nm), albeit with a significant number of smaller 1-3 nm particles also present. This is depicted in the histograms shown in Figure 9a and 10a which show a relatively broad distribution for these two samples, leading to a larger standard deviation of the particle size. With the exception of $SiO_2$, TEM demonstrated that mild calcination (300 °C) and reduction (200 °C) steps induced minimal agglomeration or growth of deposited Pt nanoparticles, essential to isolate the influence of the different supports. Ramos-Fernández et al demonstrated that in the case of Pt/ZnO, higher reduction temperatures of 350 °C promoted particle agglomeration and deactivation in the hydrogenation of cinnamaldehyde.[38] As discussed later, the small apparent difference in nanoparticle size distribution over $SiO_2$, and the presence of some smaller particles over ZnO, exerts a significant influence upon the resulting catalytic performance of these two supports relative to the other oxide supports.

## 4.3 Catalytic reaction testing

### 4.3.1 True hydrogen pressure on the reaction

The pressure exerted by the hydrogen feedstock balloon was measured by a XP5 pressure sensor. The schematic for the pressure test is shown in Figure 11 as well as the pressure reading. As the test is completed at ambient pressure, the reading 0 MPa is atmospheric pressure, which means that any increase will be an additional force supplied. The change in pressure as read from the data is an additional 0.002 MPa. This means that the overall pressure on the reaction is 1.02 atm, exceedingly close to ambient pressure.

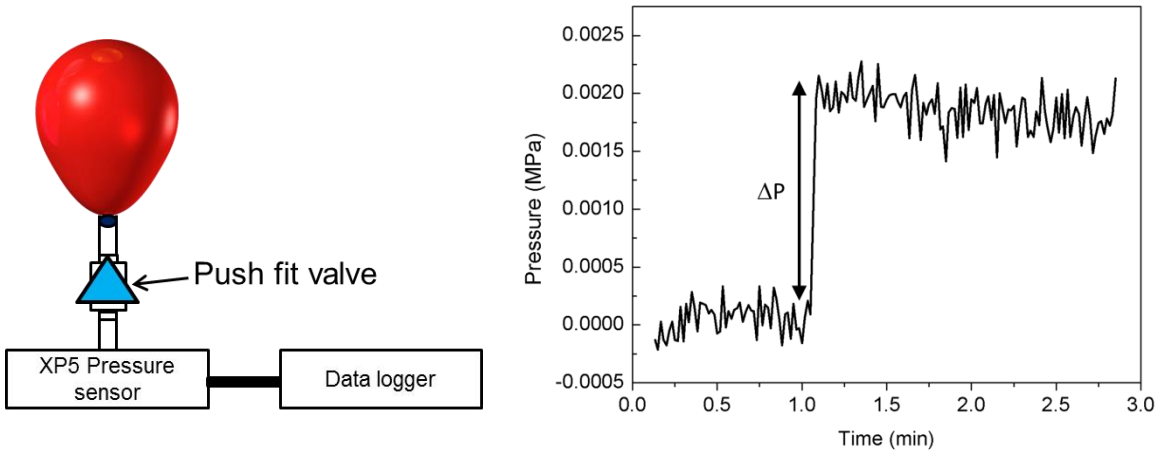


Figure 11 - Hydrogen pressure test and pressure on reaction graph.

### 4.3.2 Catalytic reaction testing

#### 4.3.2.1 Reactivity at 70 $^{o}$C (Reduced catalysts)

The performance of the five catalysts was first investigated for the hydrogenation of furfural at 70 °C with ethanol as the solvent. In all cases, the desired selective hydrogenation product, furfuryl alcohol was observed, alongside furan and 2-furaldehyde diethyl acetal (Table 3). The latter is a side-product of the reaction between furfural and the alcohol solvent (Figure 2), whose formation hinders the maximum selectivity achievable. Furfural conversion decreased in the order $Pt/CeO_2$ > $Pt/\gamma\text{-}Al_2O_3$ > Pt/MgO > $Pt/SiO_2$ > Pt/ZnO, while the selectivity to furfuryl alcohol varied between 9-70%, decreasing in the order Pt/MgO > $Pt/SiO_2$ > $Pt/\gamma\text{-}Al_2O_3$ > $Pt/CeO_2$ > Pt/ZnO. The relatively low activity of the Pt/ZnO catalyst was accompanied by the formation of furan arising from furfural

decarbonylation, as observed by Somorjai and co-workers who reported that PVP-stabilized Pt nanoparticles dispersed on mesoporous oxides including $Al_2O_3$, $TiO_2$, $Nb_2O_5$ and $Ta_2O_5$ favoured furan during vapour phase transformations of furfural.[5,22,23] The choice of oxide support, and/or precise nanoparticle size distribution, strongly influences the side reaction between furfural and the solvents.

Table 3 - Furfural hydrogenation over Pt catalysts after 7 h reaction in ethanol at 70 °C; 2-furaldehyde diethyl acetal expressed as Solvent Product (SP).

| Catalyst | Furfural conversion / % | Furfuryl alcohol selectivity / % | Furan selectivity / % | SP selectivity / % |
|---|---|---|---|---|
| $Pt/CeO_2$ | 97 | 27 | 3 | 70 |
| Pt/ZnO | 8 | 9 | 91 | 0 |
| Pt/MgO | 45 | 93 | 6 | 1 |
| $Pt/SiO_2$ | 24 | 75 | 8 | 17 |
| $Pt/\gamma\text{-}Al_2O_3$ | 58 | 72 | 3 | 25 |

The acetalization of aldehydes, including furfural, in alcoholic solvents is commonly reported in the literature (Figure 2), but is often unquantified.[1,3,12,28–31,39] Notably the addition of water forces the back reaction to furfural. The addition of base has also been found to hinder the reaction as the acetalization process is acid catalyzed.[29,30,34] Merlo et al reported an ether side product, 2-isopropoxymethylfuran, during furfural hydrogenation in 2-propanol at 10 bar and 100 °C, formed with 3.6 % selectivity over a PtSn catalyst and 22% over NiSn catalyst.[3,4,28] Similar observations were made by Vaidya et al in the same solvent for furfural hydrogenation under 20 bar hydrogen and 150 °C.[12] Furfural acetalization with methanol was also reported using a Ni based catalyst during hydrogenation,[40] while 2-furaldehyde diethyl acetal has been previously observed using ethanol as the solvent in furfural hydrogenation.[28]

In the absence of any solid catalyst, neither hydrogenation nor decarbonylation reactions were observed in the present work, although significant furfural reacted with ethanol to form 2-furaldehyde diethyl acetal (61% yield after 7 h). The parent supports were also inactive towards furfural hydrogenation (Table 4), favouring either decarbonylation to furan or acetalization with ethanol. Interestingly, the acetalization reaction on the untreated

supports was found to be inhibited in most cases due to inherent water present. The extent of the acetalization observed with the bare supports was strongly dependent on the degree of hydration of the bare support.

Table 4 - Furfural hydrogenation over the parent untreated oxide supports after 7 h reaction in ethanol at 70 °C; 2-furaldehyde diethyl acetal expressed as Solvent Product (SP).

| Catalyst | Furfural conversion / % | Furan selectivity / % | Furfuryl alcohol selectivity / % | SP selectivity / % |
|---|---|---|---|---|
| $CeO_2$ | 57 | 0 | 0 | 100 |
| ZnO | 6 | 98 | 0 | 2 |
| MgO | 0.4 | 99 | 0 | 1 |
| $SiO_2$ | 8 | 0 | 0 | 100 |
| $\gamma$-$Al_2O_3$ | 17 | 0 | 0 | 100 |

Furfural reaction over all the Pt/oxide catalysts (except $Pt/CeO_2$ which attained near complete conversion) reached a plateau in their conversions and selectivities after 7 h reaction, indicative of either catalyst deactivation or mass-transport limitation effects.

In the cases of $Pt/SiO_2$ and $Pt/CeO_2$ there was some evidence for competition between furfural hydrogenation to furfuryl alcohol vs. acetalization, with their respective selectivities exhibiting a weak anti-correlation. It is interesting to note that the acetalization side reaction, generally considered to be acid catalyzed, was suppressed over the most basic Pt/MgO and Pt/ZnO catalysts.[32,41]

#### 4.3.2.2 Reactivity at 70 $^{o}$C (The effect of solvent)

As a result of the acetalization observed during reaction in ethanol, a range of alternative solvents were investigated to determine whether acetalization could be suppressed while maintaining high rates for the primary hydrogenation of furfural to furfuryl alcohol. Since $Pt/\gamma$-$Al_2O_3$ was only moderately active towards furfural acetalization in ethanol it was selected for screening against other alcohol and non-polar solvents. The results are summarized in Table 5. Non-polar toluene and hexane resulted in low furfural conversion and comparatively high degrees of decarbonylation to furan, in accordance with previous

higher pressure studies on $Pt/SiO_2$ and $PtSn/SiO_2$ catalysts,[28] which may reflect their poor hydrogen solubilities. Amongst the alcohols, selectivity to furfuryl alcohol decreased significantly with increasing solvent chain length, with n-butanol producing high yields of furan. Selectivity towards the undesired acetal side product decreased from ethanol >> methanol > n-butanol. In the case of methanol, small amounts of 2-furaldehyde dimethyl acetal were observed after 7 h, while acetal formation was not detectable using n-butanol as the solvent (Table 5), and hence these solvents are better suited for furfural hydrogenation. This trend in acetalization reactivity is similar to that reported in the absence of a catalyst.[32,33,42,43]

Table 5 - Influence of solvent on furfural hydrogenation over $Pt/\gamma\text{-}Al_2O_3$ after 7 h reaction at 70 °C; 2-furaldehyde diethyl acetal (ethanol) and 2-furaldehyde dimethyl acetal (methanol) expressed as Solvent Product (SP).

| Solvent | Furfural conversion / % | Furfuryl alcohol selectivity / % | Furan selectivity / % | SP selectivity / % |
|---|---|---|---|---|
| Methanol | 65 | 77 | 19 | 5 |
| Ethanol | 58 | 72 | 3 | 25 |
| n-Butanol | 45 | 52 | 48 | 0 |
| Toluene | 49 | 21 | 79 | 0 |
| Hexane | 2 | 71 | 29 | 0 |

#### 4.3.2.3 The effect of temperature

Having identified methanol as the most suitable solvent for furfural hydrogenation, the impact of reaction temperature on selectivity to furfuryl alcohol was subsequently explored over the different oxide supports in an effort to further suppress the solvent side reaction. Lowering the reaction temperature from 70 $^oC$ to 50 °C surprisingly increased activity, in addition to enhancing furfuryl alcohol selectivity (Table 6) to >90 % for all the supports as compared with EtOH reaction data except ZnO. High temperature (70 $^oC$) MeOH reactions were carried out only for $\gamma\text{-}Al_2O_3$ during the solvent screening process (Table 5) and ZnO for kinetic analysis (seen later, Figure 12). Indeed, under these exceptionally mild pressure and temperature conditions, $Pt/CeO_2$ and $Pt/\gamma\text{-}Al_2O_3$ delivered approximately 80 % furfural conversion at 99 % furfuryl alcohol selectivity. A comparison of $Pt/\gamma\text{-}Al_2O_3$ at 50 °C and 70 °C reveals acetal formation as strongly temperature dependent.

Table 6 - Furfural hydrogenation over Pt catalysts after 7 h reaction in methanol at 50 °C; 2-furaldehyde dimethyl acetal expressed as Solvent Product (SP).

| Catalyst | Furfural conversion / % | Furfuryl alcohol selectivity / % | Furan selectivity / % | SP selectivity / % |
|---|---|---|---|---|
| $Pt/CeO_2$ | 77 | 98 | 1 | 1 |
| Pt/ZnO | 7 | 60 | 40 | 0 |
| Pt/MgO | 79 | 97 | 3 | 0 |
| $Pt/SiO_2$ | 35 | 90 | 7 | 3 |
| $Pt/\gamma\text{-}Al_2O_3$ | 80 | 99 | 1 | 0 |

The poorer activity of the Pt/ZnO catalyst arises from contributions of the ZnO support, which was found to favour decarbonylation, (Table 4) and possibly due to the relatively larger number of small Pt particles which may lead to site-blocking of the Pt sites by strongly bound CO.[1,5] Similar CO poisoning was reported for $SiO_2$ supported Group VIII metals during the liquid phase hydrogenation of citral.[43] $Pt/SiO_2$ exhibited activity intermediate between ZnO and the other oxides. However, it retained high selectivity towards furfuryl alcohol and hence poorer activity over silica is attributed to the larger Pt nanoparticles present and therefore lower reactive surface area. Interestingly, Pt/MgO and $Pt/SiO_2$ catalysts, which possess a relatively high number of ≤3 nm particles, favour furan formation relative to $Pt/\gamma\text{-}Al_2O_3$ and $Pt/CeO_2$. These results suggest that under our reaction conditions, selectivity in furfural hydrogenation is particle size dependent, with monodispersed Pt nanoparticles ~4 nm possessing optimal activity and selectivity.

At 50 °C, metal-support interactions, or direct catalysis by the support, appear relatively unimportant since identically sized nanoparticulate Pt behaves similarly on $CeO_2$, $\gamma\text{-}Al_2O_3$ and MgO, three widely different supports. However, the nature of the oxide support appears to be crucial in respect of regulating the dispersion of Pt nanoparticles, and hence regulating furfural decarbonylation vs. selective hydrogenation.

By taking the two catalyst extremes, $Pt/\gamma\text{-}Al_2O_3$ and Pt/ZnO, a catalyst very active and selective vs. a material which favours decarbonylation, followed by rapid deactivation. We can measure the rate of reaction per gram of Pt at varying temperatures for the two most effective solvents; this is shown in Figure 13.

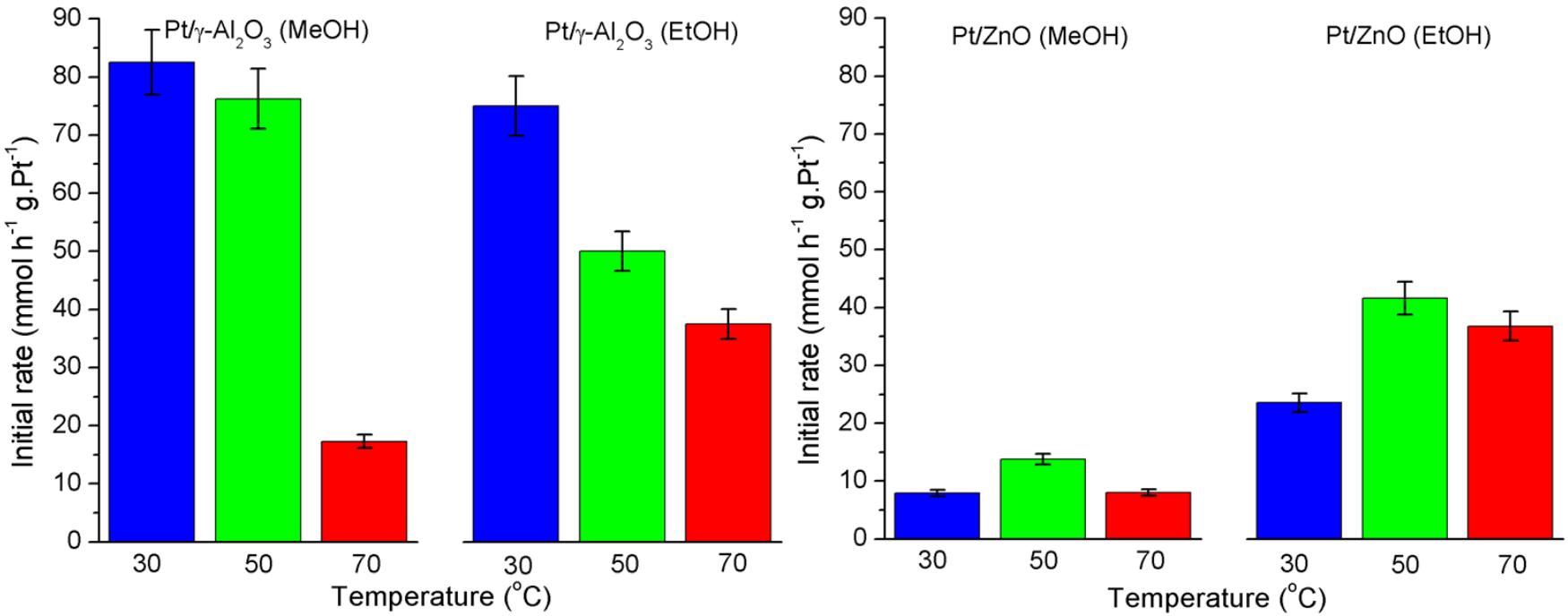


Figure 12 - The comparison of initial catalyst rate for the most and least active catalyst at different temperatures and solvents.

Figure 13 shows that the furfural reaction has many variables and it is evident that Pt/γ-$Al_2O_3$ is much more active than Pt/ZnO, both in MeOH and EtOH. However, this data shows that the catalyst itself is dependent on solvent and temperature as Pt/γ-$Al_2O_3$ is much more active in MeOH at lower temperatures whereas Pt/ZnO favoured warmer conditions in EtOH. In fact, although the reaction profiles in Figure 12 show that Pt/ZnO deactivates rapidly, the data from Figure 13 shows that the two catalysts have very similar initial rates of reaction at 70 $^{o}$C in EtOH. This data also suggests that the furfural hydrogenation is more effective at 30 $^{o}$C. However, as Figure 14 and Table 7 show, this is not the case as the overall conversion at 7 h is superior for the 50 $^{o}$C data. The importance of the 30 $^{o}$C data is that for the case of both solvents, there is no acetal formed. This galvanizes the fact that the coupling reaction between the solvent and substrate is strictly thermally driven. Lowering the reaction temperature to 30 $^{o}$C also has an effect on furan selectivity for Pt/ZnO. Although selectivies are improved towards the hydrogenation reaction pathway, the low surface area material is still rapidly deactivated.

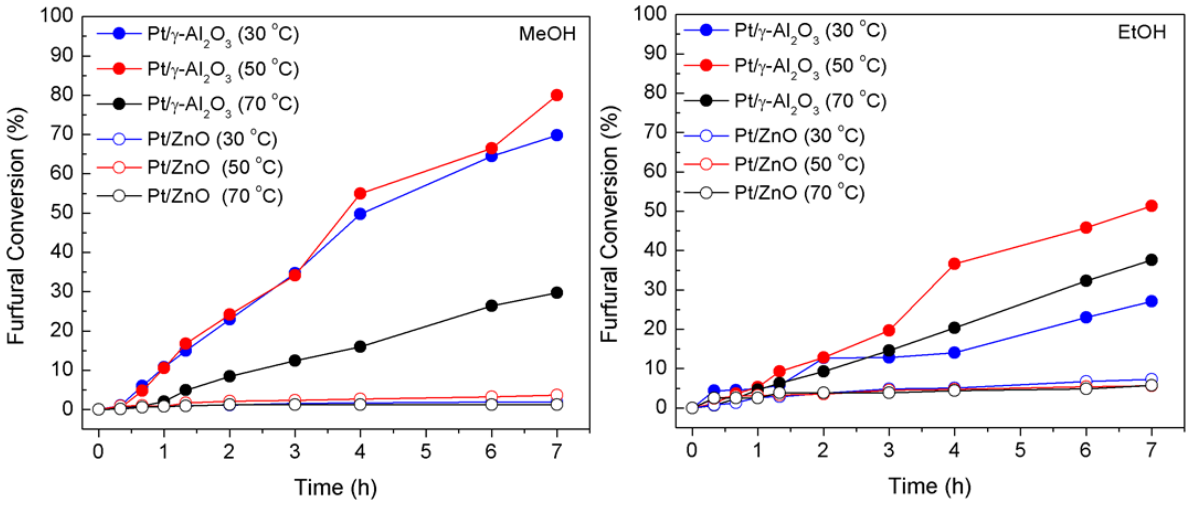


Figure 13 - Reaction profiles of Pt/γ-$Al_2O_3$ and Pt/ZnO operating under varying conditions.

The data presented in Figure 12 and Figure 13 as well as in Table 7 was acquired after a lengthy period of time. During this time the Pt nanoparticles have appears to have begun to oxidize when in storage, this is evident by the drop in higher temperature activity seen previously in Table 3. Further evidence of surface oxidation is the increase in furan selectivity, this is because furfural will adopt a different bonding position on the surface of

the particle when it is in a reduced state. As has been discussed, the production of furan leads to CO adsorption and subsequent further catalyst deactivation.

| Solvent and Temp / $^{o}$C | Catalyst | Furfural conversion / % | Furfuryl alcohol selectivity / % | Furan Selectivity / % | SP selectivity / % |
|---|---|---|---|---|---|
| MeOH – 70 | Pt/γ-$Al_2O_3$ | 29.7 | 97.1 | 1.5 | 1.4 |
| MeOH – 50 | Pt/γ-$Al_2O_3$ | 80.0 | 99.5 | 0.5 | 0 |
| MeOH – 30 | Pt/γ-$Al_2O_3$ | 69.8 | 99.4 | 0.6 | 0 |
| EtOH – 70 | Pt/γ-$Al_2O_3$ | 37.4 | 72.6 | 9.3 | 18.1 |
| EtOH – 50 | Pt/γ-$Al_2O_3$ | 51.3 | 94.5 | 3.1 | 2.4 |
| EtOH – 30 | Pt/γ-$Al_2O_3$ | 27.1 | 97.5 | 2.5 | 0 |
| MeOH – 70 | Pt/ZnO | 1.9 | 40.8 | 59.0 | 0.2 |
| MeOH – 50 | Pt/ZnO | 3.8 | 59.8 | 40.2 | 0 |
| MeOH – 30 | Pt/ZnO | 1.3 | 67.7 | 32.3 | 0 |
| EtOH – 70 | Pt/ZnO | 6.3 | 12.5 | 86.7 | 0.6 |
| EtOH – 50 | Pt/ZnO | 5.6 | 60.6 | 39.4 | 0 |
| EtOH – 30 | Pt/ZnO | 7.3 | 74 | 26 | 0 |

Table 7 – Furfural hydrogenation reaction table of conversion and selectivities for Pt/γ-$Al_2O_3$ and Pt/ZnO catalysts at varying conditions, 2-furaldehyde dimethyl acetal and furaldehyde diethyl acetal expressed as Solvent Product (SP).

#### 4.3.2.4 Recyclability of the supported Pt catalysts

The recyclability of the catalysts was also investigated for the optimum reaction conditions (50 $^{o}$C in MeOH). All catalysts were reclaimed after reaction via centrifugation, followed by a methanol wash and further centrifuging. The catalysts were then left to dry at room temperature. Once dry they were retested under identical conditions to those reported in Table 6. This process was repeated in two successive cycles. Table 8 shows that, for the Pt/$\gamma$-$Al_2O_3$, Pt/$CeO_2$, Pt/MgO and Pt/$SiO_2$, there is a marginal drop in activity as compared to Table 6 while the selectivity to furfuryl alcohol remains at the same levels. As previously postulated, Pt/ZnO appears to self-poison due to decarbonylation of furfural on ZnO support leading to Pt poisoning.

Table 8 - Furfural hydrogenation over recycled Pt catalysts after 7 h reaction in methanol at 50 °C; 2-furaldehyde dimethyl acetal expressed as Solvent Product (SP).

| Catalyst | Furfural conversion / % | Furfuryl alcohol selectivity / % | Furan selectivity / % | SP selectivity / % |
|---|---|---|---|---|
| $^{2}$Pt/$CeO_2$ | 73 | 96 | 1 | 3 |
| $^{3}$Pt/$CeO_2$ | 71 | 95 | 0 | 5 |
| $^{2}$Pt/ZnO | 0.6 | 40 | 44 | 16 |
| $^{3}$Pt/ZnO | 0.1 | 31 | 51 | 18 |
| $^{2}$Pt/MgO | 76 | 96 | 4 | 0 |
| $^{3}$Pt/MgO | 75 | 96 | 4 | 0 |
| $^{2}$Pt/$SiO_2$ | 30 | 89 | 5 | 6 |
| $^{3}$Pt/$SiO_2$ | 29 | 81 | 9 | 10 |
| $^{2}$Pt/$\gamma$-$Al_2O_3$ | 79 | 97 | 0 | 3 |
| $^{3}$Pt/$\gamma$-$Al_2O_3$ | 78 | 97 | 0 | 3 |

Where: $^{2}$ – 2$^{nd}$ cycle of testing, $^{3}$ – 3$^{rd}$ cycle of testing

## 4.4 Conclusions

The platinum catalyzed liquid phase hydrogenation of furfural was studied over five different oxide supports under mild reaction conditions. A simple and reproducible method was developed to support a narrow size distribution of stabilizer-free Pt nanoparticles over $SiO_2$, ZnO, $\gamma$-$Al_2O_3$, $CeO_2$ and MgO. Furfural hydrogenation was sensitive to Pt particle size, with those of approximately 4 nm highly active and selective for the hydrogenation reaction in methanol, even at 30 °C. Whereas, smaller Pt nanoparticles present in the MgO and $SiO_2$ catalysts promote some decarbonylation to furan. Indeed for Pt/ZnO, extensive

decarbonylation over the ZnO support appears to dominate Pt catalysis. The reaction is also strongly sensitive to the solvent selection, with alcohols more active than non-polar solvents. However, certain alcohols such as ethanol favour the formation of undesired acetal side products through reaction with furfural at 70 °C; although such competing reactions can be suppressed by lower temperature operation or through supporting Pt particles on more basic metal oxides. At 50 °C MgO, $CeO_2$ and $\gamma$-$Al_2O_3$, three very different materials in terms of their acidity, surface area, density and crystallinity, appear to be excellent supports for furfural selective hydrogenation to furfuryl alcohol. There was no evidence of strong metal-support interactions during the liquid phase hydrogenation of furfural, in contrast to that reported for the analogous vapour phase hydrogenation reaction. However, support selection appears critical to achieving the correct platinum dispersion for high furfuryl alcohol yields, with $SiO_2$ favouring large and broad particle size distributions and concomitant poorer activity and selectivity. All catalysts were found to be recyclable, maintaining both activity and selectivity after prolonged testing.

## 4.5 References


1 M. J. Taylor, L. J. Durndell, M. A. Isaacs, C. M. A. Parlett, K. Wilson, A. F. Lee and G. Kyriakou, *Appl. Catal. B Environ.*, 2016, **180**, 580–585.

2 A. B. Merlo, V. Vetere, J. F. Ruggera and M. L. Casella, *Catal. Commun.*, 2009, **10**, 1665–1669.

3 A. B. Merlo, V. Vetere, J. M. Ramallo-López, F. G. Requejo and M. L. Casella, *React. Kinet. Mech. Catal.*, 2011, **104**, 467–482.

4 V. Vetere, A. B. Merlo, J. Ruggera and M. L. Casella, *J. Braz. Chem. Soc.*, 2010, **21**, 914–920.

5 V. V Pushkarev, N. Musselwhite, K. An, S. Alayoglu and G. A. Somorjai, *Nano Lett.*, 2012, **12**, 5196–201.

6 X. Chen, L. Zhang, B. Zhang, X. Guo and X. Mu, *Sci. Rep.*, 2016, **6**, 28558.

7 J. Kijeński, P. Winiarek and T. Paryjczak, *Appl. Catal. A*, 2002, **233**, 171–182.

8 D. Shi and J. M. Vohs, *ACS Catal.*, 2015, **5**, 2177–2183.

9 M. J. Taylor, L. Jiang, J. Reichert, A. C. Papageorgiou, S. K. Beaumont, K. Wilson, A. F. Lee, J. V Barth and G. Kyriakou, *J. Phys. Chem. C*, 2017, **121**, 8490–8497.

10 A. Mandalika, L. Qin, T. K. Sato and T. Runge, *Green Chem.*, 2014, **16**, 2480–2489.

11 H. Luo, H. Li and L. Zhuang, *Chem. Lett.*, 2001, 404–405.

12 P. D. Vaidya and V. V Mahajani, *Ind. Eng. Chem.*, 2003, **42**, 3881–3885.

13 S. Sitthisa, T. Pham, T. Prasomsri, T. Sooknoi, R. G. Mallinson and D. E. Resasco, *J. Catal.*, 2011, **280**, 17–27.

14 S. Sitthisa, W. An and D. E. Resasco, *J. Catal.*, 2011, **284**, 90–101.

15 Z. Xu, H. Zhang, S. Liu, B. Zhang, H. Zhong and D. S. Su, *Int. J. Hydrogen Energy*, 2012, **37**, 17978–17983.

16 B. Nagaraja, A. Padmasri, B. Raju and K. Rama Rao, *J. Mol. Catal. A Chem.*, 2007, **265**, 90–97.

17 P. Reyes, D. Salinas, C. Campos and M. Oportus, *Quim. Nova*, 2010, **33**, 777–780.

18 S. T. Thompson and H. H. Lamb, *ACS Catal.*, 2016, **6**, 7438–7447.

19 C. Zhang, Q. Lai and J. H. Holles, *Catal. Commun.*, 2017, **89**, 77–80.

20 O'Driscoll, J. J. Leahy and T. Curtin, *Catal. Today*, 2017, **279**, 194–201.

21 W.-S. Lee, Z. Wang, W. Zheng, D. G. Vlachos and A. Bhan, *Catal. Sci. Technol.*,

2014, **4**, 2340.

22 L. R. Baker, G. Kennedy, M. Van Spronsen, A. Hervier, X. Cai, S. Chen, L.-W. Wang and G. A. Somorjai, *J. Am. Chem. Soc.*, 2012, **134**, 14208–16.

23 K. An, N. Musselwhite, G. Kennedy, V. V Pushkarev, L. R. Baker and G. A. Somorjai, *J. Colloid Interface Sci.*, 2013, **392**, 122–8.

24 L. Zheng, C. Xu, W. Liang, J. Liu, J. Liu, X. Dun, Y. Guo and Y. Yang, *Chinese J. Catal.*, 2010, **31**, 461–465.

25 B. M. Nagaraja, V. Siva Kumar, V. Shasikala, A. H. Padmasri, B. Sreedhar, B. David Raju and K. S. Rama Rao, *Catal. Commun.*, 2003, **4**, 287–293.

26 L. J. Durndell, C. M. A. Parlett, N. S. Hondow, M. A. Isaacs, K. Wilson and A. F. Lee, *Sci. Rep.*, 2015, **5**, 9425.

27 K. Yan, J. Liao, X. Wu and X. Xie, *Adv. Mater. Lett.*, 2013, **4**, 702–707.

28 A. B. Merlo, V. Vetere, J. F. Ruggera and M. L. Casella, *Catal. Commun.*, 2009, **10**, 1665–1669.

29 P. Mäki-Arvela, L.-P. Tiainen, A. K. Neyestanaki, R. Sjöholm, T.-K. Rantakylä, E. Laine, T. Salmi and D. Y. Murzin, *Appl. Catal. A Gen.*, 2002, **237**, 181–200.

30 P. G. N. Mertens, F. Cuypers, P. Vandezande, X. Ye, F. Verpoort, I. F. J. Vankelecom and D. E. De Vos, *Appl. Catal. A Gen.*, 2007, **325**, 130–139.

31 M. Audemar, C. Ciotonea, K. De Oliveira Vigier, S. Royer, A. Ungureanu, B. Dragoi, E. Dumitriu and F. Jérôme, *ChemSusChem*, 2015, **8**, 1885–1891.

32 J. Bell, D. Kubler, P. Sartwell and R. G. Zepp, *J. Org. Chem.*, 1965, **30**, 4284–4292.

33 N. Melchior, *J. Am. Chem. Soc.*, 1949, **283**, 3651–3654.

34 C. Wiles, P. Watts and S. J. Haswell, *Tetrahedron*, 2005, **61**, 5209–5217.

35 L. D. Chen, M, Schmidt, *J. Catal.*, 1978, **55**, 348–360.

36 B. K. Min, A. K. Santra and D. W. Goodman, *Catal. Today*, 2003, **85**, 113–124.

37 B. Simonsen, S, I. Chorkendorff, S. Dahl, M. Skoglundh, J. Sehested and S. Helveg, *J. Catal.*, 2011, **281**, 147–155.

38 E. V. Ramos-Fernández, A. F. P. Ferreira, A. Sepúlveda-Escribano, F. Kapteijn and F. Rodríguez-Reinoso, *J. Catal.*, 2008, **258**, 52–60.

39 K. Yan, G. Wu, T. Lafleur and C. Jarvis, *Renew. Sustain. Energy Rev.*, 2014, **38**, 663–676.

40 N. Merat, C. Godawa and A. Gaset, *J. Chem. Technol. Biotechnol.*, 2007, **48**, 145–159.

41 M. Behrens, G. Lolli, N. Muratova, I. Kasatkin, M. Hävecker, R. N. d'Alnoncourt, O. Storcheva, K. Köhler, M. Muhler and R. Schlögl, *Phys. Chem. Chem. Phys.*, 2013, **15**, 1374–81.

42 E. Adams and H. Adkins, *J. Am. Chem. Soc.*, 1925, **47**, 1358–1367.

43 U. K. Singh and M. A. Vannice, *J. Catal.*, 2001, **199**, 73–84.

# Chapter 5 - The effect of Cu in PtCu bimetallic particles and Single Atom Alloys for the transformation of furfural

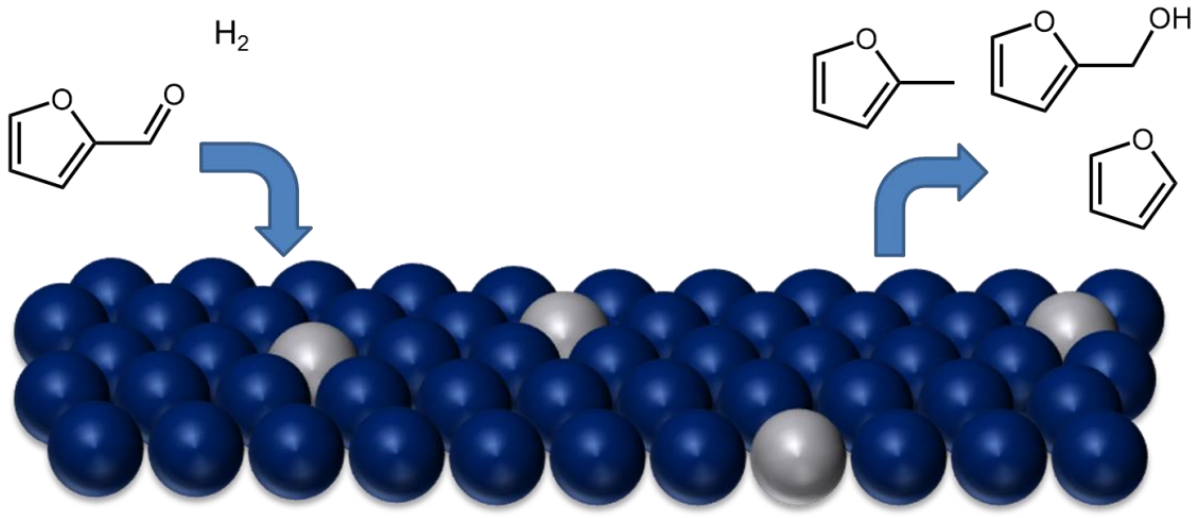

## 5.1 Introduction

The use of monodisperse supported Pt nanoparticles in Chapter 4 has shown that furfural hydrogenation can be accomplished under very mild conditions.[1] However, one important aspect is still to be considered as a matter of sustainability, which is the active metal site itself. Although highly active and selective, Pt supported catalysts are not viable materials for large scale furfural transformations, due to cost limitations. With this in mind, the purpose of this chapter is to demonstrate the effect of Cu in a PtCu bimetallic supported catalyst. Unlike other elements (Pt, Pd, Ni, Rh) Cu is unable to dissociate hydrogen at low pressures. Therefore a more forceful approach was taken by using moderate hydrogen pressures to activate the H-H bond.[2,3] The Pt rich catalyst ($Pt_{100}$), studied in Chapter 4 was diluted with Cu to generate nominal molar ratios of 50:50 and 25:75. Upon completion, further coinage metal dilution was considered, where the effect of Pt atomic entities that have been galvanically replaced into a Cu host nanoparticle could be studied. These materials are known as Single Atom Alloys (SAA,[2] as described in Chapter 1) and were synthesized as described in **Chapter 2, Section 2.1.3** using a monometallic 1 wt% Cu/$\gamma$-$Al_2O_3$ as the sacrificial host material.

In addition to this research, the effect of Cu precursor has been investigated by preparing Cu nanoparticles using two different metal salts ($Cu(NO_3)_2$ and $CuSO_4$). This was carried out to determine whether residual sulphur from $CuSO_4$ can cause either a promotional effect,[4,5] or, as seen for some hydrogenation reactions, act as a poison or inhibitant.[6] This precursor was used in comparison with $Cu(NO_3)_2$, nitrates which are relatively simple to decompose when thermally treated, leaving limited nitrogen based residues on the surface of the nanoparticles.[7]

As well as a metal precursor, hydrogen pressures were broadly investigated to truly stretch the functionality of the bimetallic systems, in an attempt to unlock alternate reaction pathways while under a mild temperature such as hydrogendeoxygenation (HDO) or ring opening. In Industry, furfural hydrogenation is traditionally performed at high temperature.[8] This study also monitors the effect Cu has on the production of 2-furaldehyde dimethyl acetal, a thermally driven reaction, which was not previously observed in Chapter

4 for Pt rich catalysts across multiple supports operating at low temperatures.[1] Hydrogenolysis (HDO) of reactively formed furfural alcohol to methyl furan was also not observed in the liquid phase hydrogenation of furfural when using dispersed Pt catalysts, as opposed to UHV studies on an extended Pt(111) surface.[9] The HDO reaction pathway has been discussed in the past when using Cu rich catalysts for gas phase reactions.[10,11]

As described in Chapter 2, bimetallic catalysts were synthesized using a method not too dissimilar to that used for monometallic Pt catalysts. By following this colloidal route we were able to adapt the existing hydrogenation system which utilized a Pt nanoparticle size of ~4 nm, previously reported as an ideal size for high furfuryl alcohol selectivity.[1,12] The aim of using this size of nanoparticle was to customize bimetallic particles of similar size and maintain a tight size distribution, as in the past the literature has dictated that products are Pt nanoparticle size specific.[12] Smaller Pt nanoparticles <4 nm have been found to be far more selective towards decarbonylation reaction pathways.[12] Particles between 4 and 11 nm are more suited for hydrogenation.

## 5.2 Catalyst Characterization

### 5.2.1 Monometallic supported Cu catalysts (High loading, proof of method development)

To ascertain the effect of Cu on the PtCu system, first a pure Cu sample was generated using both nitrate and sulphate precursors with the reduction protocol mentioned in Chapter 2. This was followed by the addition of $H_2PtCl_4.3H_2O$ in the precursor addition step of the synthesis to generate catalysts with the nominal molar ratios of $Pt_{25}Cu_{75}$ and $Pt_{50}Cu_{50}$. For ease of differentiation, each family of catalysts will be denoted with an (N) or (S) to represent the Cu precursor used.

As a starting point, the typical synthetic procedure shown previously in Chapter 2 was completed with an intended high copper loading (10%). This process determined whether the method would be successful and also gave an idea of the reducibility of each Cu precursor.

Once synthesized, both materials created from the nitrate and sulphate precursors were calcined in the typical way reported (300 $^{o}$C for 3 h) to remove the PVP capping agent.[1,13,14] Wide XRD scans were then completed to determine whether (i) Cu particles had formed, which oxidation state the copper was in and if the Cu species are measurable also, (ii) does the Cu presence affect the alumina support? Figure 1 below shows a pair of stacked diffractograms, which very clearly show that the Cu salts in both cases reduced to generate metallic Cu and oxide species. In the case of the Cu (N) material there is very clear presence of $Cu_2O$ at 36.5$^{o}$ and 42$^{o}$. After calcination there is also a presence of CuO (~39$^{o}$). A key point is that the alumina structure appears to be unchanged and so the possibility of Cu-spinel structures is negligible. However, when the sulphur precursor is used there is a drastic change to the Cu species formed. Although post calcination there is evidence of $Cu_2O$, there is also a strong signal for metallic Cu. This could mean that the residual sulphur on the surface of the Cu may restrict oxide formation. During the synthesis process, the use of acetone and continuous centrifugation is used to 'clean' the nanoparticles. This involves the removal of weakly interacting capping agent (PVP) and the residual diol, as well as the majority of the free surface bound sulphur if present. However, this is not the case as the S 2p proved to be present in the XPS of a thermally processed monometallic Cu (S), shown later. Additionally, there are very intense peaks at 32$^{o}$ and 34$^{o}$ which are indicative of CuS. Copper sulfide, specifically covellite, has been synthesized during the reduction process of the metal salt. This means that the majority of the precursor itself was not reduced in the polyol process. Instead, it formed a stable sulfide material which, as seen in the XP spectra (Figure 2), has a substantial surface concentration of sulphur. Interestingly, the work completed by Zhou and co-workers[15] who also use a similar method of nanoparticle synthesis claim that there is no presence of residual sulphur nor sulphur based compounds present.

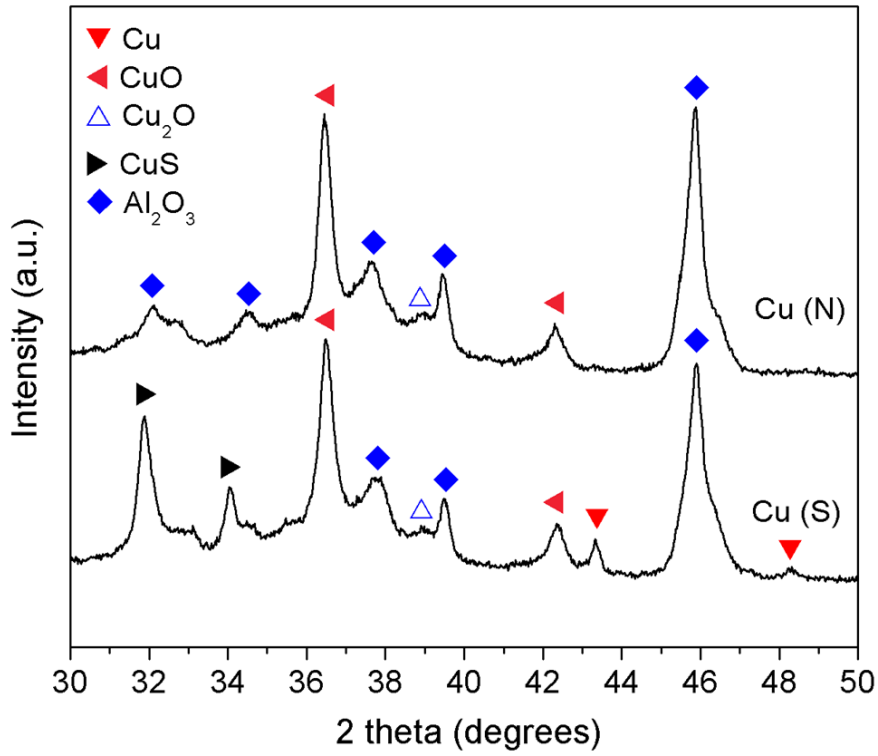


Figure 1 - PXRD diffractogram of high Cu loaded catalysts after calcination.

Particle size analysis was completed using the Scherrer equation (Chapter 2). ICP-OES and surface area analysis were completed on both of these materials to determine the Cu wt% and whether the surface area of the catalyst had diminished (Table 1). Both well-defined CuO peaks (36° and 42°) were used as a basis for particle size measurements. This information can be seen in Table 1 below.

Table 1 - Bulk elemental analysis, particle size and surface area measurements of the high Cu catalysts ($^{H}$Cu). Surface copper oxide concentration was also determined by XPS.

| **Catalyst** | **Cu loading (wt%)[a]** | **Particle size (nm)[a]** | **Surface area ($m^2$ $g^{-1}$)[b]** | **Surface copper oxide (%)[c]** |
|---|---|---|---|---|
| $^{H}$Cu (N) | 5.6 | 25.5 | 24.1 | 21.1 |
| $^{H}$Cu (S) | 8.0 | 24.7 | 22.6 | 7.9 |

a - Particle size as estimated by PXRD
b - BET surface area from $N_2$ porosimetry
c – Surface CuO determined by XPS (See Figure 2)

Although the diffractograms in Figure 1 show differences in the copper species formed between the precursors used, it does prove that Cu particle size is similar in both cases for CuO. This means that the method itself is proficient at generating a Cu species of similar size. Surface area measurements show that there is not a dramatic decrease in the overall catalyst surface area, even with the addition of CuS for the $^{H}$Cu (S) sample.

In Figure 2, X-ray Photoelectron Spectroscopy shows the expected Cu 2p doublet for both catalysts with the binding energies for the Cu $2p_{3/2}$ and Cu $2p_{1/2}$ situated at 932.4 eV and 952.2 eV respectively.[16] Additionally, for both of the high Cu loaded catalysts, there are satellite peaks at 941.1 eV and 961.7 eV. The presence of these peaks is agreeable with XRD (Figure 1) proving that these catalysts have oxidized copper.[16] Figure 2b shows the S 2p region where there is a clear sulphur signal at 168.7 eV. This binding energy is indicative of bulk sulphate.[17] As elemental sulphur has a binding energy of 164.1 eV, the signal present in this material is clearly still in the form of $CuSO_4$.[18] The surface mass ratios of copper and sulphur, as determined by XPS, show that the Cu 2p to S 2p ratio is 30:70. Due to the rich sulphur content, the actual concentration of surface copper oxide for the $^{H}$Cu (S) material is 7.9%, whereas for the $^{H}$Cu (N) sample comprises 21.1% copper oxide, as shown in Table 1.

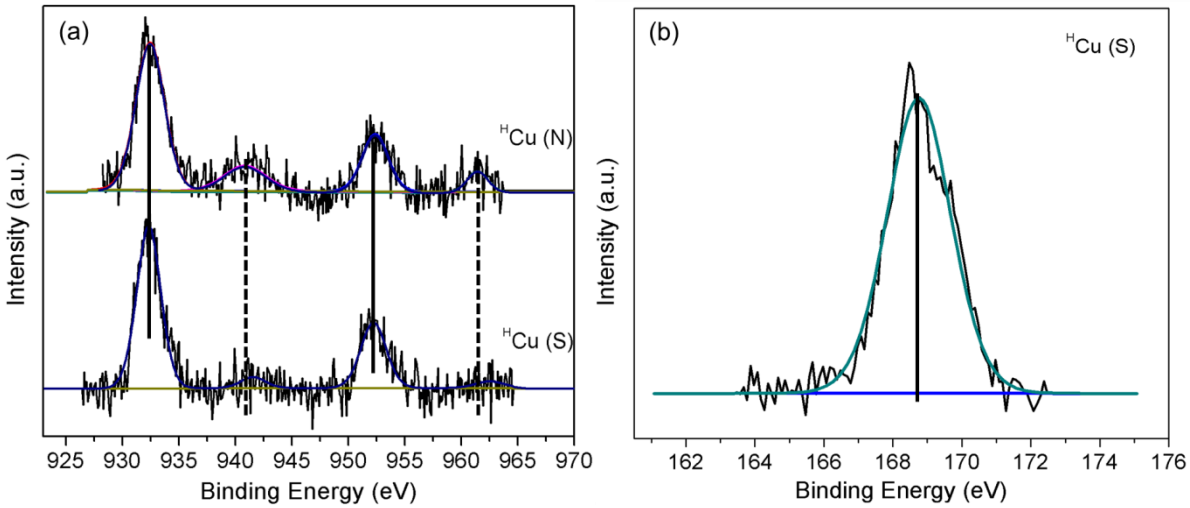


Figure 2 - XP spectra of (a) Cu 2p doublet (solid lines) and additional satellite peaks (dotted lines). (b) S 2p signal for the sulphur containing catalyst, $^{H}$Cu (S).

Clearly both precursors can be used to synthesize high loaded nano-copper catalysts. However, the high residual sulphur on the Cu surface in the form of bulk sulphate, as well as the formation of CuS when using large quantities of $CuSO_4$, mean that this precursor is not ideal. Whereas, the $Cu(NO_3)_2$ seems to form much more copper oxide which can be easily reduced under a hydrogen atmosphere.[13,14,19]

### 5.2.2 Monometallic Cu catalysts (Low loading intended for bimetallic synthesis)

As proof of the concept that Cu precursors can be effectively reduced and deposited on the alumina surface, metal loadings were radically reduced to bring the overall loading to ~1 wt%. Figure 3 shows the 1% Cu (N) suspension after all of the precursor was added over the 2 h period.

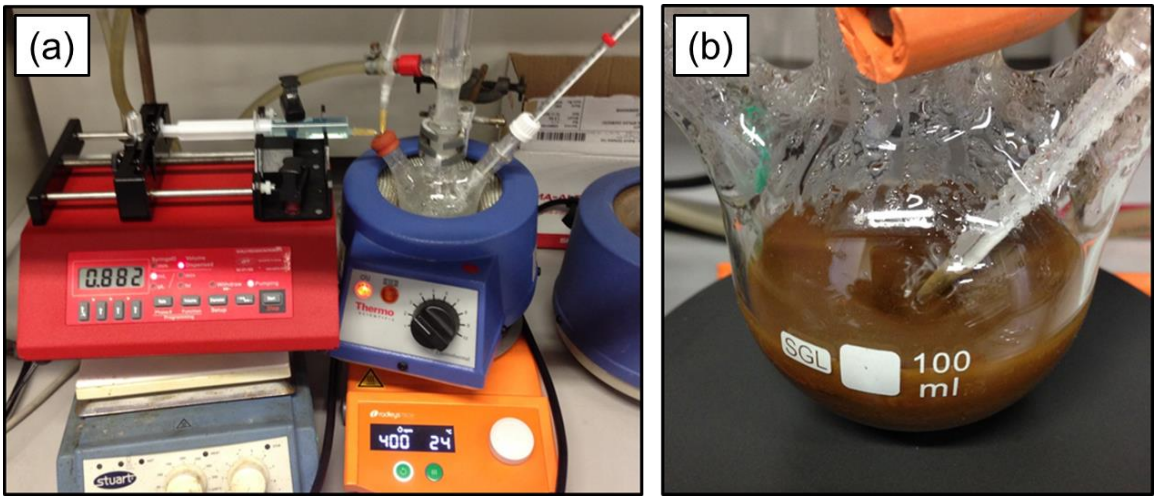


Figure 3 – (a) the gradual addition of precursor solution via syringe pump and (b) the Cu suspension upon reduction.

After centrifugation with successive washing and finally suspending in ethanol, an aliquot was removed (<20 μL) and scanned by TEM. This is shown in Figure 4, presenting both the shape of the Cu particles and an average size of 1.7 ± 0.6 nm. As there is no support present the particles have a high contrast. However, there is a large mass in the centre of the image; this is due to carbon contamination build up as the suspension still contains polyvinylpyrrolidone (PVP) and possibly residual ethylene glycol.

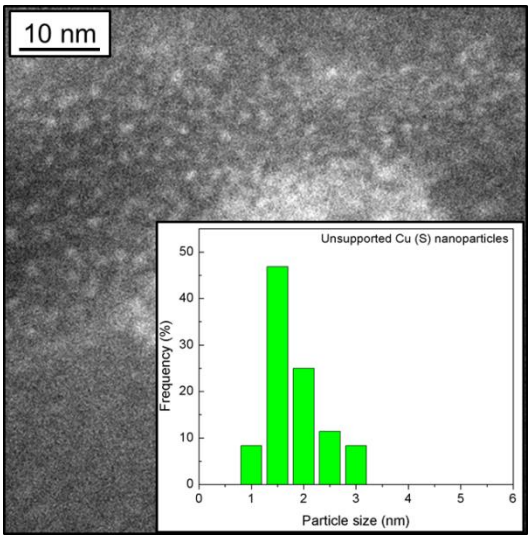


Figure 4 - A representative TEM image of unsupported Cu nanoparticles as well a size distribution histogram.

As it has been shown above that the particle size between precursors is very similar at high loading, it can be assumed that those measured for this unsupported image will be comparable with the size of unsupported particles generated from a sulphate precursor. Suspensions were added to the $\gamma$-$Al_2O_3$ support and calcined to remove the PVP capping agent.

### 5.2.3 Monometallic and Bimetallic catalyst characterization

#### 5.2.3.1 Monometallic and Bimetallic ICP-OES

To determine whether the reduction process was successful for Pt, Cu and PtCu catalysts, ICP-OES was completed, Equations 1 and 2 show how the metal ratios were calculated. The protocol followed for acid digestion was as described in Chapter 2. The results for this can be seen in Table 2. The deviation between Cu loading with each precursor is much lower for these materials than for those shown in Table 1. This could be due to a greater ratio of reduction media and metal salt or fewer losses when transferring and centrifuging the Cu solutions.

Table 2 - ICP-OES data for monometallic and bimetallic catalysts

| Catalyst | Pt / wt% | Cu / wt% | Pt / mol | Cu /mol | Total metal /mol | True ratio |
|---|---|---|---|---|---|---|
| $Cu_{100}$ (S) | - | 0.5 | - | $1.6 \times 10^{-6}$ | $1.6 \times 10^{-6}$ | 100 |
| $Pt_{16}Cu_{84}$ (S) | 0.4 | 0.7 | $2.8 \times 10^{-7}$ | $1.8 \times 10^{-6}$ | $2.1 \times 10^{-6}$ | 16:84 |
| $Pt_{43}Cu_{57}$ (S) | 0.6 | 0.2 | $5.8 \times 10^{-7}$ | $7.6 \times 10^{-7}$ | $1.3 \times 10^{-6}$ | 43:57 |
| $Pt_{100}$ | 1.2 | - | $1.3 \times 10^{-6}$ | - | $1.3 \times 10^{-6}$ | 100 |
| $Cu_{100}$ (N) | - | 0.7 | - | $1.6 \times 10^{-6}$ | $1.6 \times 10^{-6}$ | 100 |
| $Pt_{18}Cu_{82}$ (N) | 0.2 | 0.4 | $2.1 \times 10^{-7}$ | $9.8 \times 10^{-7}$ | $1.2 \times 10^{-6}$ | 18:82 |
| $Pt_{38}Cu_{62}$ (N) | 0.5 | 0.3 | $5.0 \times 10^{-7}$ | $8.2 \times 10^{-7}$ | $1.3 \times 10^{-6}$ | 38:62 |

$$\text{Metal mol} = \frac{\left(\text{Mass of catalyst} \times \frac{\text{Metal loading}}{100}\right)}{\text{RMM of metal}}$$ Equation 1 – Number of moles for each metal

$$\text{PtCu ratio} = \frac{\text{Metal mol}_1}{\text{Metal mol}_2} \times 100$$ Equation 2 – True PtCu ratio

The metal loadings for all bimetallic and monometallic samples show that, with the exception of $Cu_{100}$ (S), all catalysts have an overall metal loading of around 1%. The data also shows that in general the catalysts synthesized with the $CuSO_4$ precursor are in closer agreement with the nominal molar ratios. This could be that the precursor was able to reduce and form bimetallic particles more efficiently than $Cu(NO_3)_2$ as the overall platinum content appears to be slightly lower. However, the active metal content for each monometallic catalyst is around the same number of moles. This is also comparable with the bimetallic catalysts as the overall active metal (Pt and Cu) moles are concordant across all synthesized catalysts.

### 5.2.3.2 Monometallic and Bimetallic PtCu Powder X-ray Diffraction (Nitrate)

To determine the presence of metallic particles, the analysis was completed post calcination to remove surface bound residual capping agent (polyvinylpyrrolidone) at 300 $^{o}$C for 3 h.[1,13,14] The diffractogram stack is shown in Figure 5.

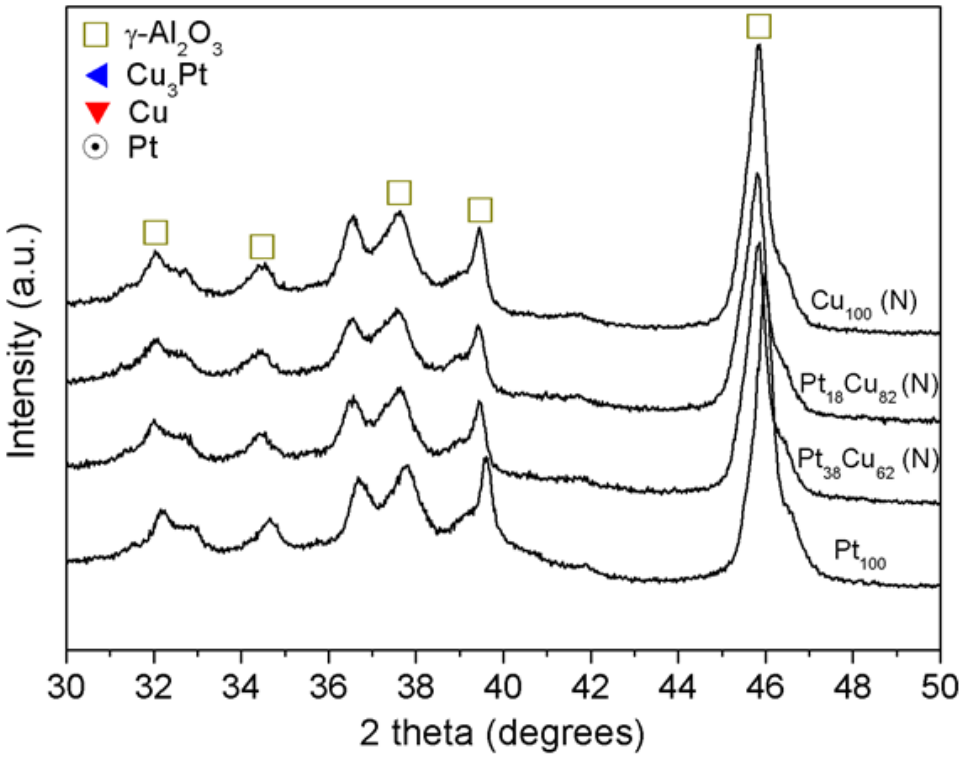


Figure 5 - PXRD diffractogram arrangement showing no metallic species after calcination.

As previously mentioned in Chapter 4, unlabeled reflections between the γ-$Al_2O_3$ peaks are support impurities in the form of δ-$Al_2O_3$. The diffractogram show the as calcined materials present no metallic Pt or Cu nor do they show oxidized species. It is also noteworthy that there has been no modification to the large alumina region between $32^o$ – $40^o$, meaning that there has been no deformation to the alumina support. To determine whether further thermal processing would sinter or form bimetallic particles, the catalysts were each reduced ex situ in a tube furnace under flowing hydrogen (~60 mL $min^{-1}$) at 300 $^oC$ for 3 h. This temperature was used as it is known that CuO will reduce in the temperature range 200 – 300 $^oC$.[19–21] The subsequent diffractogram array is shown in Figure 6.

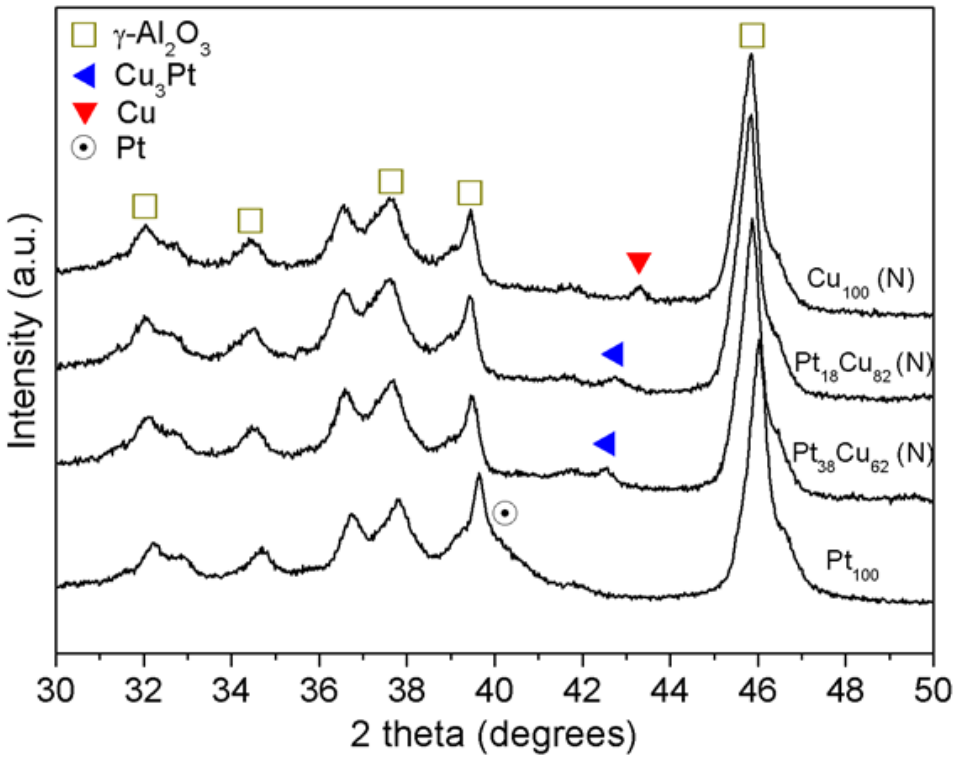


Figure 6 - PXRD diffractogram showing metallic species after reduction at 300 $^{o}$C in $H_2$.

Figure 6 shows that the reduction process has indeed generated a peak at 43$^{o}$, which is indicative of Cu(111), a metallic species. Due to an overlap with γ-$Al_2O_3$ there is no visible evidence of metallic Pt other than slight broadening in the peak at 39.5$^{o}$. The expected reflection position for Pt(111), as indicated by ICDD's PDF-2 2012 database, is marked on Figures 6 and 7. Interestingly, as Cu is reduced, a peak is formed between 42.5 and 43$^{o}$ depending on metal ratios, which is indexed as $Cu_3Pt$ and has a cubic structure with a space group of $Pm\bar{3}m$. This peak is clear evidence of a bimetallic species and as the peak is seen to move closer to the metal of higher concentration it shows that the reduction process is a necessary requirement to alloy the metals. A promising outcome is that the majority of the reduced metal has formed a bimetallic species as there is no Cu(111) reflection in the bimetallic samples. Once again, there has been no modification to the alumina in the form of spinel structures upon reduction of the Cu.

To further analyze the thermal stability of the bimetallic materials, the catalysts were reduced at 500 $^{o}$C for 3 h under flowing hydrogen, using the same flow rate as mentioned

above. As expected, Figure 7 shows that there is no oxidized Cu; there is, however, a slight increase in particle size for $Cu_{100}$ and the Cu rich alloy, $Pt_{18}Cu_{82}$. Particle sizes, as estimated by the Scherrer equation (**Chapter 2, Section 2.2.3**), are shown in Table 3. This diffractogram once again shows that there is no alteration to the alumina superstructure. This is a vital point as we can clearly state that any catalysis is due strictly to the bimetallic particles rather than alumina polymorphs.

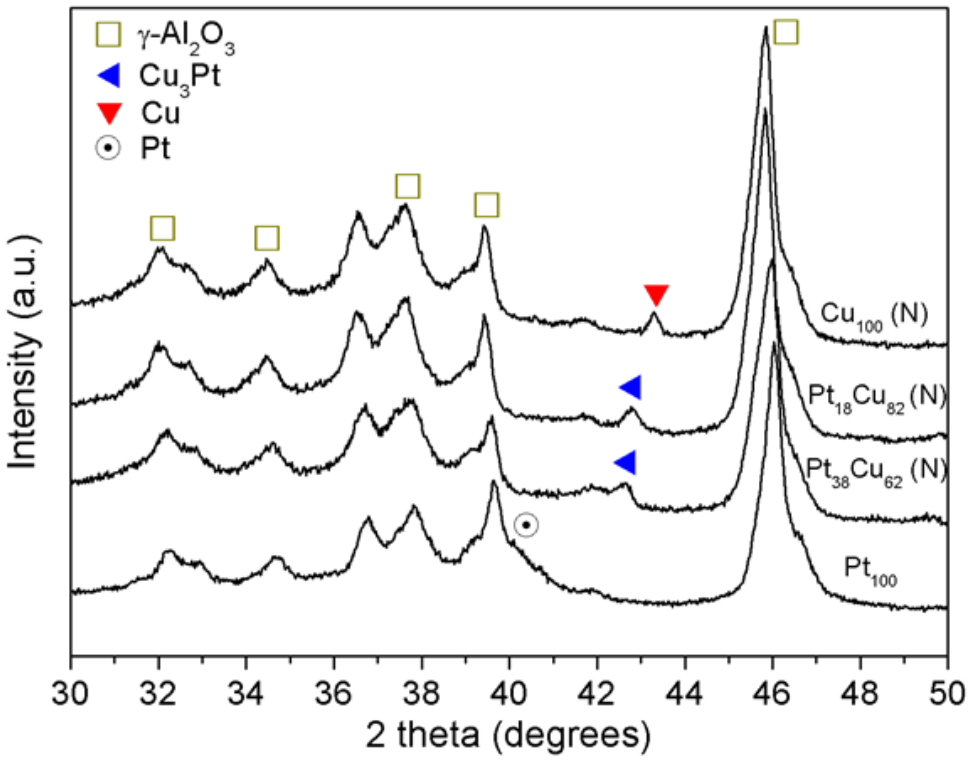


Figure 7 - PXRD diffractogram array showing metallic species after reduction at 500 $^{o}$C in $H_2$.

The literature reports that Pt nanoparticles begin to sinter above 700 $^{o}$C, which offers a reason why there is no substantial shouldering on the alumina peak around 40$^{o}$.[22,23] This could also explain why the $Pt_{38}Cu_{62}$ particles do not appear to increase in size (Table 3), inferring that the Pt content is stabilizing the Cu. Such stabilization has already been discussed for PtCu thin films which have varying ratios of metals.[24]

Table 3 - Particle size estimation by PXRD depending on thermal processing conditions

| Catalyst | Condition | Avg. crystallite size (nm) |
|---|---|---|
| $Pt_{100}$ | Calcination | - |
| | Reduction, 300 $^{o}$C | - |
| | Reduction, 500 $^{o}$C | - |
| $Pt_{38}Cu_{62}$ (N) | Calcination | - |
| | Reduction, 300 $^{o}$C | 8.4 |
| | Reduction, 500 $^{o}$C | 9.1 |
| $Pt_{18}Cu_{82}$ (N) | Calcination | - |
| | Reduction, 300 $^{o}$C | 7.9 |
| | Reduction, 500 $^{o}$C | 11.7 |
| $Cu_{100}$ (N) | Calcination | - |
| | Reduction, 300 $^{o}$C | 5.8 |
| | Reduction, 500 $^{o}$C | 6.9 |

#### 5.2.3.3 Monometallic and Bimetallic PtCu Powder X-ray Diffraction (Sulphate)

The bimetallic catalysts synthesized using the $CuSO_4$ precursor were analyzed via PXRD to determine the particle size, as well as the presence of CuS (Figure 8 and Table 4). The diffractograms show that, although at a lower intensity, the bimetallic particles are still measurable. By manually integrating the peak and obtaining the FWHM, particle size can be calculated, this being said due to a significant noise, the (S) data points were averaged to increase the signal to noise ratio. The particle sizes were found to be slightly smaller than the (N) materials, with the exception of the $Cu_{100}$ which was found to be larger. There is still a low signal for CuS at 32$^{o}$, suggesting that the precursor is still not fully reduced when using a lower metal content. The presence of this also showed a decrease in $Cu_3Pt$ which was easily discernable for the (N) family. For the case of $Pt_{43}Cu_{62}$, the $Cu_3Pt$ peak has shifted further towards the Pt(111) area. The catalyst reduction process, in the presence of flowing hydrogen (**Chapter 2, Section 2.1.2**) once the nanoparticles are supported, is not sufficient to reduce CuS to $Cu^0$, which has been thoroughly studied in the literature.[25,26] The residual sulphur present is a clear sign that $CuSO_4$ is not an appropriate precursor to be used to make pure bimetallic nanoparticles.

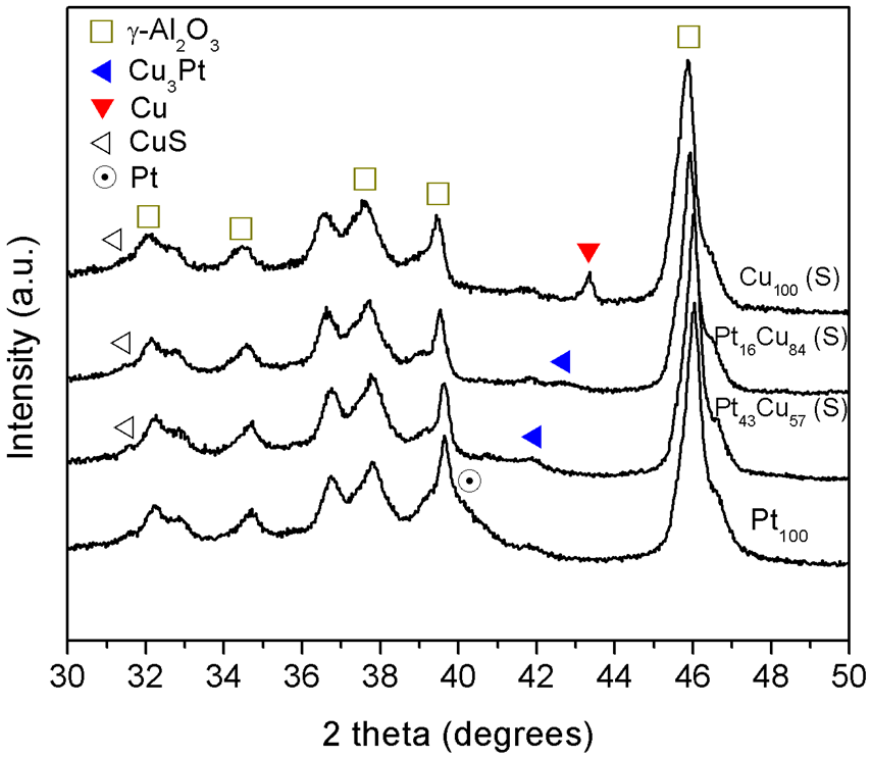


Figure 8 - PXRD diffractogram showing the bimetallic and monometallic catalysts synthesized with the sulphur containing precursor after reduction at 300 $^{o}$C in $H_2$

Table 4 - Particle size estimation by PXRD for catalysts synthesized using $CuSO_4$ and reduced at 300 $^{o}$C

| Catalyst | Avg. crystallite size (nm) |
|---|---|
| $Pt_{100}$ | - |
| $Pt_{43}Cu_{57}$ (S) | 6.7 |
| $Pt_{16}Cu_{84}$ (S) | 5.6 |
| $Cu_{100}$ (S) | 7.3 |

### 5.2.3.4 Monometallic Pt and Cu Transmission Electron Microscopy

As previously seen in Chapter 4, very monodisperse platinum nanoparticles can be synthesized and clearly imaged. Figure 9 demonstrates that increasing the synthesis temperature to 140 $^{o}$C has had no effect on the size or the shape of the platinum nanoparticles. Table 5 shows the $Pt_{100}$ particle size to be 4.4 ± 0.8 nm. This value is very close to those previously synthesized and measured on $\gamma$-$Al_2O_3$ at 4.0 ± 0.5 nm.[1] These values are comparable even though they are measured on two different instruments with different calibrations.

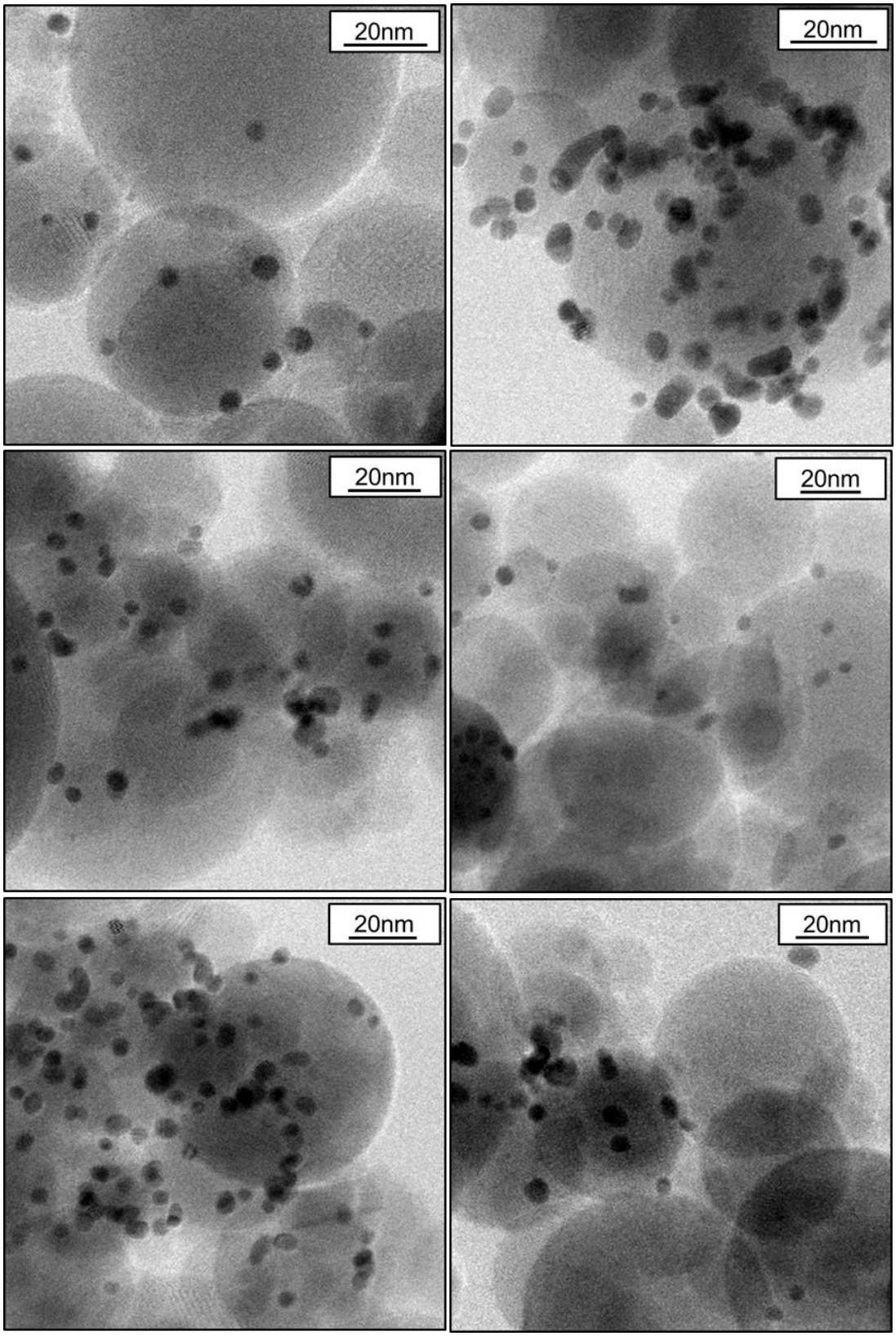


Figure 9 - Transmission electron micrographs of $Pt_{100}/\gamma\text{-}Al_2O_3$ at various areas on the grid and at different magnifications.

Figure 9 shows very clear images of Pt nanoparticles. This clarity is due to the large electron density of platinum. The ability to differentiate the particles from the alumina support is known as Z contrast. However, metals such as copper have poorer electron density and will not appear as clearly defined as metals such as Pt, Au, Ir and Pd.[1,27–29] This led to difficulties in distinguishing Cu nanoparticles from $\gamma$-$Al_2O_3$ crystallites, as the particles synthesized were also spherical in nature. Classification of Cu entities was achieved by observing deformities in the spherical structure, comparing bright and dark field images, as well as lattice spacing measurements, where possible. All TEM images shown are of Cu and $Pt_xCu_x$ materials where $Cu(NO_3)_2$ was the precursor used. As the XRD and XPS clearly show a sulphur presence in the high copper loaded materials, as well as low alloy peak ($Cu_3Pt$) intensity for bimetallic materials (Figure 8), these catalysts were not imaged.

Figure 10 shows a bright field, high resolution image of two supported Cu nanoparticles. Upon focusing, the lattice spacing is clearly visible and can be measured. By taking an average of the measured distances in the plot profile, we can see that the interplanar distance is 0.22 nm. This value is a perfect match to the Cu(111) face, reported in the literature.[13,14,30–32] Figures 11 and 12 show two different areas on the TEM grid presenting singular Cu nanoparticles with measured lattice distances.

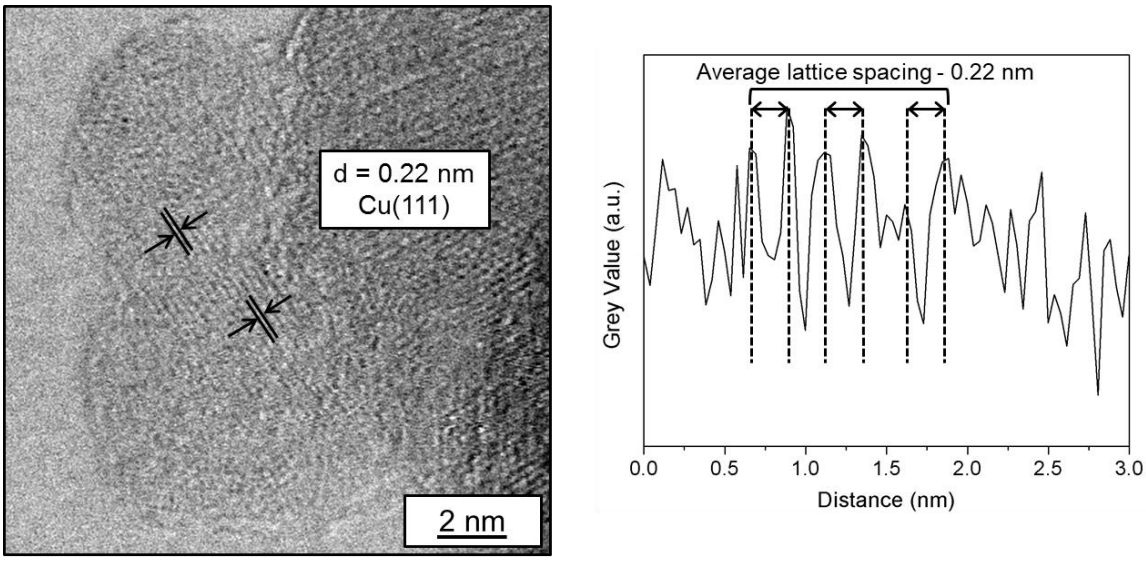


Figure 10 - Transmission electron micrograph of $Cu_{100}/\gamma\text{-}Al_2O_3$, showing two Cu particles and corresponding lattice spacing measurements.

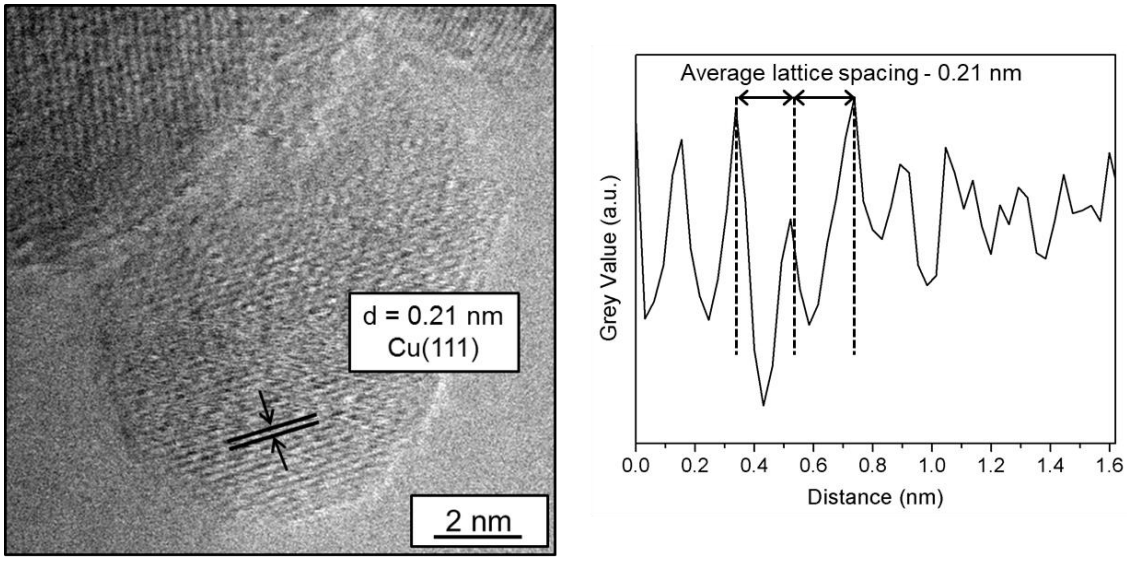


Figure 11 - Transmission electron micrograph of $Cu_{100}/\gamma\text{-}Al_2O_3$, showing an individual particle and corresponding lattice spacing measurements.

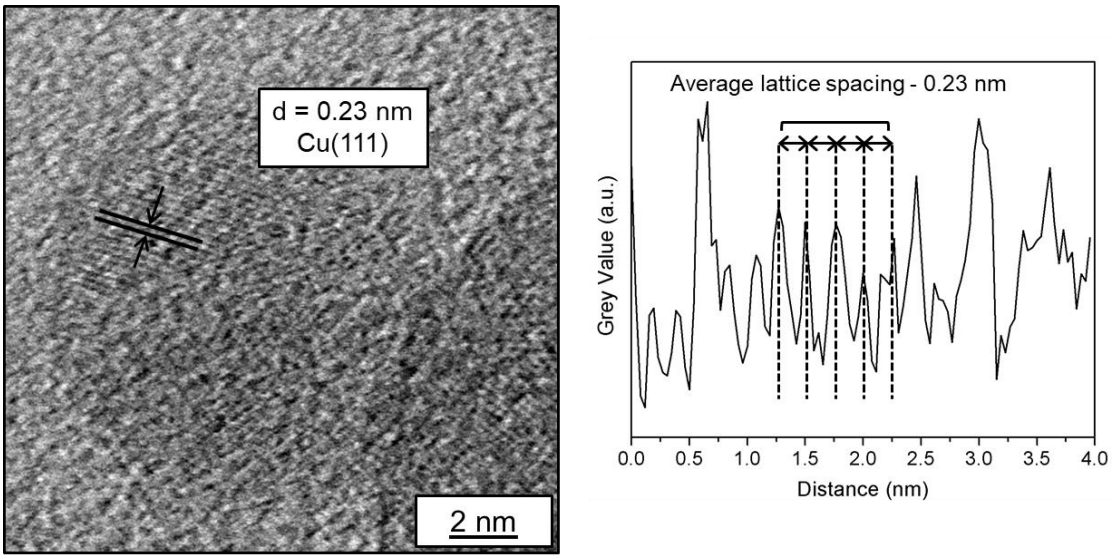


Figure 12 - Transmission electron micrograph of $Cu_{100}/\gamma\text{-}Al_2O_3$, showing a single Cu particle and corresponding lattice spacing measurements.

Figures 10-12 show individual Cu particles discernable by resolving the lattice spacing of the Cu(111) face. However, shape effects, as well as subtle differences in the Z contrast have also proved to be an effective way to measure Cu nanoparticle size. This is presented in Figure 13 where Cu particles are seen on the edge of an alumina particle. By monitoring the dark field image we can differentiate between the nanoparticle and the oxide support.

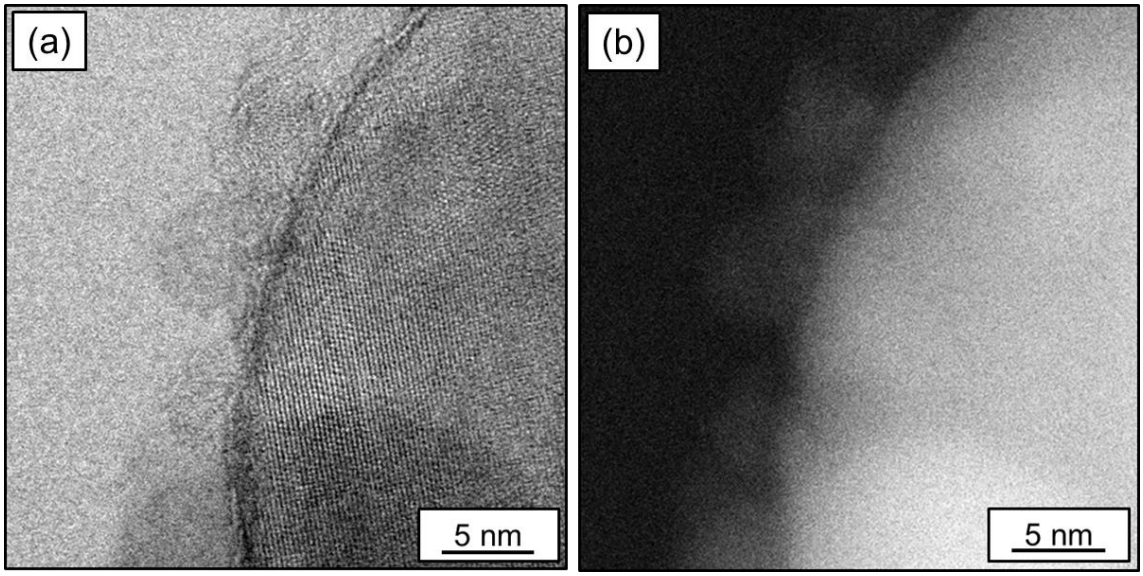


Figure 13 - Bright field (a) and Dark field (b) micrographs showing a series of Cu (N) nanoparticles attached to the $\gamma$-$Al_2O_3$ support.

#### 5.2.3.5 Bimetallic $Pt_{38}Cu_{62}$ (N) Transmission Electron Microscopy

Determination of bimetallic particles proved to be far easier due to the Pt content (Figures 14 and 15). The added electron density provided clear contrast to differentiate between Cu and $\gamma$-$Al_2O_3$. Nanoparticles were imaged with STEM, specifically high-angle annular dark field imaging (HAADF). These images were recorded along with EDX line scans and atomic mapping. The measurements show the true ratio of the metals in each particle. This is represented by dots of yellow for Cu and purple for Pt (Figures 16 and 17). By not scanning sulphur containing catalysts, EDX line scans are more viable as the residual S content would cause issues with both Cu and Pt determination.

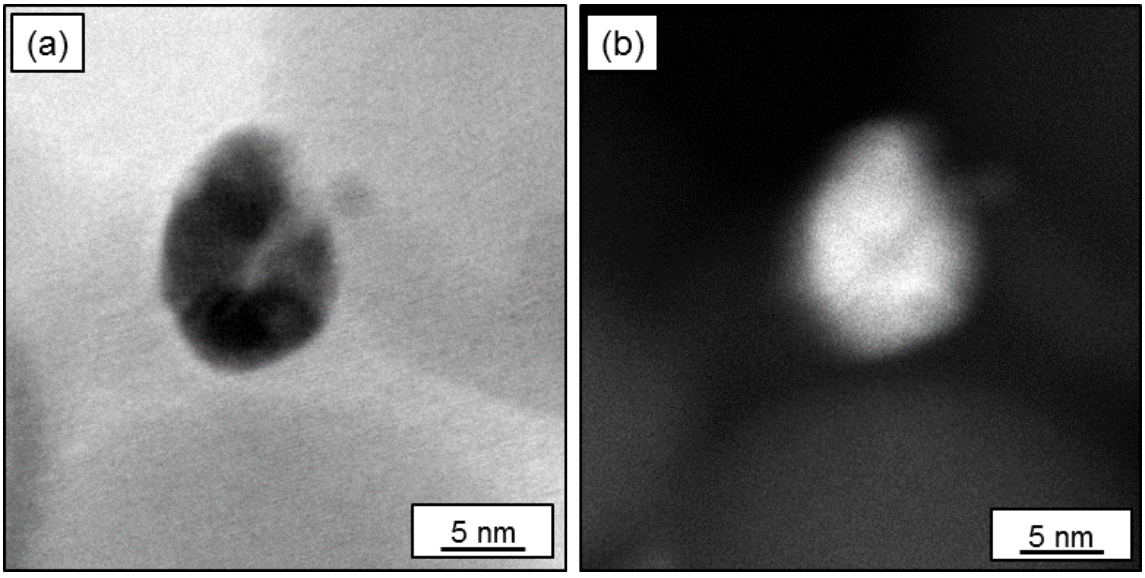


Figure 14 - Bright field (a) and Dark field (b) imagery of an individual $Pt_{38}Cu_{62}$ (N) bimetallic nanoparticle.

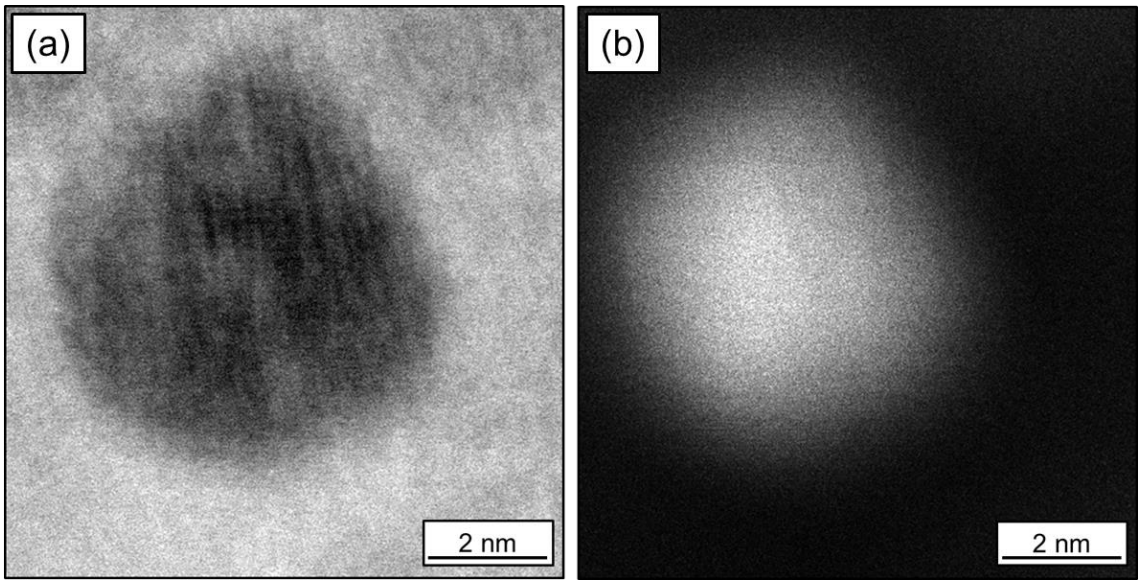


Figure 15 - Bright field (a) and Dark field (b) imagery of a second $Pt_{38}Cu_{62}$ (N) bimetallic nanoparticle.

As can be seen in both Figures 14 and 15, the shape of the bimetallic particles is spherical in nature with areas of varying contrast on the surface.

Energy Dispersive X-ray Spectroscopy (EDX) was completed for particles to show the atomic ratios of Cu and Pt. Figure 16 demonstrates the power of this technique, as a single particle was captured and scanned. Over the course of 2 minutes a full scan is completed line by line in repetition, similar to a raster scan completed for STM images (Chapter 3). With each pass, signals are refined and the intensity is built up showing elements such as Pt, Cu, Al, and Ni. Signals for Si and O were also detected but removed due to saturation of the analyzer. Silicon was not present in the sample so the signal was from the analyzer itself. Similarly, the Ni signal is due to the grid used for the microscopy. The coloured markings show a random dispersion of Cu and Pt with no areas of high concentration of a specific metal. The surface atomic ratio of Cu and Pt for this particle was found to be 47.9% and 52.1% respectively.

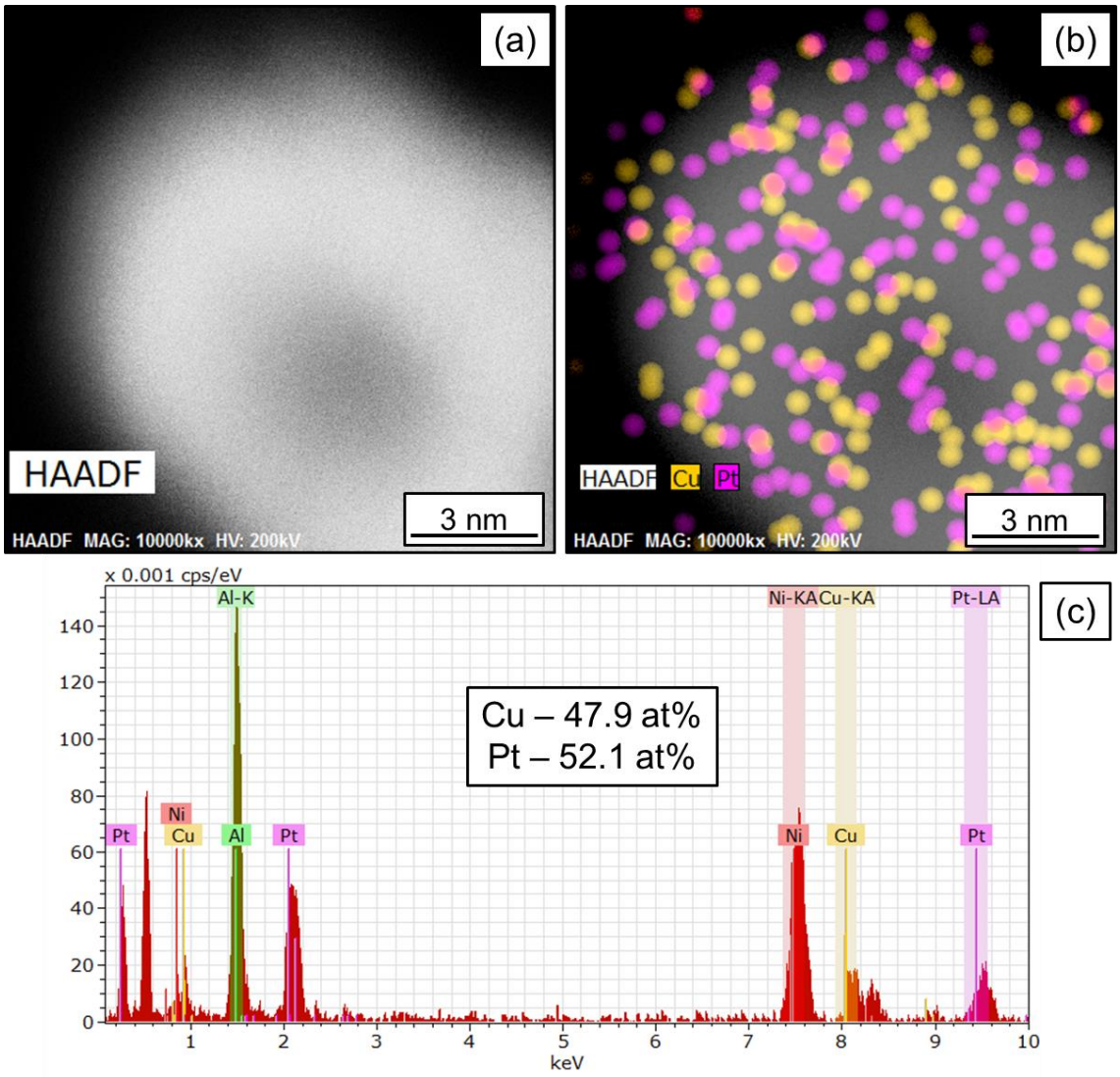


Figure 16 – A single bimetallic $Pt_{38}Cu_{62}$ (N) particle with EDX line scan and atomic dispersion.

Figure 17 shows another bimetallic particle which has a greater metal content compared with that seen in Figure 16. This is represented by both the additional markers in the HAADF image as well as the EDX image, which shows a greater intensity of both Pt and Cu. The resulting surface atomic ratios outputted were 55.2% and 44.8% for Cu and Pt respectively. Other regions scanned showed similar atomic ratios, which were also accompanied by some particles with a slightly greater Cu content than Pt. The maximum surface Cu content for a single bimetallic particle seen was ~70%. There were no particles observed with a surface Pt majority.

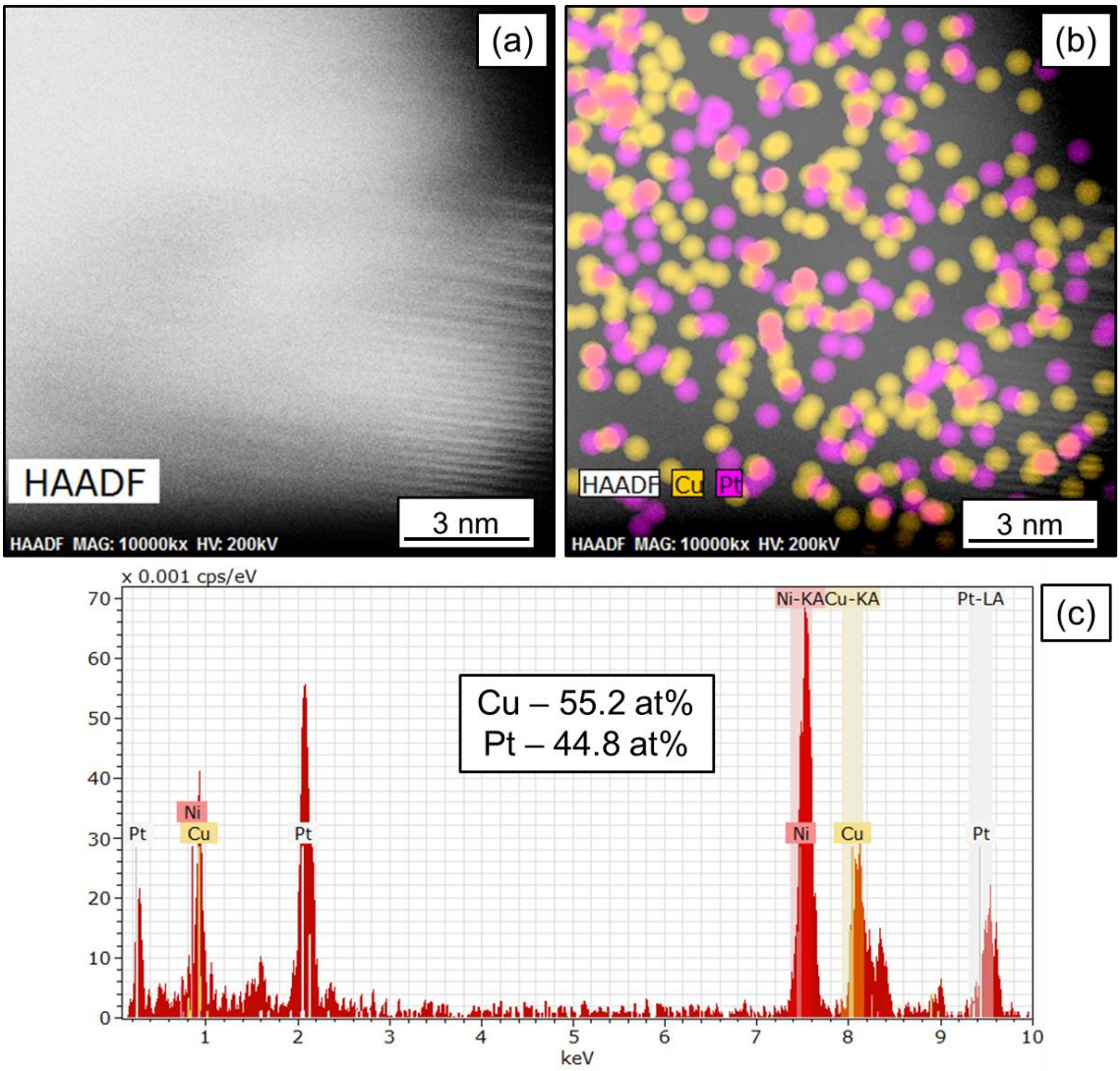


Figure 17 – (a) A dark field image of a single bimetallic $Pt_{38}Cu_{62}$ (N) particle with (b) atomic dispersion and (c) EDX line scan.

### 5.2.3.6 Bimetallic $Pt_{18}Cu_{82}$ (N) Transmission Electron Microscopy

Micrographs of the $Pt_{18}Cu_{82}$ catalyst are shown in Figures 18 and 19. Interestingly, as the Pt content is reduced further there is a distinct difference in Z contrast of the particle. Previously, Figures 14 and 15 showed bimetallic particles with very distinct contrast due to the alloyed platinum. However, the dark field image in Figure 18 shows a particle with a much lower contrast and it is very clear that the particles have a majority of surface Cu, which is in agreement with Figures 10-12. This is reinforced by the evident lattice spacing when focused with the plot profile in Figure 18 showing that the bimetallic particle has an

interplanar spacing of 0.21nm. This spacing was shown in Figures 9-12 which represent the Cu(111) face.

Figure 19 shows a pair of bimetallic particles with complementary bright and dark field images. Once again the reduced Pt content for this sample has shown a resolved particle with lattice spacing of around 0.22 nm, which is in agreement with the Cu(111) face. However, as reported by Kang and Cao,[33,34] the lattice spacing for a $Cu_3Pt$ alloy is between 0.218 and 0.224 nm. This means that as the spacing is slightly larger than the one measured for the monometallic Cu nanoparticles, it could be alloyed with a Cu majority. There are also areas on the isolated nanoparticle with a subtle change in contrast. The increase in Z contrast for these areas is indicative of a heavier element. Potentially, for these particles, there are areas of atomically dispersed platinum, either present as individual entities or as small clusters. These areas are highlighted by a yellow circle.

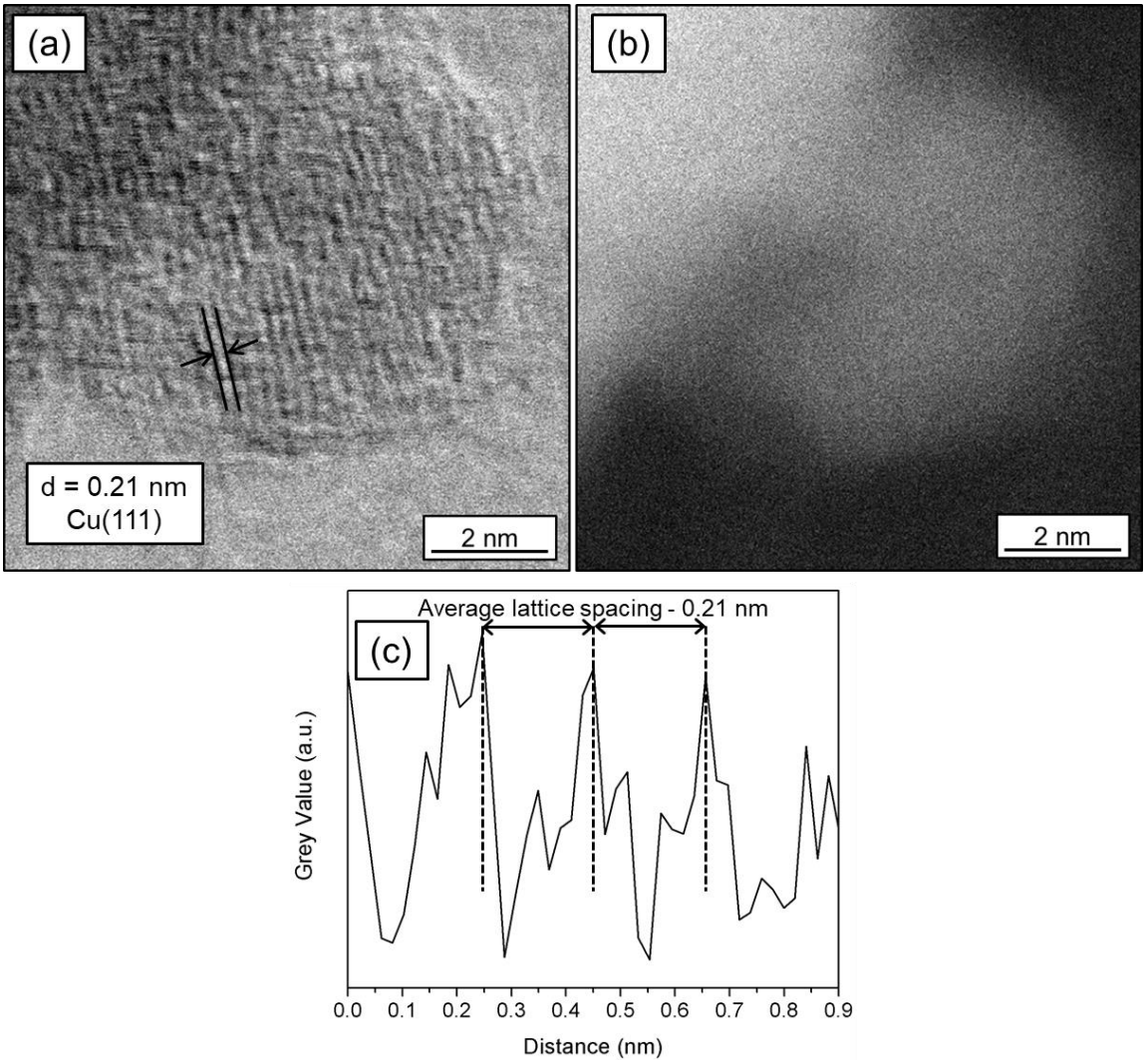


Figure 18 – TEM image of $Pt_{18}Cu_{82}$ (N) particle with surface profile, where (a) is a bright field image of a single particle, (b) is the corresponding dark field image and (c) is the surface plot profile.

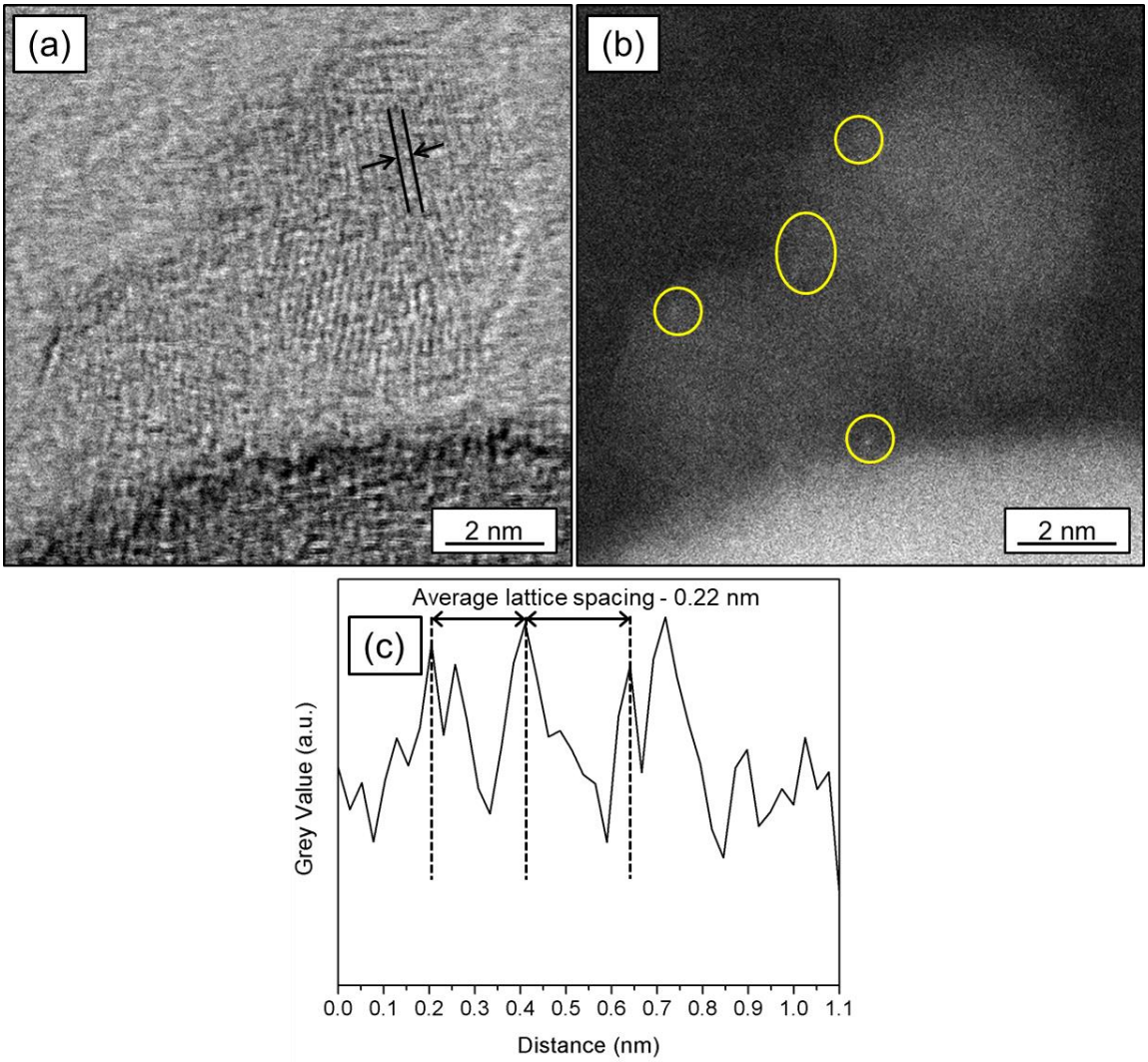


Figure 19 – A Pair of bimetallic $Pt_{18}Cu_{82}$ particles with surface profile and yellow circles highlighting potential Pt rich areas where, (a) is a bright field image, (b) is a dark field and (c) is the surface profile.

Particle sizes were measured by TEM and averaged for all materials; this is shown in Table 5. Particle sizes are in very close proximity to those estimated from the PXRD peak integration. In both cases, it was found that the $Pt_{38}Cu_{62}$ bimetallic had a slightly larger particle size in general, possibly due to the marginally higher overall active metal content.

Table 5 - Particle size as determined by TEM (catalysts were reduced ex situ at 300 $^{o}$C).

| Catalyst | Particle size (nm)[a] | Avg. Crystallite size (nm)[b] |
|---|---|---|
| $Pt_{100}$ | 4.4 ± 0.8 | - |
| $Pt_{38}Cu_{62}$ (N) | 7.4 ± 3.7 | 8.4 |
| $Pt_{18}Cu_{82}$ (N) | 6.7 ± 2.3 | 7.9 |
| $Cu_{100}$ (N) | 6.4 ± 1.6 | 5.8 |

a – Particle size as measured by TEM
b – Avg. Crystallite size as estimated by PXRD

### 5.2.3.7 CO Chemisorption and Surface area measurements

Surface Pt dispersion was determined for both the monometallic Pt catalyst and the bimetallic materials. CO binds to Pt in an a-top fashion **(Chapter 2, Section 2.2.7 and references as well as Figure 10)** and due to repulsive forces between the CO and Pt, a full monolayer coverage is not possible. In fact the stoichiometry for Pt:CO was calculated to be 0.68 **(Chapter 2, Section 2.2.6)**. The true coverage possible was experimentally derived and calculated to be around 0.7 ML. Therefore, the stoichiometric value is considered for calculating both crystallite size and Pt dispersion when using this technique.[35,36] Due to the in situ reduction process before CO titrations at 300 $^{o}$C, it can be assume that the oxidation state of the Pt is $Pt^{0}$. The presence of Cu appeared to make the uptake of CO onto the Pt sites very limited and therefore Pt dispersions were obtained by monitoring subtle differences in CO uptake when at ~293 K. Surface area measurements obtained through nitrogen physisorption as well as CO titration data are shown in Table 6. Crystallite sizes were also measured using this method of analysis and these values were found to be within the error of the measured particles shown in the TEM images (**Sections 5.2.3.3 and 5.2.3.4**). Catalyst surface area measurements appear to show that the relatively low $\gamma$-$Al_2O_3$ surface seems to slightly decrease as the Cu loading increases, whereas the $Pt_{100}$ catalyst exhibits the highest surface area at 38.8 $m^2$ $g^{-1}$. This is marginally higher than the surface area measured for the $Pt/\gamma$-$Al_2O_3$ synthesized and used in Chapter 4 due to a greater metal loading (34 $m^2$ $g^{-1}$, 1.9 wt%).

Table 6 – Catalyst surface area and surface Pt dispersion as well as crystallite size obtained through CO titration.

| **Catalyst** | Surface area ($m^2 g^{-1}$)[a] | Pt dispersion (%) | Particle size (nm)[b] |
|---|---|---|---|
| $Pt_{100}$ | 38.8 | 13.4 | 3.0 |
| $Pt_{38}Cu_{62}$ (N) | 31.4 | 20.1 | 8.4 |
| $Pt_{18}Cu_{82}$ (N) | 28.3 | 29.4 | 5.8 |
| $Cu_{100}$ (N) | 32.5 | - | - |
| $Pt_{43}Cu_{57}$ (S) | 32.9 | 20.6 | 7.1 |
| $Pt_{16}Cu_{84}$ (S) | 30.1 | 27.0 | 6.3 |
| $Cu_{100}$ (S) | 33.3 | - | - |

a - BET surface area from $N_2$ porosimetry
b - As obtained by CO Chemisorption

Table 6 also includes the various Pt dispersions for each of the bimetallic catalysts from both families, which show an inversely proportional trend. As the Pt content is reduced, the surface Pt species become more dispersed. By plotting the dispersions against the true metal loading shows that the trend is not completely linear and forms a curve (Figure 20). This is possibly due to the alloying effect of the Cu, which has been found to restrict CO adsorption when alloyed with Pd.[37] Combining this factor with a larger particle size compared to pure Pt had a slightly adverse effect on the surface dispersion measurements. Specifically, the $Pt_{38}Cu_{62}$ samples appeared to show a lower dispersion than expected. The Pt has been clearly shown not to be concentrated in specific areas but to have a random arrangement throughout the particle (EDX, Figures 16 and 17). This is the reason why the values for the bimetallic particles are lower than expected and do not fit a linear relationship with respect to Pt loading.

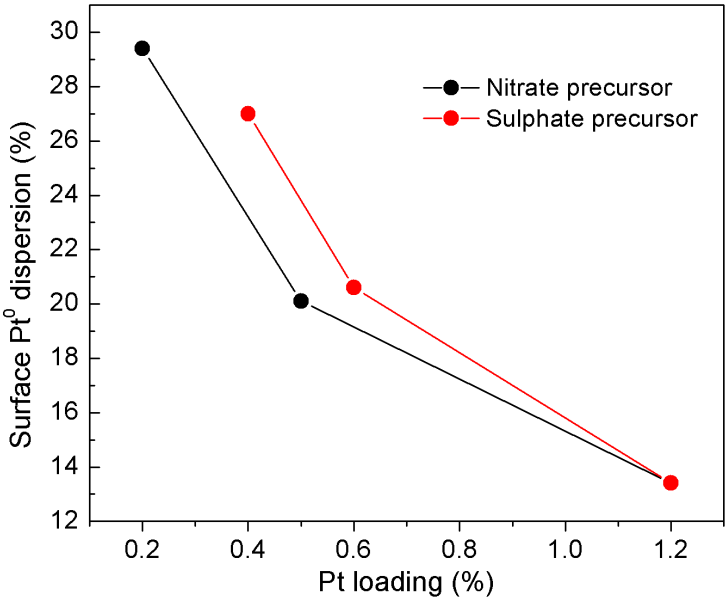


Figure 20 – Surface $Pt^0$ dispersions for all bimetallic catalysts against true metal loading, as determined by ICP-OES.

#### 5.2.3.8 X-ray Photoelectron Spectroscopy

XPS was completed for both monometallic and bimetallic catalysts. Due to the clear overlap with the Al 2p region, there was very limited/no signal for the Pt 4f region. However, as shown in Figures 21b and Figure 21c, the Pt 4d peaks are useable, although they are shown to build upon a C 1s satellite. Due to very poor signal to noise ratios, the $Pt4d_{5/2}$ appears to be shifted for $Pt_{38}Cu_{62}$ (Figure 21b). Possibly, a true shift to higher binding energy could also be attributed to effects from building on the satellite peak. However, the peak fitting for Cu was simpler as there was no peak overlap for the Cu 2p region. This is presented in Figure 21a which shows that the $Cu_{100}$ has peak positions at 932 eV (Cu $2p_{3/2}$) and 952 eV (Cu $2p_{1/2}$). These values are very close to the binding energies for metallic copper reported previously.[38–40] Although it is suggested that Cu(I) oxide has very similar binding energy to $Cu^0$, this oxidation state has only been seen in XRD analysis when utilizing much higher Cu loadings (Figure 1). The gradual addition of Pt appears to have caused a substantial shift in binding energy for the $Pt_{38}Cu_{62}$ catalyst. The Cu 2p signal has shifted by 0.5 eV to a lower binding energy and this shift is indicative of an alloy formation with Pt.[33,41,42] Nevertheless, the movement to a lower binding energy for Cu 2p is a slightly larger shift than previously reported for PtCu alloy nanotubes.[41] Figure 21d shows a scan of the $Pt_{100}$ catalyst in the Pt 4d region. This data was acquired with the

monochromator installed, which means that the counts for this scan are lower than the bimetallic catalysts. However, the signal to noise ratios are improved, this clearly shows the position of the Pt 4d peaks as well as the correct positioning and doublet intensity for the Pt $4d_{5/2}$ and Pt $4d_{3/2}$.

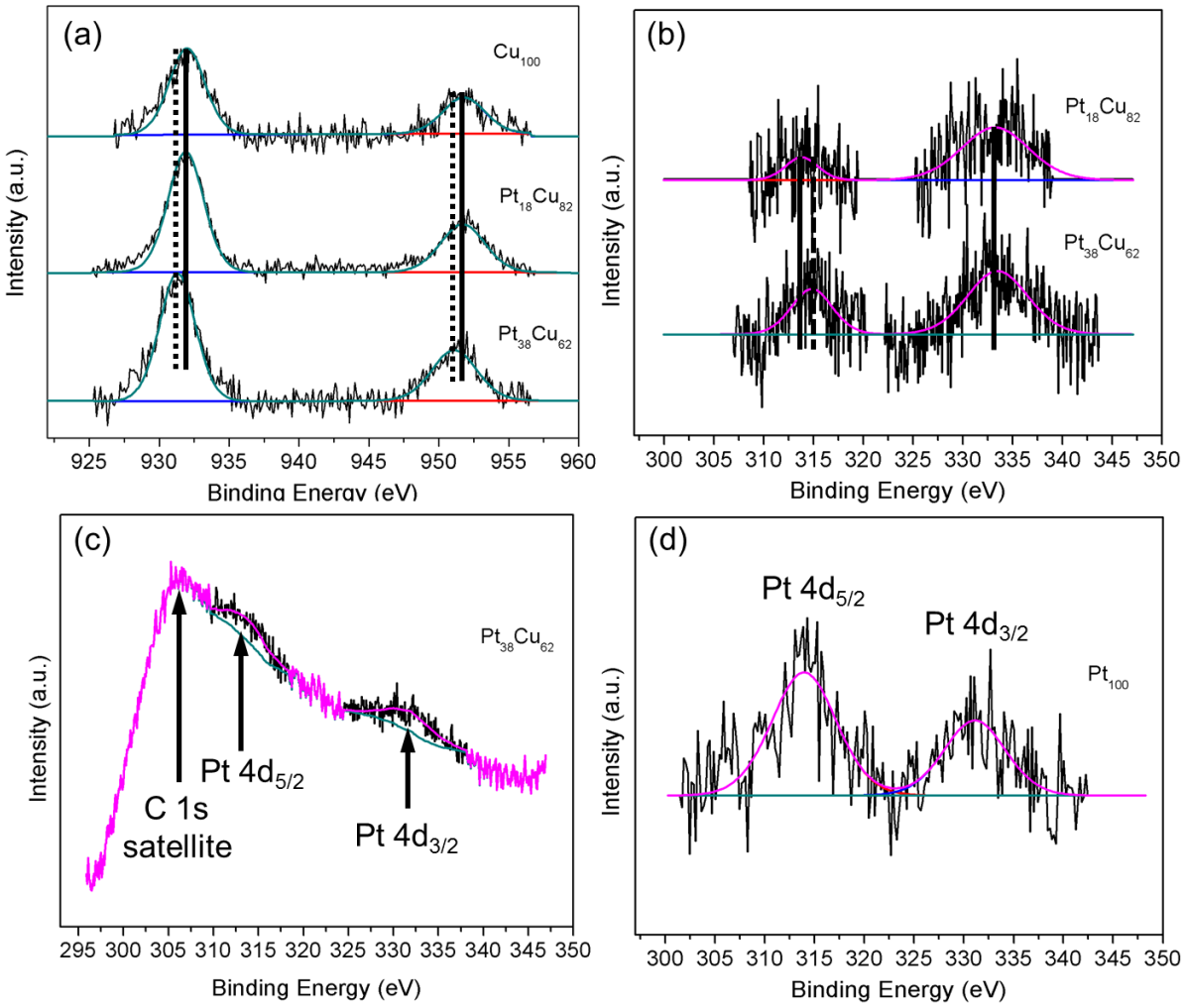


Figure 21 - XPS Peak fitting of (a) Cu 2p doublet at 932 eV (Cu $2p_{3/2}$) and 952 eV (Cu $2p_{1/2}$) in both monometallic Cu and bimetallic (N) catalysts (solid line), a shift in binding energy for $Pt_{38}Cu_{62}$ is shown by a dotted line. (b) Pt 4d peaks for the bimetallic catalysts proving that Pt resides on the surface of the particles. (c) the origin of the Pd 4d signal building upon a C 1s satellite. Finally (d) is a scan of the Pt 4d region on the monometallic $Pt_{100}$ as a reference.

For clarity, the acquisition and processing of the Cu LMM region has been completed using Mg Kα radiation, opposed to Al Kα, which has been used for the fitting of the Cu 2p regions seen above. Chemical shifts are more observable when analyzing the $L_3VV$ peak of the Cu LMM region. For example, metallic Cu has a $L_3VV$ binding energy of 335.0 eV, whereas the binding energies for CuO and $Cu_2O$ are 335.9 eV and 336.8 eV respectively.[43] These shifts are much broader than those observed for the Cu 2p and therefore will definitively confirm the presence of surface copper oxide. Figure 22 shows a series of overlaid spectra of the Cu LMM region for the two bimetallic catalysts and the pure Cu monometallic species after reduction. The plot clearly shows that the $L_3VV$ peak is situated at 335.03 eV, which means that for the three catalysts after reduction at 300 $^oC$ in flowing hydrogen, there is no surface oxide present, nor any variation of Cu oxidation state for the bimetallic catalysts. The Cu auger region for metallic Cu has two distinctive features. Loss of these peaks or broadening of the $L_3VV$ means that the Cu has begun to form surface oxide or is in fact bulk copper oxide (both oxidation states).[43,44]

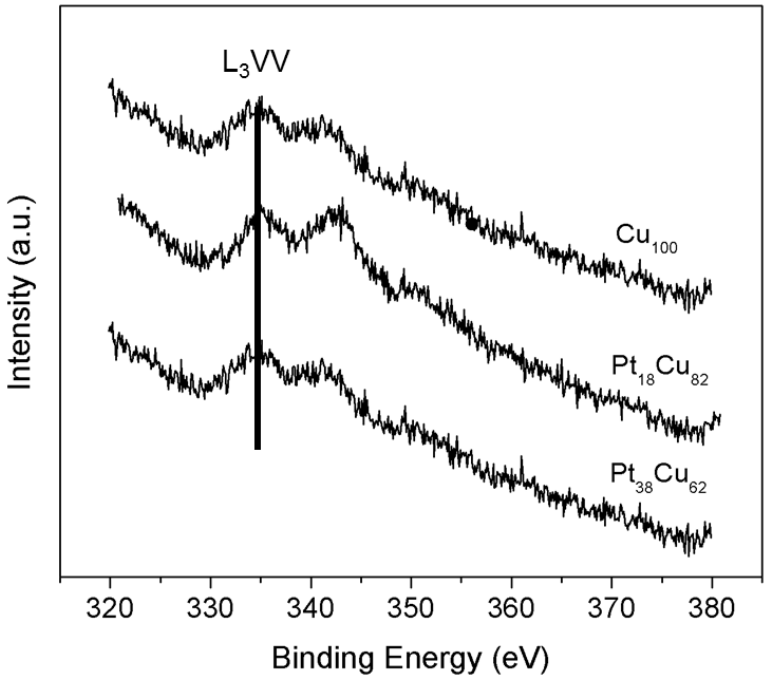


Figure 22 – Stacked XP spectra of the Cu LMM region, demonstrating the absence of copper oxide post reduction, the $L_3VV$ peak alignment is shown by a solid line.

By fitting the Cu 2p and the visible Pt 4d regions, the surface concentration can be measured for each metal of the bimetallic catalysts. These values are shown in Table 7 and the percentages can be compared with the percentage ratios observed in EDX analysis. These values are comparable with ICP data for $Pt_{38}Cu_{62}$ (N) catalyst which has shown a surface Pt concentration 36.7% and 63.3% for Cu. Also, the surface concentrations of 21% (Pt) and 79% (Cu) are close to the ICP values shown for $Pt_{18}Cu_{82}$. By isolating a single bimetallic nanoparticle and completing Energy Dispersive Spectroscopy, we can prove that the values shown in Figure 15 are nearly identical to the nominal values. As this technique is not surface sensitive, more of the Pt is detected that resides in the bulk of the nanoparticles, due to Pt possessing a higher surface energy.[45,46]

Table 7 - Surface Pt and Cu metal concentration from XPS.

| **Catalyst** | Surface Pt loading/wt% | Surface Cu loading/wt% |
|---|---|---|
| $Pt_{100}$ | 100 | - |
| $Pt_{38}Cu_{62}$ (N) | 36.7 | 63.3 |
| $Pt_{18}Cu_{82}$ (N) | 21.0 | 79.0 |
| $Cu_{100}$ (N) | - | 100 |

Due to the low loadings used for these materials, the monochromator on the XPS instrument was removed. Doing so radically increased the counts registered and metal signals were detectable. However, these measurements were not carried out for catalysts generated with the sulphur containing precursor due to an instrument malfunction at the time. As the method used was the same for each copper salt, it can be assumed that the surface metal ratios are of similar percentages to the catalysts shown above. Albeit the PXRD showed a small reflection suggesting CuS formation (Figure 8), which means that the surface may only contain residual sulphur or small areas of bulk sulphate (Figure 2).

### 5.2.4 Single Atom Alloy Characterization

Single Atom Alloys were synthesized using the $Cu(NO_3)_2$ precursor and characterized by nitrogen physisorption, ICP-OES, HRTEM, PXRD and XPS. The reduced surface atoms from the host Cu (N) nanoparticles were galvanically replaced in dilute acid solution with

chloroplatinic acid. Platinum dispersion measured via CO titration was not completed due to the low Pt content in the materials and therefore, a large amount of sample would be required for a single measurement, or possibly, it would be out of the detection limit for the instrument. It was therefore assumed that the Pt dispersion was 100% as the entirety of the Pt resides on the catalyst surface.[47–49]

#### 5.2.4.1 SAA composition and surface area analysis

Single Atom Alloy catalysts were digested and handled in the same way as the bimetallic and monometallic catalysts mentioned previously. Diluted Pt metal loadings and Cu host content is shown along with the true atomic ratios in Table 8. The nominal Pt loadings for the atomically dispersed catalysts were 0.05 wt% and 0.005 wt%. The Cu host nanoparticles were created in the same way as those described in Chapter 2 with the intended Cu loading identical to the monometallic Cu catalyst for direct comparison.

Table 8 - SAA active metal composition as determined by ICP-OES.

| Catalyst | Pt / wt% | Cu / wt% | Pt / mol | Cu /mol | Atomic ratio (Pt:Cu) | Surface area ($m^2 g^{-1}$) |
|---|---|---|---|---|---|---|
| $Pt_1Cu_{20}$ | 0.09 | 0.5 | $8.8 \times 10^{-8}$ | $1.5 \times 10^{-6}$ | 1:20 | 33.4 |
| $Pt_{0.5}Cu_{250}$ | 0.004 | 0.6 | $3.9 \times 10^{-9}$ | $1.8 \times 10^{-6}$ | 0.5:250 | 35.2 |

The metal loadings determined by ICP-OES show that the initial SAA catalyst, $Pt_1Cu_{20}$, appears to contain a greater Pt content than expected and that the Cu loading is slightly lower, although very close relative to the $Cu_{100}$ molar loading of $1.6 \times 10^{-6}$ mol. This ratio of metals provides the catalyst with an atomic ratio of 1:20, which means that for every Pt atom present, there should be approximately 20 Cu atoms. The second SAA synthesized has around 22.5 times less Pt present than the $Pt_1Cu_{20}$ catalyst mentioned previously. This, in relation to a slightly higher Cu loading (possibly due to less Cu/Pt exchange), provides an atomic ratio of 0.5:250, meaning that for every Pt atom there should be 500 Cu atoms. This level of Pt dilution should lead to Cu nanoparticles with true isolated Pt entities instead of surface aggregations or mixed alloy particles.

Surface area measurements are not greatly dissimilar to the surface area of the monometallic Cu catalyst (32.5 $m^2 g^{-1}$), albeit marginally higher. The most dilute disperse catalyst ($Pt_{0.5}Cu_{250}$) exhibits the largest surface area of 35.2 $m^2 g^{-1}$. This increase could indicate that the galvanic replacement process had a mild effect on the $\gamma$-$Al_2O_3$ superstructure.

### 5.2.4.2 SAA textural analysis

X-ray diffraction was completed for the Pt atomically dispersed materials after the galvanic replacement process. These materials have previously seen thermal processing in the form of calcination to remove the nanoparticle capping agent and reduction to generate an oxide free material **(Chapter 2, Section 2.1.3)**. Both thermal treatment regimes are the same magnitude as the bimetallic and monometallic nanoparticles. However, this range of samples has had an additional parameter introduced; the acidified solution under reflux (100 $^oC$). The diffractogram stack in Figure 23 shows that both of the SAA catalysts have a peak as expected for the Cu(111) reflection. Interestingly, the particle size acquired through the XRD analysis states that the Cu species is of 6 nm for the $Pt_{0.5}Cu_{250}$ catalyst, whereas it is 5 nm for $Pt_1Cu_{20}$. This slight drop in particle size could be because of a greater galvanic replacement process (more Pt added) or due to an overall more acidic solution being used, causing the host particles to be mildly digested. The Cu particles themselves were all synthesized from the same batch and so should have the same particle size.

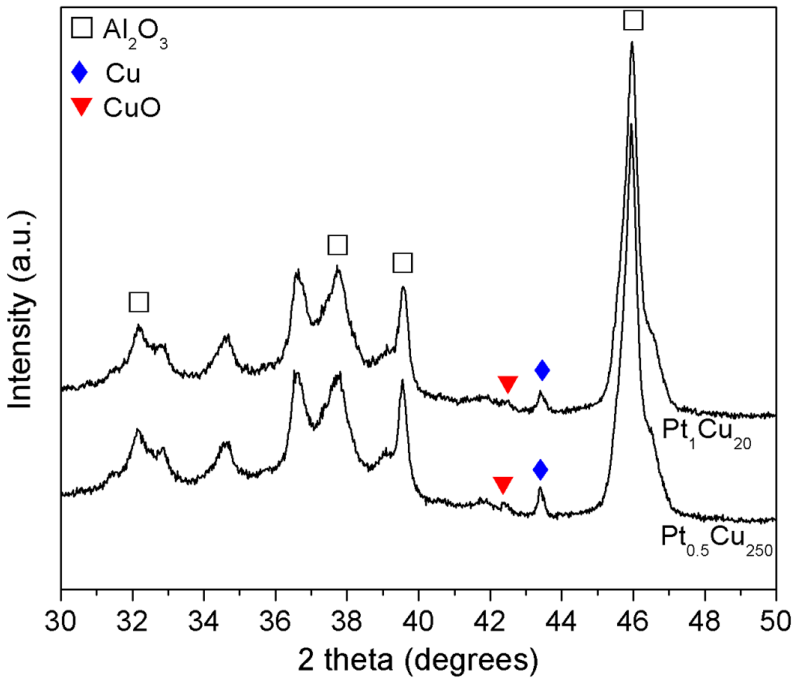


Figure 23 - X-ray diffractograms of the as made Single Atom Alloy catalysts.

For the lowest Pt containing material there is a small reflection indicating CuO, which could mean that the Cu regions not possessing a Pt entity have oxidized slightly. This peak is also observed for $Pt_1Cu_{20}$, the intensity is however lower suggesting that the Pt present is restricting oxide formation. There is also no shouldering present in both materials in the $40^o$ region, which is typically recorded for Pt(111). This is very positive and suggests that surface agglomerates have not been created, in this region or the $Cu_3Pt$ reflection shown previously (Figure 6). This also means that there are no larger structures of mixed metal alloys.

### 5.2.4.3 SAA X-ray Photoelectron Spectroscopy

Similar to the XPS analysis of the bimetallic nanoparticles, this technique is able to inform whether the Cu host particles are metallic in nature or if there is surface oxide. As galvanic replacement is a surface process, it can be assumed that the Pt deposited in Cu vacancies will be visible. This will also indicate whether the Pt atoms migrate to the bulk Cu particle to minimize their surface energy or remain on the surface. Figure 24a shows the overlaid Cu 2p peak fitting for the $Pt_1Cu_{20}$ catalyst against the monometallic Cu sample. The

expected Cu 2p doublet, with peaks at 932 eV (Cu $2p_{3/2}$) and 952 eV (Cu $2p_{1/2}$) can clearly be seen to align with the host material. This shows that there is no peak shifting, unlike, the $Pt_{38}Cu_{62}$ bimetallic catalyst presented in Figure 21. This factor, as well as proof from the PXRD (Figure 23), confirms that there is no bulk alloy formation as with the bimetallic nanoparticles. Figure 24b shows the Pt 4d region where Pt peaks can clearly be seen, proving that the replacement process deposits Pt atoms on the surface or within the first few layers of Cu atoms. These peaks have a notable intensity due to the 100% surface $Pt^0$ dispersion. TEM images, in Figures 26 and 27, prove that the catalyst $Pt_1Cu_{20}$ has a high dispersion of Pt atoms on the Cu nanoparticle. However, these atoms are not fully isolated and are often seen with a neighboring Pt atom (definition of a single atom is included in Chapter 1). In fact, this catalyst has a surface Pt and Cu concentration of 14.3% and 85.7% respectively. Looking closer at these values, the true atom ratio is actually 1:9; this ratio is close to the measured ratio of 1:20 by ICP-OES.

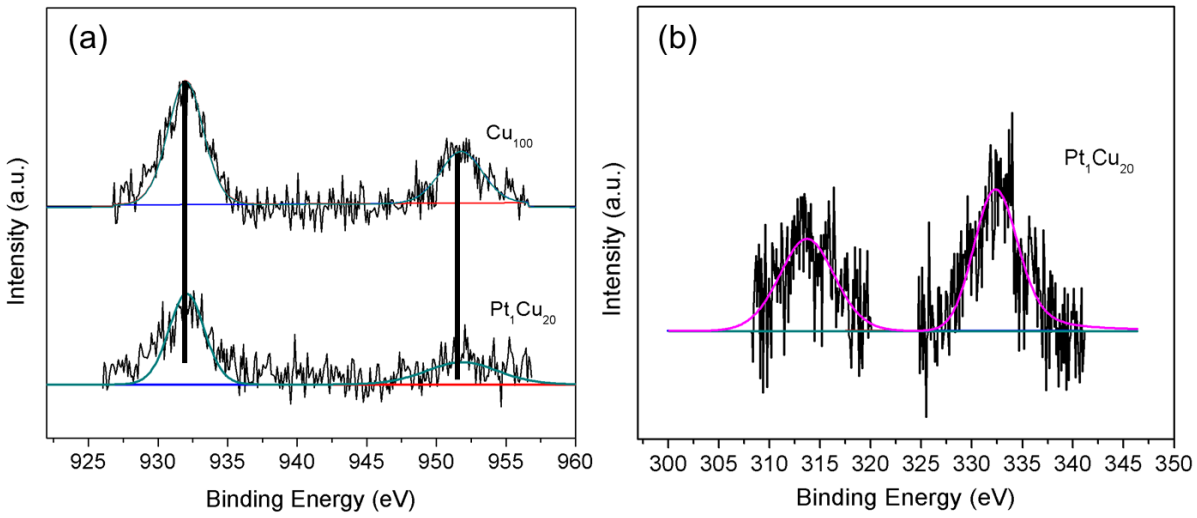


Figure 24 – XP Spectra of (a) Cu 2p region for $Pt_1Cu_{20}$ compared with the monometallic $Cu_{100}$ host material and (b) the Pt 4d region for the SAA, proving that the Pt is on the surface of the catalyst.

The Cu 2p fitting also shows no addition of satellite peaks between 932 eV (Cu $2p_{3/2}$) and 952 eV (Cu $2p_{1/2}$). The lack of these peaks means that there is not an oxide surface majority. The definitive proof of surface oxide is shown in Figure 25 where the Cu LMM region is plotted against the monometallic Cu host material already shown in Figure 22.

The overlaid spectra in Figure 25 show that there is a substantial difference in the shape of the peak as well as loss of the second Cu auger feature. Broadening of this peak is indicative of CuO; Cu(I), if present, would shift this peak by 2 eV to a lower binding energy. This is not the case as the peak is subtly broadened,[43,44] which means that the Cu present in the catalyst has a level of surface oxidation after the galvanic replacement process. This is easily noticeable by XPS due to the sensitivity of the surface based technique.

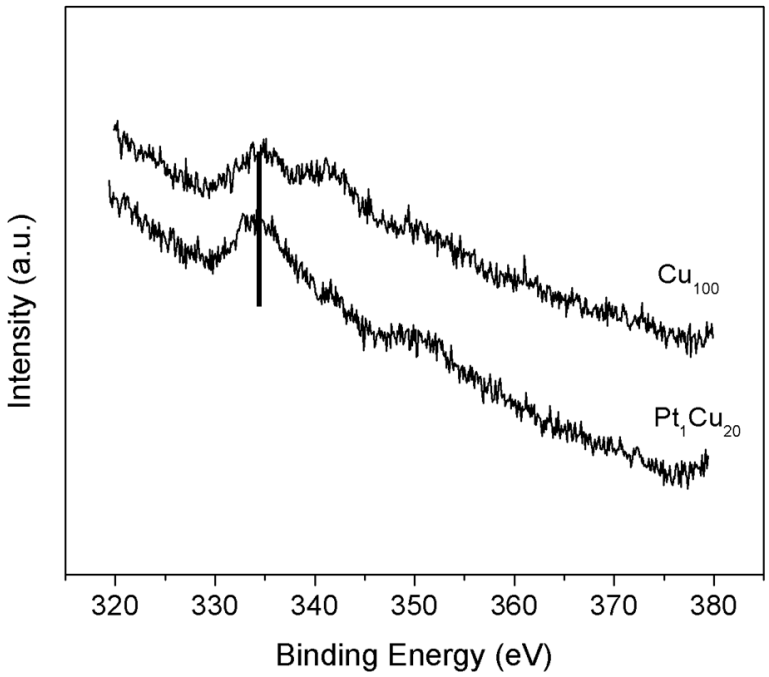


Figure 25 - XP spectra overlaid of the Cu LMM region, showing a noticeable change in oxidation state after galvanic replacement.

#### 5.2.4.4 SAA Atomically resolved microscopy and EDX

Initial microscopy observations are that the Cu particle size is smaller than the original monometallic sample (Figures 10-12 and Table 3). It is assumed that the brief period of reflux in the acidified solution began to digest the host particle as the atom exchange took place. Evidence of single Pt atoms deposited into a Cu lattice ($Pt_1Cu_{20}$) is shown in Figures 26 and 27, where higher contrast heavy metal entities are clearly shown in the dark field imagery. As a visual aid, yellow circles are used to denote a selection of Pt atoms.

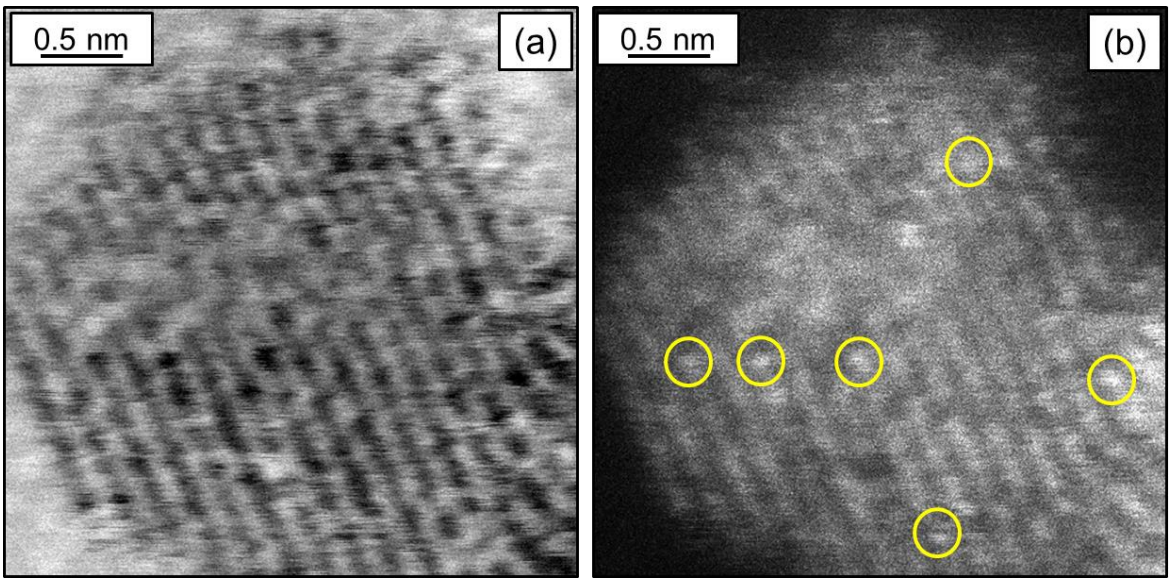


Figure 26 - Image of an individual Cu (N) host nanoparticle with single Pt entities ($Pt_1Cu_{20}$) (highlighted by yellow circles) where, (a) is the bright field image and (b) is the corresponding dark field image.

Although it is obvious that Pt atoms have indeed been incorporated into a Cu lattice, the overall Pt loading of this material is clearly still too high as the atoms are not truly 'isolated'. This means that the atoms have a series of other atoms in close proximity to one and other. Figure 26 is possibly the best image to demonstrate this point as the atoms can be clearly seen in both forms of imagery. There are areas where atoms are extremely close to one and other and in some cases side by side in the lattice spacing. Such observations have been reported by Lucci et al who describe, for their $Pt_2Cu_6/\gamma\text{-}Al_2O_3$ SAA, that the higher Pt surface concentration led to some atom aggregation and surface bound Pt clusters.[14] The atom arrangement in Figures 26 and 27 shows that this catalyst is not a 'Single Site Heterogeneous Catalyst' (SSHC) either, as the atoms are not spatially isolated (equal distance between all atoms).[50] Possibly, the more appropriate classification for this synthesized SAA, is an 'Atomically Dispersed Supported Metal Catalyst' (ADSMC) as the positioning of the atoms is very random but they are in proximity to form dimer/trimer species, which is in agreement with Lucci and co-workers.[14,48,49]

Clarification of the cluster species mentioned was accomplished by EXAFS analysis where Lucci and co-workers were able to clearly resolve Pt-Pt bonds.[14]

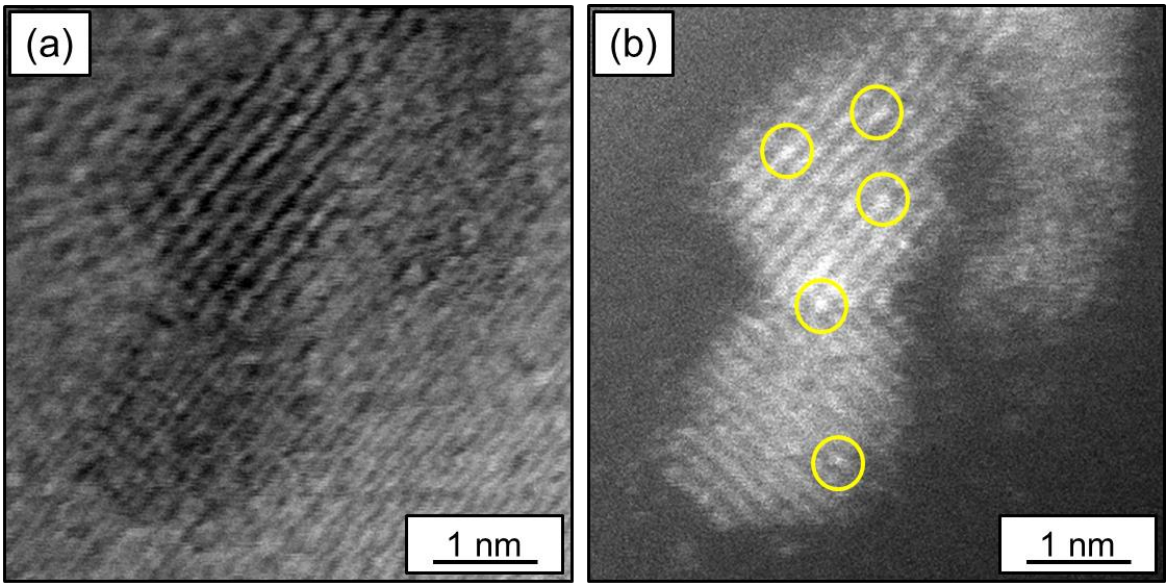


Figure 27 – Two Cu (N) nanoparticles with surface platinum atoms ($Pt_1Cu_{20}$) (highlighted in yellow circles) where, (a) is a bright field image and (b) is the corresponding dark field image.

Energy Dispersive Spectroscopy was completed for this sample, targeting a Cu host particle and scanning for the same length of time as the bimetallic catalysts shown previously. Figure 28 shows such a scan where the atomic ratios for Cu and Pt are of similar ratios as those measured by XPS analysis (85.7% and 14.3%). As the focused beam can rapidly destroy sections of the grid or produce atom displacement (causing the Pt atoms to agglomerate), the microscope magnification for EDX analysis was decreased. However, the lack of magnification means that Pt atoms are not visible for the images shown in Figure 28, although, by careful examination, individual Pt atoms can be seen (bright field image). The area of EDX analysis is illustrated by a large yellow circle at the bottom of the TEM image (Figure 28).

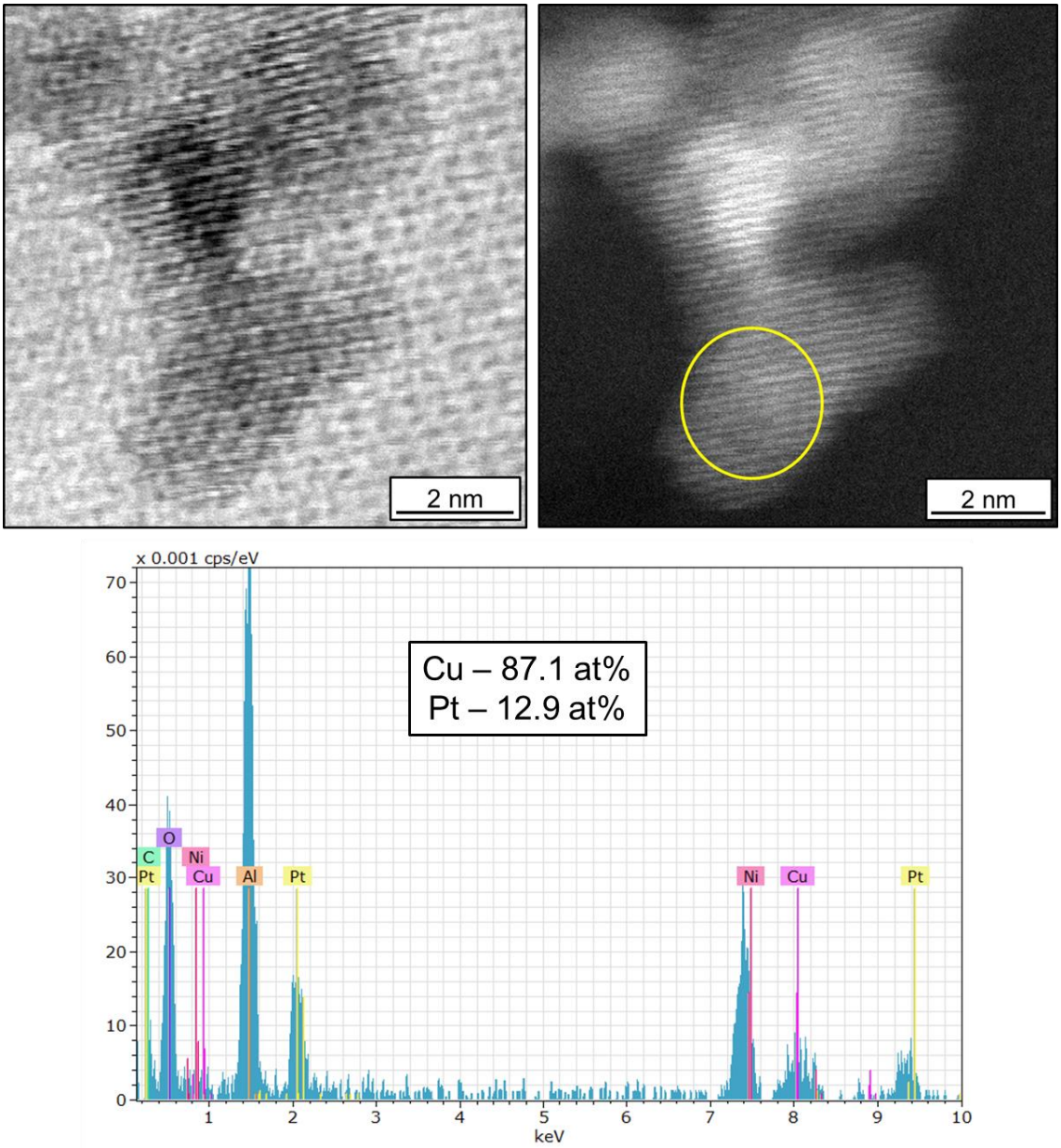


Figure 28 – A selected area of the $Pt_1Cu_{20}$ catalyst with EDX line scan and atomic dispersions.

## 5.3 The Selective Hydrogenation of Furfural

Unlike the work presented in Chapter 4, the selective hydrogenation of furfural was carried out under varying hydrogen pressures (1.5, 10 and 20 bar) opposed to near atmospheric pressure, using the various metal ratios described above (Table 2). Comparisons were made between the bimetallic catalysts originating from a nitrate or sulphur containing Cu precursor to evaluate whether the presence of sulphur acts to promote hydrogenation or as a hindrance of the catalysis.[4,5] Due to the efficiency of mild temperature reactions shown in Chapter 4, all experimentation was carried out at this constant temperature (50 $^{o}$C), which is used to limit furan production and subsequent surface poisoning carried out by decarbonylation of the parent material, as well as to negate acetalization side reactions.[1,51–53] Initial catalytic screening was completed metal free, with the bare support ($\gamma$-$Al_2O_3$) calcined and reduced in situ using the protocol mentioned in Chapter 2. Across all three pressures, the support presented no hydrogenation or acetal based reaction products. However, there was a furfural conversion of <2% entirely selective towards furan, which is in agreement with Chapter 4.

### 5.3.1 Supported Cu catalysts, with and without the presence of Sulphur

Hydrogenation reactions were carried out on the pure ~1% Cu catalysts. The literature has previously reported that high Cu loaded monometallic catalysts (Chapter 1) can be used for furfural hydrogenation. Typically, this is accomplished by using either extreme reaction conditions (vapour phase reactors). Sitthisa et al[11] have shown that 10 wt% Cu catalysts have potential as very selective materials for furfuryl alcohol production. However, the rate of hydrogenation is very slow due to the inability to dissociate hydrogen on the surface.[11,54–60] Copper catalysis for furfural transformation is clearly a hot topic as copper itself is vastly cheaper than Platinum (£0.004 and £25 per gram respectively).[61] Although not widely seen, especially for liquid phase reactions, Pt can be used to generate methyl furan via the HDO reaction pathway,[9] which was presented in Chapter 3. Generally, Pd is used much more extensively for this reaction.[62,63] Recently, it has been shown that the HDO reaction pathway can be accessible using pure $Cu/Al_2O_3$ at high reaction temperature (200 $^{o}$C), or in the presence of a second metal such as Co or Pd.[10,37]

Figure 29 shows both the reaction progression profiles (Figure 29a) and the normalized initial rate per mass of Cu in the Cu (N) catalyst (Figure 29b). For comparison with bimetallic catalysts, this was recorded after the first hour. So that the materials could be reduced in situ, the near ambient reaction was carried out in the autoclave with the pressure measured by the pressure gauge on the cylinder. This was confirmed by a second gauge on the reactor platform. As expected, the low pressure experiment provided a very low furfural conversion overall. As the pressure was increased, a greater concentration of hydrogen molecules could be provided for activation and therefore hydrogenation. This being said, initial rates across all pressures used were very low, even for the highest pressure (20 bar), surprisingly. The rates of reaction appear to increase after 2 h for all reactions, with 10 and 20 bar having the highest rates, which are similar until 3 h when the 10 bar reaction begins to lose activity, starting to reach a plateau at around 5 h. Interestingly, by observing Figure 29c, a magnified reaction profile clearly shows two distinctive rates of reaction; the first ($R_1$) between 0-2h and the second ($R_2$) from 2-5h. The initial rate can be attributed to either a catalyst cleaning procedure, where surface oxide has developed due to oxygen pre-dissolved in the reaction mixture interacting with the catalyst or the pre-reduction process at 300 $^{o}$C for 0.5 h being insufficient. Although the reaction mixture was purged before reaction, the inherent oxygen content appears to inhibit the initial rate of reaction for this catalyst. The second rate, after the 2 h period, clearly shows a stark increase when the cleaning process is complete and hydrogen is able to activate. This is important as CuO or $Cu_2O$ are not able to activate hydrogen in any form.[64] As the operating temperature of the reaction is very low (50 $^{o}$C), the rate of reduction is very slow. The drop in activity (after 5 h) could be attributed to greater furan selectivity at lower pressures (Table 9). This would leave surface bound carbon and reduce the number of active sites available. Copper has been reported in the literature to deactivate over time due to coking.[8,59]

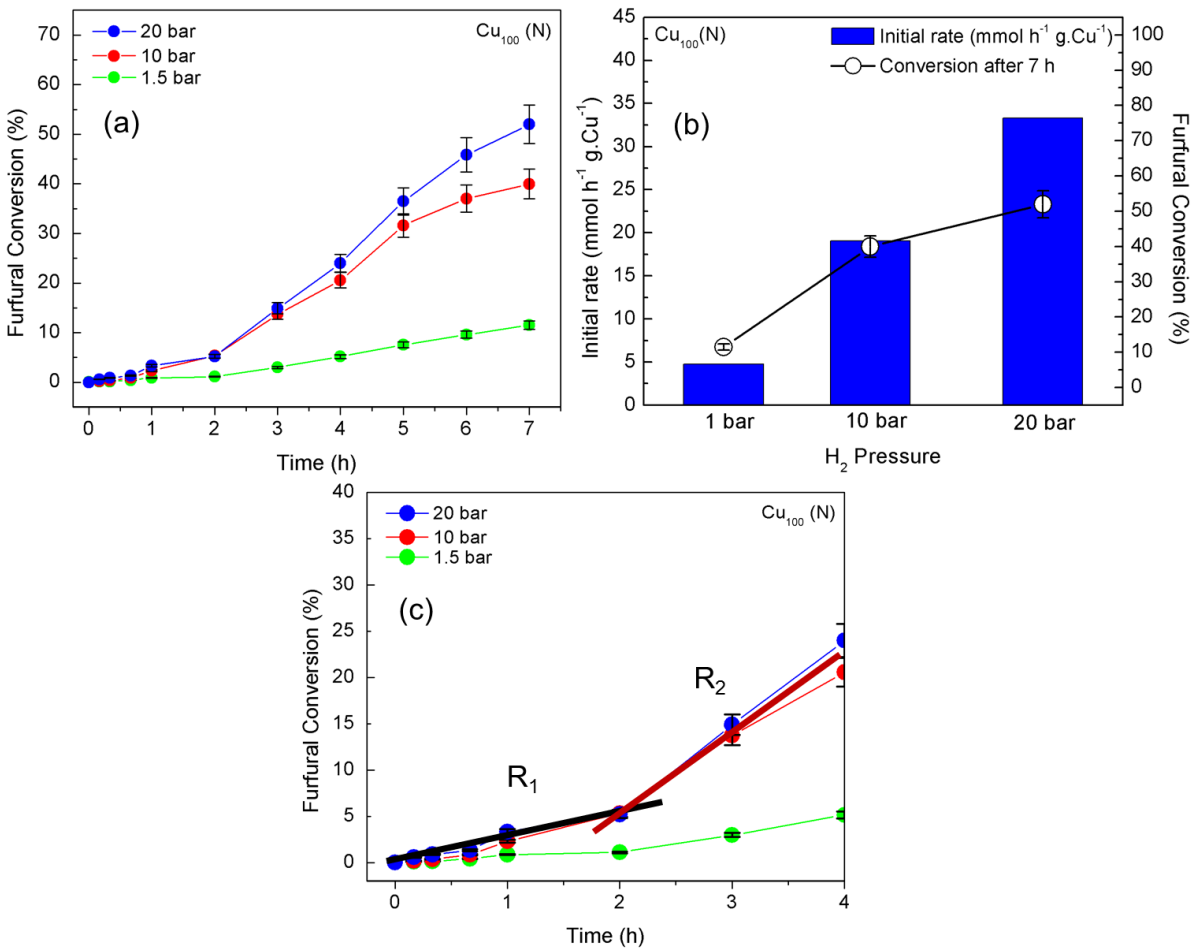


Figure 29 – (a) Furfural conversion reaction profiles, (b) initial rates of reaction per mass of Cu in the Cu (N) catalyst at varying hydrogen pressure. (c) a magnified reaction profile showing the two distinctive rates of reaction ($R_1$ is represented by a solid black line and $R_2$ is shown by a solid red line).

Although very similar, the initial rates taken (up to the first hour) are subtly higher when greater pressure is used, possibly due to faster surface oxide removal. It is the hydrogen introduced to the reaction mixture (hydrogen proving to be very soluble in methanol, as shown in Chapter 4) that is re-reducing the catalyst over the initial period of time.[1,65,66] This is also why the initial rates are marginally higher for each pressure as more $H_2$ molecules can find a metallic surface because oxidized copper will not activate $H_2$.[64]

In comparison, the two copper catalysts synthesized with different precursors exhibit similar initial rates of furfural conversion for each pressure (Figure 30b). Figure 30a shows the reaction profiles over 7 h across the hydrogen pressures used. The difference between these two materials is the lower activity after 2 h resulting in a diminished conversion over

7 h for the case of the $Cu_{100}$ (S) catalyst. The surface cleaning process, $R_1$, indicated in Figure 29c shows that rates improve for (N) based catalysts after 2 h. When (S) samples are analyzed the rates do not benefit as fast from this effect, instead they begin to build after 3 h. The residual sulphur bound individually or as bulk sulphate may have a further detrimental effect on the catalyst. The two rates are shown in Figure 30c. By normalizing the initial rates of reaction with the mass of Cu in the sample (determined by ICP), the rates per gram of Cu show that the $Cu_{100}$ (S) is in fact superior to the $Cu_{100}$ (N) material across all pressures. However, this is not a benefit as the initial rate favours furan production. The normalized graphs seen in Figures 29 and 30 are also shown in Figure 31 for ease of comparison.

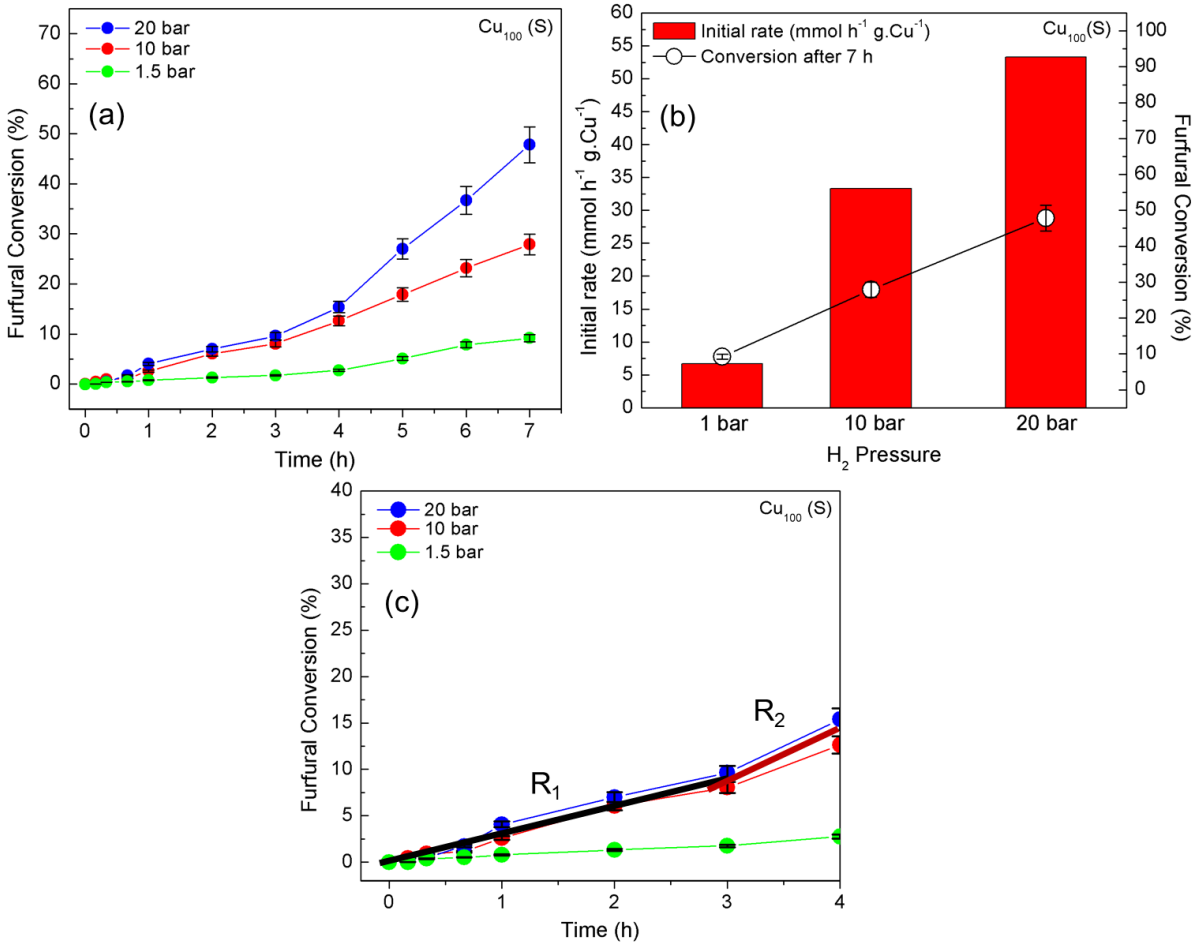


Figure 30 – (a) Furfural conversion reaction profiles, (b) initial rates of reaction per mass of Cu in the Cu (S) catalyst at varying hydrogen pressure. (c) a magnified reaction profile showing the two distinctive rates of reaction ($R_1$ is represented by a solid black line and $R_2$ is shown by a solid red line).

The other difference between the two catalysts and possibly the reason why there is a lowered activity, is in the reaction selectivites shown in Table 9. The Cu (N) catalyst appears to be mildly selective towards furfuryl alcohol at near ambient pressure (21.5 %), rapidly increasing as more hydrogen is supplied to the surface (10 bar, 89.2 % and 20 bar, 96.8%). However, the Cu (S) species has very much lower furfuryl alcohol selectivity, presenting only 10.9 % at near ambient conditions, this value only increasing to 74.9 % at 10 bar and marginally increasing further to 81.0% for the 20 bar. This catalyst appears to be more adept at accessing the decarbonylation reaction pathway. The production of furan and subsequent evolution of CO is often the cause of catalyst poisoning. However, Cu(S) catalysts appear to rapidly generate furan, leading to a slightly higher initial rate. Although potentially restricting hydrogen contact with the surface, the remaining sulphur content appears to be the driving force behind this dramatic selectivity change towards furan. While not acting as a direct poison for this reaction, surface bound sulphur appears to act as a promoter for decarbonylation reaction pathways, leading to the eventual poisoning. This could mean that on a Cu surface, hydrogenation reactions are favoured on the most highly coordinated sites were sulphur is known to reside, as reported by Kitchin and co-workers.[67] Their simulation study on Cu (100), (110) and (111), found that the sulphur adsorption energy is at its highest when the coverage is at its lowest. Also, due to an electronic structure modification, the role of sulphur not only poisons reaction sites but on the whole deactivates the metal surface. A comparative UHV study on the water gas shift reaction was completed by Campbell and Koel who found that Cu(111) poisoning was subject to steric sulphur blocking sites responsible for water adsorption.

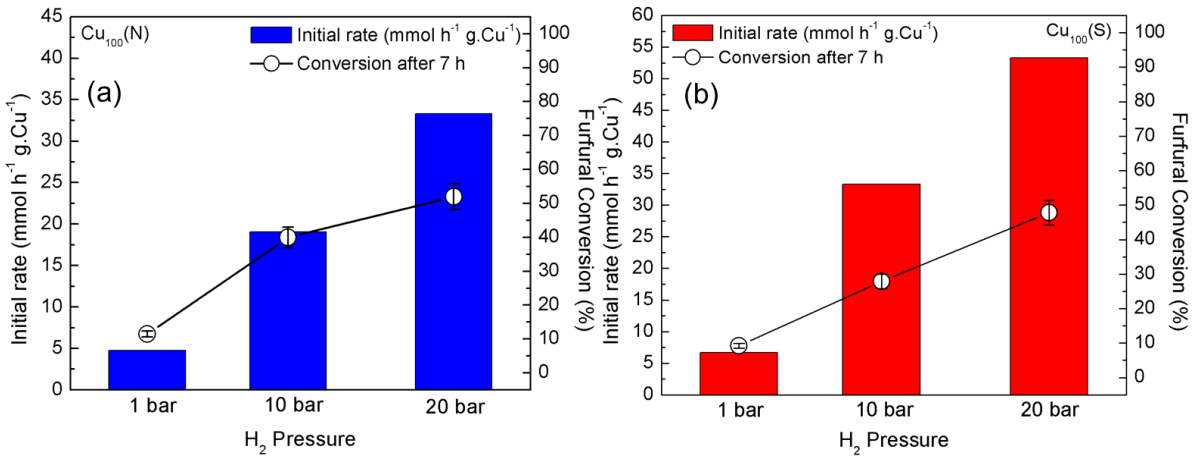


Figure 31 - A comparison of the two Cu based catalysts (a) $Cu_{100}$ (N) and (b) $Cu_{100}$ (S) display both the initial rates of reaction (normalized per gram of Cu) for each pressure, taken after the first hour of reaction and the overall furfural conversion after 7 h.

Copper catalysts operating at low temperature (50 $^{o}$C) appear to not to be suitable for the acetal side reaction to form furaldehyde dimethyl acetal. This system is comparable with the monometallic study completed in Chapter 4 where it is shown that acetal reactions are thermally driven.[1,68,69] Other potential side reactions, such as furan hydrogenation or HDO reactions following on from furfuryl alcohol production, were also not seen for both Cu systems.

Table 9 – Reactivity of both Cu catalysts at varying $H_2$ pressures, selectivities taken after 7 h.

| Catalyst | $H_2$ Pressure (bar) | Conversion (%) | Furan S (%) | Furfuryl alcohol S (%) |
|---|---|---|---|---|
| $Cu_{100}$ (N) | 1.5 | 11.5 | 69.1 | 21.5 |
| | 10 | 39.9 | 10.8 | 89.2 |
| | 20 | 52.0 | 3.2 | 96.8 |
| $Cu_{100}$ (S) | 1.5 | 9.2 | 89.1 | 10.9 |
| | 10 | 27.9 | 25.1 | 74.9 |
| | 20 | 47.9 | 19.0 | 81.0 |

S – Selectivity (%)

### 5.3.2 The effect of Cu in PtCu bimetallic catalysts

#### 5.3.2.1 Bimetallic catalysts generated from the $Cu(NO_3)_2$ precursor

It has been shown previously by using numerous characterization techniques that bimetallic PtCu catalysts were successfully synthesized in a wide range of Pt:Cu compositions (Figures 6, 16, 17 and Table 7). For this family of catalysts, initial rates of reaction are calculated to consider both Pt and Cu, as both metals have been shown to be active for furfural transformation. By accounting for the Cu present in the catalysts, the materials can truly be assessed to determine potential benefits from the alloyed system, whether this being promotion in furfural conversion or additional products formed.

The activities of the monometallic Pt (1.2 wt%) and bimetallic (N) catalysts, $Pt_{38}Cu_{62}$ and $Pt_{18}Cu_{82}$ are represented in Figure 32. It shows that across all hydrogen pressures used, both monometallic Pt and bimetallic catalysts are superior in terms of initial rate and overall conversion over 7 h compared with $Cu_{100}$ (N). This activity is amplified for the bimetallic catalysts, as initial rates per gram of active metal are much higher than the monometallic Pt catalyst. Interestingly, in Figure 32, for the case of 1.5 and 10 bar, $Pt_{38}Cu_{62}$ (N) exhibits a substantially faster initial rate than $Pt_{100}$ (2 times and 1.6 times faster respectively), which means that the alloyed particles promote the transformation of furfural. This may be because the binary metal surface has two characteristics (i) hydrogen is readily activated on Pt sites, spilling over onto adjacent Cu and (ii) furfural could prefer to adsorb on $Cu_3Pt$ sites rather than monometallic counterparts. Density Functional Theory (DFT) completed by Liu and co-workers[70] has predicted, using the PBE and optB86b functionals, that the binding energy of furfural on Cu(111) is much lower than that of Pt(111), 0.47 eV and 1.07 eV respectively. This difference could mean that the furfural will prefer to bind to Cu isolated regions, where it is met by pre-dissociated hydrogen for rapid transformation before being released back into the liquid phase, or that the alloyed $Cu_3Pt$ regions have a lower binding energy than Pt(111) but higher than Cu(111). This means that in comparison with the monometallic catalyst, where a predicted binding energy could be 1.07 eV, a '50:50' ratio may be the difference in energy of the two metal surfaces, 0.77 eV. Another alternative would be a change in adsorption geometry as furfural will adsorb in different orientations on Pt(111), depending on deviations in surface population (Chapter

3). Electronic modifiers induced through the alloy process could result in differences in furfural's geometry, leading to a tilted or even perpendicular orientations.[9,71,72]

This effect appears to be less obvious when considering the $Pt_{18}Cu_{82}$ catalyst, which demonstrates a lower rate of reaction than the other two catalysts. This is potentially due to such a low bulk Pt content that the catalyst begins to adopt, in part, the characteristics of $Cu_{100}$. However, the most dilute Pt bimetallic catalyst still shows a clear Pt promotional effect in comparison with the monometallic Cu catalyst (14 times as active at 1.5 bar, 5.9 times for 10 bar and 3.4 times for 20 bar). The alloy effect appears to be lost when operating at 20 bar where both bimetallic species have reduced initial rates in comparison with the pure Pt which exhibits an incredibly high rate of reaction.

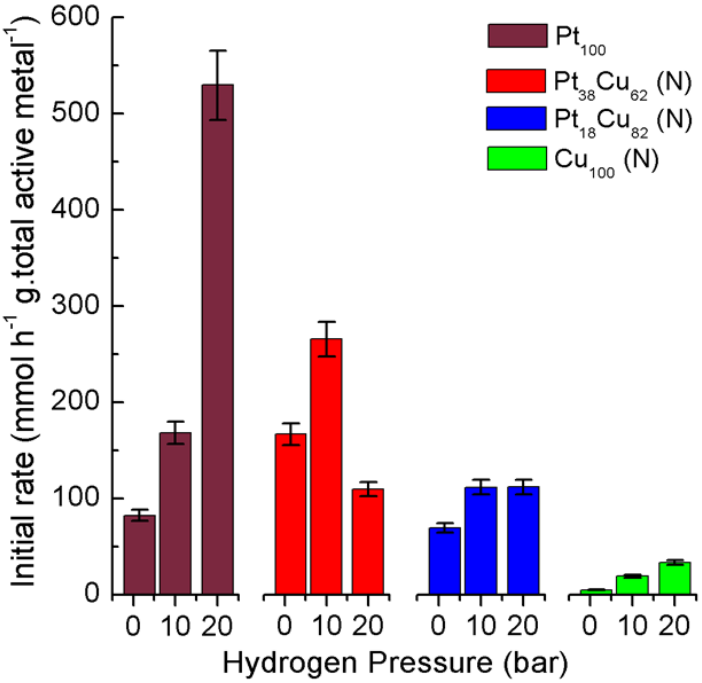


Figure 32 - Initial rates per gram of active metal for Pt, Cu and PtCu bimetallic catalysts across 3 hydrogen pressures.

The reaction profiles for each hydrogen pressure regime across monometallic and bimetallic catalysts are shown in Figure 33. For the case of the 20 bar hydrogen reactions both bimetallic catalysts appear to operate in a similar fashion, whereas the $Pt_{100}$ catalyst reaches its maximum conversion at 2 h. As it is clear that Pt is this active when operating at this pressure, it could mean that the rate of hydrogen dissociation and subsequent spillover

is in fact causing furfural adsorption rate limitations for the binary metal systems. This could also explain why the initial rates for both 10 and 20 bar reactions are very similar for the $Pt_{18}Cu_{82}$ catalyst. Competitive adsorption of $H_{ads}$ against $furfural_{ads}$ is causing reaction site blockage and limiting the furfural transformation. Reactivity for all catalysts is much lower for the 1.5 bar reaction. As expected, the omission of hydrogen in the system has provided a much lower initial rate and overall conversion for each material. This being said, the $Pt_{38}Cu_{62}$ catalyst provided a much higher initial rate of reaction than the pure Pt catalyst, albeit slowing down after the first hour. The monometallic Cu was also not active under these conditions; however, the low addition of Pt forming an alloyed entity ($Pt_{18}Cu_{82}$) radically increased the rate and overall conversion over the 7 h period.

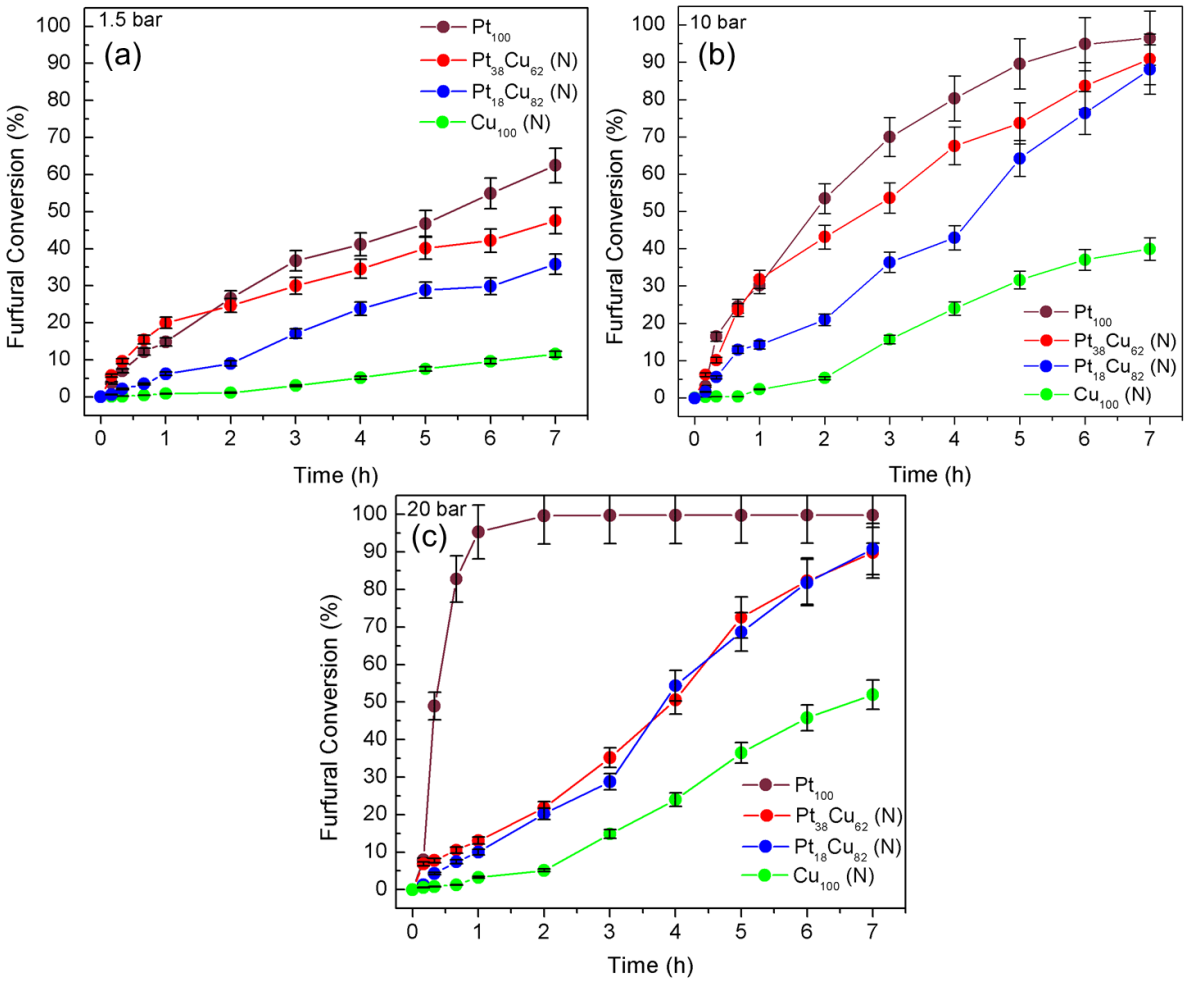


Figure 33 - Conversion profiles for bimetallic (N) catalysts showing the effect of pressure on each reaction, where (a) is at near ambient conditions (1.5 bar), (b) is at 10 bar and (c) is at 20 bar.

By using the CO dispersion measurements, as well as the XP spectra and XRD diffractograms, (Figure 6 and Figures 20-22), it is clear there is no surface $PtO_2$ present on the catalysts or in Pt bulk as all materials were reduced before analysis either ex situ or in situ. Therefore, the total surface Pt species can be calculated and plotted to show how the individual catalysts performed against one and other in the initial hour. This plot is in Figure 34, and shows that at 1.5 and 10 bar, the turnover frequencies for both bimetallic catalysts are superior to the pure Pt catalyst which possesses the greatest surface Pt content as well as the lowest $Pt^0$ dispersion. The reaction profiles for the 20 bar data show that the bimetallic catalysts have a diminished activity in comparison with the lower pressures used (Figure 33). Figure 34 shows that the TOF (turnover frequencies, as defined in Equations 3-5) for both of these catalysts is very similar. This means that the surface Pt has been saturated with hydrogen, restricting the furfural adsorption, which draws a similar comparison with a single crystal when the surface is fully saturated with hydrogen. Chapter 3 shows that when the Pt(111) surface contains around 0.5 ML of $H_2$, the amount of furfural required to generate a monolayer is substantially less.[9]

$$\text{Surf. Pt (mmol)} = \frac{\text{Total Pt(mmol)}}{\text{Dispersion (\%)}} \qquad \text{Equation 3 – Surface Pt determination}$$

$$\text{Surf. } Pt^0 \text{ (mmol)} = \text{Surf. Pt} \times \left(\frac{100 - PtO_2 \text{ content}}{100}\right) \qquad \text{Equation 4 – Surface } Pt^0 \text{ content}$$

$$\text{Turnover frequency per } Pt^0 \text{ site} = \frac{\text{Initial rate (mmol } h^{-1})}{\text{Surf. } Pt^0} \qquad \text{Equation 5 – TOF per } Pt^0 \text{ site}$$

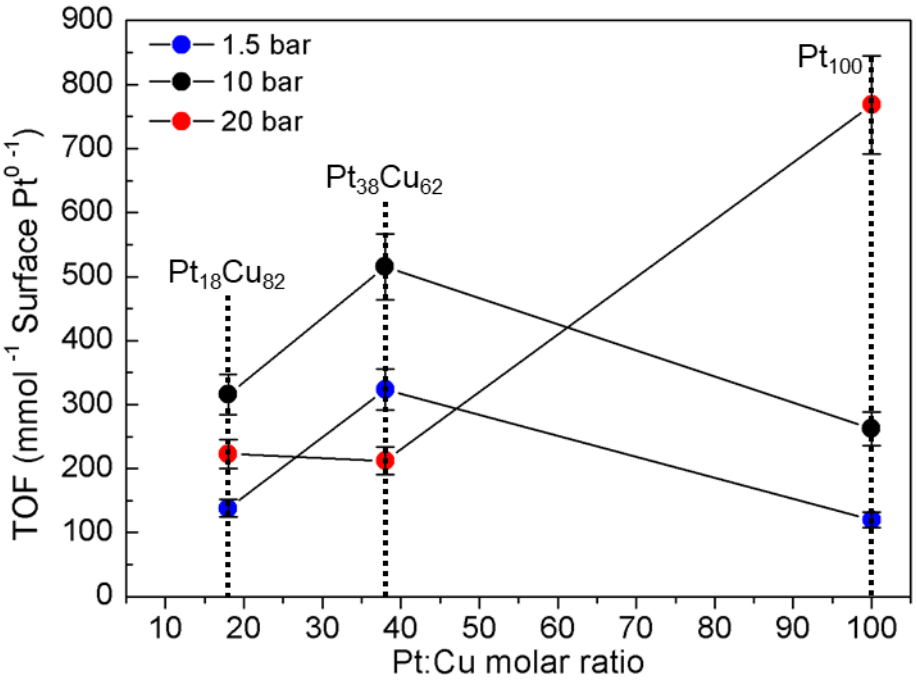


Figure 34 – Turnover frequencies per Pt and PtCu (N) catalysts across three different pressures

Reaction selectivities after 7 h are displayed in Table 10. As previously shown with the monometallic Pt data presented in Chapter 4, the furfural hydrogenation reaction was thoroughly optimized to the maximize reaction selectivity and activity by using the appropriate solvent, catalyst support and temperature. When increasing hydrogen pressure, the selectivities appear not to dramatically vary for $Pt_{100}$, with the exception of a quantifiable amount of tetrahydrofurfuryl alcohol (THFA) being detected. Previously, this was only observed by mass spectrometry at trace levels. The selectivity towards furan also began to slowly increase, however, due to the low temperature used, the thermally dependent acetal reaction was omitted. Even at the highest pressure (20 bar) there was no other aromatic hydrogenation products or hydrogendeoxygenation, typically observed in the literature with Pd systems.

By alloying Cu with Pt, there was no major difference between selectivities once again, especially for the $Pt_{38}Cu_{62}$ catalyst. The catalyst on the whole appeared to operate comparably with the $Pt_{100}$ catalyst in terms of activity, albeit at much higher initial rates than the monometallic material. However, this material was found to generate around 2.6

times more furan and the resulting CO formed appeared not to deactivate the catalyst. As the pressure was increased to the maximum (20 bar), the selectivity shifted back towards furfuryl alcohol. It has been mentioned that the loss of initial activity, is due to surface saturation from hydrogen leading to a competitive adsorption with the substrate. This could also be the reason why the bimetallic catalysts both created over 3 times more THFA than the $Pt_{100}$.

However, the $Pt_{18}Cu_{82}$ material is unique, as not only is the conversion of furfural is very high at 10 and 20 bar but the selectivies are completely different at lower pressures. This catalyst presents an 88.1% conversion after 7 h with an incredible selectivity towards furan (37.2%). Typically, this level of decarbonylation leads to rapid deactivation due to substantial carbon laydown. Instead, by observing the reaction profile, the consumption of furfural continues in almost a linear fashion from the initial 40 minutes to the 7 h period. This trend infers that the Cu component is protecting the Pt from poisoning through a-top binding mode for CO adsorption (Chapter 2). This electronic effect has previously been discussed in the literature.[37,73,74] The 'Pt protection' theory involves an electronic effect from the Cu, where the electron density can spill over onto the Pt, repelling CO molecules.[37] This phenomena was also a reason why CO titration experiments were very difficult to conduct for all bimetallic systems, requiring a large quantity of sample. This understanding could prove crucial for scale up operations and for the recyclability of Pt catalysts in this area of work. By alloying the surface with Cu and when working at pressure, the surface would be protected from any CO formed and reduce the overall cost of materials; a two birds one stone scenario. This is even more important in the field of Single Atom Alloys, as a single Pt atom will readily adsorb a CO molecule.[14,73–75] At this point the lone active site is made redundant and eventually the catalyst will be completely useless. Recent work from Liu et al has shown that this Pt protection can be used on atomic entities when under UHV.[74] At the lowest pressure (1.5 bar) the Cu rich bimetallic appeared to perform more like the monometallic Cu, exhibiting a promoted activity but also possessing a higher selectivity towards decarbonylation.

Table 10 - Reaction selectivities for Pt containing bimetallic (N) and monometallic catalysts across 3 pressures, selectivities taken after 7 h.

| Catalyst | $H_2$ Pressure (bar) | Conversion (%) | Furan S (%) | Furfuryl alcohol S (%) | THFA S (%) |
|---|---|---|---|---|---|
| $Pt_{100}$ | 1.5 | 62.4 | 0.4 | 99.6 | 0 |
| | 10 | 96.5 | 0.8 | 99.2 | 0 |
| | 20 | 99.8 | 0.9 | 98.9 | 0.2 |
| $Pt_{38}Cu_{62}$ (N) | 1.5 | 47.6 | 9.2 | 90.8 | 0 |
| | 10 | 90.9 | 2.1 | 97.9 | 0 |
| | 20 | 90.0 | 0.9 | 98.1 | 0.9 |
| $Pt_{18}Cu_{82}$ (N) | 1.5 | 35.8 | 45.5 | 54.5 | 0 |
| | 10 | 88.1 | 37.2 | 62.8 | 0 |
| | 20 | 90.8 | 1.3 | 97.6 | 0.8 |
| $Cu_{100}$ (N) | 1.5 | 11.5 | 71.7 | 28.3 | 0 |
| | 10 | 39.9 | 10.8 | 89.2 | 0 |
| | 20 | 52.0 | 3.2 | 96.8 | 0 |

S - Selectivity (%)
THFA – Tetrahydrofurfuryl alcohol

#### 5.3.2.2 Bimetallic catalysts generated from the $CuSO_4$ precursor

The same experimental regimes were used for the second family of bimetallic catalysts synthesized by using the sulphur containing precursor. Although the sulphur content was clearly low, it was still observable by PXRD (Figure 8), the reaction data for these catalysts is also proof that there is still surface bound sulphur. This is similar to the monometallic Cu catalyst which showed a diminished activity in comparison with the Cu (N) counterpart. Reaction profiles for these reactions are shown in Figure 35. Curiously, both of the bimetallic (S) catalysts appear to operate in a very similar fashion for all pressures used, where the only observable difference is that of the initial rates. The conversion over the first hour was monitored and normalized per gram of total active metal (Figure 36). Here it is evident that the $Pt_{43}Cu_{57}$ (S) is superior to that of the other bimetallic catalyst ($Pt_{16}Cu_{84}$). It is clearly more efficient than the monometallic Pt for 10 bar reaction pressures and also for the (N) counterpart of similar molar ratios.

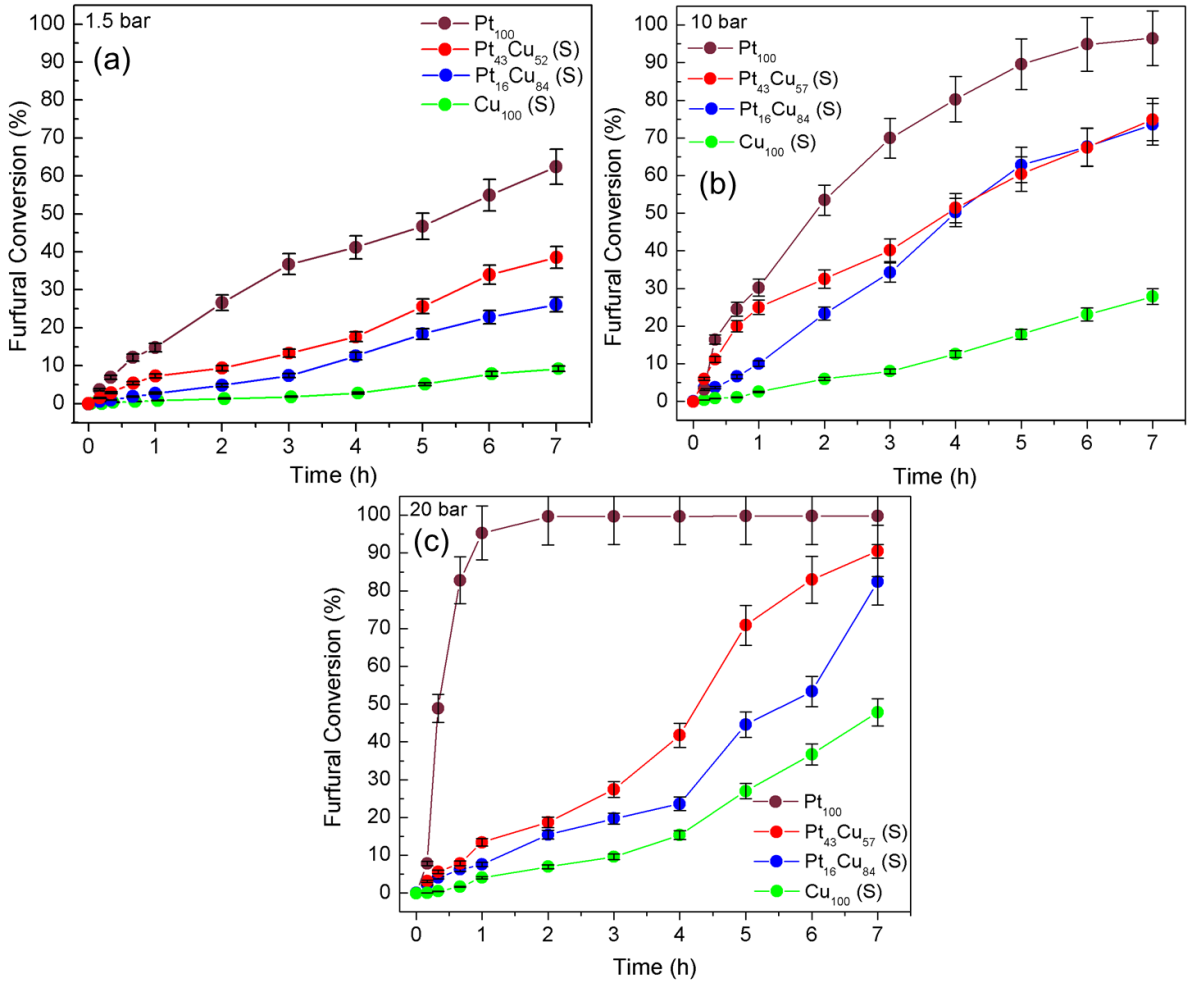


Figure 35 - Conversion profiles for bimetallic (S) catalysts showing the effect of pressure on each reaction where, (a) is at near ambient conditions (1.5 bar), (b) is at 10 bar and (c) is at 20 bar.

However, this observed rate for the (S) catalyst at 208.9 mmol $h^{-1}$ g.total active $metal^{-1}$ is inferior to the sulphur free catalyst which reports a normalized rate of 265.5 9 mmol $h^{-1}$ g.total active $metal^{-1}$. This being said, the (S) family of catalysts also falls foul of poorer activity when the hydrogen pressure is increased to 20 bar. As previously discussed, residual sulphur will reside in areas of high coordination, which will passivate the catalyst activity. However, both '50:50' molar ratio catalysts from the two sets exhibit very similar values of ~100 mmol $h^{-1}$ g.total active $metal^{-1}$. As expected, the $Pt_{16}Cu_{84}$ (S) catalyst out performs the monometallic $Cu_{100}$ (S) across the three pressure experiments. This catalyst contains the most active metal, as compared with all other catalysts used, for this set of

experiments. As a result, when normalizing initial rates per gram of active metal, the values are far lower than the (N) material with the same molar ratios. In fact, the differences between rates are very large with a 4.3 times greater initial rate at 1.5 bar for the sulphur free material, which is also reflected as hydrogen pressure increases to 10 bar with a 1.9 times greater rate. Unlike the 43:57 ratio materials, the sulphur containing $Pt_{16}Cu_{84}$ catalyst has a diminished rate at 20 bar with a 2.5 times decrease in rate of reaction over the first hour per mass of total active metal.

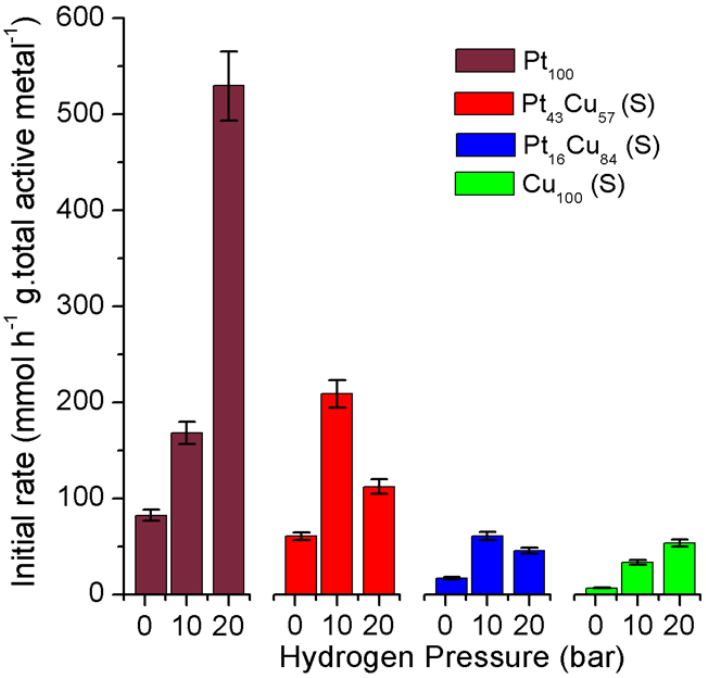


Figure 36 - Initial rates per gram of active metal for Pt, Cu (S) and PtCu (S) bimetallic catalysts across 3 hydrogen pressures.

By considering the Pt dispersion measurements in Table 6 and Figure 20, turnover frequencies for this family of catalysts can be calculated by making the assumption that the total surface Pt is metallic in nature. Figure 37 shows the turnover frequencies for each catalyst at the three reaction conditions. As the metal loadings are slightly higher than the (N) family and have lower rates of reaction, the TOF value is much lower in comparison with the sulphur free material, with only the $Pt_{43}Cu_{57}$ (S) providing a marginally higher TOF value than the monometallic Pt when operating at 10 bar,

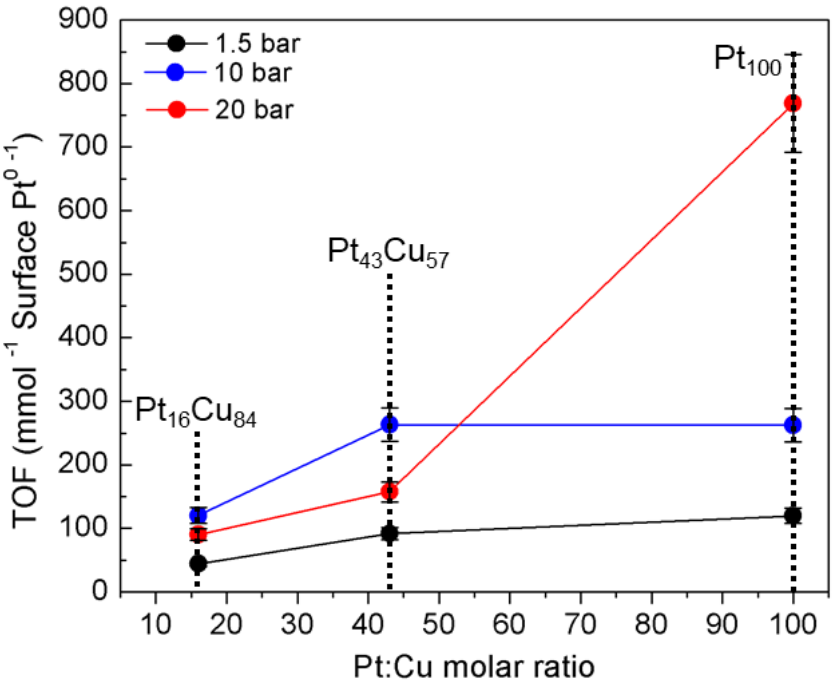


Figure 37 - Turnover frequencies per surface Pt across three different pressures, for the pure Pt and (S) based bimetallic catalysts.

Figure 38 shows a true turnover frequency comparison between both sets of bimetallic catalysts against the monometallic Pt species. By combining Figures 34 and 37, a unified TOF figure is generated where circles with solid lines represent (N) based catalysts and squares with dotted lines are (S) synthesized materials. This figure clearly shows the differences between the two sets of catalysts as the (N) based materials, although possessing less metal, out-perform the other catalysts dramatically. The shape of the plots is very similar for both materials where 10 bar data shows the 38:62 molar ratio catalyst to be superior vs. the $Pt_{100}$ and where the $Pt_{38}Cu_{62}$ (N) exhibits a TOF of 515 $mmol^{-1}$ opposed to 263 $mmol^{-1}$ shown by the $Pt_{43}Cu_{57}$ (S). This is a 1.96 times greater turnover frequency achieved when using the sulphur free catalyst. However, due to the extremely high rate of reaction for the $Pt_{100}$ monometallic, all bimetallic alternatives suffer from far lower catalytic turnover, with the (N) family still more efficient than the other materials. For mild conditions, the catalysts synthesized using the nitrate precursor show turnover frequencies to be higher than the monometallic Pt material, whereas the binary alloy materials with residual sulphur content have extremely low TOF for 1.5 bar reactions.

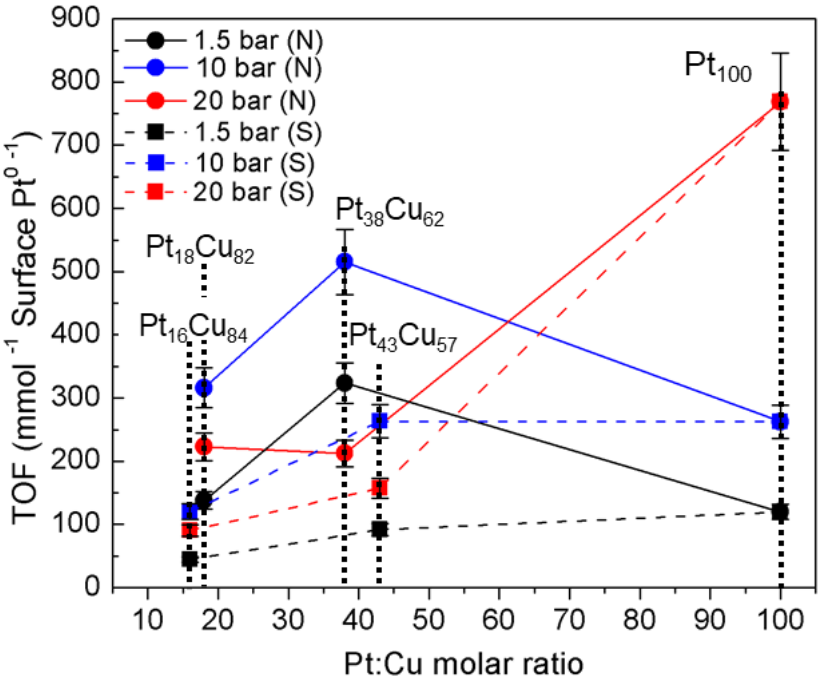


Figure 38 – A comparison of turnover frequencies for both binary alloy families where circles and solid lines represent (N) catalysts and squares connected with dotted lines are (S) materials.

The selectivities from the (S) materials shown in Table 11 indicate they are unlike the monometallic Cu (S) catalyst, which shows a dominating furan selectivity. The bimetallic catalysts are actually very selective towards furfuryl alcohol when operating at 10 – 20 bar. These values are comparable with the (N) set of materials, albeit substantially lower TOF and furfural conversion over the 7 h period. Also, with the exception of the 43:57 ratio (operating at 10 bar), these catalysts show no observable tetrahydrofurfuryl alcohol via hydrogenation of the aromatic structure of the adsorbed furfuryl alcohol. Over hydrogenation is normally seen to happen after 4 h of reaction for the (N) materials, increasing slowly over time. When operating at 50 $^{o}$C under various pressures in methanol, the materials with residual sulphur do not produce acetal based side reactions with furfural. They also do not conduct a low temperature HDO reaction, which means that the optimized conditions are still effective for this family of bimetallic catalysts. The true difference between the sets of binary alloys is clearly the rate of hydrogen activation. This is hindered by the presence of the surface bound sulphur, which is known for its steric effects and also for favouring adsorption in areas of highest co-ordination.

Table 11 - Reaction selectivities for Pt containing bimetallic (S) and monometallic catalysts across 3 pressures, selectivities taken after 7 h.

| Catalyst | $H_2$ Pressure (bar) | Conversion (%) | Furan S (%) | Furfuryl alcohol S (%) | THFA S (%) |
|---|---|---|---|---|---|
| $Pt_{100}$ | 1.5 | 62.4 | 0.8 | 99.6 | 0 |
| | 10 | 96.5 | 0.8 | 99.2 | 0 |
| | 20 | 99.8 | 0.9 | 98.9 | 0.2 |
| $Pt_{43}Cu_{57}$ (S) | 1.5 | 38.6 | 41.5 | 58.5 | 0 |
| | 10 | 74.9 | 3.3 | 95.8 | 0.9 |
| | 20 | 90.6 | 0.8 | 99.2 | 0 |
| $Pt_{16}Cu_{84}$ (S) | 1.5 | 26.2 | 66.3 | 33.7 | 0 |
| | 10 | 73.6 | 4.7 | 95.3 | 0 |
| | 20 | 82.4 | 1.5 | 98.5 | 0 |
| $Cu_{100}$ (S) | 1.5 | 9.2 | 89.1 | 10.9 | 0 |
| | 10 | 27.9 | 25.1 | 74.9 | 0 |
| | 20 | 47.9 | 19.0 | 81.0 | 0 |

S - Selectivity (%)
THFA – Tetrahydrofurfuryl alcohol

### 5.3.3 Single Atom Alloy vs. Binary Alloy Catalysts

The ultimate noble metal dilution study occurs at the atomic level.[2,13,14,74,76–78] Catalytic materials have been synthesized by substantially reducing Pt loading by over 10 times lower than the $Pt_{100}$ catalyst (1.2%). In comparison this is ~24 times less Pt than the original monometallic 2% Pt/γ-$Al_2O_3$ catalyst synthesized and tested in Chapter 4. The overall composition of the Single Atom Alloy (SAA) contains a copper rich active face, where surface atoms are replaced with atomic entities of Pt. Once again, the intended Cu loading was compared with that used in the bimetallic catalysts (~0.7 wt%). Previously, assignment of the bimetallic materials was represented by a ratio of the total molar quantity of each metal in the catalyst. However, atomically dispersed alloyed materials are represented in terms of the Pt:Cu atom ratio not the molar ratio. The SAA materials created and tested are denoted as $Pt_1Cu_{20}$, which means that for each dispersed Pt atom there are 20 Cu atoms. The second SAA synthesized has substantially less Pt present (22.5 times less Pt), whereas the sacrificial Cu loading remains similar for both materials. It has already been shown in Figure 23 that after galvanic replacement, although reduced prior to atom deposition, the synthesis encourages some surface CuO formation, which is present in both

SAA catalysts. However, for the XPS analysis, there are no satellite peaks between the Cu 2p doublet, often a characteristic feature of CuO (Figure 24). On the other hand, for the Cu LMM as compared with the reduced $Cu_{100}$ host catalyst (Figure 25), there is loss of a feature as well as significant broadening of the $L_3VV$ peak. This is a telltale sign of surface oxidation.[20,43,64]

The reaction profiles presented in Figures 29 and 33 show that $Cu_{100}$ (N) has an initial period of limited activity, which gradually increases as furfural is hydrogenated (hydrogen is activated). As mentioned previously, this period of minimal activity is when a layer of oxide has formed after adding the reaction mixture and the initial few hours of the reaction creates the process by which the catalyst re-reduces under mild conditions. It is intended that the critically low Pt content (0.09% and 0.004%) will have an effect on this reaction, boosting the rate of conversion in the same manner as seen in the bimetallic data (Figures 33 and 35). For this reason, the initial rate is the point at which the reaction truly begins and as soon as the oxide is fully reduced. Alternatively, when individual Pt atoms which inherently possess a higher surface energy than the host Cu atoms, the hydrogen pressure exerted during the reaction will cause the isolated Pt atoms to migrate up through the bulk host particle to the surface. Theoretical work has been completed by Skriver and Rosengaard[46] and more recently by Vitos and co-workers[45] who have comparable surface energy values for Cu and Pt. Vitos et al, who used a full charge density (FCD) functional, calculated the surface energy per metal on a number of low index faces ((100), (110) and (111)). By observing the dominant Cu face using XRD and TEM (Figures 7, 10-12 and 23), we can confirm that the surface energy of Cu per atom in a (111) array is 0.70 eV.[45,46] On the other hand, the surface energy of Pt per atom in the (111) structure is much higher at 1.0 eV[45,46] The SAA vs. binary alloy reaction profiles presented in Figure 39 show that by using 1.5 bar (near ambient pressure) there is no observable atom migration, which is evidenced by a lack of promotional effect. However, for the case of the $Pt_1Cu_{20}$ catalyst when pressure is applied to the system (10 bar), there is rapid furfural consumption after the 2 h period. This promotional effect is mirrored at higher pressure (20 bar) where the 'induction period', surface cleaning process or rate of Pt atom migration, is increased, as shown by the rapid furfural conversion over the 0.67 h period (shorter induction period).

Figure 40 shows similar reaction profiles plotted against the monometallic Cu host material without galvanic replacement (profiles seen in Figure 30). This Figure shows the true beneficial effect of atom replacement for the Cu (N) species where reaction conversions are increased by many orders of magnitude. Furthermore, the most dilute SAA ($Pt_{0.5}Cu_{250}$) does not seem to present a shift in the rate of atom migration. This could be because the substantial decrease in Pt content does not exhibit the same effect. This could also mean that the lower Pt content reduces the rate of surface cleaning. However, increasing the pressure does produce an increase in the initial rate of reaction (post induction period), leading to a higher conversion over the 7 h period.

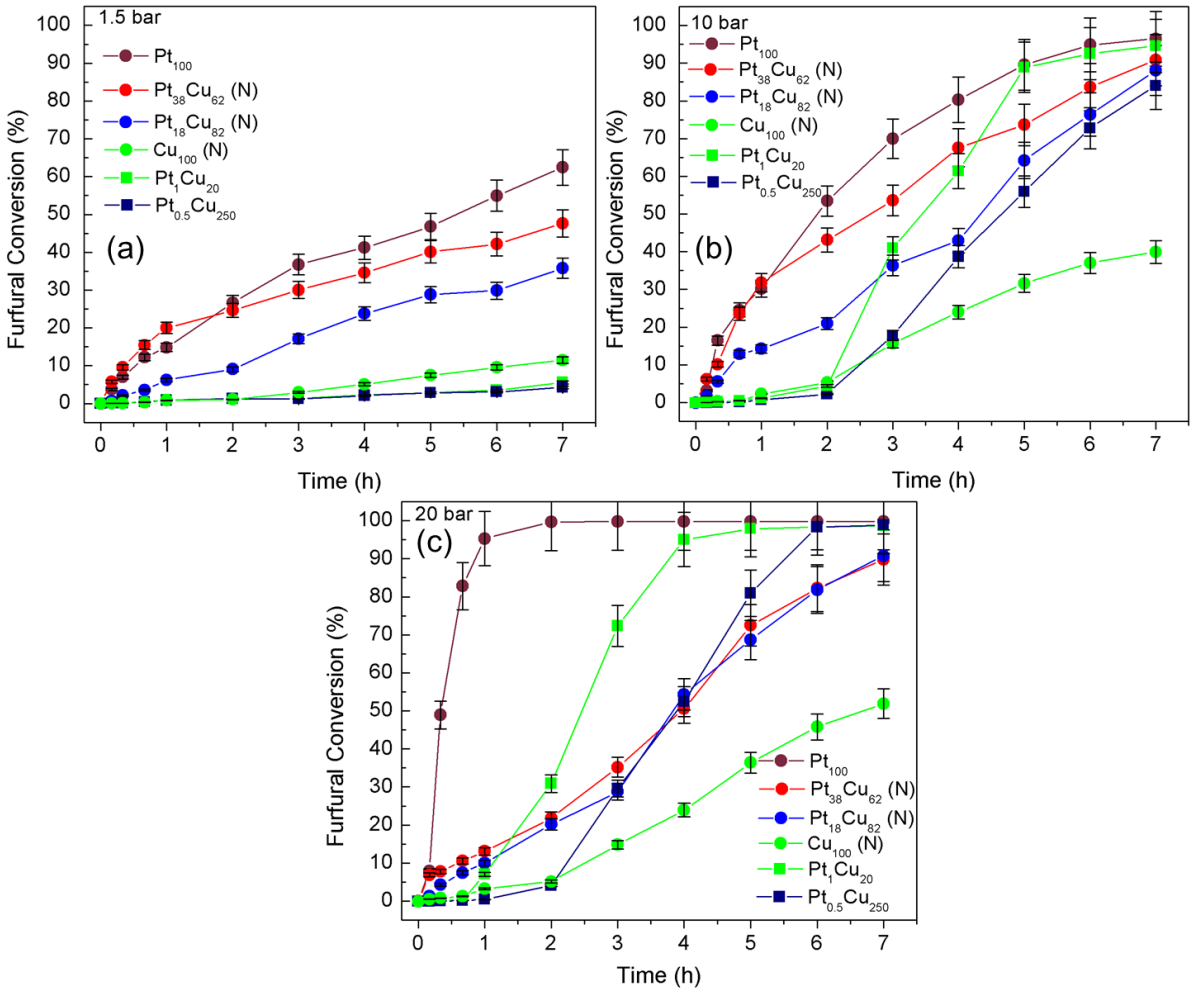


Figure 39 - Conversion profiles for Single Atom Alloy catalysts vs. monometallic Pt and binary alloy (N) catalysts across 3 different pressure regimes. SAA are represented by squares, nanoparticle based materials are represented by circles. (a) is reactions at near ambient pressure (1.5 bar), (b) is at 10 bar and (c) is at 20 bar.

In Figure 40, to make the reaction profiles more evident, error bars are not included as these are all present in previous iterations of this graph (Figures 30 and 39). For the SAA, the effect of pressure is far more significant than the bimetallic alloy nanoparticles. Bimetallic nanoparticles suffer from a slower rate of reaction due to competitive adsorption when operating at 20 bar. The SAA catalysts on the other hand have far less Pt sites that can dissociate hydrogen. As a result the hydrogen spillover from isolated Pt atoms can efficiently react with furfural bound to the larger Cu regions. $Pt_1Cu_{20}$ is by far the most effective catalyst for this reaction, under the conditions used and after the induction period, it exhibits initial rates of reaction that easily exceed the most active bimetallic catalyst, $Pt_{38}Cu_{62}$ (N), at 10 bar and even outperform the pure Pt material at 20 bar when normalized for mass of active metal (Figure 41). By also considering surface oxide formation during the addition of the reaction solution, the initial 2 h period (highlighted by a circle), as discussed previously for monometallic Cu, is still shown for SAAs. However, the difference between these materials is represented by $R_2$ (second rate of reaction for $Cu_{100}$ after surface cleaning) and $R_{2(SAA)}$. The SAA accelerated rate could also be attributed to surface oxide restricting $H_2$ spillover effects. Once the surface has been cleaned, rapid dissociation and hydrogenation occur. The rate of surface cleaning is seen to be enhanced for $Pt_1Cu_{20}$ at 20 bar where $R_{2(SAA*)}$ is shown to start from 40 min. The increased Pt loading appears to quicken the oxide reduction process.

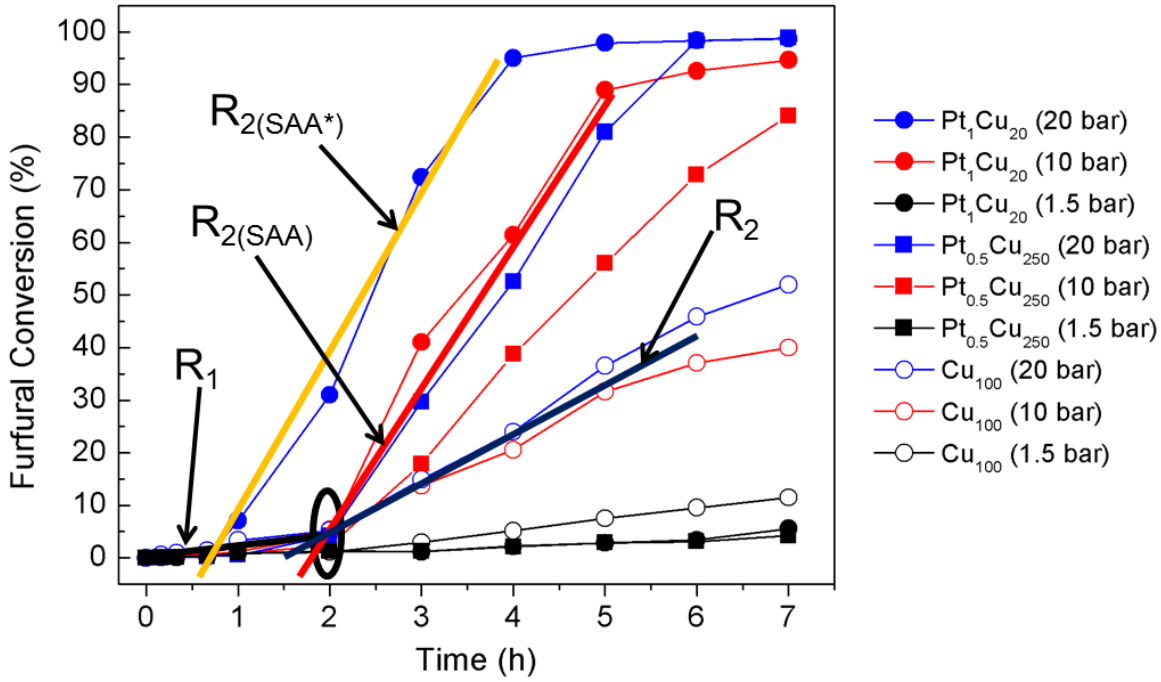


Figure 40 - Reaction profiles for both Single Atom Alloy catalysts vs. monometallic host $Cu_{100}$ across the range of pressures. Where $R_1$ (solid black line) is the initial pre-cleaning rate of reaction, $R_2$ (solid dark blue line) the second rate of reaction for $Cu_{100}$ post cleaning, $R_{2(SAA)}$ (solid red line) is the rate of reaction for SAA catalysts post cleaning and $R_{2(SAA*)}$ (solid green line) the enhanced rate of reaction for $Pt_1Cu_{20}$ operating at 20 bar.

By considering the total active metal content across the catalysts, a like-for-like analysis of Pt monometallic, PtCu bimetallic and SAA catalysts can take place. Comparative analysis is also shown in Figure 42 for the SAA vs. monometallic Cu catalysts. By taking 10 bar as the optimum pressure for the bimetallic catalysts, the difference in normalized rate across the three species can be represented as **$Pt_1Cu_{20}$ > $Pt_{38}Cu_{62}$ (N) > $Pt_{100}$**, where the values for each are 1058.8, 265.5 and 168.3 mmol $h^{-1}$ g.active $metal^{-1}$, respectively. This means that the SAA has a normalized rate ~4 times faster than the most active bimetallic catalyst and ~6.3 times more active than the 4.4 nm monometallic Pt nanoparticles.

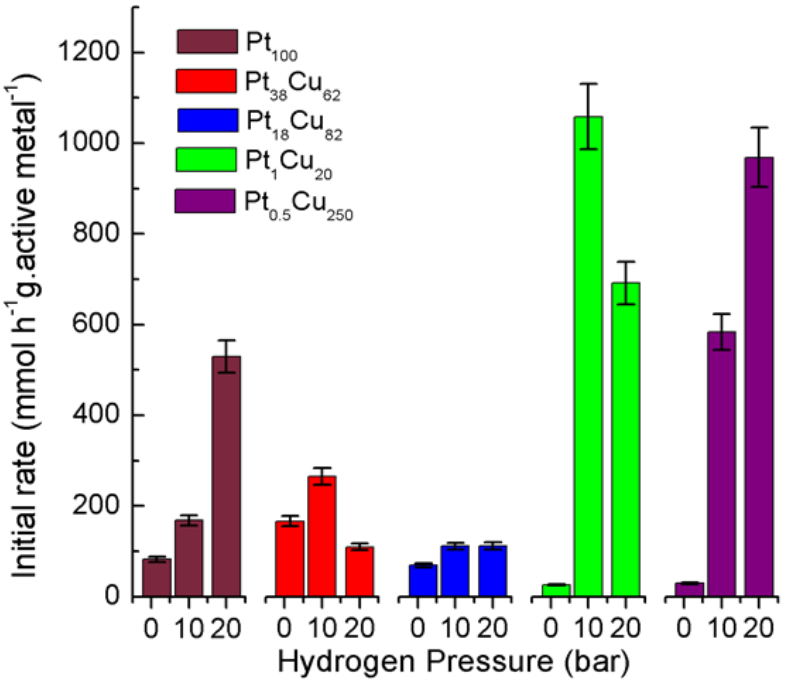


Figure 41 – Initial rates per gram of active metal for $Pt_{100}$, PtCu (N) bimetallic catalysts and SAA catalysts (post induction period) across 3 hydrogen pressures.

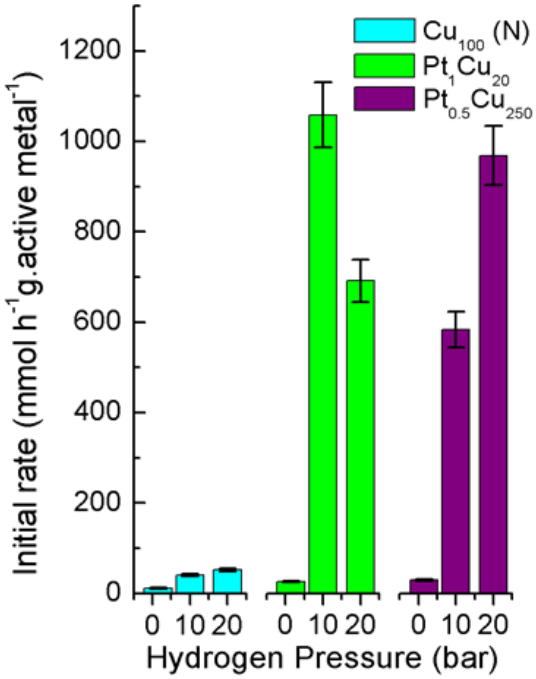


Figure 42 - Initial rates per gram of active metal for $Cu_{100}$ vs. SAA catalysts (post induction period) across 3 hydrogen pressures.

It was previously mentioned that CO titration measurements were not completed for SAAs due to the critically low Pt loading; which would require a substantially large amount of sample. Distinguishing differences in peak height when supplying 50 μL of CO per cycle would be extremely difficult, possibly beyond the limit of detection for the ChemBET instrument. From previous characterization data, (Figures 26-28), it is confirmed that the SAA catalysts possess atomically dispersed Pt. With this in mind, it is assumed as per the definition of a Single Atom Alloy (Chapter 1) that the surface Pt dispersion is 100%, as all of the Pt is on the surface.[47–49] With this assumption we can calculate turnover frequencies in the same manner as the monometallic and bimetallic nanoparticles. A comparison of turnover frequencies for all the Pt containing catalysts utilizing a $Cu(NO_3)_2$ precursor are shown in Figure 43.

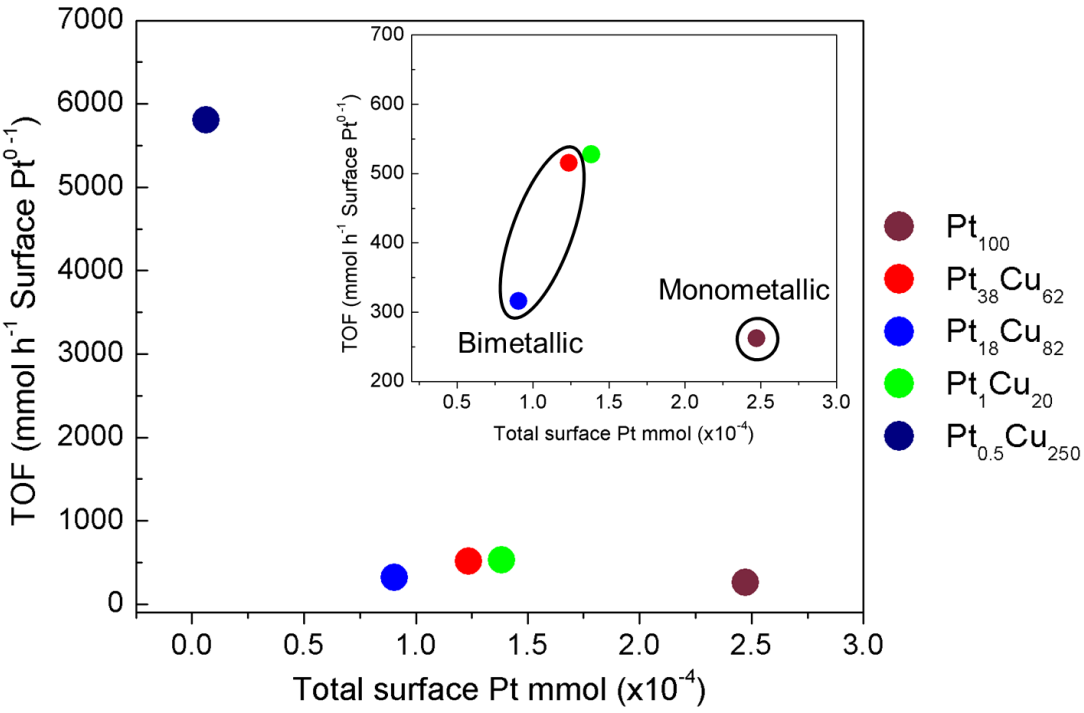


Figure 43 – Comparative TOF per surface Pt (mmol) for each catalyst operating at 10 bar, bimetallic (N), monometallic and SAA with the highest Pt content magnified in the inset image.

Combining the main section of Figure 43 with the inset image enables a clear distinction between bimetallic nanoparticles and $Pt_1Cu_{20}$ SAA to be made. Throughout this thesis the theory behind Single Atom Alloys is that the overall Pt content in the catalyst is at a

critically low point. However, logically, these systems will have a higher quantity of surface Pt than the other catalysts due to the fact they have no bulk structure. This means that for $Pt_1Cu_{20}$, where true catalytic activity is observed (post induction period), the TOF of the surface Pt is twice that of the monometallic Pt catalyst. This is not as high as previously expected and could mean that the initial atom migration point is not the point at which all of the single atoms have moved out of the bulk Cu. On the other hand, $Pt_{0.5}Cu_{250}$ which contains the lowest overall Pt content (surface $Pt^0$ - $6.1x10^{-6}$ mmol) can be described as a true Single Atom Alloy as the ratio of Pt to Cu is vast. By using the same period of time as the $Pt_1Cu_{20}$ catalyst, the post induction period point ($R_{2SAA}$) shows a very high initial rate of reaction. By using this value, as well as the Pt content and 100% atom dispersion, this catalyst presents a TOF of 5809 $h^{-1}$ a value which is over 10 times higher than the $Pt_1Cu_{20}$ SAA containing approximately 20 times less Pt. The most dilute SAA exhibits a TOF value around 22 times higher than the highly active Pt monometallic catalyst. The measure of TOF is useful as it shows the true efficiency of the Pt active sites in each catalyst. This being said, for the monometallic and bimetallic catalysts, these reaction sites are active immediately, whereas, the Single Atom Alloys both possess an induction period which provides a period of limited hydrogenation. During this time (initial 2 h of reaction), the other materials ($Pt_{100}$, $Pt_{38}Cu_{62}$ and $Pt_{18}Cu_{82)}$ when at 10 bar, present much higher conversions, 53.5%, 43.1% and 21.0% of the substrate respectively.

Table 12 shows reaction selectivities across the three pressures for the Single Atom Alloy catalysts. As marked by their incredible rates of reaction after the allotted period of time when operating at pressure, the atom efficient catalysts convert 94.6% ($Pt_1Cu_{20}$) and 84.1% ($Pt_{0.5}Cu_{250}$) when operating at 10 bar pressure. This increases to 98.7% and 98.9% respectively as pressure is raised to 20 bar. After the induction process occurs and the Single Atom Alloys are ‘activated’ the selectivity towards furfuryl alcohol is over 92% in both cases. However, if the materials are not activated, the catalysts operate in a very similar way to bulk Cu nanoparticles, providing poor activity over the 7 h period with selectivities favouring decarbonylation reaction pathways. Unlike the bimetallic nanoparticles there was no detectable C=C hydrogenation in the furan ring. Likewise there was no acetal or methyl furan produced in these reactions.

Table 12 - Reactivity of atomically dispersed Pt, immobilized on Cu nanoparticles across 3 pressures, selectivities taken after 7 h.

| Catalyst | $H_2$ Pressure (bar) | Conversion (%) | Furan S (%) | Furfuryl alcohol S (%) |
|---|---|---|---|---|
| $Pt_1Cu_{20}$ | 1.5 | 5.5 | 98.5 | 1.5 |
| | 10 | 94.6 | 9.8 | 92.2 |
| | 20 | 98.7 | 1.6 | 98.4 |
| $Pt_{0.5}Cu_{250}$ | 1.5 | 4.3 | 93.1 | 6.9 |
| | 10 | 84.1 | 5.9 | 94.1 |
| | 20 | 98.9 | 2.7 | 97.3 |

## 5.4 Conclusions

The protocol for generating bimetallic catalysts has proven to be very effective for creating catalysts with varying amounts of platinum and copper. This was accomplished using two different Cu precursors (nitrate and sulphate). Upon reducing the formed catalysts at 300 $^oC$ under a hydrogen atmosphere, a very prominent $Cu_3Pt$ peak was seen for the alloyed catalysts. Both the bimetallic and monometallic catalysts also proved to be thermally stable up to 500 $^oC$, showing that particle growth through sintering was not possible. The literature reports that Pt is stable up to temperatures over 600 $^oC$. Thermal processing, as well as addition of Cu, proved not to form spinel structures with the alumina support. These materials were thoroughly characterized by TEM, EDX, XPS, ICP-OES and CO titrations. It was found that the alloying process generated slightly larger nanoparticles than the monometallic $Pt_{100}$ material, ~8 nm vs. 4.4 nm for pure Pt. Upon imaging the bimetallic particles, EDX spectra were recorded and elemental mapping proved that the intended metal ratios/experimental ratios were in agreement with one and other. Surface metal composition determined via XPS also compared well with EDX analysis of the metal ratios present. X-ray Photoelectron Spectroscopy showed that the Cu content of the bimetallic nanoparticles contained no surface oxide, as observed by the Cu LMM suggesting no loss of features nor broadening of the $L_3VV$ peak. Interestingly, there was a subtle shift in Cu 2p for the $Pt_{38}Cu_{62}$ catalyst suggesting that the alloying of the Cu had caused an electronic effect in the material.

By creating a monometallic Cu/$\gamma$-$Al_2O_3$ material, following the methodology shown in Chapter 2, Cu particles could be calcined (removal of capping agent) and then reduced. Upon reduction the catalyst was transferred to an acidified solution where galvanic replacement successfully took place forming a SAA catalyst, or an 'Atomically Dispersed Supported Metal Catalyst' (ADSMC),[48,49] shown in Figures 26 and 27. TEM analysis of these materials clearly shows the presence of Pt atoms, albeit, they cannot be construed as true isolated species as there are a number of neighboring Pt atomic entities. XRD analysis of these materials does not show a $Cu_3Pt$ peak, which is encouraging as the atomic entities have not agglomerated and alloyed with the host particle during the galvanic replacement process.

Catalytic testing proved that a low loading of Cu on $\gamma$-$Al_2O_3$ resulted in a very poor furfural conversion over 7 h with selectivities favouring furfuryl alcohol only once pressure is applied to the system (>10 bar). However, alloying Pt and Cu together to form binary alloy nanoparticles resulted in a dramatic increase in furfural conversion over time. For the 38:62 ratio bimetallic from the (N) family, there was a beneficial effect on the reaction (from 1.5 – 10 bar). This involved comparable conversion and selectivies. As the monometallic Pt bench mark catalyst, the bimetallic catalyst boasted superior rates of reaction and once normalized for metal content, proved to be orders of magnitude superior with TOF more than doubling. The bimetallic catalysts from both families of materials (N and S) showed diminished activity at 20 bar, suggesting that due to competitive adsorption, $H_2$ was rapidly activated restricting adsorption of furfural. Residual sulphur on the bimetallic catalyst formed through the deposition of $CuSO_4$, had a lower activity as compared to the nitrate based materials overall. This is due to the steric effect of sulphur on the surface and its affinity to bind with sites of highest co-ordination. Ultimately, between the two families of bimetallics, the reactions reach similar conversions after 7 h, which means that the sulphur on the whole has no ill effect on the life of the catalyst. However, for the case of the monometallic Cu, the sulphur component appears to promote furan. This is represented by much higher selectivity towards the decarbonylation product.

Initial rates for bimetallic catalysts per gram of Pt have been found to be superior to the $Pt_{100}$ catalyst. The introduction of Cu into the nanoparticle was found to be beneficial by (i) generating a bimetallic surface ($Cu_3Pt$) that appears to adsorb furfural more readily than pure Pt sites, and (ii) protect the Pt sites from poisoning via CO formed through decarbonylation reaction pathways. Increasing the hydrogen pressure was found to produce a small amount of tetrahydrofurfuryl alcohol. As the best operating reaction conditions for this system are still relatively mild in comparison with those seen in the literature (50 $^{o}$C at 10 bar) and by using reduced Pt content, the data has shown that PtCu bimetallic catalysts are a viable, green and environmentally friendly alternative to current industrial systems.

Finally, the use of atom efficient Single Atom Alloys, although often scrutinized for their ability to readily poison, have been shown to be dramatically more active after a period of induction, when Pt entities could potentially migrate from the bulk Cu particle where they have minimized their energy during the reduction process. Alternatively, by the addition of dissolved oxygen in the reaction solution which can oxidize the Cu surface. After this point ($R_1$ to $R_{2SAA}$, as shown in Figure 40) the true initial rates of reaction are worlds apart from any of the data shown in this thesis, proving to be more active than the monometallic Pt catalyst which exhibited incredible initial rates when at 20 bar. Turnover frequencies for both SAA materials tested proved to be higher than all other tested materials, with the most dilute alloy ($Pt_{0.5}Cu_{250}$) seen to be over 10 times more active than its SAA counterpart, $Pt_1Cu_{20}$, and over 20 times more active than 4.4 nm Pt nanoparticles, which were proven to be highly active in the literature.[1,12]

## 5.5 References


1 M. J. Taylor, L. J. Durndell, M. A. Isaacs, C. M. A. Parlett, K. Wilson, A. F. Lee and G. Kyriakou, *Appl. Catal. B Environ.*, 2016, **180**, 580–585.

2 G. Kyriakou, M. B. Boucher, A. D. Jewell, E. A. Lewis, T. J. Lawton, A. E. Baber, H. L. Tierney, M. Flytzani-Stephanopoulos and E. C. H. Sykes, *Science*, 2012, **335**, 1209–12.

3 H. L. Tierney, A. E. Baber, J. R. Kitchin and E. C. H. Sykes, *Phys. Rev. Lett.*, 2009, **103**, 1–4.

4 M. E. Chiu, G. Kyriakou, F. J. Williams, D. J. Watson, M. S. Tikhov and R. M. Lambert, *Chem Commun*, 2006, 1283–1285.

5 M. E. Chiu, D. J. Watson, G. Kyriakou, M. S. Tikhov and R. M. Lambert, *Angew. Chemie - Int. Ed.*, 2006, **45**, 7530–7534.

6 J. Barbier, E. Lamy-Pitara, P. Marecot, J. P. Boitiaux, J. Cosyns and F. Verna, *Adv. Catal.*, 1990, **37**, 279–318.

7 P. Rylander, *Catalytic Hydrogenation over Platinum Metals*, Academic Press, New York, 1967.

8 A. Mandalika, L. Qin, T. K. Sato and T. Runge, *Green Chem.*, 2014, **16**, 2480–2489.

9 M. J. Taylor, L. Jiang, J. Reichert, A. C. Papageorgiou, S. K. Beaumont, K. Wilson, A. F. Lee, J. V Barth and G. Kyriakou, *J. Phys. Chem. C*, 2017, **121**, 8490–8497.

10 S. Srivastava, G. C. Jadeja and J. Parikh, *RSC Adv.*, 2016, **6**, 1649–1658.

11 S. Sitthisa, T. Sooknoi, Y. Ma, P. B. Balbuena and D. E. Resasco, *J. Catal.*, 2011, **277**, 1–13.

12 V. V Pushkarev, N. Musselwhite, K. An, S. Alayoglu and G. A. Somorjai, *Nano Lett.*, 2012, **12**, 5196–201.

13 M. B. Boucher, B. Zugic, G. Cladaras, J. Kammert, M. D. Marcinkowski, T. J. Lawton, E. C. H. Sykes and M. Flytzani-Stephanopoulos, *Phys. Chem. Chem. Phys.*, 2013, **15**, 12187–96.

14 F. R. Lucci, J. Liu, M. D. Marcinkowski, M. Yang, L. F. Allard, M. Flytzani-Stephanopoulos and E. C. H. Sykes, *Nat. Commun.*, 2015, **6**, 8550.

15 S. Zhou, B. Varughese, B. Eichhorn, G. Jackson and K. McIlwrath, *Angew. Chemie - Int. Ed.*, 2005, **44**, 4539–4543.

16 C. J. Powell and A. Jablonski, *NIST Electron Inelastic-Mean-Free-Path Database*, 2010.

17 F. M. Doyle, R. Woods and G. H. Kelsall, *Electrochemistry in Mineral and Metal Processing 8*, The Electrochemical Society, Illustrate., 2010.

18 V. Krylova and M. Andruleviçius, *Int. J. Photoenergy*, 2009, **3**, 1–7.

19 L. Kundakovic and M. Flytzani-Stephanopoulos, *Appl. Catal. A-General*, 1998, **171**, 13–29.

20 J. Pike, S. W. Chan, F. Zhang, X. Wang and J. Hanson, *Appl. Catal. A Gen.*, 2006, **303**, 273–277.

21 Y. Li, Q. Fu and M. Flytzani-Stephanopoulos, *Appl. Catal. B Environ.*, 2000, **27**, 179–191.

22 L. D. Chen, M, Schmidt, *J. Catal.*, 1978, **55**, 348–360.

23 T. Tanabe, Y. Nagai, K. Dohmae, H. Sobukawa and H. Shinjoh, *J. Catal.*, 2008, **257**, 117–124.

24 A. K. Schuppert, A. Savan, A. Ludwig and K. J. J. Mayrhofer, *Electrochim. Acta*, 2014, **144**, 332–340.

25 C. Macken and B. K. Hodnett, *Ind. Eng. Chem. Res.*, 1998, **5885**, 2611–2617.

26 A. A. Dubale, A. G. Tamirat, H.-M. Chen, T. A. Berhe, C.-J. Pan, W.-N. Su and B.-J. Hwang, *J. Mater. Chem. A*, 2016, **4**, 2205–2216.

27 I. V. Yentekakis, G. Goula, P. Panagiotopoulou, S. Kampouri, M. J. Taylor, G. Kyriakou and R. M. Lambert, *Appl. Catal. B Environ.*, 2016, **192**, 357–364.

28 M. T. Alotaibi, M. J. Taylor, D. Liu, S. K. Beaumont and G. Kyriakou, *Surf. Sci.*, 2016, **646**, 179–185.

29 C. M. A. Parlett, M. A. Isaacs, S. K. Beaumont, L. M. Bingham, N. S. Hondow, K. Wilson and A. F. Lee, *Nat. Mater.*, 2015, **15**, 178–182.

30 C. J. Villagomez, O. Guillermet, S. Goudeau, F. Ample, H. Xu, C. Coudret, X. Bouju, T. Zambelli and S. Gauthier, *J. Chem. Phys.*, 2010, **132**.

31 A. Nath and A. Khare, *J. Appl. Phys.*, 2011, **110**.

32 X. Wang, J. Zhuang, Q. Peng and Y. Li, *Nature*, 2005, **437**, 121–124.

33 W. Kang, R. Li, D. Wei, S. Xu, S. Wei and H. Li, *RSC Adv.*, 2015, **5**, 94210–94215.

34 L. Cao, G. Zhang, W. Lu, X. Qin, Z. Shao, B. Yi, G. Lu, S. Sun, A. Zettl, Y. Wang,

X. Duan, T. Mueller, Y. Huang, N. Markovic, G. Somorjai, P. Yang and V. R. Stamenkovic, *RSC Adv.*, 2016, **6**, 39993–40001.

35 B. Shan, Y. Zhao, J. Hyun, N. Kapur, J. B. Nicholas and K. Cho, *J. Phys. Chem. C*, 2009, **113**, 6088–6092.

36 R. Chen, Z. Chen, B. Ma, X. Hao, N. Kapur, J. Hyun, K. Cho and B. Shan, *Comput. Theor. Chem.*, 2012, **987**, 77–83.

37 K. Fulajtárova, T. Soták, M. Hronec, I. Vávra, E. Dobročka and M. Omastová, *Appl. Catal. A Gen.*, 2015, **502**, 78–85.

38 T. Ghodselahi, M. A. Vesaghi, A. Shafiekhani, A. Baghizadeh and M. Lameii, *Appl. Surf. Sci.*, 2008, **255**, 2730–2734.

39 M. C. Biesinger, L. W. M. Lau, A. R. Gerson and R. S. C. Smart, *Appl. Surf. Sci.*, 2010, **257**, 887–898.

40 G. Fierro, M. Lo Jacono, M. Inversi, R. Dragone and P. Porta, *Top. Catal.*, 2000, **10**, 39–48.

41 A. L. Wang, C. Zhang, W. Zhou, Y. Y. Tong and G.-R. Li, *AlChE Lett.*, 2016, **62**, 975–983.

42 Z. Xu, H. Zhang, S. Liu, B. Zhang, H. Zhong and D. S. Su, *Int. J. Hydrogen Energy*, 2012, **37**, 17978–17983.

43 O. P. H. Vaughan, G. Kyriakou, N. MacLeod, M. Tikhov and R. M. Lambert, *J. Catal.*, 2005, **236**, 401–404.

44 T. Yano, M. Ebizuka, S. Shibata and M. Yamane, *J. Electron Spectros. Relat. Phenomena*, 2003, **131**–**132**, 133–144.

45 L. Vitos, A. V. Ruban, H. L. Skriver and J. Kollár, *Surf. Sci.*, 1998, **411**, 186–202.

46 H. L. Skriver and N. M. Rosengaard, *Phys. Rev. B*, 1992, **46**, 7157–7168.

47 B. C. Gates, *Chem. Rev.*, 1995, **95**, 511–522.

48 M. Flytzani-Stephanopoulos and B. C. Gates, *Annu. Rev. Chem. Biomol. Eng.*, 2012, **3**, 545–574.

49 J. Liu, *ACS Catal.*, 2016, **7**, 34–59.

50 J. M. Thomas, R. Raja and D. W. Lewis, *Angew. Chemie - Int. Ed.*, 2005, **44**, 6456–6482.

51 J. Bell, D. Kubler, P. Sartwell and R. G. Zepp, *J. Org. Chem.*, 1965, **30**, 4284–4292.

52 E. Adams and H. Adkins, *J. Am. Chem. Soc.*, 1925, **47**, 1358–1367.

53 N. Minne and H. Adkins, *J. Am. Chem. Soc.*, 1933, **55**, 299-309.

54 S. Sitthisa and D. E. Resasco, *Catal. Letters*, 2011, **141**, 784–791.

55 M. M. Villaverde, T. F. Garetto and A. J. Marchi, *Catal. Commun.*, 2015, **58**, 6–10.

56 M. M. Villaverde, N. M. Bertero, T. F. Garetto and A. J. Marchi, *Catal. Today*, 2013, **213**, 87–92.

57 Z. Liangke, X. Chenghua, L. Wenbiao, L. Jianying, L. Jun, D. Xingjie, G. Yan and Y. Yingchun, *Chinese J. Catal.*, 2010, **31**, 461–465.

58 B. M. Nagaraja, V. Siva Kumar, V. Shasikala, A. H. Padmasri, B. Sreedhar, B. David Raju and K. S. Rama Rao, *Catal. Commun.*, 2003, **4**, 287–293.

59 R. Rao, R. Baker and M. Vannice, *Catal. Letters*, 1999, **60**, 51–57.

60 B. Nagaraja, A. Padmasri, B. Raju and K. Rama Rao, *J. Mol. Catal. A Chem.*, 2007, **265**, 90–97.

61 UKBullion, *Curr. Price Pt per gram - 02/04/17*.

62 O. F. Aldosari, S. Iqbal, P. J. Miedziak, G. L. Brett, D. R. Jones, X. Liu, J. K. Edwards, D. J. Morgan, D. K. Knight and G. J. Hutchings, *Catal. Sci. Technol.*, 2016, **6**, 234-242.

63 S. Iqbal, X. Liu, O. F. Aldosari, P. J. Miedziak, J. K. Edwards, G. L. Brett, A. Akram, G. M. King, T. E. Davies, D. J. Morgan, D. K. Knight and G. J. Hutchings, *Catal. Sci. Technol.*, 2014, **4**, 2280.

64 J. Y. Kim, J. A. Rodriguez, J. C. Hanson, A. I. Frenkel and P. L. Lee, *J. Am. Chem. Soc.*, 2003, **125**, 10684–10692.

65 T. Katayama and T. Nitta, *J. Chem. Eng. Data*, 1976, **21**, 194–196.

66 F. Takemura and A. Yabe, *J. Chem. Eng. Data*, 1996, **41**, 1141–1143.

67 N. İnoğlu and J. R. Kitchin, *Mol. Simul.*, 2009, **35**, 936–941.

68 H. Adkins and E. Adams, *J. Am. Chem. Soc.*, 1925, **47**, 1043–1048.

69 N. Melchior, *J. Am. Chem. Soc.*, 1949, **283**, 3651–3654.

70 B. Liu, L. Cheng, L. Curtiss and J. Greeley, *Surf. Sci.*, 2014, **622**, 51–59.

71 S. M. Rogers, C. R. A. Catlow, C. E. Chan-Thaw, A. Chutia, N. Jian, R. E. Palmer, M. Perdjon, A. Thetford, N. Dimitratos, A. Villa and P. P. Wells, *ACS Catal.*, 2017, **7**, 2266–2274.

72 D. Shi and J. M. Vohs, *ACS Catal.*, 2015, **5**, 2177–2183.

73 K. Yuge, Y. Koyama, A. Kuwabara and I. Tanaka, *J. Phys. Condens. Matter*, 2014, **26**, 355006.

74 J. Liu, F. R. Lucci, M. Yang, S. Lee, M. D. Marcinkowski, A. J. Therrien, C. T. Williams, E. C. H. Sykes and M. Flytzani-Stephanopoulos, *J. Am. Chem. Soc.*, 2016, **138**, 6396–6399.

75 F. R. Lucci, M. D. Marcinkowski, T. J. Lawton and E. C. H. Sykes, *J. Phys. Chem. C*, 2015, **119**, 24351–24357.

76 J. Lin, B. Qiao, N. Li, L. Li, X. Sun, J. Liu, X. Wang and T. Zhang, *Chem. Commun.*, 2015, **51**, 7911–7914.

77 H. Wei, X. Liu, A. Wang, L. Zhang, B. Qiao, X. Yang, Y. Huang, S. Miao, J. Liu and T. Zhang, *Nat. Commun.*, 2014, **5**, 1–8.

78 B. Qiao, A. Wang, X. Yang, L. F. Allard, Z. Jiang, Y. Cui, J. Liu, J. Li and T. Zhang, *Nat. Chem.*, 2011, **3**, 634–641.

# Chapter 6 – Conclusions and Future work

## 6.1 Conclusions

### 6.1.1 The catalytic hydrogenation and HDO of furfural on a Pt extended surface

The purpose of this project was to understand the furfural hydrogenation reaction on platinum in a variety of environments. The first study (Chapter 3) was carried out on a model catalytic system using a Pt(111) single crystal under ultra-high vacuum.[1] It was found that the reaction was dependent on a number of conditions such as furfural exposure and the dosing order of the furfural or hydrogen. This led to observable differences in molecular geometry and therefore, the furfural bonding position on Pt(111). Orientation differences were characterized via STM and TPR. On a clean surface, the furfural favoured only one reaction pathway, decarbonylation, which is where the dominant product furan was observed with substantial surface carbon laydown preventing further adsorption. As the furfural exposure was increased, the conversion was found to decrease. This fall in furan production is clearly due to the steric crowding on the surface as the parent molecule was seen to order into a side on, tilted geometry at high coverage. As the furfural was unable to auto-hydrogenate due to furfural desorption rate limitations, an additional hydrogen source was used. It was found that the exposure order was of high importance and that supplying furfural onto the bare surface inhibited the subsequent dissociation and chemisorption of hydrogen, which prevented hydrogenation. However, by introducing furfural to a hydrogen pre-covered (0.4 ML) surface, furfuryl alcohol and methyl furan were formed. The excess hydrogen allowed the HDO reaction pathway by over converting the adsorbed furfuryl alcohol. Once again surface coverage varied the reaction selectivity proving that at a higher exposure the tilted furfural in the presence of hydrogen favoured hydrogenation over HDO. This is summarized in Figure 1 with Figure 1a showing the conversion and selectivity of the furfural reaction on a bare Pt(111) surface. The selectivity towards furan does not vary dramatically upon increasing exposure. Figure 1b shows the furfural reaction on a hydrogen pre-covered surface with the hydrogen presence remaining the same throughout the TPR experiments. It was found that the presence of hydrogen passivated the surface carbon formation as furfural exposure was increased.

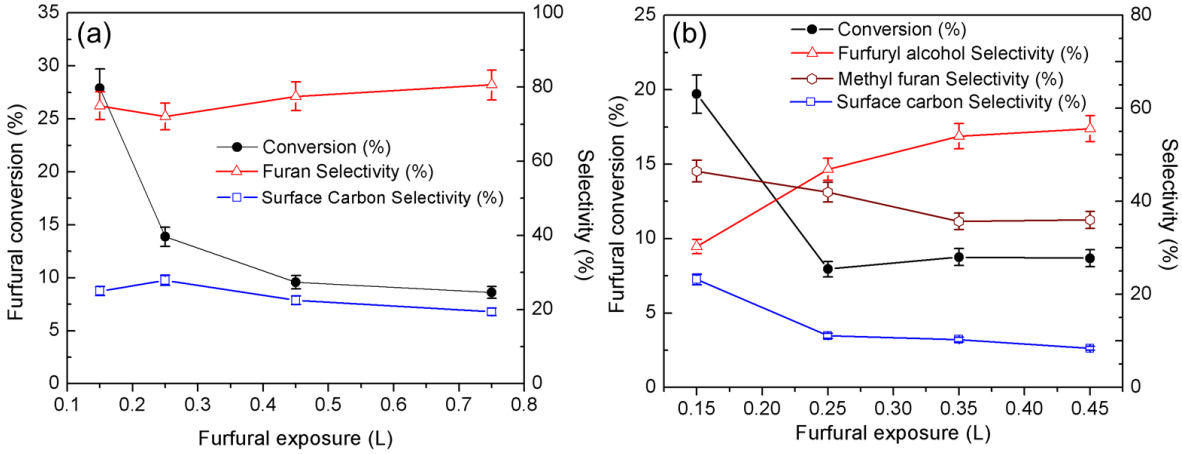


Figure 1 - Where (a) is the reactivity of the Pt(111) at varying furfural exposure. (b) Furfural reactivity over Pt(111) pre-exposed to 100 L $H_2$ as a function of furfural exposure.

### 6.1.2 Highly selective hydrogenation of furfural over supported Pt nanoparticles under mild conditions

Highly monodisperse size specific Pt nanoparticles were synthesized via a modified polyol method and dispersed on a number of oxide supports, $SiO_2$, ZnO, $\gamma$-$Al_2O_3$, $CeO_2$ and MgO.[2] These catalysts were then applied to the liquid phase hydrogenation of furfural under near ambient hydrogen pressure, where temperature and reaction solvent proved to be imperative when optimizing the selectivity and activity of the catalyst. Initial reactions were carried out in ethanol at 70 $^{o}$C, which was found to generate a high selectivity towards acetal based side reactions. Although these are very useful in the perfume and flavourings industries, this was not the desired product for furfural upgrading. To choose the most selective catalyst from the series ($\gamma$-$Al_2O_3$) a solvent screening process was carried out where a range of solvents with different carbon chain length (alcohols) as well as solvents with various polarities and hydrogen solubility were investigated. It was found that methanol was the most effective solvent for the reaction, possessing a high hydrogen solubility but requiring a large amount of energy to generate hemiacetal species (intermediate for acetalization). The system was optimized further by reducing the operational temperature, which decreased acetal side reactions to 0% across all catalysts and brought selectivities to almost 100% for furfuryl alcohol with very high activity for three Pt based catalysts supported on, $\gamma$-$Al_2O_3$, $CeO_2$ and MgO. These catalysts also proved

to be highly recyclable across three cycles. However, Pt/ZnO proved to readily deactivate due to CO adsorption generated through the decarbonylation reaction pathway.

### 6.1.3 The effect of Cu in PtCu bimetallic particles and Single Atom Alloys for the transformation of furfural

Following on from the monometallic work completed in Chapter 4, bimetallic PtCu catalysts were synthesized at various molar ratios to dilute the noble metal content. This method of synthesis was adapted from the one used for the monodisperse particles shown in Chapter 4, which had an average particle size of ~4 nm for $\gamma$-$Al_2O_3$. It involved adding a second precursor ($Cu(NO_3)_2$ or $CuSO_4$) at the same time as the $H_2PtCl_6.xH_2O$ via syringe pump. Once suspended, the nanoparticles were deposited on $\gamma$-$Al_2O_3$, which were characterized thoroughly with PXRD, XPS, HRTEM and EDX. They all displayed signs of PtCu alloy formation with the presence of a $Cu_3Pt$ region (PXRD), a visible shift in the Cu 2p region (XPS) and line scans showing individual nanoparticles containing a random arrangement of Pt and Cu atoms. Metal loadings and surface concentrations, as determined by ICP-OES and XPS, show that all the catalysts synthesized from the (N) family had molar ratios that matched very closely with the two forms of characterization. The bimetallic particles were also found to be thermally stable. Electron microscopy measurements confirmed that the bimetallic particle size, in conjunction with PXRD and chemical titration (CO chemisorption), to be slightly larger than the monometallic Pt nanoparticles (an increase from 4.4 – 8 nm). Hydrogenation reactions were carried out at various pressures (~1.5, 10 and 20 bar), with the solvent and temperature remaining the same as the optimized conditions mentioned in Chapter 4. For the (N) family of catalysts, both the bimetallic materials exhibited superior TOFs than the monometallic Pt catalyst when operating at 1.5 and 10 bar. Normalizing initial rates of reaction per gram of active metal proved that the $Pt_{38}Cu_{62}$ outperformed the $Pt_{100}$ catalyst by 2 times (1.5 bar) and 1.6 times (10 bar). When operating at the highest pressure (20 bar) both the bimetallic catalysts suffered from diminished rates of reaction, which were attributed to competitive adsorption, where the hydrogen spillover from the Pt sites to Cu regions restricted the uptake of furfural. This was not the case for the $Pt_{100}$ which demonstrated TOFs almost 4 times greater than the bimetallic counter parts. However, after 7 h all the Pt containing

catalysts presented conversions of ~90% with very high selectivities towards furfuryl alcohol.

Binary alloys synthesized using the sulphur containing precursor produced catalysts which were comparable with the (N) family in terms of Pt dispersion, bimetallic particle size (XRD) and high selectivity towards furfuryl alcohol when operating at high pressure. The issue with this family of materials is that although washed and thermally processed, the nanoparticles appear to be hindered by residual sulphur. This element is sterically unfavoured because it binds to areas of highest co-ordination and restricts hydrogen activation or furfural adsorption. Surface bound sulphur appears to promote furan selectivity when at low pressure, while only dampening initial catalyst activity when higher pressures are used. Turnover frequencies for the two families of materials show the $CuSO_4$ born materials to be very much inferior, as TOF values are substantially lower.

#### 6.1.3.1 Furfural hydrogenation with Single Atom Alloys in the liquid phase

Single Atom Alloys were successfully synthesized via galvanic replacement of sacrificial host Cu nanoparticles. By using critically low Pt loadings, the reaction profile of these catalysts appeared to be very similar to the monometallic Cu species until a point of induction was overcome. The period of induction accounts for the time at which surface CuO formed through oxygen dissolved in the reaction mixture is reduced, so that hydrogen can successfully move from the atomic Pt entities to the Cu host particle. It could also be the migration of the Pt single atoms from the bulk Cu particle to the surface,[3,4] at which time the active sites rapidly dissociate hydrogen. This then reacts with the surface bound furfural on the Cu sites via hydrogen spillover.[5] Alternatively, the process is represented by incredibly high initial rates of reaction; observable at both 10 and 20 bar $H_2$ for both SAA materials ($Pt_1Cu_{20}$ and $Pt_{0.5}Cu_{250}$). The SAA with the lowest Pt content presented a slightly lower rate of reaction post induction, as less hydrogen was supplied to the Cu surface. Reactions conducted at ~1.5 bar suggested that the catalysts operate as a pure Cu species, showing no promotional effect from the atomic entities as they reside in the Cu bulk. Carbon monoxide titration could not be completed for these catalysts and therefore TOF were calculated in the same way shown for the bimetallic catalyst by assuming that, for an

atomically dispersed catalyst, the surface dispersion is 100% (Figure 2).[6,7] The initial rate per gram of active metal post atom migration, compared with the initial hour of the bimetallic reaction, proved to be orders of magnitude higher than all of the bimetallic and monometallic catalysts at both 10 and 20 bar. The comparison was made at these points as the SAA exhibits true turnover once the material is activated, whereas the nanoparticle alloys are active from the start of the reaction and no in situ activation is required, whether involving atom migration of surface cleaning (oxide reduction).

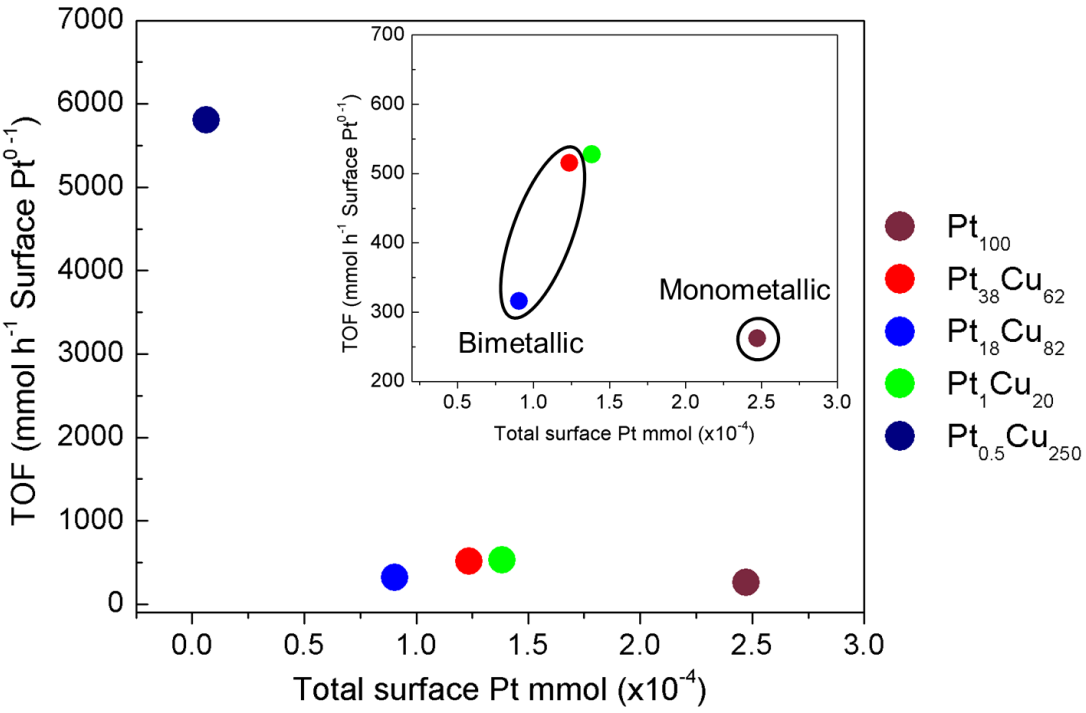


Figure 2 - Comparative TOF per surface Pt (mmol) for each catalyst operating at 10 bar.

By normalizing these results further, taking into consideration the economic viability of Pt as an active component, binary alloy nanoparticles were far more active and cheaper in terms of Pt than the monometallic catalysts shown in Chapter 4. However, Single Atom Alloy catalysts are not only superior in terms of activity but are also more economically viable in comparison with current catalytic packages used in industry. The cost of platinum content per gram of total catalyst synthesized, for each catalyst shown in Figure 2, is presented in Table 1. At the time of writing this thesis the price of Pt was £25 per gram.

Table 1 - The price of the Pt component for 1 g of synthesized catalyst

| Catalyst | Price per of Pt component (£) |
|---|---|
| $Pt_{100}$ | 0.2997 |
| $Pt_{38}Cu_{62}$ (N) | 0.0999 |
| $Pt_{18}Cu_{82}$ (N) | 0.0500 |
| $Pt_1Cu_{20}$ | 0.0225 |
| $Pt_{0.5}Cu_{250}$ | 0.0010 |

## 6.2 Future work

### 6.2.1 The hydrogenation and HDO of furfural on a Pt(111)

To better tie the work reported in Chapter 3 to the other projects in this thesis, the furfural transformation reactions should also be carried out on a bare and modified Cu(111) surface. As Cu(111) was the dominant face produced for nanoparticles (Chapter 5), Pt atoms could then be deposited via a source at increasing coverage to simulate (i) a bimetallic alloyed surface, by using a surface coverage of 0.5 ML and 0.25 ML ($Pt_{50}Cu_{50}$, $Pt_{25}Cu_{75}$) and (ii) very low exposures to generate a dilute disperse surface, <0.05 ML.[8,9,5,10,11] These measurements would determine whether there is an alloy effect promoting the hydrogenation reaction whilst protecting the Pt sites from carbon laydown. These measurements would also be interesting to ascertain whether aromatic hydrogenation occurs when Pt is accompanied by Cu. This over hydrogenation was briefly seen in the liquid phase reactions but not seen on the bare Pt(111) measurements. By altering the surface structure, molecular geometry should also be different; this could prove to be very interesting, as reaction selectivity tends to be dependent on this aspect.

### 6.2.2 Near ambient pressure liquid phase furfural hydrogenation with $Pt/MO_x$

The near ambient liquid phase reactions were optimized to maximize furfuryl alcohol selectivity whilst presenting high activity. A future development would be to determine initial rates and compare TOFs for each of the catalysts, also to contrast this with reactions where $H_2$ is gently bubbled through the reaction in place of a static atmosphere.

### 6.2.3 The effect of a co-metal for binary alloy catalysts

It has been shown, in great detail, that by using the modified polyol procedure, bimetallic nanoparticles can be synthesized with accurate control over metal ratios. However, using a second metal in place of Cu could provide greater activity for the system by possibly exploring reaction pathways leading to methyl furan or ring opening products. This may prove to be very beneficial for a number of chemical industries. Alternatively, the existing system could be modified to move away from conditions tailored to selective hydrogenation and shift to slightly harsher conditions in an attempt to create a PtCu synergistic effect to produce other products.

### 6.2.4 Single Atom Alloys for liquid phase hydrogenation reactions

The characterization and catalytic data displayed in Chapter 5 explicitly provides the evidence and benefit of SAA catalysts. However, further characterization in the form of Extended X-ray Absorption Fine Structure (EXAFS) could be used to probe the presence of Pt-Pt bonds. This should be completed before the reaction to determine the presence of clusters and during the furfural transformation. The operando experimentation would infer whether atom migration leads to aggregation or if the atomic entities remain isolated. The reusability of such materials should also be considered for future work, which would be accomplished by supplying a second amount of substrate after the 7 h period. By adding more furfural, the activated SAA should rapidly hydrogenate the molecule without removing the catalyst and suffer from deactivation as the surface atoms return to the bulk Cu or if surface layers of CuO form.

## 6.3 References


1 M. J. Taylor, L. Jiang, J. Reichert, A. C. Papageorgiou, S. K. Beaumont, K. Wilson, A. F. Lee, J. V Barth and G. Kyriakou, *J. Phys. Chem. C*, 2017, **121**, 8490–8497.

2 M. J. Taylor, L. J. Durndell, M. A. Isaacs, C. M. A. Parlett, K. Wilson, A. F. Lee and G. Kyriakou, *Appl. Catal. B Environ.*, 2016, **180**, 580–585.

3 L. Vitos, A. V. Ruban, H. L. Skriver and J. Kollár, *Surf. Sci.*, 1998, **411**, 186–202.

4 H. L. Skriver and N. M. Rosengaard, *Phys. Rev. B*, 1992, **46**, 7157–7168.

5 F. R. Lucci, M. D. Marcinkowski, T. J. Lawton and E. C. H. Sykes, *J. Phys. Chem. C*, 2015, **119**, 24351–24357.

6 B. C. Gates, *Chem. Rev.*, 1995, **95**, 511–522.

7 J. Liu, *ACS Catal.*, 2016, **7**, 34–59.

8 M. D. Marcinkowski, J. Liu, C. J. Murphy, M. L. Liriano, N. A. Wasio, F. R. Lucci, M. Flytzani-Stephanopoulos and E. C. H. Sykes, *ACS Catal.*, 2017, **7**, 413–420.

9 F. R. Lucci, J. Liu, M. D. Marcinkowski, M. Yang, L. F. Allard, M. Flytzani-Stephanopoulos and E. C. H. Sykes, *Nat. Commun.*, 2015, **6**, 8550.

10 J. Liu, F. R. Lucci, M. Yang, S. Lee, M. D. Marcinkowski, A. J. Therrien, C. T. Williams, E. C. H. Sykes and M. Flytzani-Stephanopoulos, *J. Am. Chem. Soc.*, 2016, **138**, 6396–6399.

11 G. Kyriakou, M. B. Boucher, A. D. Jewell, E. A. Lewis, T. J. Lawton, A. E. Baber, H. L. Tierney, M. Flytzani-Stephanopoulos and E. C. H. Sykes, *Science*, 2012, **335**, 1209–12.